ROMA TRE UNIVERSITY

DEPARTMENT OF MATHEMATICS AND PHYSICS

DOCTORAL SCHOOL IN MATHEMATICS AND PHYSICS

XXX CYCLE

PH.D. THESIS IN PHYSICS

WATER VAPOR MEASUREMENTS IN THE ARCTIC MIDDLE ATMOSPHERE BY MEANS OF A NOVEL GROUND-BASED MICROWAVE SPECTROMETER

Author:

GABRIELE MEVI

Tutor:

PROF. WOLFANGO PLASTINO

DOTT. GIOVANNI MUSCARI

Ph.D. program coordinator:

PROF. GIUSEPPE DE GRASSI

Rome, 2017

for my grandparents…

Index

Introduction

This Ph.D. thesis is centered on the development and improvement of the acquisition software and the data analysis algorithms of the ground-based 22.23 GHz spectrometer VESPA-22 (water Vapor Emission Spectrometer for Polar Atmosphere at 22 GHz), on the instrument installation and on the analysis of the first year of data collected. The instrument measures the 22.23 GHz water vapor emission line with a bandwidth of 500 MHz and a frequency resolution of 31 kHz, in order to retrieve the middle atmospheric water vapor profile and the atmospheric opacity.

The long time series of measurements provided by a ground spectrometer is a useful tool to study the Arctic climate, the atmospheric chemical composition and the air mass dynamic. The tropospheric water vapor is the major responsible for the greenhouse effect on the planet and also its stratospheric component has a measurable effect on the atmosphere and the surface radiation budget (Solomon et al., 2010). Water vapor is also related to many chemical processes occurring in the Arctic stratosphere, such as the ozone depletion (Solomon, 1999). The stratospheric water vapor, due to its long lifetime, can be also used as a tracer to study dynamic processes such as the polar vortex (Lahoz et al., 1993). The long term series of measurements of water vapor vertical profiles by ground-based spectrometers are particularly valuable to derive trends (Nedoluha et al., 1999).

VESPA-22 is at the moment installed at the THAAO (Thule High Arctic Atmospheric Observatory) located at Thule Air Base, Greenland (76.53°N, 68.70°E). It is designed to operate automatically with minimum need of maintenance; it employs an uncooled front-end characterized by a receiver temperature of about 180 K and its quasi-optical system presents a full width at half maximum angle of 3.5°. The instrument calibration is performed automatically by a noise diode; the emission temperature of this element is measured two times an hour through the observation of a black body at ambient temperature and of the sky at 60° of elevation. The retrieved profiles obtained inverting a 24-hour integration spectra present a sensitivity higher than 0.8 from about 25 to 72 km of altitude, a vertical resolution from about 12 to 23 km (depending on altitude) and an overall 1σ uncertainty between 5 and 12 %.

During the Ph.D. work, I have expanded, automated and further developed the VESPA-22 acquisition software, allowing the instrument to perform all the routine tasks in a remote location without needing of maintenance by local personnel. The instrument and the acquisition software proved to work reliably: VESPA-22 collected measurements for more than a year with few interruption periods characterized by very poor weather.

I also improved the measurement procedures used by the instrument and data analysis codes. In particular, many efforts of this work were directed to the development of a reliable retrieval algorithm, used to obtain the vertical water vapor concentration profiles from the measured spectra.

I participated in the VESPA-22 installation campaign occurred in July 2016 at Thule and to a preparatory campaign which took place on February-March 2016 in order to setup the THAAO laboratory to host the instrument.

I analyzed the first year of data of the instrument, from July 2016 to July 2017 and compared VESPA-22 and satellite instrument Aura/MLS (Waters et al., 2006) water vapor datasets in order to evaluate VESPA-22 results. In the sensitivity range of VESPA-22 retrievals, the intercomparison between VESPA-22 dataset and Aura/MLS dataset convolved with VESPA-22 averaging kernels reveals a correlation coefficient of about 0.9 or higher and an average difference reaching its maximum of -5% or -0.2 ppmv at the top of the sensitivity range.

I employed the VESPA-22 opacity measurements collected during fair weather to obtain an estimate of precipitable water vapor (PWV) through a fit with the measurements of the HATPRO (Humidity And Temperature Profilers) radiometer (Rose and Czekala, 2007) installed at the THAAO, as described by the work of Deuber et al. (2005). The difference between the PWV values measured by HATPRO and estimate by VESPA-22 allows the estimation of the uncertainty of this technique, equal to 8%.

This thesis is divided into 6 chapters. Chapter 1 is a general introduction to the importance of water vapor in the Arctic atmosphere. In chapter 2 the general theoretical concept on which is based the instrument are shown. Chapter 3 describes the instrumentation, the acquisition software, the operations executed by the instrument and measurement techniques employed by VESPA. Chapter 4 is dedicated to the VESPA-22 retrieval algorithm, while in Chapter 5 the uncertainty of the retrieved profiles is shown, with the contributions of the various parameters used in data analysis. Chapter 6 reports the VESPA-22 preparatory and installation campaigns, the first year of data collected from 15 July 2016 to 2 July 2017 and the comparison with MLS dataset. The data have been analyzed to evaluate the descending rate of the air masses inside the polar vortex and the correlation of the measured water vapor mixing ratio with the potential vorticity during winter. The data collected during fair weather were used to evaluate the amount of precipitable water vapor with the procedure described by Deuber et al. (2005).

Part of this work was submitted to the AMT (Atmospheric Measurement Techniques) journal with the title “VESPA-22: a ground-based microwave spectrometer for long-term measurements of Polar stratospheric water vapor” for the publication on the special issue “Twenty five years of operations of the Network for the Detection of Atmospheric Composition Change (NDACC)” with authors Gabriele Mevi, Giovanni Muscari, Pietro Paolo Bertagnolio, Irene Fiorucci, and Giandomenico Pace.

The work was also the object of an oral presentation at the EGU 2017 General Assembly and at the 2015 and 2016 SIF (Società Italiana di Fisica) Congresses. It was also the subject of a poster presentation at the ARCA (ARctic present Climatic change and pAst extreme events) meeting in 2016.

Chapter 1

The water vapor in the atmosphere

1.1 Sources, sinks and general circulation

The main source of water vapor in the atmosphere is the surface evaporation. The water vapor concentration is governed by the strong dependence of the saturation vapor pressure on temperature $e_s(T)$, described by the Clausius-Clapeyron relation

$$e_s\left(T\right) = e_s\left(T_0\right) e^{-\frac{L(T)}{R}} \quad , \tag{1.1}$$

where T_0 is the reference temperature of 300 K, $L(T)$ is the evaporation latent heat and R is the water vapor gas constant. The excess water vapor condenses or sublimes to form clouds and precipitation. As a consequence of the constant and negative temperature laps rate of approximately −5 K/km, the water vapor concentration shows a decrease in the troposphere with a scale height in the order of 2 km (Figure 1.1). Because of this steep decrease, about the 50% of the water vapor columnar content is concentrated in the first 1.5 km of the troposphere and above 5 km of altitude is present about 5% of the total columnar content; this percentage decreases to less than 1% above the tropopause. In the stratosphere, the air is a thousand times drier with respect to the lower troposphere. The water vapor enters in stratosphere at the tropics, due to deep convection phenomena of this region. The tropical tropopause acts as a cold trap, condensing the major part of the ascending air water vapor and leading to a freeze-dried stratosphere. The water vapor slowly ascends to the higher atmospheric layer and is transported poleward from planetary waves following the Brewer-Dobson circulation.

A second important source of stratospheric moisture is the methane oxidation and its reaction with the ultraviolet radiation (Remsberg et al., 1984), summarized by the Eq. (1.2) and (1.3)

$$CH_4 + 3O_2 + h\nu \rightarrow 2H_2O + CO + O_3 \quad , \tag{1.2}$$

$$CH_4 + OH \rightarrow CH_3 + H_2O \quad . \tag{1.3}$$

Brewer (1949) stated the need for a downward motion above the poles that compensates for the ascending branch over the equator. This large-scale subsidence is observed over the winter poles, where air from the upper part of the atmosphere descends to the lower stratosphere (Lahoz et al., 1993).

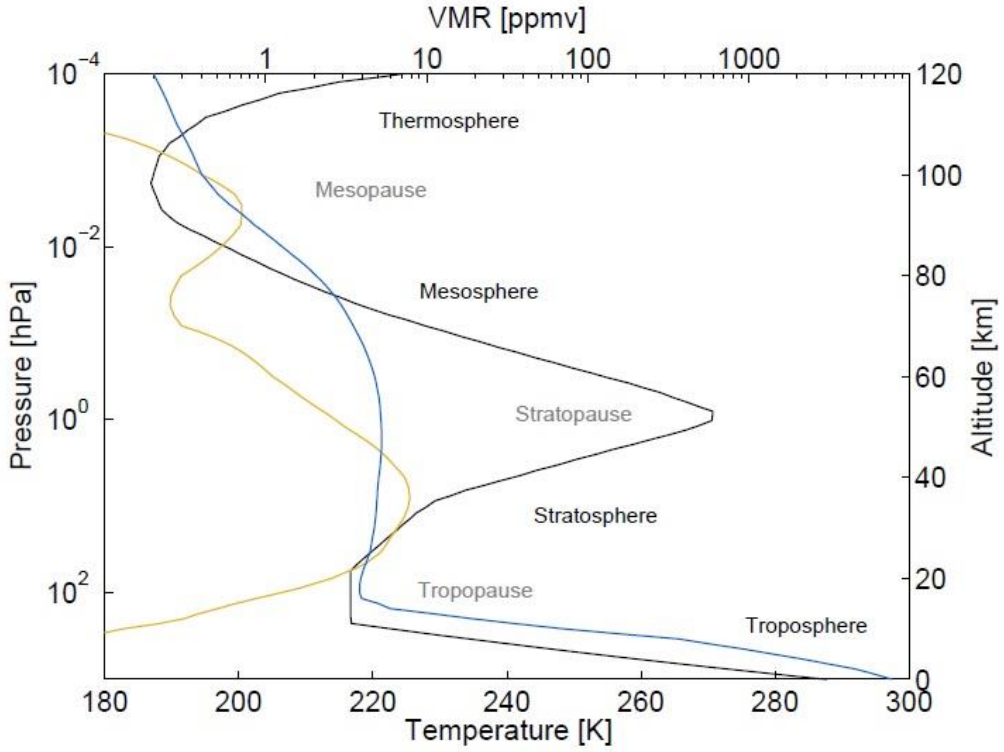

Figure 1.1: The mean temperature (black line), ozone (yellow line) and water vapor (blue line) concentration profiles from US standard atmosphere of 1976.

Figure 1.2 is a scheme of the Brewer-Dobson circulation: the water vapor enters in the stratosphere from the deep convection at the tropics and is transported poleward by the planetary waves along the isentropic surfaces. In the scheme the dashed and solid tiny lines represents the isentropic surfaces identified by their potential temperature value whereas the tick line is the tropopause.

Figure 1.3 displays the monthly and zonal mean of water vapor collected by the satellite instrument AURA/MLS (Waters et al., 2006) on August 2008 and February 2009. The subsidence is clearly visible in the winter pole and is more pronounced in the Antarctica, due to a stronger polar vortex (see next section), causing the maximum of water vapor concentration at 10 hPa. A minimum in water vapor concentration characterizes the winter polar troposphere and the tropical tropopause, due to the low temperature of the tropical tropopause leading the precipitation of the major part of the water vapor.

The water vapor is removed in the upper mesosphere and thermosphere by photolysis from the ultraviolet radiation, Eq. (1.4) and (1.5), whereas in the stratosphere and the lower mesosphere it reacts with atomic oxygen, Eq. (1.6).

The destruction processes dominate over the methane oxidation at about 50 km.

$$H_2O + h\nu\left(\lambda < 200\,nm\right) \rightarrow OH + H \ , \tag{1.4}$$

$$H_2O + h\nu\left(\lambda < 147\,nm\right) \rightarrow H_2 + O\left(^1D\right) \quad , \tag{1.5}$$

$$H_2O + O\left(^1D\right) \rightarrow 2OH \ . \tag{1.6}$$

The water vapor has a permanence time in stratosphere of the order of months, therefore can be used as a tracer to study the air masses dynamic.

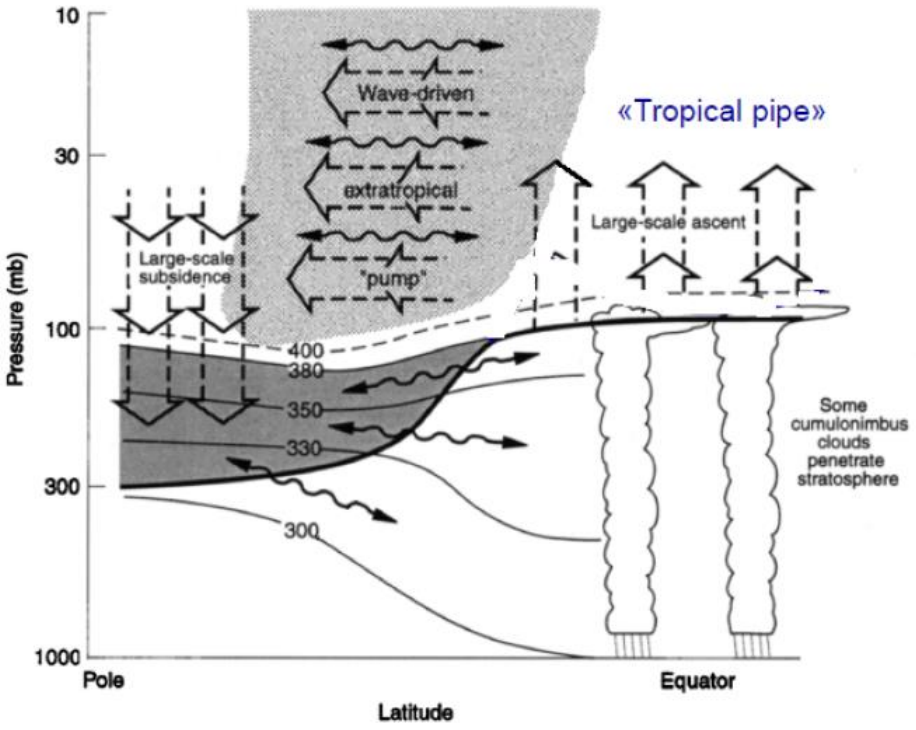

Figure 1.2: A scheme of the Brewer-Dobson circulation (Holton et al., 1995) in which it is visible the large scale subsidence occurring at the poles in winter. The thin lines represent the isentropic surfaces with their respective potential temperatures whereas the thick line represents the tropopause.

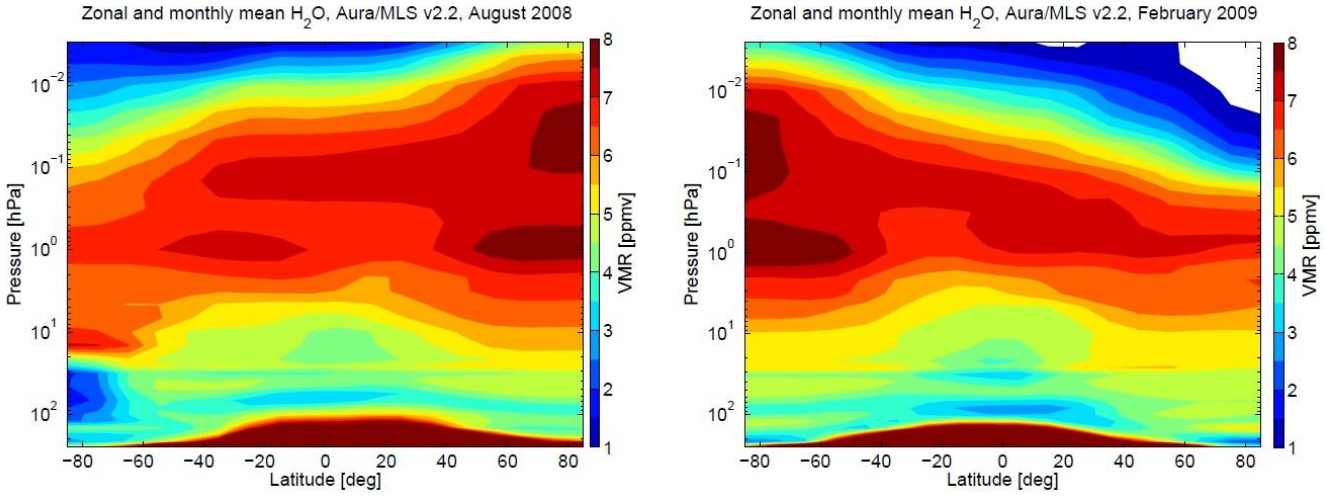

Figure 1.3: The zonal and monthly mean of H_2O measured by AURA/MLS satellite on August 2008 (left panel) and February 2009 (right panel) (from Figure 1.2 of Haefele, 2009).

1.2 The water vapor in the polar atmosphere

The polar atmosphere is the location of some unique phenomena caused by the low temperature and the lack of light during winter. During polar night, a strong temperature gradient with respect to the lower latitude regions is the cause of the formation of strong winds that insulate the polar stratosphere, avoiding the intrusion of warmer air from midlatitude regions. This phenomenon is called polar vortex. In winter, therefore, the temperature inside the vortex drops to very low values, reaching 180 K in the Antarctic stratosphere (Figure 1.4). The polar vortex acts with more efficiency in Antarctica, whereas in the Arctic this phenomenon is disturbed by enhanced wave activity due to the disposition of the continents in the Northern hemisphere. The polar vortex ends in spring when the return of the light provokes the disappearing of the thermal gradient that produces the zonal winds.

The low temperature inside the polar vortex allows the formation of Polar Stratospheric Clouds (PSC). The PSCs are composed primarily of ice particle and nitric acid and contributes to the removing of water vapor from polar stratosphere through the sedimentation as ice crystals. The sedimentation acts with more efficiency in Antarctica, where a more stable polar vortex determines a colder stratosphere, whereas in the Arctic, where the vortex is weaker, the temperature falls only occasionally below the threshold for clouds formation. Figure 1.4 shows an example of the winter temperature time series measured in Arctic and Antarctica during years 1978-2002 in stratosphere, (WMO/UNEP International Scientific Assessments of Ozone Depletion: 2010, available at https://www.esrl.noaa.gov/csd/assessments/ozone/2010/). The Arctic is characterized by higher temperatures and a larger variability.

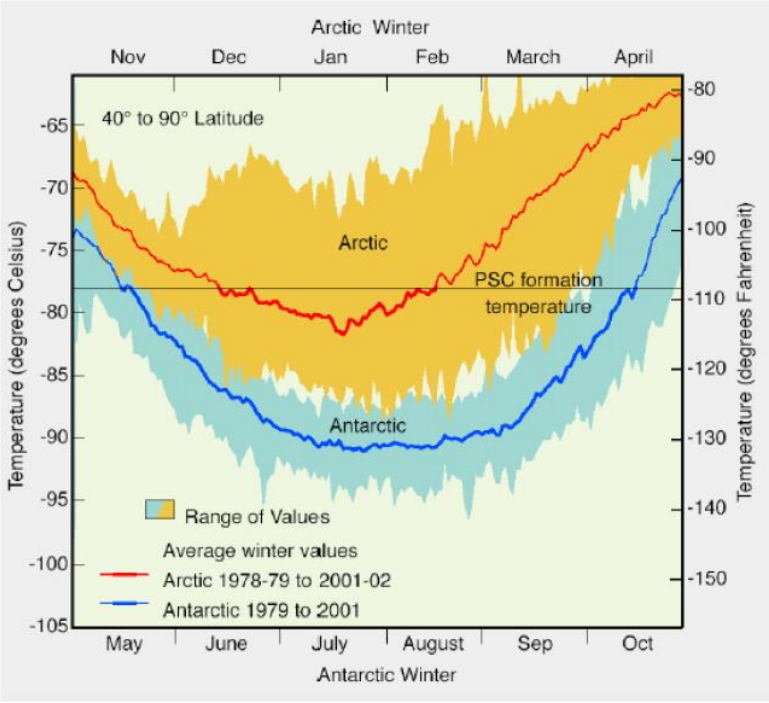

Figure 1.4: The winter temperature measured in the Arctic/Antarctic stratosphere during years 1978-2002. The yellow and cyan colored areas represent the area covered by the different years temperature time series measured respectively in Arctic and Antarctica. The red and cyan lines are the mean temperatures over time of respectively Arctic and Antarctica, whereas the black line represents the threshold temperature for PSC formation.

In the polar mesosphere during summer, a large scale upwelling of the air mass can be measured, with water vapor concentration that can reach about 10-15 ppmv (Summers and Siskind, 1999), visible also in Figure 1.3. Because of the adiabatic cooling, the polar mesosphere is the coldest point in the atmosphere. The low temperature allows the formation of a second layer of ice clouds, the Polar Mesospheric Clouds (PMC, Fieder et al., 2009) that can be found in a thin layer between 82 and 84 km.

The water vapor concentration profile can show a local maximum at about 68 km (Bevilacqua et al., 1985; Nedoluha et al., 1996). The presence of this maximum is not in accord with the chemistry illustrated in Section 1.1; therefore Summers and Siskind (1999) suggest heterogeneous reactions on the surface of meteoric dust.

Water vapor does not react directly with the major part of chemical species present in the atmosphere. However, through reactions (1.4) and (1.6) it is indirectly involved in many chemical processes as source of hydroxyl radical. This particle is one of the most important oxidizing agents in the atmosphere and plays an important role in the ozone destruction that can be observed in the early spring at the poles (Summers and Conway, 2000). Water vapor contributes to the ozone depletion also through the formation of the PSC. The ozone depletion is caused primarily by the interaction of the ozone with the chlorine

compounds. During winter inside the polar vortex, the temperature can fall below 188 K at 20 km provoking the formation of the PSC and allowing the chlorine compounds deposition on their surface. With the return of the Sun in spring, the chlorine molecules photo-dissociation provokes the catalytic destruction of the ozone. The PSCs accelerate the destruction processes granting a catalytic surface where the reactions can take place. The insulation of the air inside the polar vortex can lead to the almost complete depletion of the ozone layer during spring.

The ozone depletion is more pronounced in the Antarctica with respect to the Arctic, due to the more stable polar vortex in the southern hemisphere. However, during the last decade extremely cold winters have occasionally occurred in the Arctic stratosphere, allowing the formation of a stable vortex with ozone depletion comparable to the Antarctica (Manney et al., 2011).

1.3 The water vapor trend and the radiation budget

The atmospheric composition regulates the surface temperature through the greenhouse effect. The water vapor is the dominant contributor to infrared opacity and is the major greenhouse gas of the planet, which accounts for about 60% of the total greenhouse effect (Solomon et al, 2010). The anthropogenic activities are modifying the atmospheric composition through the emissions of carbon dioxide, methane and other greenhouse gases. These emissions rise the surface temperature that, according to Eq. (1.1) provokes an increase of water vapor concentration in the atmosphere that in turn increases the greenhouse effect (with the assumption that relative humidity remains constant). Approximately half of the predicted warming in response to an anthropogenic increase in greenhouse gases such as CO_2 is due to this water vapor feedback effect (Held and Soden 2000; Soden et al. 2005).

Figure 1.5 shows the zonally-averaged, annual temperature anomalies from land stations only (data from Jones et al., 1999) as a function of latitude and time (from Alley et al., 2003). Although this figure does not include information for the ice-covered Arctic Ocean, it is clear that the high-latitude terrestrial environment has experienced significant variability, more so than have low latitudes. Substantial high-latitude warming from about 1920 to 1940 was followed by cooling until about 1970 and then another period of marked warming that extends through the present. The earlier warming was confined largely to high latitudes. The more recent warming shown in Figure 1.5 is clearly very different in that it appears in essentially all latitudes examined. Although the major part of the water vapor is in troposphere, the stratospheric component of this gas has an important role in the radiative budget. Stratospheric water vapor constitutes a small positive anthropogenic radiative forcing considering the portion that is produced by methane oxidation, as methane concentrations are altered by human activities (Forster and Shine 2002; Forster et al. 2007). More water vapor in stratosphere results in cooling of the upper atmosphere and a warmer tropopause and lower stratosphere (Solomon et al., 2010).

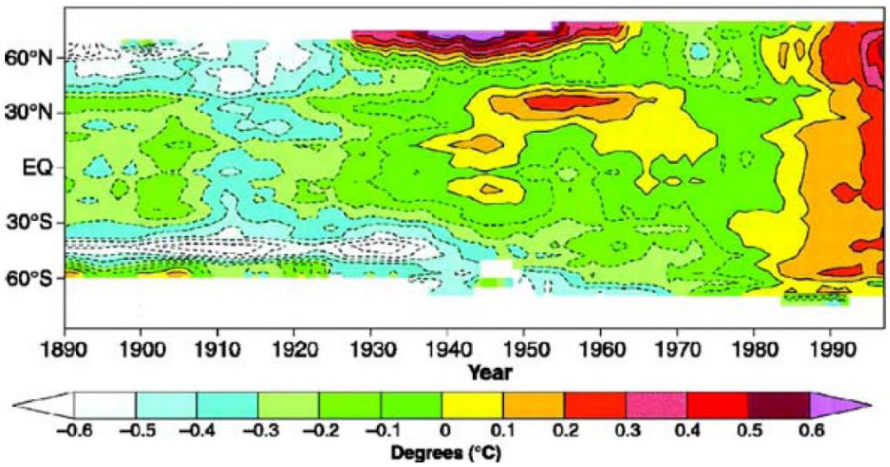

Figure 1.5: The surface temperature variation (zonal mean) measured at different latitudes versus time (Alley et al., 2003, original data from Jones et al., 1999)

The processes that lead to long-term variations in stratospheric and mesospheric water vapor are not completely understood. Positive trends were observed during the period from 1980 to 2010 (Nedoluha et al., 1999, Rosenlof et al., 2001, Hurst et al., 2011). Figure 1.6 displays the water vapor frost point hygrometer measurements presented by Hurst et al. (2011). A positive trend characterizes the years 1980-2000 (Period 1 and 2 in the figure) with an inversion of tendency after 2000 (Period 3), when a drop of water vapor of about -0.4 ppmv was estimated (Randel et al., 2006) and again a positive trend characterizing the last 5 years analyzed from 2005 to 2010. The climatic models did not predict the tendency inversion of the Period 3.

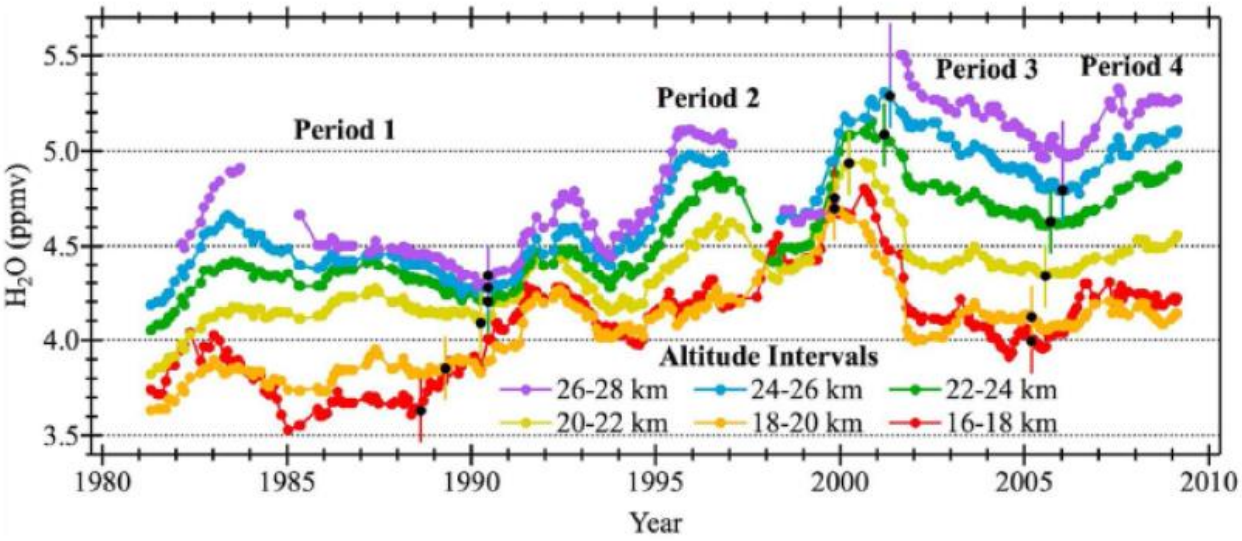

Figure 1.6: Frost point hygrometer measurements at Boulder (Colorado) (Hurst et al., 2011) at different altitudes, from 1981 to 2009.

Oltmans et al. (2000) suggested that only one half of these changes are related to the increase of methane due to the anthropogenic activities. This trend is going along with a cooling trend in the tropical tropopause, which would be likely to cause a negative trend in stratospheric water vapor (Simmons et al., 1999; Randel et al., 2000). Solomon et al. (2010) relate the water vapor variations with an increase of the deep convective phenomena and with a diminishing of the air mass flux in the tropical circulation that allows a more efficient methane oxidation, with more formation of water vapor. Rosenlof and Leid (2008) suggest changes in the tropical tropopause dynamic caused by wave driving and changing in the sea surface temperatures.

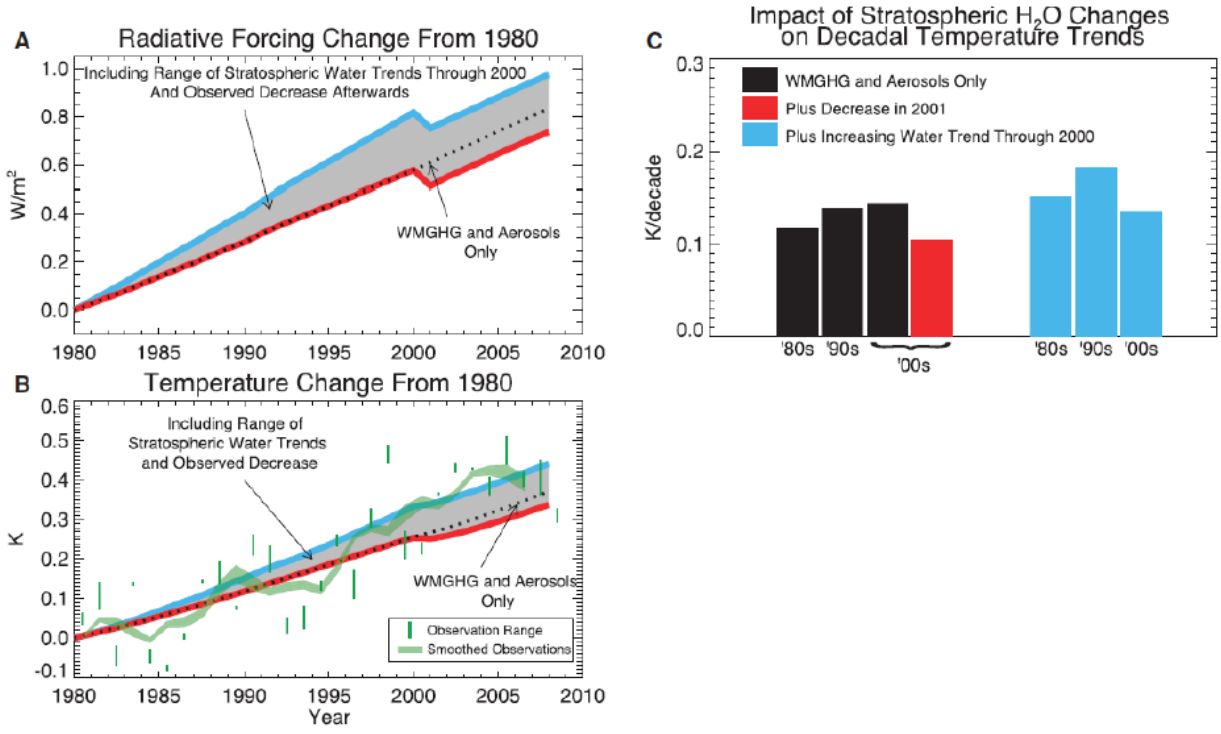

Figure 1.7: Graphs from Solomon et al. (2010) that evidence the importance of stratospheric water vapor in the surface warming rate. The cyan/red line is the prediction of a model that take/not take into account the stratospheric water vapor contribution to the radiative forcing (panel a) and to the temperature variation (panel b). The green line represents the observations. Panel c presents a summary of the predicted warming rates by the different models.

The work of Solomon et al. (2010) reveals the importance of taking into account the stratospheric water vapor and its variation in climatic studies. The authors account 10% of surface warming rate to the stratospheric water vapor variation measured from 1980 to 2000. The same authors assert that the decrease measured after 2000 lowered the surface warming rate. A summary of these results is shown in Figure 1.7, from Solomon et al. (2010). The long term series of measurements of water vapor mixing ratio vertical profiles are of particular interest in the Arctic region. This region, due to the Arctic Amplification (Serreze and Francis, 2006), shows an enhanced sensitivity to the climate change as can be seen by the relative maximum at high latitude that can be observed in the last decades of Figure 1.5. This is caused by a positive

feedback that links the atmospheric composition, surface temperature variations and the ice coverage. The increase of the surface temperature provokes the melting of the ice coverage, reducing the surface albedo. This, in turn, leads an increase of visible radiation absorbed by earth and sea that is emitted as long wave radiation.

In this scenario, the long term series of measurements of water vapor vertical profiles by ground-based spectrometer are particularly valuable to derive trends and allow intercalibrating consecutive satellite missions to compile global long term data sets.

Chapter 2

The measurement physical principles

2.1 Middle atmospheric water vapor remote sensing by microwave spectroscopy

The Polar Regions are complex systems in which the unique conditions allow the observation of many peculiar phenomena. In the Arctic, the strong correlation between atmosphere, cryosphere, dynamical processes leads to a greater sensibility to the climatic changes with respect to other latitudes. As explained in the previous chapter, the water vapor plays a central role in many climatic and chemical processes of the region, so the measurements of this gas in both troposphere and stratosphere are crucial for improving the knowledge of Arctic system.

The water vapor in troposphere and stratosphere is measured mainly through radiosondes and spectrometers. The radiosondes can obtain water vapor profiles with higher precision and vertical resolution with respect to the indirect measurements. However, the observations number is limited by the measurements high cost; furthermore, the measurements are limited to the troposphere and lower stratosphere up to about 25 km of altitude for the normal radiosondes, so they do not provide information on upper stratospheric and mesospheric water vapor. The ozonesondes can reach upper altitudes but the cost of this measurement technique is even higher.

The spectroscopy is an ideal technique to obtain long term measurements of atmospheric components. The vertical concentration profiles can be retrieved deconvolving the measured spectra. Installing a spectrometer on a satellite allows the instrument measurements to cover the entire globe. The satellite instruments perform often a limb sounding measurement, reaching a higher level of precision with respect to a ground-based observation. However, a satellite mission presents great costs and the lifetime of the spectrometer is limited to the mission life span, often less than five years.

The ground-based spectroscopy is a less expensive and reliable technique to obtain the long term measurements needed to characterize the atmosphere of a particular region. The ground-based instruments, given to their potentially long life span and reliability, can be used as a reference to compare and calibrate satellite data from different missions.

The instrument described in this work is a microwave spectrometer; microwave spectrometers observe the emission from molecular rotational transitions. This measurement technique was born in the second part of ’70 to retrieve the atmospheric trace gases concentration. The microwave spectrometers present several advantages with respect to instruments working at other frequencies (such as infrared spectrometer):

- many atmospheric species present rotational states well populated at the typical temperatures of troposphere, stratosphere and mesosphere;
- the rotational transitions are at equilibrium in both stratosphere and mesosphere;
- at this low frequencies, the contribute of the scattered radiation in the radiative transfer equation can be neglected, simplifying the measurement equations;
- the microwave spectrometers measure the molecular emission, so they can operate on both day and night;
- microwave spectrometers are relatively less expensive with respect to infrared or visible spectrometers.

However, this technique presents some disadvantages:

- the integration period needed to reach a satisfying signal to noise ratio can be of the order of hours;
- instruments observing stratosphere and mesosphere need an atmosphere characterized by a low opacity in order to obtain measurements with an acceptable signal to noise ratio. For this reason, the ideal installation sites are the Polar Regions and all the areas with a low amount of precipitable water vapor, such as high mountains or desert sites.

Figure 2.1 shows the atmospheric emission spectrum in the microwave region (0-300 GHz) as seen from different altitudes. The major part of oxygen and water vapor are concentrated in the first kilometers of the troposphere, so the minor intensity of these gases emissions at higher altitude is due to the lower amount of molecules observed by the instrument. The broadening of the emission lines is related to the atmospheric pressure, as it will be explained in Section 2.3.

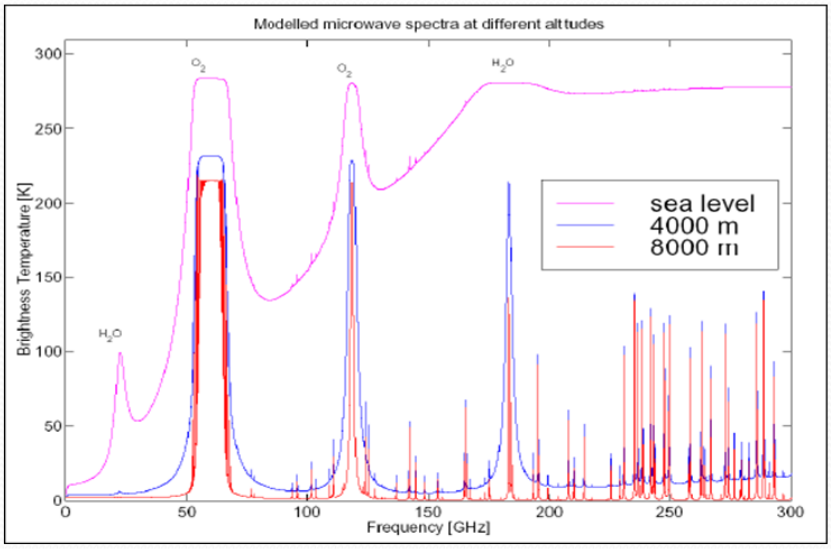

Figure 2.1: The microwave (0-300 GHz) emission spectrum of the atmosphere as it would be observed from different altitude levels (Kaempfer et al., 2013).

The instrument described in this work observes the water vapor emission line at 22.23 GHz. Although the water vapor transition at this frequency presents a reduced intensity with respect to other water vapor emission line such as the 183 GHz line, the measurement at 22.23 GHz presents two main advantages.

- The 183 GHz region at sea level is characterized by a higher opacity with respect to the 22.23 GHz region, leading a larger absorption of the stratospheric signal by troposphere and reducing the signal to noise ratio of the measurements.
- The 183 GHz front-end electronics, in particular the low noise amplificators, require a liquid nitrogen refrigeration system in order to properly work, whereas the 22.23 GHz signals can be amplified by low noise amplificators at ambient temperature. Furthermore the amount of liquid nitrogen required for a 22.23 GHz spectrometer can be reduced to the just several tens of liters at year, used for the calibration operations. These peculiarities fit better the requirement of a reliable instrument able to work automatically in a remote observation situ with minimum need of local maintenance.

2.2 The Schwarzschild equation in the microwave region

The radiative transfer is the physical theory describing the radiation absorption and emission processes in gases. The main equation describing the radiative transfer in the atmosphere is the Schwarzschild equation. The wavelength at 22.23 GHz is about 1 cm, much larger of the majority of atmospheric hydrometeors. According to Thompson scattering description, the scattering contribution can be neglected and the radiative transfer equation can be composed just of absorption and emission terms.

This section presents the solution for the microwave radiation propagation in absence of scattering. The quantities characterized by the subscript ν are frequency dependent. Before describing the radiative transfer equations it is useful to describe the *emission coefficient* at a certain frequency $\varepsilon_{\nu,s}$ of an object, defined as the ratio between the emissions produced by the object itself and the emission of a black body at the same physical temperature at that frequency. According to this definition the emission coefficient is a dimensionless number with the property $\varepsilon_{\nu,s} < 1$. In a similar way the *absorption coefficient* at a certain frequency $\alpha_{\nu,s}$ of an object can be defined as the ratio between the radiation absorbed by the object itself and the radiation absorbed by a black body at the same physical temperature at that frequency. In a gaseous medium such as the atmosphere, the absorbing and emitting power of the gas molecules at a certain frequency can be described by the absorption and emission coefficient for unit of length, α_ν and ε_ν respectively, with the dimension of $[lenght]^{-1}$.

The Eq. (2.1) is the Schwarzschild equation for the microwave region and describes the propagation of the radiation in the atmosphere with the negligible scattering approximation.

$$\frac{dI_\nu}{ds} = -I_\nu \alpha_\nu + \varepsilon_\nu B_\nu (T) \ . \tag{2.1}$$

The first and second term on the right side respectively represents the variation of the radiation due to absorption and emission processes occurring in the radiation path. $B_\nu(T)$ is the black body emission described in Eq. (2.2).

$$B_\nu = \frac{2h\nu^3}{c^2} \frac{1}{e^{\frac{h\nu}{kT}} - 1} \ , \tag{2.2}$$

where h and k are respectively the Planck and Boltzmann constants. The *absorption coefficient* α_ν of the gas layer depends on the gas density ρ and the *extinction coefficient* κ_ν $[length^2]$, a spectroscopic parameter depending on both frequency and gas temperature.

$$d\alpha_\nu (s,T) = \rho(s)\kappa_\nu (T) ds \ , \tag{2.3}$$

In the atmosphere layer of interest for this work, the Kirkoff law, Eq. (2.4), relates the emission and absorption coefficients.

$$\alpha_\nu = \varepsilon_\nu \ . \tag{2.4}$$

In order to obtain a simple solution, Eq. (2.1) can be integrated following the line of sight of the instrument from the ground s_0 to the top of the atmosphere s_{toa}, obtaining using also Eq. (2.4):

$$I_\nu (s_0) = I_\nu (s_{toa}) e^{-\tau_\nu (s_{toa})} + \int_{s_0}^{s_{toa}} B_\nu \left(T(s)\right) e^{-\tau_\nu (s)} \alpha_\nu (s) ds \ , \tag{2.5}$$

where $\tau_\nu(s)$ is the atmospheric opacity defined according to Eq. (2.3) as

$$\tau_\nu (s) = \int_{s_0}^{s} \rho(s') \kappa_\nu \left(T(s')\right) ds' = \int_{s_0}^{s} \alpha_\nu (s') ds' \ . \tag{2.6}$$

From Eq. (2.6) a relation between atmospheric opacity and atmospheric absorption can be obtained.

$$\alpha_\nu = \frac{d\tau_\nu}{ds} \ . \tag{2.7}$$

In Eq. (2.5) the term on the left side is the signal that can be measured by an instrument observing the atmosphere on the line sight defined by the s parameter. The first term on the right side describes the emission coming from outside the atmosphere (generally the cosmic background radiation in the microwave region, defined as the emission of a black body at a 2.725 K), whereas the second term is the sum of emission coming from the different atmospheric layers in the line of sight. Both the emission terms are attenuated by the atmospheric opacity calculated from the instrument to the emission point.

In the microwave region, the black body emission function can be expressed using the Rayleigh-Jeans approximation

$$B_\nu = \frac{2h\nu^3}{c^2}\frac{1}{e^{\frac{h\nu}{kT}}-1} \simeq \frac{2h\nu^3}{c^2}\frac{kT}{h\nu} = \frac{2kT}{\lambda^2} \ , \tag{2.8}$$

where λ is the wavelength. Eq. (2.8) shows a linear relation between physical temperature and emitted radiation.

The *brightness temperature* of a body T_ν can be defined as the temperature of a black body emitting the same amount of radiation of that body at a certain frequency.

Following this definition, the body emission in the microwave region can be described according to Eq. (2.9)

$$I_{\nu,e} = B_\nu\left(T_\nu\right) \simeq \frac{2kT_\nu}{\lambda^2} \ . \tag{2.9}$$

Therefore from Eq. (2.1)

$$I_{\nu,e} = \alpha_{\nu,s} B_\nu\left(T\right) \simeq \alpha_{\nu,s}\frac{2kT}{\lambda^2} \ . \tag{2.10}$$

Therefore, using the Rayleigh-Jeans approximation the brightness temperature can be expressed as

$$T_\nu = \alpha_{\nu,s} T \ . \tag{2.11}$$

The black body function represents the maximum emission for a physical body at a certain temperature, so $a_{\nu,s} \leq 1$ and $T_\nu \leq T$. Expressing the signal received and the extra-atmospheric signal in terms of brightness temperatures and using the Rayleigh-Jeans approximation Eq. (2.5) can be modified as

$$T_\nu\left(s_0\right) = T_\nu\left(s_{toa}\right)e^{-\tau_\nu\left(s_{toa}\right)} + \int_{s_0}^{s_{toa}} T\left(s\right)e^{-\tau_\nu\left(s\right)}\alpha_\nu\left(s\right)ds \ . \tag{2.12}$$

According to Eq. (2.12) and (2.8) in this work all signal intensities are expressed in brightness temperature.

The Eq. (2.12) describes the propagation of microwave radiation in a generic direction. However, it can be useful to refer the propagation in relation to the *elevation angle* θ that is defined as the complementary angle with respect to the zenithal angle and it is the angle of the propagation path with respect to the horizontal plane.

The Eq. (2.13) describes the relation between ds and dz with respect to the elevation angle θ

$$ds = dz\mu\left(\theta\right) \ , \tag{2.13}$$

where $\mu(\theta)$ is the *air mass factor* and represents the geometrical variation of the distance on the propagation path *s* with respect to the vertical axis *z*. In general, the air mass factor takes into account the Earth curvature, the elevation angle and the altitude of the instrument; for ground measurements, a good approximation is expressed by the Eq. (2.14) , (de Zafra, 1995),

$$\mu\left(\theta\right) = \frac{R + z_{trop}}{\sqrt{\left(R + z_{trop}\right)^2 - \left(\left(R + z_0\right)\cos\left(\theta\right)\right)^2}} \ , \tag{2.14}$$

where R is the Earth radius, $z_{trop} = 3\ km$ and z_0 is the altitude of the instrument installation site (220 m).

Eq. (2.12) can be simplified in case of horizontal homogeneous atmosphere that allows neglecting the dependence of the different variables with respect to the horizontal axis x and y. This condition is useful to represent the stratosphere and mesosphere, in which the horizontal variation scale is larger than the dimensions of the portion of atmosphere observed by the instrument, and the troposphere, during fair weather or with a uniform cloudy coverage. In case of horizontal homogeneous atmosphere the Eq. (2.12) and (2.6) can be simplified

$$\tau_\nu(s) = \int_{z(s_0)}^{z(s)} \alpha_\nu(z')\mu(\theta)dz' = \int_{z_0}^{z} \alpha_\nu(z')\mu(\theta)dz' = \mu(\theta)\tau_\nu(z) \ , \tag{2.15}$$

$$T_\nu(z_0) = T_\nu(z_{toa})e^{-\tau_{\nu,z}(z_{toa})\mu(\theta)} + \mu(\theta)\int_{z_0}^{z_{toa}} T(z)e^{-\tau_{\nu,z}(z)\mu(\theta)}\alpha_\nu(z)dz \ , \tag{2.16}$$

where the integral variable is now z according to Eq. (2.13). $\tau_\nu(z)$ is the *atmospheric zenithal opacity*, the opacity along the z-axis. The Eq. (2.15) and (2.16) are the main equations describing the radiative transfer processes in this work.

2.3 Concepts of microwave spectroscopy

Atoms and molecules can only assume quantized internal energetic states. An atom or molecule can change its internal state by the absorption and emission processes through the interaction with a photon. The frequency ν_{mn} of this photon is proportional to the energy difference between the two states E_m and E_n:

$$\nu_{mn} = \frac{E_m - E_n}{h} \ , \tag{2.17}$$

where h is the Planck constant. In the microwave region, the water vapor most important transitions produce photons at the frequencies of 22.235 GHz and 181.235 GHz. The instrument on which is based this work observes the 22.235 GHz transition between the rotational states characterized by the quantum numbers $6_{16} \rightarrow 5_{23}$.

The molecular emissions cannot be described just as monochromatic emissions. A single transition is associated with an interval of possible frequencies centered on ν_{mn}. The *spectral form* relates the emission intensity and the frequency and it is described by the function $F(\nu, \nu_{mn})$.

The first physical principle determining the spectral form is the Heisenberg Indetermination Principle

$$\Delta\nu > \frac{1}{2\pi\Delta t} \ . \tag{2.18}$$

According to Eq. (2.18) for a certain emission line, the photons are generated following a probability density function with its maximum value centered on the transition frequency ν_{mn}. The full width at half maximum of this probability density

function is inversely proportional to the decay time of the higher energy state. This process is also called natural broadening and can be neglected for atmospheric studies in the microwave region.

Another effect determining the spectral form is the Doppler Effect. The molecular thermal agitation moves the molecules with respect to the observer. The Doppler Effect modifies the observed frequency according to the Eq. (2.19)

$$\nu = \nu_{mn}\left(1+\frac{V\cos(\gamma)}{c}\right), \tag{2.19}$$

where ν is the measured frequency and $V\cos(\gamma)$ the velocity component along the observatory direction and c the speed of light. The Doppler function $F_D(\nu,\nu_{mn})$ that describes the intensity of the transition as a function of frequency is represented in Eq. (2.20) according to Maxwell velocity distribution

$$F_D(\nu,\nu_{mn}) = \frac{c}{u\sqrt{\pi}\nu_{mn}} e^{-\frac{c^2(\nu-\nu_m)^2}{u^2\nu_{mn}^2}}, \tag{2.20}$$

where $u = \sqrt{2kT/m}$ with m the molecular mass. The Doppler Effect gives a Gaussian shape to the emission line with a half width at half maximum $\Delta\nu_D$ equal to

$$\Delta\nu_D = \frac{u}{c}\sqrt{\ln 2}\nu_{mn}\ . \tag{2.21}$$

For the water vapor transition at 22.235 GHz at 300 K, $\Delta\nu_D$ is equal to 32.5 kHz. The Doppler broadening is relevant in determining the emission line shape in the upper stratosphere and mesosphere.

Another important effect in the atmosphere is the pressure broadening, caused by the molecular collisions. These collisions reduce the decay time of the higher energy state, provoking a broadening of the spectral line according to the Eq. (2.22). An alternative way to explain the effect is to take into account the molecules translation energy. This energy can interact with the photon energy, increasing or decreasing it and allowing the emission or absorption of photons with different frequency with respect to the transition frequency. The number of collisions is related to the gas pressure *P*. There are several models describing the pressure broadening; Eq. (2.22) uses a Lorentzian line shape (apart from the multiplying factor, $(\nu/\nu_{mn})^2 \approx 1$ for the microwave frequencies)

$$F_L(\nu,\nu_{mn}) = \frac{1}{\pi}\left(\frac{\nu}{\nu_{mn}}\right)^2 \frac{\Delta\nu_L}{(\nu-\nu_{mn})^2+\Delta\nu_L^2} \tag{2.22}$$

$$\Delta\nu_L = wP(z)\left(\frac{T_0}{T(z)}\right)^x, \tag{2.23}$$

Where *w* and *x* are constants and T_0 is a reference temperature. The pressure broadening is the most relevant effect determining the emission line shape in the troposphere and stratosphere. However, Eq. (2.22) can be used up to about 50 km

of altitude; at higher altitudes, where the pressure drops, the pressure broadening and Doppler broadening effects are comparable, therefore a more accurate description of the spectral form that involves both the phenomena is required. Above 80 km of altitude, the line shape is dominated by Doppler Effect.

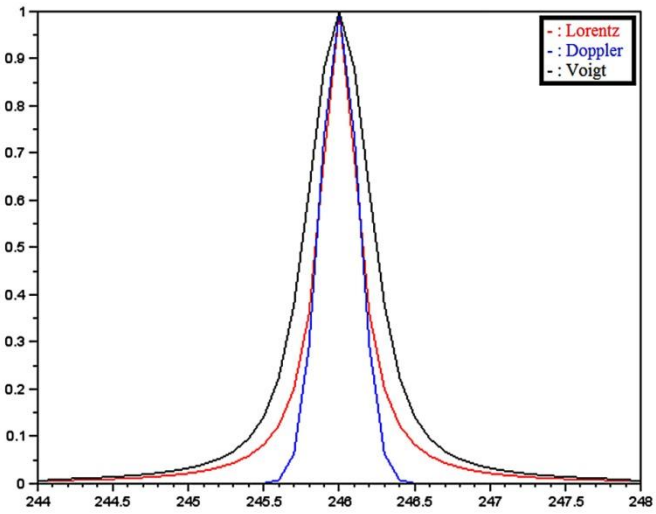

Figure 2.2: The Lorentz, Doppler and Voigt line shape.

A function describing the emission line broadening that takes into account both the Doppler and the pressure broadenings is the Voigt function, a spectral form resulting from the convolution of the two broadening mechanisms:

$$F_V\left(\nu,\nu_{mn}\right)=\int F_D\left(\nu',\nu_{mn}\right)F_L\left(\nu'-\nu,\nu_{mn}\right)d\nu' \ . \tag{2.24}$$

The Voigt profile tends to be equal to F_L in the troposphere whereas it tends to be equal to F_D in the upper mesosphere. Figure 2.2 shows the Voigt function resulting from a convolution of a Doppler and a Lorentzian line shape.

According to Eq. (2.16) the signal measured by a ground-based instrument is the integral of the emissions from all the atmospheric molecules in the line of sight. Knowing the pressure and temperature vertical profiles, the line shape dependence from these two atmospheric parameters can be used to perform a deconvolution of the received signal, allowing the retrieval of the concentration profile of the emitting species.

2.4 Electronic concepts

2.4.1 The system temperature and the measurement noise

The receiver of a spectrometer associates to an incoming radiation at a certain frequency an electronic signal, in term of Volts or counts, proportional to the radiation intensity according to Eq. (2.25)

$$V_{sky} = g\left(T_{sky} + T_{rec}\right) . \tag{2.25}$$

In Eq. (2.25) g is the gain factor, T_{sky} is the signal intensity coming from the atmosphere and T_{rec} is the *receiver temperature* all expressed as brightness temperatures. The receiver temperature represents the emissions generated by the elements composing the instrument.

The *system temperature* is the sum of the atmospheric signal and receiver temperature

$$T_{sys} = T_{sky} + T_{rec} . \tag{2.26}$$

The spectrometer measurements are affected by the random noise σ_T. The random noise intensity can be reduced integrating a measurement over time, according to Eq. (2.27) from de Zafra (1995)

$$\sigma_T = \frac{2T_{sys}}{\sqrt{\Delta\nu\, t_{obs}}} , \tag{2.27}$$

where $\Delta\nu$ is the instrument resolution and t_{obs} the total measurement time and the factor 2 is due to the measurement technique employed by the spectrometer described in this work (Jannsen, 1993).

2.4.2 The heterodyne receiver

In order to analyze a signal using an electronic device such as a spectrum analyzer, it could be necessary to reduce its frequency taking care of avoiding information losses. This operation can be achieved using nonlinear circuits as the *heterodyne receiver*.

This element mixes the incoming signal with a *local signal* or *carrier*, a sinusoidal wave of known intensity and frequency ν_0, produced by an element called *local oscillator*. The nonlinear element output current can be approximated at the second order:

$$I = aV + bV^2 + \ldots . \tag{2.28}$$

In a heterodyne receiver, the input of the nonlinear circuit is a combination of the incoming signal and the local signal. Representing the incoming signal as a simple sine wave $Asin(2\pi\nu t)$ and the carrier as $Bsin(2\pi\nu_0 t)$, the input signal is

$$V = A\sin\left(2\pi\nu t\right) + B\sin\left(2\pi\nu_0 t\right) . \tag{2.29}$$

The output current, approximated at second order, is then

$$I = \mathrm{a}\,A\sin(2\pi\nu t) + aB\sin(2\pi\nu_0 t) + bA^2\sin(2\pi\nu t) + bB^2\sin(2\pi\nu_0 t) + 2\,\mathrm{bAB}\sin(2\pi\nu t)\sin(2\pi\nu_0 t)\ . \quad (2.30)$$

The last term can be decomposed as

$$\sin(2\pi\nu t)\sin(2\pi\nu_0 t) = \frac{1}{2}\left[\cos(2\pi|\nu-\nu_0|t) + \cos(2\pi(\nu+\nu_0)t)\right]\ . \quad (2.31)$$

A pass-band filter is used to select the term with frequency $|\nu - \nu_0|$. In this way, the incoming signal frequency is reduced in a coherent way, introducing just a phase shift of $\pi/2$.

A real signal is composed by a convolution of simple sine waves. This can introduce a potential problem because both the components at frequency $\tilde{\nu} + \nu_0$ and $\nu_0 - \tilde{\nu}$ will be reduced to the same frequency $\tilde{\nu}$. Therefore the output signal is composed of the sum of all the components included in two frequency regions called *upper* and *lower sidebands*. Figure 2.3 represents the two sidebands symmetrical with respect to the carrier frequency. In order to avoid signal artifacts, the frequency range of interest needs to be completely included in one of the sideband, called *signal sideband*; the other sideband, the *image sideband*, should contain some easily recognizable structure that can be a-posteriori removed or it should be suppressed using an appropriate filter.

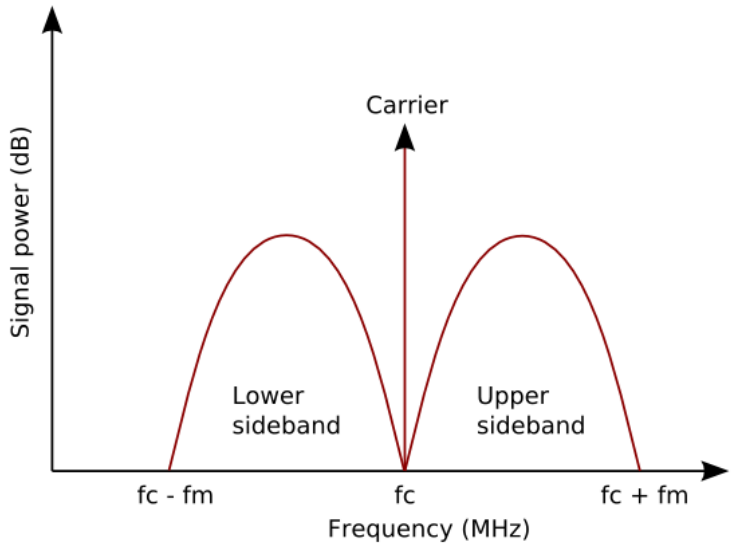

Figure 2.3: Representation of the upper and lower sideband symmetrical with respect to the carrier frequency

2.5 The quasi-optical systems

The microwave spectrometers utilize antennas and often reflectors to collect the atmospheric signal and channeling through the wave guide to the front end electronics. Such a system for microwave measurements is called a *quasi-optical system*. The interaction of the radiation with the different elements composing the spectrometer is described by the electromagnetic waves propagation. For microwave frequencies, the waves' propagation is modeled by the Helmotz equation and its *Gaussian beam* solution. This section provides a brief description of the Gaussian beam solution; for a more compete discussion on the subject the reader should consult Gori (1997).

2.5.1 The Gaussian beams

The electromagnetic waves amplitudes and phase are described by the Helmotz equation:

$$\left(\Delta + k^2\right)\psi = 0\,. \tag{2.32}$$

The general solution describing a wave propagating along the *z* axis with an amplitude and phase changing in the space is

$$\psi\left(x,y,z\right) = u\left(x,y,z\right)e^{ikz}\ . \tag{2.33}$$

The term $u(x,y,z)$ is a complex scalar function describing the wave amplitude and phase space dependence. The *paraxial approximation* is a constraint to the Eq. (2.32) consisting in considering the *z* derivative of the amplitude function *u* a slowly-varying function of *z*

$$\left|\frac{\partial^2 u}{\partial z^2}\right| \ll \left|k\frac{\partial u}{\partial z}\right|\ . \tag{2.34}$$

The *u* function determines the wave envelope so the Eq. (2.34) states the wave envelope changes slowly on distances compared to the wavelength. Applying the Eq. (2.33) and (2.34) to the Eq. (2.32) the differential equation becomes

$$\left(\frac{\partial^2}{\partial x^2} + \frac{\partial^2}{\partial y^2}\right)u - 2ik\frac{\partial u}{\partial z} = 0\ . \tag{2.35}$$

The instrument described in this work employs an antenna characterized by a cylindrical symmetry. Therefore the solution of the Eq. (2.35) maintains this kind of symmetry. Eq. (2.36) describes a Gaussian beam with cylindrical symmetry:

$$\mathbf{E} = \mathbf{E}_0\,\frac{w_0}{w}\exp\left(-\frac{r^2}{w^2} - i\frac{\pi r^2}{\lambda R} + i\varphi\right)\exp\left(ikz - i\omega t\right)\ , \tag{2.36}$$

where r is the distance from the optical axis of the system. The imaginary term in the exponential describes the phase variation of a spherical wave front with R the curvature radius of the equiphasic surfaces of the wave front, described by Eq. (2.37).

$$R = z + \frac{1}{z}\left(\frac{\pi w_0^2}{\lambda}\right)^2 , \tag{2.37}$$

The real term has a Gaussian shape, whose variance is a function of the distance along the propagation axis z:

$$w = w_0\sqrt{1+\left(\frac{\lambda z}{\pi w_0^2}\right)^2} . \tag{2.38}$$

The factor φ of Eq. (2.36) is defined *Gaussian phase shift* and is described by:

$$\tan(\varphi) = \frac{\lambda z}{\pi w_0^2} . \tag{2.39}$$

If $z = 0$, R diverges. The area characterized by $z = 0$ is called *beam waist*. Here the equiphasic surface is a plane as in the plane waves. The function w describes the distance with respect to propagation axis where the beam intensity diminishes of a factor $1/e$ and it is called *beam radius*. The value w_0 is defined *beam waist radius* and represents the minimum value of the beam radius. The quantity $z_c = \pi w_0^2/\lambda$ is called *confocal parameter*.

The Figure 2.4 shows a scheme of a Gaussian beam.

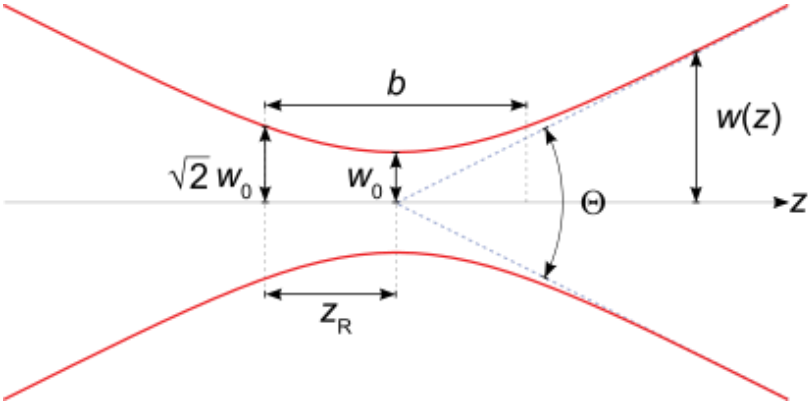

Figure 2.4: A scheme describing the Gaussian beam with cylindrical symmetry. The red line represents the area where the beam intensity is diminished by a factor $1/e$.

Observing the previous equations some important properties of the Gaussian beams can be derived:

- the product between w and beam intensity is constant;
- the maximum intensity is reached in the beam waist with $z = 0$ and $r = 0$;

- the phase curvature radius diverges at $z = 0$, has a minimum in z_c and tends to z when $z \gg z_c$;
- the angle $\Theta = \arctan(w/z)$ defined as *propagation angle* in the far field ($z \gg z_c$) tends to the constant value Θ_0 called *asymptotic propagation angle*

$$\Theta_0 = \lim_{z \gg z_c} \arctan\left(\frac{w}{z}\right) = \arctan\left(\frac{\lambda}{\pi w_0}\right). \tag{2.40}$$

According to Eq. (2.40) a larger beam waist radius corresponds to a lesser asymptotic propagation angle. Can be also useful to define the *half power beam angle* defined as the angle with respect to the propagation axis where the beam intensity is 50% of the maximum

$$\theta_{3dB} = \frac{1}{1.18}\arctan\left(\frac{\lambda}{\pi w_0}\right). \tag{2.41}$$

2.5.2 The antenna

The antenna is the element that collects the radiation from the free space and guides it to a wave guide. The antenna has the important function to selectively collect radiation from a certain direction.

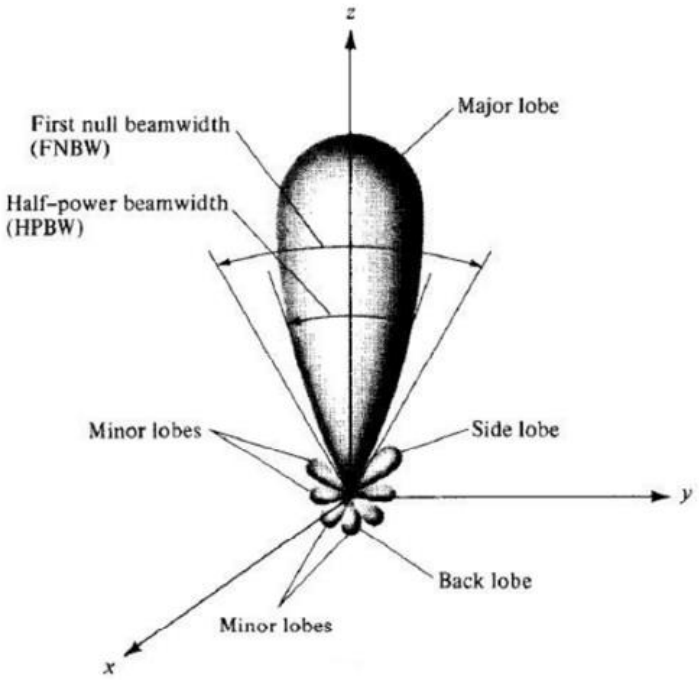

Figure 2.5: A scheme of the antenna gain characteristics (Bertagnolio, 2013).

Using the Rayleigh Jeans approximation the brightness temperature of the signal collected by the antenna or *antenna temperature* T_a can be written as

$$T_a = \int_{4\pi} \frac{A(\theta,\phi)}{\lambda^2} T_\nu(\theta,\phi)\, d\Omega = \int_{4\pi} g(\theta,\phi) T_\nu(\theta,\phi)\, d\Omega \ , \tag{2.42}$$

where $g(\theta,\phi) = A/\lambda^2$ is the antenna gain. The Figure 2.5 shows a scheme illustrating the characteristics of the antenna gain. The gain lobe containing the maximum is called *major lobe* or *principal lobe*. The half power beam width is the major lobe angle containing the 50% of the total gain. The first null beam width is the angular span between the first pattern nulls adjacent to the major lobe. The major lobe axis is defined as antenna *optic axis*. The antennas have also side and back lobes, where the gain is often orders of magnitude less intense with respect to the major lobe; this is an important characteristic in order to avoid the antenna collecting signals from undesired directions.

2.6 Inverse problems theory

The inverse problem theory is a mathematical instrument used to analyze the indirect measurements. For a general discussion on this subject, the reader should consult Rodgers (2000). A generic physical state *x* is related to the measured quantity *y* through the relation

$$y = f(x) \ . \tag{2.43}$$

The quantity *x* and *y* are generally continuous functions. In this study the atmospheric spectrum is measured to obtain the water vapor concentration vertical profile, $y(\nu)$ and $x(\nu)$. The mathematical operator f is a functional, mapping the x function to the y function. The relation f contains the physics of the phenomenon; for example the f relating the spectra and the water vapor profiles is composed by the radiative transfer process and the description of the spectral form of the emissions at the different altitudes (Section 2.2 and 2.3). In order to obtain the information about the state *x* the Eq. (2.43) needs to be inverted.

$$x = f^{-1}(y) \tag{2.44}$$

Solving the eq. (2.44) requires the existence and uniqueness of the *x*.

Many of the relations *f* in geophysics, as the Eq. (2.16), are in form of convolution

$$y(\nu) = y_0 + \int Q(\nu, z)\, x(z)\, dz \ . \tag{2.45}$$

In this type of problems, called Fredholm problems, a large variation of the state *x* often produces small variations in *y* that could be comparable with the measurement noise. In such situations, the result of a direct inversion of the forward model produces solutions extremely sensible to the noise level, as described in the following paragraph.

The case of interest for this work is represented by the Eq. (2.16). Comparing this last equation with the (2.45) reveals that the unknown state *x* is the $\rho(z)$ and

$$Q(\nu,z)=T(z)\kappa(\nu,z)e^{-\tau(z)}\ , \tag{2.46}$$

where the dependence of the temperature to the *z* in $\kappa(\nu,T(z))$ are been explicated**.** The radiative transfer problem is not a linear problem, for the fact that $\tau(z)$ depends on $\rho(z)$; however, the problem can be approximated considering the opacity as independent by the solution $\rho(z)$.

2.6.1 Numerical inversion

The most common way to resolve an indirect problem such as the Eq. (2.45) is a numerical algorithm, computing the solution in a limited amount of points in the *z-axis*. Although the function *y* is a continuous function, an instrument can just perform discrete measurements; the function *y* is naturally reduced in the measurement process to the *measurement vector* **y**. In the same way, the solution *x* is calculated in a limited amount of points and reduced to the *state vector* **x**. Hereafter *m* is the number of elements composing **y** and *n* the number of elements composing **x**. Generally, a measurement vector composed by $m \geq n$ elements is needed to obtain a state vector of *n* independent elements.

In a numerical inversion, the relation *f* between measurement and state is represented by the model, $\mathbf{F}(\mathbf{x})$. This model reflects the actual scientific knowledge of the phenomenon and can be affected by approximations depending on the level of precision needed in the study.

$$\mathbf{y}=\mathbf{F}(\mathbf{x})\ . \tag{2.47}$$

The **F** operator can be non-linear as seen in the radiative transfer example. However, for many problems, the operator can be expanded to the first order around the vector state $\mathbf{x}_a$, called *apriori state*, obtaining

$$\mathbf{y}=\mathbf{y}_a+\left.\frac{\partial\mathbf{F}(\mathbf{x})}{\partial\mathbf{x}}\right|_{\mathbf{x}=\mathbf{x}_a}(\mathbf{x}-\mathbf{x}_a)=\mathbf{y}_a+\mathbf{K}(\mathbf{x}-\mathbf{x}_a)\ , \tag{2.48}$$

where $\mathbf{y}_a=\mathbf{F}(\mathbf{x}_a)$. The matrix **K** is called *jacobian or weighting function matrix* and it is the Frechét derivative of the model; it is a $m \times n$ matrix whose elements are defined as

$$K_{ij}=\frac{\partial y_i}{\partial x_j}\ . \tag{2.49}$$

K quantifies the response of the measurement vector element *i* to a variation of the state vector element *j*. The columns of **K** are called weighting functions and represent the response of the measurement vector to a variation of the element *i* of **x**.

Taking into account the measurement error, $\boldsymbol{\varepsilon}$, Eq. (2.48) can be rewritten as

$$\mathbf{y} = \mathbf{y}_a + \mathbf{K}\left(\mathbf{x} - \mathbf{x}_a\right) + \boldsymbol{\varepsilon} \ . \tag{2.50}$$

In order to obtain the state **x**, the linear system of Eq. (2.48) could be simply inverted, but the problem remains affected by instability and the other issues described in the previous paragraph due to the measurement uncertainty.

In Figure 2.6 is shown an example of the weighting functions calculated for the 22.23 GHz water vapor emission line at different altitudes with a frequency resolution of 31 kHz using a radiative transfer simulation software (ARTS, Eriksson et al., 2011). A variation in the water vapor concentration at higher altitudes produces variations in the spectrum localized mostly in the region near the emission line peak, whereas a change in the water vapor concentration at lower altitude produces variations that can be easier identified on a wider frequency interval.

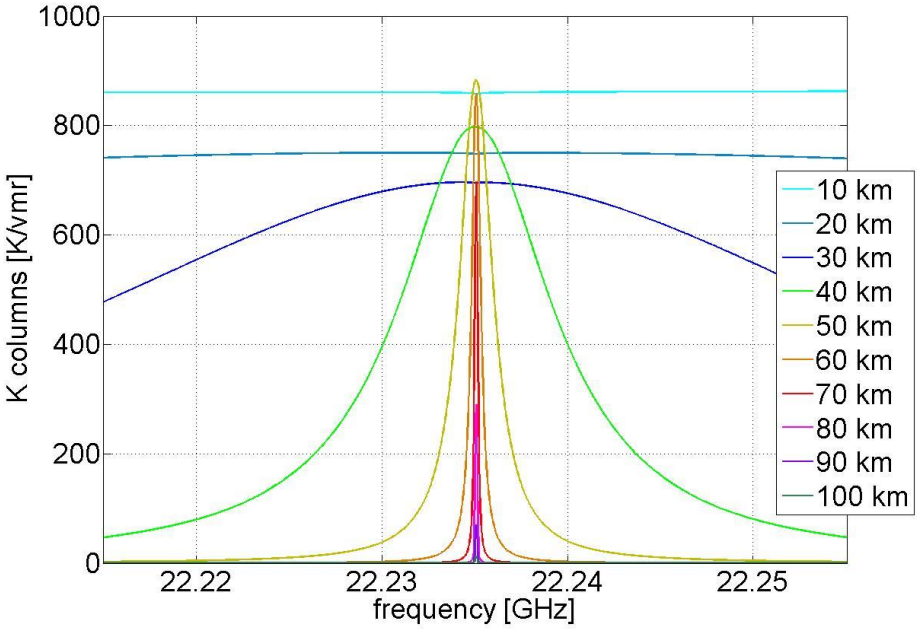

Figure 2.6: The 22.23 GHz water vapor emission line weighting functions simulated using the radiative transfer simulation software ARTS (Erikkson et al., 2011)

2.6.2 The optimal estimation for Gaussian probability density functions

The real measurements are affected by the measurement uncertainty; therefore it is not possible to associate a unique state **x** to a measurement vector **y**. Defined *state space* the ensemble of the possible state vectors and *measurement space* the ensemble of the possible measurement vectors, due to the measurement uncertainty, the model $\mathbf{F}(\mathbf{x})$ maps a single state

vector in a region of the measurements space and vice versa, there is a region of the state space associated to a single measurement.

The statistic approach to this kind of problem consists in assigning a probability density function (pdf) to the various elements involved in the problem, in order to obtain a solution in a statistical way. A constraint can be imposed to the possible solution: in the atmospheric studies the extra information coming from the knowledge about the local climatology that is inserted in the problem. This knowledge acts like a virtual measurement and provides an estimation of the solution. The information gathered by the measurements updates this apriori-knowledge.

In this work, an *apriori profile* is used in order to represent the local mean state of the water vapor profile. The apriori profile is also the state $\mathbf{x}_a$ around which is centered the linearization process of the Eq. (2.46).

This paragraph describes an equation to calculate the expected value of $\hat{\mathbf{x}}$ from the $P(\mathbf{x}|\mathbf{y})$, the pdf to observe the state $\mathbf{x}$ measuring the vector $\mathbf{y}$. The procedure used to obtain the $\hat{\mathbf{x}}$ using this kind of approach is called *retrieval algorithm* or, more simply, *retrieval*.

In order to simplify the notation, the linear problem is described by the Eq. (2.51)

$$\mathbf{y} = \mathbf{K}\mathbf{x} \tag{2.51}$$

As hypothesis, a Gaussian shape is assumed for the different pdfs. The generic multidimensional gaussian associated to a vector $\mathbf{y}$ is in the form

$$P(\mathbf{y}) = \frac{\exp\left(-\frac{1}{2}(\mathbf{y}-\hat{\mathbf{y}})^{\mathbf{T}}\mathbf{S}_{\mathbf{y}}^{-1}(\mathbf{y}-\hat{\mathbf{y}})\right)}{\sqrt{|\mathbf{S}_{\mathbf{y}}|(2\pi)^m}}\ , \tag{2.52}$$

where $\hat{\mathbf{y}}$ is the expected value, the apex $\mathbf{T}$ indicates the transposition operation and the $\mathbf{S}_y$ is the covariance matrix associated to the vector. This matrix is composed accordingly to the Eq. (2.53)

$$S_{\mathbf{y},ij} = \sigma_{i,j}\ , \tag{2.53}$$

where σ_{ij} is the variance of the element i of the vector if $i = j$ or the covariance between the element i and j otherwise.

Defining $\mathbf{S}_\varepsilon$ the covariance matrix describing the measurement uncertainty, $P(\mathbf{y}|\mathbf{x})$ can be expressed as

$$-2\ln\left(P(\mathbf{y}\,|\,\mathbf{x})\right) = (\mathbf{y}-\mathbf{K}\mathbf{x})^{\mathbf{T}}\mathbf{S}_{\boldsymbol{\varepsilon}}^{-1}(\mathbf{y}-\mathbf{K}\mathbf{x}) + c_1\ , \tag{2.54}$$

where c_1 is the normalization constant. The expected value from this pdf is $\mathbf{K}\mathbf{x}$.

$P(\mathbf{x})$ represents the knowledge of the atmosphere *before* performing the measurement. This pdf is associated to the apriori profile and can be described as

$$-2\ln\left(P(\mathbf{x})\right) = (\mathbf{x}-\mathbf{x}_a)^{\mathbf{T}}\mathbf{S}_a^{-1}(\mathbf{x}-\mathbf{x}_a) + c_2\ . \tag{2.55}$$

Using now the Bayes theorem the expression for $P(\mathbf{x}|\mathbf{y})$ can be derived

$$-2\ln\left(P\left(\mathbf{x}\,|\,\mathbf{y}\right)\right)=\left(\mathbf{y}-\mathbf{K}\mathbf{x}\right)^{\mathbf{T}}\mathbf{S}_{\varepsilon}^{-1}\left(\mathbf{y}-\mathbf{K}\mathbf{x}\right)+\left(\mathbf{x}-\mathbf{x}_{a}\right)^{\mathbf{T}}\mathbf{S}_{a}^{-1}\left(\mathbf{x}-\mathbf{x}_{a}\right)+c_{3}\ . \tag{2.56}$$

$P(\mathbf{y})$ refers to the probability to obtain a certain measurement vector *before* performing the measurement. A measurement device can generally assume all the values allowed in its measurement range with the same probability. Therefore, this pdf can be considered as constant and can be included in the normalization factor c_3. This equation describes again a gaussian pdf. The Eq. (2.56) can be written as

$$-2\ln\left(P\left(\mathbf{x}\,|\,\mathbf{y}\right)\right)=\left(\mathbf{x}-\hat{\mathbf{x}}\right)^{\mathbf{T}}\mathbf{S}^{-1}\left(\mathbf{x}-\hat{\mathbf{x}}\right)+c_{4}\ . \tag{2.57}$$

The quantity $\hat{\mathbf{x}}$ is the state representing the expected value of the Eq. (2.57) and therefore the result of the inversion process of the measurement $\mathbf{y}$, given a local climatology represented by the state $\mathbf{x}_a$. The Eq. (2.56) can be reduced to the Eq. (2.57) equating the various terms. Eq. (2.58) is obtained equating the quadratic terms of $\mathbf{x}$

$$\mathbf{x}^{\mathbf{T}}\mathrm{K}^{\mathbf{T}}\mathbf{S}_{\varepsilon}^{-1}\mathbf{K}\mathbf{x}+\mathbf{x}^{\mathbf{T}}\mathbf{S}_{a}^{-1}\mathbf{x}=\mathbf{x}^{\mathbf{T}}\mathbf{S}^{-1}\mathbf{x}\ , \tag{2.58}$$

that allows writing

$$\mathbf{S}^{-1}=\mathbf{K}^{\mathbf{T}}\mathbf{S}_{\varepsilon}^{-1}\mathbf{K}+\mathbf{S}_{a}^{-1}\ . \tag{2.59}$$

This is the covariance matrix of the retrieval; it contains the variance and covariance information about the solution $\hat{\mathbf{x}}$ and can be used to estimate the uncertainty of the result.

Equating the linear term of $\mathbf{x}^{\mathbf{T}}$ produces the Eq. (2.60)

$$\left(\mathbf{K}\mathbf{x}\right)^{\mathbf{T}}\mathbf{S}_{\varepsilon}^{-1}\mathbf{y}+\mathbf{x}^{\mathbf{T}}\mathbf{S}_{a}^{-1}\mathbf{x}_{a}=\mathbf{x}^{\mathbf{T}}\mathbf{S}^{-1}\hat{\mathbf{x}}\ . \tag{2.60}$$

During the measurement the real atmospheric state $\mathbf{x}$ is not known**,** so it can be replaced in Eq. (2.58), using Eq. (2.59) and (2.60) to obtain

$$\mathbf{K}^{\mathbf{T}}\mathbf{S}_{\varepsilon}^{-1}\mathbf{y}+\mathbf{S}_{a}^{-1}\mathbf{x}_{a}=\left(\mathbf{K}^{\mathbf{T}}\mathbf{S}_{\varepsilon}^{-1}\mathbf{K}+\mathbf{S}_{a}^{-1}\right)\hat{\mathbf{x}}\ , \tag{2.61}$$

$$\hat{\mathbf{x}}=\left(\mathbf{K}^{\mathbf{T}}\mathbf{S}_{\varepsilon}^{-1}\mathbf{K}+\mathbf{S}_{a}^{-1}\right)^{-1}\left(\mathbf{K}^{\mathbf{T}}\mathbf{S}_{\varepsilon}^{-1}\mathbf{y}+\mathbf{S}_{a}^{-1}\mathbf{x}_{a}\right)\ . \tag{2.62}$$

If the problem linearization was performed around the state $\mathbf{x}_a$, it can be shown that

$$\hat{\mathbf{x}}=\mathbf{x}_{a}+\left(\mathbf{K}^{\mathbf{T}}\mathbf{S}_{\varepsilon}^{-1}\mathbf{K}+\mathbf{S}_{a}^{-1}\right)^{-1}\mathbf{K}^{\mathbf{T}}\mathbf{S}_{\varepsilon}^{-1}\left(\mathbf{y}-\mathbf{y}_{a}\right)\ . \tag{2.63}$$

The expected state $\hat{\mathbf{x}}$ result of the retrieval is defined as *retrieved state* or, *retrieved profile* if is a vertical concentration profile.

Eq. (2.62) can be associated to the weighted mean between two measurements x_1 and x_2, each one with its variance:

$$x=\left(\frac{1}{\sigma_{1}^{2}}+\frac{1}{\sigma_{2}^{2}}\right)^{-1}\left(\frac{x_{1}}{\sigma_{1}^{2}}+\frac{x_{2}}{\sigma_{2}^{2}}\right)\ . \tag{2.64}$$

The term $\mathbf{K^T S_\varepsilon^{-1} y}$ represents the information gathered by the measurement whereas the term $\mathbf{S_a^{-1} x_a}$ the information gathered by the apriori profile. The matrices $\mathbf{S}_\varepsilon$ and $\mathbf{S}_a$ define the relative importance of the two information sources.

The *gain matrix* $\mathbf{G}$ can be defined as

$$\mathbf{G} = \left(\mathbf{K}^{\mathrm{T}}\mathbf{S}_{\varepsilon}^{-1}\mathbf{K} + \mathbf{S}_a^{-1}\right)^{-1}\mathbf{K}^{\mathrm{T}}\mathbf{S}_{\varepsilon}^{-1} \,. \tag{2.65}$$

This matrix defines the sensitivity of the retrieval result to the variations in the measurement. Using the Eq. (2.65) the Eq. (2.63) can be written as

$$\hat{\mathbf{x}} = \mathbf{x}_a + \mathbf{G}\left(\mathbf{y} - \mathbf{y}_a\right) \,. \tag{2.66}$$

Using the Eq. (2.48) the Eq. (2.66) can be written as

$$\hat{\mathbf{x}} = \mathbf{x}_a + \mathbf{GK}\left(\mathbf{x} - \mathbf{x}_a\right) = \mathbf{x}_a + \mathbf{A}\left(\mathbf{x} - \mathbf{x}_a\right) \,, \tag{2.67}$$

where the matrix $\mathbf{A}$ is the *averaging kernel matrix* defined as

$$\mathbf{A} = \mathbf{GK} = \frac{\partial \hat{\mathbf{x}}}{\partial \mathbf{x}} \,. \tag{2.68}$$

This matrix describes the sensitivity of the retrieved state to the variations of the real state. The rows of *A* are called *averaging kernels* (AK) and represents the sensitivity of the retrieval at a given altitude to variations in the atmosphere at all altitudes (Rodger, 2000). When they are well-peaked functions, centered at their nominal altitude, a perturbation in the real state is attributed to the correct altitude in the retrieved state.

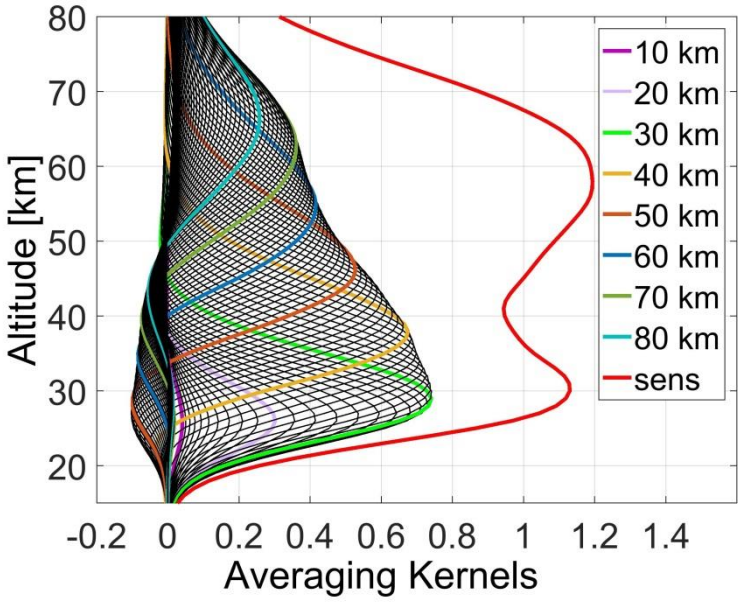

Figure 2.7: Rows of A matrix multiplied by a factor 10 as function of altitude (some *A* functions are highlighted with their associated altitude shown in the legend). Sensitivity is shown in red.

Furthermore, the sum of the AK is defined *sensitivity* of the retrieved profile to atmospheric variations. Sensitivity values close to one indicate that the major contribution to the solution comes from the measurement rather than from the apriori.
Figure 2.7 shows an example of AK functions (multiplied by a factor ten) and sensitivity. Some AKs are colored to better indicate their reference altitude.
Although the retrieved profile is calculated on a grid of *n* points, the vector $\hat{\mathbf{x}}$ can be characterized by some correlation between the different vector elements. For this reason in the retrieved profile, some small scale structure cannot be revealed if the scale length of these is less than the retrieval resolution. A measure of the retrieval resolution is the full width at half maximum of the AKs. These functions contain the information of how a certain altitude of $\hat{\mathbf{x}}$ profile is related to what is happening in the true state $\mathbf{x}$ at all the different altitudes. The element *i* of the retrieved state is calculated adding contributes from the entire vector $\mathbf{x}$ modulated with the AK associated to that altitude. In other word the retrieved profile can be seen as a smoothed version of the true state $\mathbf{x}$.
After calculating the retrieved profile $\hat{\mathbf{x}}$, a useful parameter to define the inversion quality is the fit spectrum $\mathbf{y}_{fit}$

$$\mathbf{y}_{fit} = \mathbf{x}_a + \mathbf{K}\left(\hat{\mathbf{x}} - \mathbf{x}_a\right) . \tag{2.69}$$

This quantity represents the spectrum associated with the retrieved state by the linearized model. A good inversion algorithm aspires to minimize the difference between measured and fit spectra, called *residual*, without introducing nonphysical oscillations in the retrieved profile. The study of the residual can also help to individuate artifacts afflicting the measured spectrum and to compute the noise level afflicting the measurements.

Chapter 3

The microwave spectrometer VESPA-22

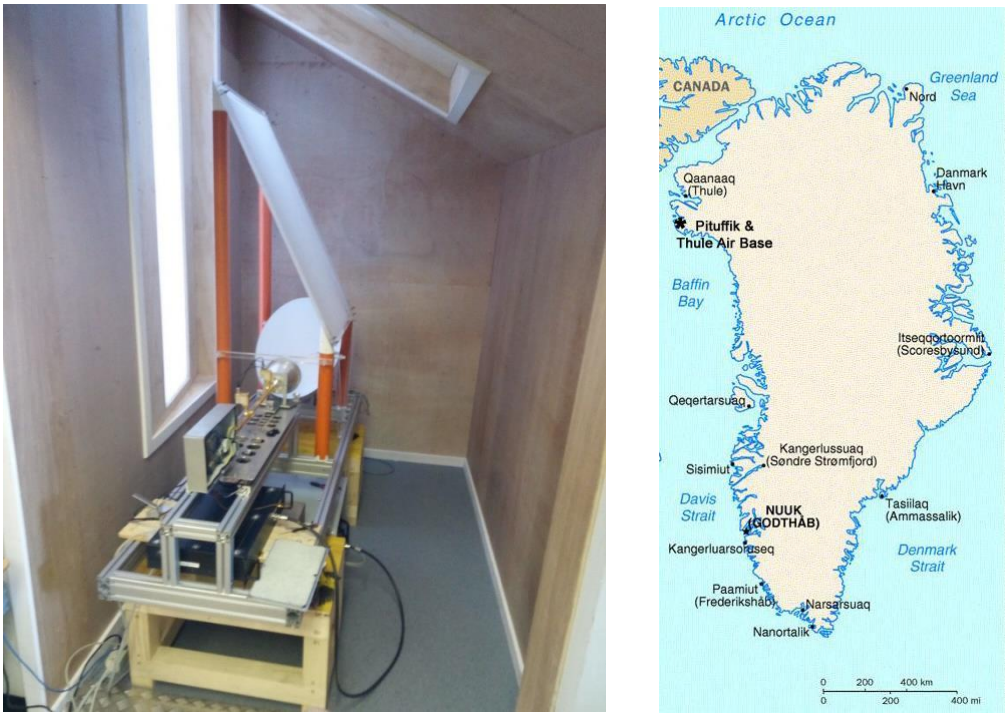

Figure 3.1: A picture of VESPA-22 installed at the THAAO (left) and a Greenland map (right).

VESPA-22 (water Vapor Emission Spectrometer for Polar Atmosphere at 22 GHz) is a microwave spectrometer designed to retrieve vertical water vapor profile in stratosphere and mesosphere (Figure 3.1). The instrument was designed and built at the Istituto Nazionale di Geofisica e Vulcanologia (INGV) located in Rome. As part of this Ph.D. work, I installed the instrument at the Thule High Arctic Atmospheric Observatory (THAAO; http://www.thuleatmos-it.it/), in Thule Air Base (76.5° N, 68.8° W), Greenland, in July 2016. This observatory is part of the Network for Detection of Atmospheric Composition Change (NDACC) and has an ideal position to study the Arctic atmosphere. The instrument is situated on the West Coast of Greenland as can be seen in Figure 3.1 (right), and it is installed on a hill close to the coast called South Mountain, at about 220 m of altitude (Figure 3.2).

Thule Air Base is covered by snow for the major part of the year, except during summer; during winter, the sea is covered by ice. This particular environment proves useful to study the interaction between atmosphere and cryosphere typical of the Arctic amplification. Thule Air Base claims a decennial history of atmospheric studies and the THAAO hosts several instruments for the trace gases, radiation and atmosphere monitoring: the microwave spectrometer GBMS (Ground-based Microwave Spectrometer), an infrared spectrometer, a LIDAR system, many instruments for irradiance measurements such as pyrgeometers and pyranometers, a HATPRO radiometer ((Humidity And Temperature Profilers) and two meteorological stations.

Figure 3.2: A satellite vision of Thule Air Base during summer with a star indicating the THAAO position on South Mountain. On the right in the picture the final portion of a glacier can be seen.

The measurement of stratospheric and mesospheric water vapor imposes specific challenges with respect to other gases measurement due to the major part of water vapor concentrated in the troposphere. The water vapor emits a 22.23 GHz signal with a brightness temperature of the order of 40 K; the major part of this irradiance is emitted by the troposphere; just about the 1% of this signal can be ascribed by stratospheric and mesospheric water vapor emission. In order to minimize the absorption of the stratospheric signal from the troposphere and maximizing the ratio between stratospheric and tropospheric signal intensity, it is necessary to take measurement in a site characterized by low opacity. The THAAO offers the ideal environment for this kind of measurements, due to the extremely dry atmosphere characterizing the Arctic.

This chapter describes the various elements composing VESPA-22, represented in the scheme in Figure 3.3.

VESPA-22 collects the microwave radiation emitted by water vapor transition at 22.235 GHz with a spectral resolution of 31 kHz and a bandwidth of 500 MHz. It can retrieve water vapor profiles with a temporal resolution of 2-4 profiles a day, depending on weather conditions. The instrument can also measure the sky opacity with a temporal resolution of few minutes.

The instrument is characterized by a receiver temperature of about 180 K, measured through a liquid nitrogen calibration (see paragraph 3.8.1). A quasi-optical system composed of a choked horn antenna and an off axis parabolic reflector collects the incoming radiation. The reflector can rotate to collect the signal from different elevation angles through a PC-controlled motor. An encoder constantly monitors the reflector rotation angle. In addition, the antenna can move back and forth along its optical axis through another PC-controlled motor (quarter wavelength shift in the scheme) in order to minimize standing waves caused by multiple reflections in the quasi-optical system.

The front-end electronics receive the signal from the antenna. Here the signal is amplified and down converted by the heterodyne receivers to be analyzed by the back end spectrometer. Two noise diodes are installed in the wave guide carrying the signal. These two elements produce a signal stable in time that is used to calibrate the measurements, as explained in Sections 3.8 and 3.9.

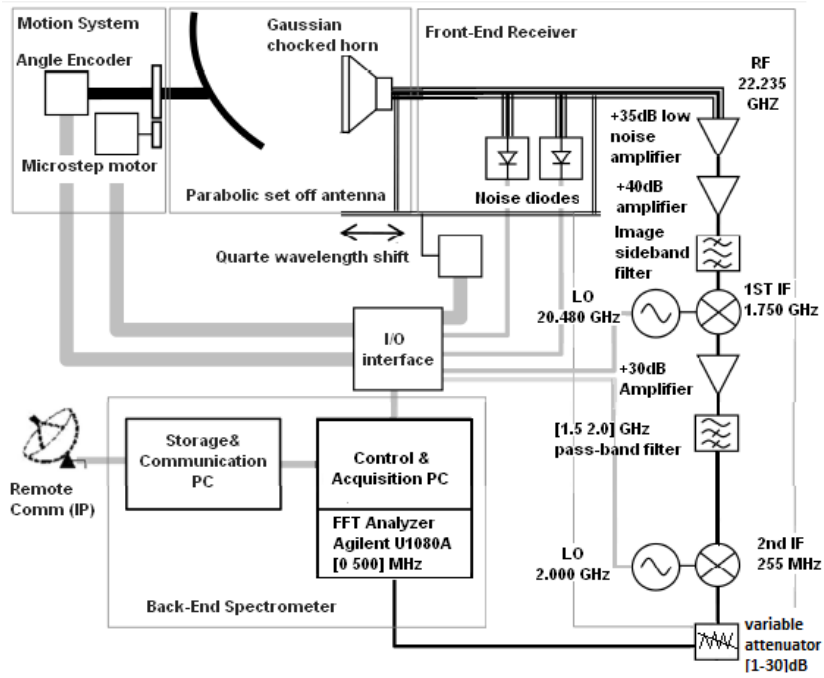

Figure 3.3: A scheme of VESPA-22

3.1 The antenna

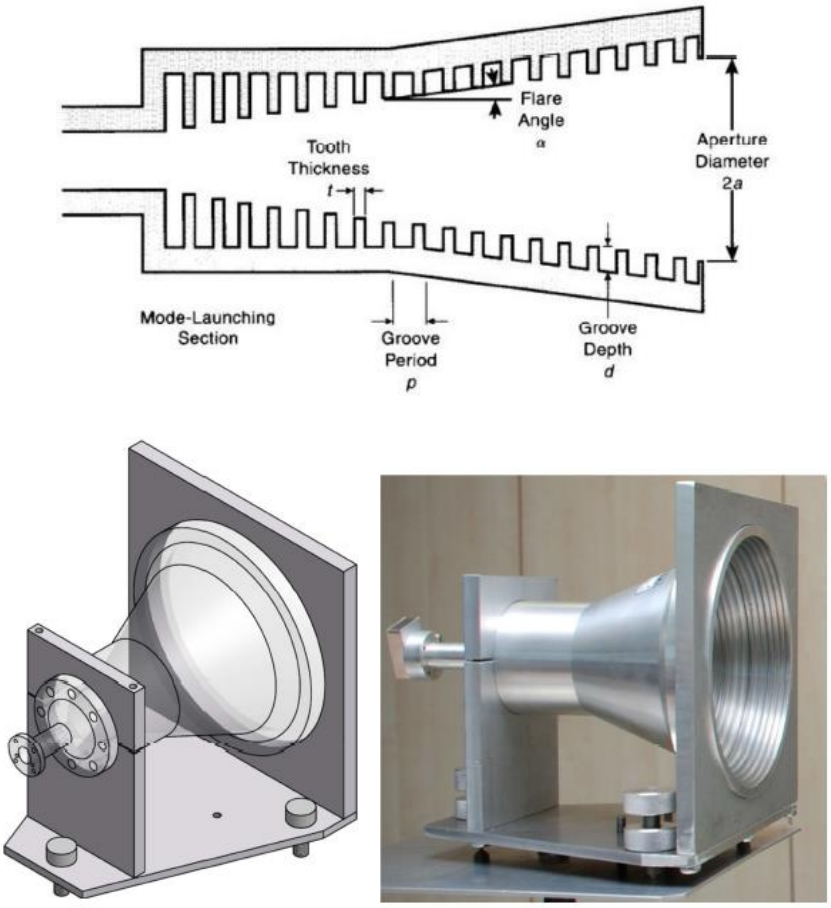

Figure 3.4: A scheme describing an antenna section (top, from Goldsmith, 1998); the VESPA-22 choked horn antenna (bottom, from Bertagnolio, 2013).

VESPA-22 employs a choked horn antenna (Bertagnolio et al., 2012) (Figure 3.4) designed and manufactured by the Public University of Navarra and described by Teniente et al. (2002). This kind of antenna presents a cylindrical symmetry, a far field directivity of about 23.5 dB and low side lobes. The half-power beamwidth (HPBW) of the feed horn alone is measured at approximately 12.5°, and the first-null beam-width (FNBW) is approximately 60°. The first side lobe has an intensity more than 35 dB lower than the main lobe. This high directivity is important to receive the water vapor stratospheric signal (intensity of the order of 1 K) without collecting radiation from other objects near the antenna at ambient temperature. Along

the whole spectral range observed by VESPA-22, the only significant spectral-dependent feature in the antenna pattern is a widening of the main lobe with decreasing frequency.

The antenna radiation diagram can be approximated at 99.85% with a gaussian beam waist (see paragraph 2.5.1) with beam waist radius of 22.4 mm (Bertagnolio et al., 2012). The circular shape was chosen to have a consistent response from different observation angles, such as those necessary for the balanced beam-switching technique.

The antenna is installed on an adjustable aluminum support in order to correctly align the antenna axis with the reflector axis. The antenna-reflector axis is called *optical axis* of the instrument.

3.2 The parabolic reflector

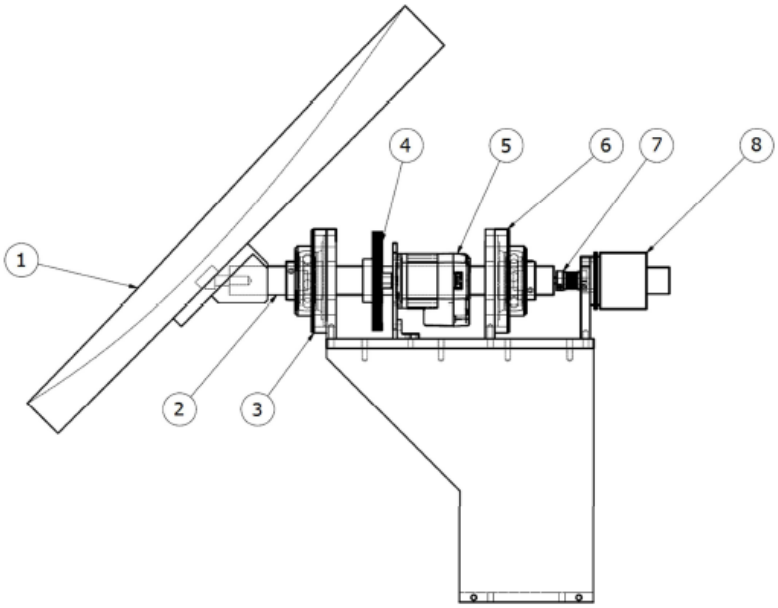

Figure 3.5: A scheme of the parabolic reflector and its mechanics; 1) parabolic reflector, 2) reflector axis, 3) and 6) ball bearings, 4) gear for motion transmission, 5) programmable motor, 7) flexible coupling, 8) encoder (from Bertagnolio, 2013).

The reflector is the element that allows VESPA-22 to observe the radiation from different directions. This element can rotate on the vertical plane perpendicular to the antenna axis, determining the elevation angle of the measurement. The reflector has an off axis parabolic shape designed to maximize the coupling with the antenna gaussian beam. The quasi-optical system, antenna and parabolic mirror, has a full width at half maximum $\theta_{3dB} = 3.5°$ (Bertagnolio et al., 2012) with a beam waist

radius of 83 mm. This high directivity of the system allows observation of angles as low as 12° above the horizon without collecting radiation from the ground.

The reflector axis is aligned with the antenna axis and connected to an encoder; this element is able to measure the rotation angle of the reflector. Figure 3.5 shows the technical scheme of the reflector whereas Figure 3.6 is a picture of the reflector during the test stage at the laboratory in Rome.

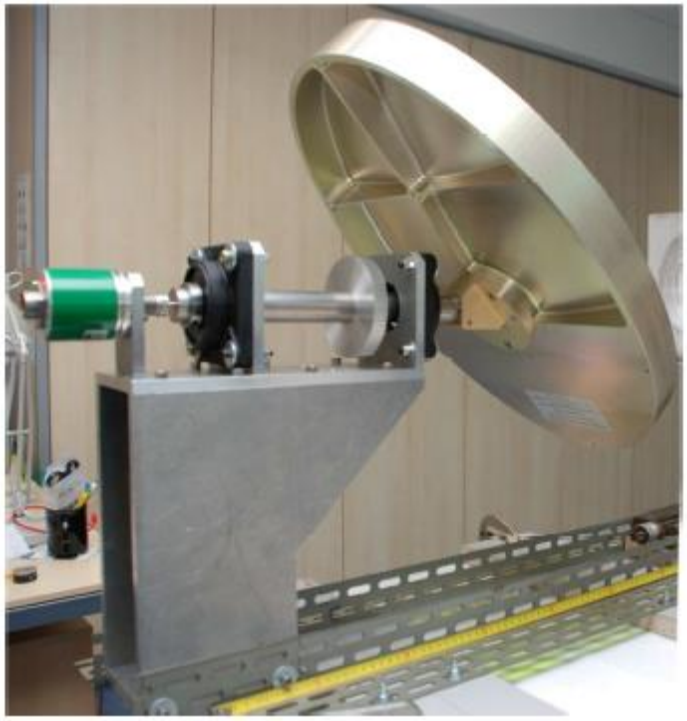

Figure 3.6: A picture of the parabolic reflector (Bertagnolio, 2013).

In Figure 3.7 the relative position and distance d between the antenna and the reflector are shown. The distance is obtained imposing that the antenna beam radius at the distance d, $w(d)$ is equal to the beam waist of the parabolic reflector. Imposing this constraint, the distance d is equal to 41.7 cm (Bertagnolio et al., 2012).

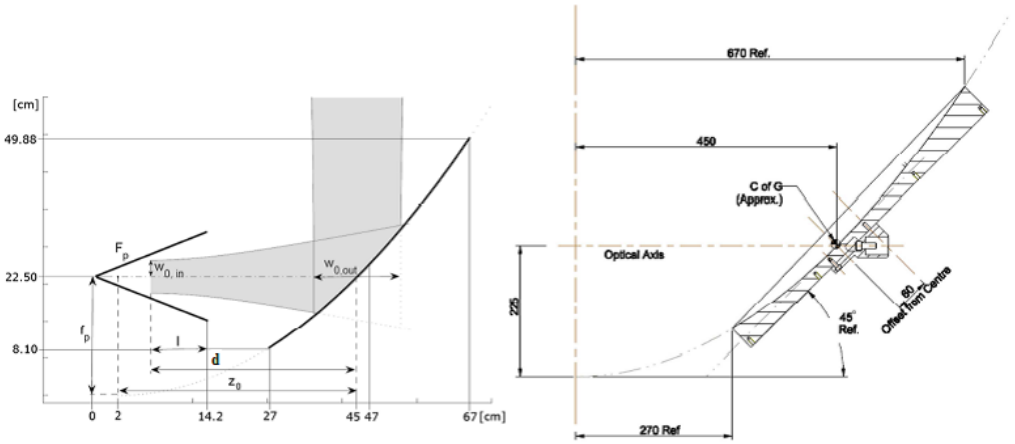

Figure 3.7: A scheme from the original design of VESPA-22 quasi-optical system, (Bertagnolio, 2013).

3.3 The path length modulator

Stationary waves can produce artifacts afflicting the measured spectra. The path length modulator is a system studied to minimize this issue. It consists of a metallic plate moved by a programmable motor on which the antenna is installed. During measurements, the antenna is moved by this system back and forth along the optical axis of a distance equal to $\lambda/4$ (about 3.3 mm, with λ the wavelength associated to 23.235 GHz) around the position of maximum coupling between antenna and reflector. Averaging together the data obtained in the two different antenna positions, the stationary waves can be minimized by destructive interference.

In order to avoid potential drifts in the relative position between antenna and reflector, I installed two photodiodes on the antenna support (Figure 3.8). These elements are used to reset the antenna in the correct position every 24 hours.

I developed a procedure used to reset the antenna position. It starts with a check of the status of the photodiodes. If both the photodiodes are not operating correctly the procedure is aborted and a warning indicator is shown on the acquisition software.

The photodiodes are installed at a known distance d_{pho} with respect to the position of the antenna plate supports (see Figure 3.8) on which the antenna and the reflector have the maximum coupling. In order to reset the antenna to the correct position the antenna plate is moved toward the photodiodes by the programmable motor. The photodiodes are connected to the motor and send a signal to it when the antenna plate supports are inside the cavity between each photodiode's "arms". The motor is programmed to immediately stop the motion when it receives this signal and then it moves the plate in the opposite direction of the distance d_{pho}, placing the antenna plate to the correct position to maximize the antenna-reflector coupling.

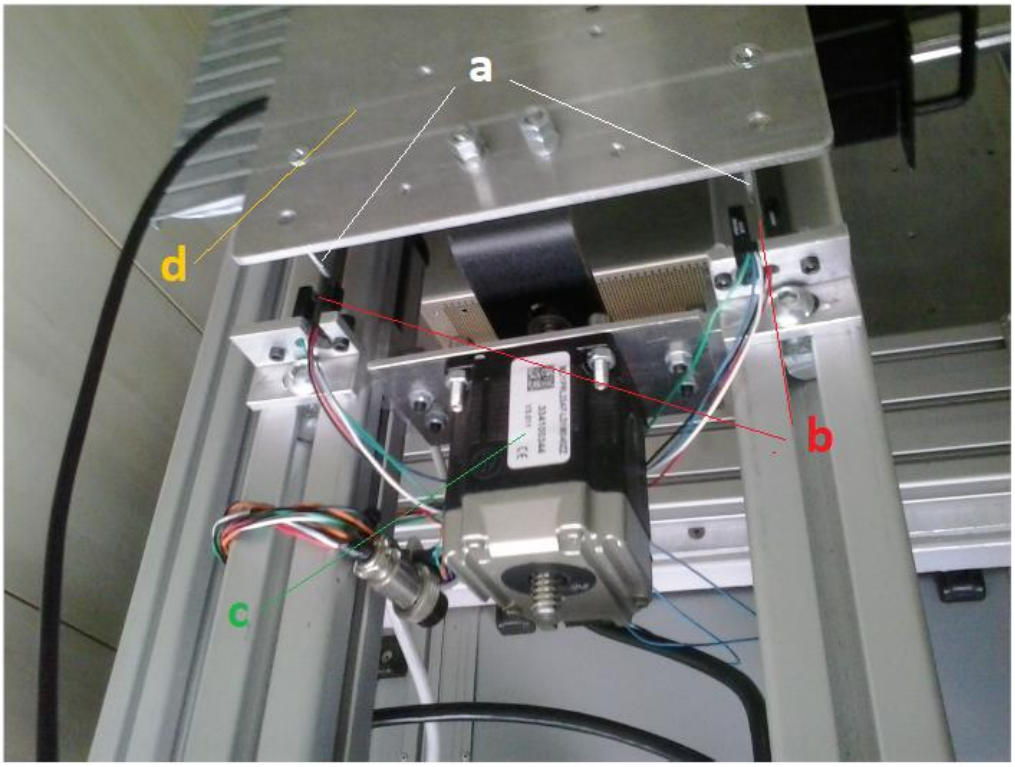

Figure 3.8: A photo of the plate and motor of the path length modulator and the two photodiodes (installed on the supports bar on the left and right); (a) the antenna plate supports, (b) the photodiodes, (c) the programmable motor, (d) the antenna plate.

3.4 The front end electronics

The front end electronics of the instrument receive the incoming signal from the quasi-optical system through the wave guide. The signal is immediately amplified by a low noise amplifier with 35 dB gain (see Figure 3.3). The amplifier noise should be as low as possible. Several instruments employ amplifiers that need a cryogenic system; these elements produce a high gain with low noise but the needing of a cryogenic system is problematic for an instrument such as VESPA-22, designed to automatically work in remote observation sites. Therefore, VESPA-22 employs a low noise amplifier, working at ambient temperature. Two noise diodes manufactured by Noisecom, elements producing a stable signal, are inserted in the waveguide before the first stage low noise amplifier by means of a 20 dB broadwall coupler (see Figure 3.3). The first noise diode, producing a signal of about 117 K, is used to perform automatic calibrations and the second to ensure the stability over time of the first one, as described by Gomez et al. (2012). I integrated the second noise diode in the VESPA-22 Acquisition software during the Ph.D. work. The calibration scheme is described in Section 3.8. A second amplification stage increases the signal intensity of 40 dB. A heterodyne receiver with a carrier signal of 20.480 GHz reduces the signal

frequency; the signal is contained in the upper sideband, whereas the lower sideband has been previously suppresses by a filter. The signal, now centered at 1.750 GHz, is amplified by 30 dB amplifier and passes through a second pass band filter that selects the component between 1.5 and 2.0 GHz. A second heterodyne circuit with a carrier of 2.0 GHz reduces the signal frequency between 0 and 500 MHz. The signal in this heterodyne receiver is contained in the lower sideband, whereas the upper sideband has been previously suppressed by the filter. A PC-controlled variable attenuator reduces the signal intensity to be correctly analyzed by the FFTS.

VESPA-22 employs an Agilent U1080A FFTS to analyze the signals. This device samples the signal with a frequency of 1 Gsamples/s, for a frequency range between 0 and 500 MHz. The incoming signal is integrated for a user controlled number milliseconds and digitalized using 8 bit of information. The user can select the signal intensity range used in the digitalization process; VESPA-22 employs an intensity range between 0 and 0.5 Volt, so it is important to set the programmable attenuator in the front end electronic to obtain the signal intensity within this range. An FPGA (Field-programmable gate array) computes the fast Fourier transform of the digitalized signal, obtaining the spectrum on 16384 channels with a frequency resolution of 31 kHz.

3.5 The observatory and measurements conditions

VESPA-22 employs several panels made of eccosorb CV-3 by Emerson and Cuming (thereafter simply eccosorb) as black body sources. Eccosorb CV is a premium quality tapered broadband microwave absorber. It is a moderately flexible urethane foam material having a front surface cut to a convoluted (egg-carton) shape. Because of the rounded convolutions and lack of sharp corners and points, Eccosorb CV is the preferred absorber for millimeter wave frequencies and for very wide incidence angles. There is no degradation in performance at incidence angles out to 60° off-normal. This material present a reflectivity at 22.23 GHz of about -40 dB and its emission can be considered as black body emission within 0.01%.

VESPA-22 is installed indoor to preserve it from the strong winds and storms which occur during the Polar winter season. It is located in a small wooden annex to the main observatory in order to minimize the presence of metal surfaces, which could produce standing waves (see Figure 3.9). The indoor installation prevents the deposition of snow and dust, as well as the condensation of water droplets, on the quasi-optical system, therefore improving the durability of the equipment. Additionally, the parabolic mirror and its driving motor are not exposed to strong winds, and VESPA-22 is therefore characterized by a pointing offset very stable with time. The spectrometer observes the sky through two 5-cm thick Plastazote LD15 windows, one covering the observation at angles from 10° to 60° above the horizon, called *signal window*, and a smaller one covering the zenith direction, *zenith window* (see Figure 3.9). This material was tested in the laboratory and proved to have a small absorption in the microwave region of interest. I designed the windows during this Ph.D. work to adapt to the gaussian beam of the quasi-optical system. In order to do this the gaussian beam dimensions have been

characterized in laboratory through the use of a black body made with a strip of eccosorb; with the instrument pointing the sky the FFTS was programmed to compute the mean spectral intensity of the received signal with an accumulation time of 0.5 seconds. Depending on the sky conditions, this measurement is affected by a natural variability of about 0.03% (of the order of 5-10 counts). The edge of the gaussian beam was defined as the distance with respect to the beam axis where a variation in the mean spectral intensity equal to two times the natural variability can be observed. The windows opacity was estimated during VESPA-22 installation and it was measured to be less than 0.0005 Nepers. The windows are not perpendicular with respect to the antenna beam in order to minimize the formation of standing waves. On the outside, the signal window is placed at about 1.5 m from the ground, in order to avoid to be blocked by snow during winter; furthermore, two powerful fans are utilized to blow off the snow from the observing windows, limiting deposition or ice formation.

Figure 3.9: A photo of the exterior of the wooden annex hosting VESPA-22. The observing window of the signal beam is visible on the side of the annex. The fan blowing on the zenith windows can be seen on the roof; the other fan was not yet installed at the time this photo was taken.

As explained in 3.9, VESPA-22 compares the sky emission from the zenith direction to the sky emission coming from an angle close to the horizon in order to perform a stratospheric measurement. In this thesis the observation angle close to the horizon is called *signal angle*, the zenith emission measured by the instrument is indicated as *reference beam*, whereas the emission from the signal angle is defined *signal beam*. The zenith is observed through a Delrin® acetal homopolymer resin sheet (hereafter simply delrin) that adds a grey body emission to the zenith emission (see Figure 3.1); this element forms an

angle with the incident beam equal to the Brewster's angle, in order to minimize the reflection and the formation of standing waves.

The laboratory hosts also a meteorological station with temperature, pressure and relative humidity sensors. The temperature inside the annex is also monitored by two other temperature sensors, one placed inside an eccosorb black body used for calibrations, as described in Section 3.8, and the other placed on the delrin grey body. I integrated the measurements of the meteorological station and all these different sensors with the VESPA-22 Acquisition Software described in the next section.

3.6 Acquisition software

The acquisition software controls all the VESPA-22 operations. The programming language used is LabView, a visual block programming language in which the programmer represents the various operations as a block diagram (see Figure 3.10 for an example of the main sequence of VESPA-22 acquisition system). This language can interact with all the subsystems composing the instrument, such as the motors, the encoder, the FFTS, the noise diodes, the variable attenuator and the meteorological station; it is also a modular code in which the block operations are subroutines easily upgradable without changing the main sequence.

Part of my work for the completion of this thesis was directed to the upgrade and expansion of the initial acquisition code already available (Bertagnolio, 2012), allowing VESPA-22 to operate automatically and reliably for all the routine tasks.

The main task was to create a reliable software that would allow VESPA-22 to operate with the minimum amount of maintenance by local technicians. With this goal in mind, I developed an automatic mode for the instrument. The automatic mode is a cycle of operations that allows VESPA-22 to take measurements and controls the correct function of the different subsystems. The automatic mode cycle starts checking the status of the different subsystem such as the motors, the meteorological station or the FFTS. The position of both the path length modulator and the reflector is then reset: the first one to the distance d of maximum coupling with the reflector and the second to the horizontal position (observation angle 0°). An automatic calibration of the FFTS is then executed using the dedicated firmware. This internal calibration allows the FFTS to take into account the temperature variation inside of the observatory that could produce a drift in the measured spectra. The instrument then measures the FFTS dark signal (the signal measured by the FFTS in absence of input) by setting the variable attenuator to the maximum attenuation of 31 dB. The dark signal is subtracted to every spectrum measured by the instrument and it has an intensity of about 0.3% with respect to the mean value of the measured spectra.

The instrument then performs a tipping curve and two complete data acquisition measurements (Section 3.9 and paragraph 3.8.2). At the beginning of each one of these operations, the control program acquires measurements from the indoor temperature sensors and from the meteorological station; at the end of each one, the positions of the mobile elements of VESPA-22 are resettled as described above in order to minimize errors in the measurement angle due to incorrect

positioning. Then the cycle restarts; the entire automatic cycle takes about 36 minutes. This operation cycle proved to be reliable during this first year of operations of VESPA-22, from July 2016 to July 2017. In particular, due to the indoor installation and the checks on the mobile elements, VESPA-22 is characterized by a pointing offset very stable with time.

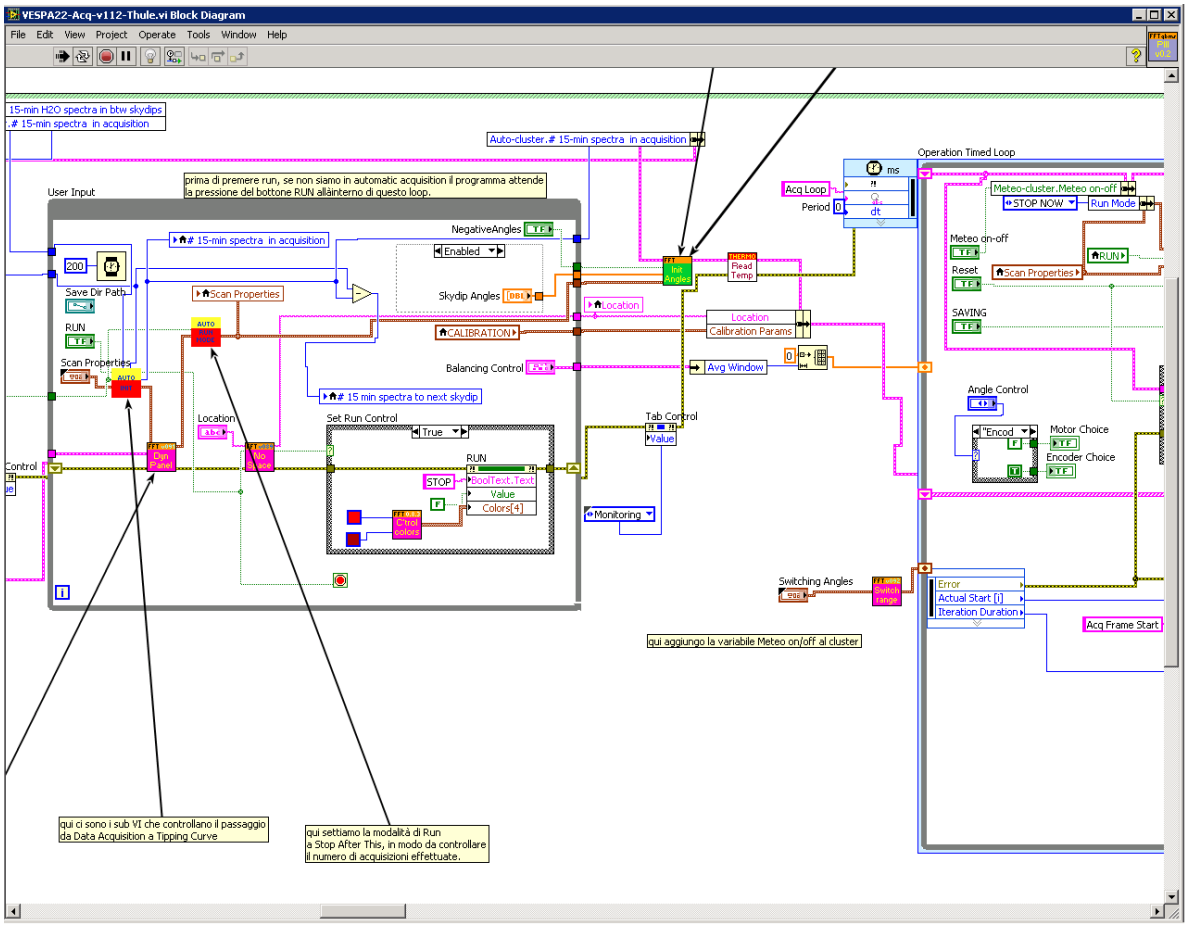

Figure 3.10: An example of a LabView code. A block diagram with the information passing through the wires represents the various operations executed by the software.

During this Ph.D. work, the Sun pointing procedure was integrated in the VESPA-22 acquisition system. The Sun Pointing is a procedure to evaluate the difference between the observation angle measured by the encoder and the real angle at which the instrument is pointing through the Sun position (see Section 3.11). The Sun pointing is automatically executed one time a day during the period of the year in which the Sun position can be directly observed by the instrument. The second noise diode was included in the system in order to check the stability of the first one. The photodiodes were installed and the procedure of repositioning for the antenna in order to maintain the correct distance antenna-reflector was developed.

In July 2016, during the transport of the instrument to Thule, the coupler connecting encoder and reflector supporting axis was damaged. This led to incorrect angle measurements by the encoder. In absence of a substituting piece, I elaborated an emergency system for the observation angle measurement. The observation angle was measured checking the motor position by questioning the motor firmware and calculating the correspondent observation angle by means of the relation between motor steps and reflector rotation angle. This "emergency encoder" proved to be reliable, determining the mirror position with a small difference with respect to the encoder (supposedly) correct measurement (less than 0.05°) allowing VESPA-22 to continue the operations for days until the coupler was properly replaced in late July. The emergency encoder is still included in the acquisition software, resulting in two measurements of the observation angle, one by the encoder and the other through the motor internal firmware, as can be seen in Figure 3.24, where three indicators for the observation angle can be found. The first of these shows the angle measured by the encoder, the second the angle measured using the internal motor firmware, whereas the third the angle that used for the instrument calculation (the encoder angle in this case). Observing the difference between these indicators can reveal encoder or motor problems.

I directed many efforts to minimize the switching time of the reflector from the observation of the signal angle to the zenith, in order to increase the effective integration time of a measurement.

Several other minor bugs were fixed and improvements were implemented in the acquisition software during the installation of the spectrometer at the THAAO.

3.6.1 The front panel

The Front Panel is the graphic interface for the Acquisition Software designed to control every operation of the instrument. The front panel has three different masks: the Service Mask, the FFTS Mask and the Monitoring Mask. I worked to improve the Front Panel in order to present to the user all the useful information and warnings about the VESPA-22 status. The Service Mask (Figure 3.11) receives the input by the user and presents the different operation that VESPA-22 can execute. On the left side in Figure 3.11, there are several indicators to monitor the correct state of the data acquisition, together with the buttons start/stop measurement, reset measurement and save measurement. The right side hosts the buttons and the switches for the setting of the different operations of the instrument, together with useful indicators (such as, for example, the brightness temperature of the noise diodes). The figure shows two graphs monitoring the temperature measured by the different sensors (the upper graph) and the residuals of the Tipping Curve Technique (bottom graph), described in Section 3.8.2. In the first graph, the purple dots are the measurements from the temperature sensor of the meteorological station outside the annex, the blue and yellow dots show the temperature of different components of the FFTS, and the red and green dots show the temperature of respectively the delrin and the hot body, measured by the two thermometers inside the annex.

The Figure 3.12 shows the FFTS Mask of the Front Panel. Here the user can set the FFTS parameter, such as the interval of digitalization of the incoming signal (between 0 and 0.5 V here), and check the FFTS status.

The Monitoring Mask of the Front Panel shows to the user the measured data; the elements composing this last mask depend on the operation executed by the instrument.

Figure 3.11: The front panel of the VESPA-22 acquisition software. A particular of the Service mask

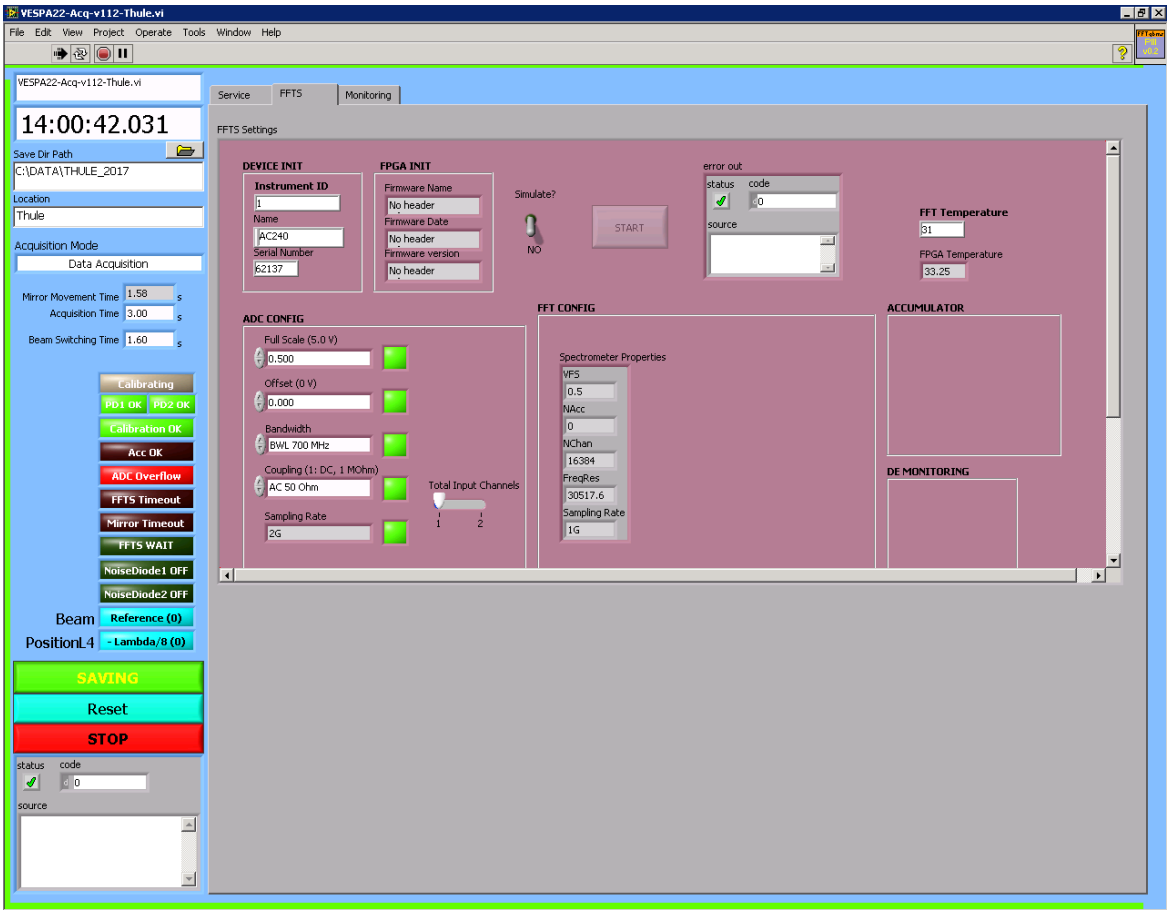

Figure 3.12: The FFTS Mask of the Front Panel.

3.7 Measurement equations

The following sections describe the measurement equations and techniques employed by VESPA-22. As part of my Ph.D., I worked to improve the operations executed by the instrument to perform the various measurements through the Acquisition Software programming and to improve and develop reliable data analysis codes for the results analysis.

The Eq. (3.1), derived in Section 2.2 using the horizontally homogeneous atmosphere approximation, describes the radiation received by an instrument at the ground observing the sky with an elevation angle θ.

$$T_S(\theta) = T_\nu(z_{toa}) e^{-\tau_{\nu,z}(z_{toa})\mu(\theta)} + \mu(\theta) \int_{z_0}^{z_{toa}} T(z) e^{-\tau_{\nu,z}(z)\mu(\theta)} \alpha_\nu(z) dz \ . \tag{3.1}$$

In order to simplify this equation, the following approximations can be adopted (Nedoluha et al., 1995).

- The major part of the incoming radiation measured by VESPA-22 comes from the lower troposphere, where more than 90% of the total amount of water vapor is present. The emission line from this layer is characterized by a half width at half maximum that is larger than the bandwidth of the instrument (see Eq. (2.23) for the pressure dependence of the emission line width) and can be approximated with a frequency constant emission. The troposphere itself is represented as an isothermal domain absorbing the signal to be measured from the stratosphere. The temperature characterizing this domain T_{trop} is the troposphere average temperature, weighted with the water vapor density

$$T_{trop} = \frac{\int_{tropo} \rho(z) T(z) dz}{\int_{tropo} \rho(z) dz} , \tag{3.2}$$

  where $\rho(z)$ is the water vapor density and T the physical temperature; both quantities are integrated on the troposphere.

- The contribution of the stratospheric water vapor absorption to the opacity τ is small with respect to the tropospheric contribution and can be neglected. A measurement of atmospheric opacity as those carried out using the tipping curve technique (Section 3.8.2) can be considered a measurement of tropospheric opacity. I tested this approximation by calculating the atmospheric opacity by means of the radiative transfer simulation software ARTS (Eriksson et al., 2011) and using water vapor vertical profiles with and without their stratospheric component. At the frequency of maximum absorption, the contribution of the stratospheric profile to the atmospheric opacity is between 2% and 5% depending on the season. This contribution is even lower for frequencies far away from the line center. The difference between the opacity calculated using a normal vertical water vapor profile and a profile with no water vapor above the tropopause is between 0.4% and 1.3% depending on the season when averaged over the VESPA-22 frequency range. In Figure 3.13, the opacity calculated by ARTS using complete water vapor profiles from the ground to 110 km altitude and the opacity calculated with the same profiles but with no water vapor above the tropopause are displayed in panel (a), whereas panel (b) and (c) display the absolute and relative difference calculated between the tropospheric opacity and complete profile opacity. The simulation employs water vapor, temperature and pressure profiles measured above Eureka station (80.0°N -85.9°W), Canada, on 18 July 2016, 10 December 2016, and 21 May 2017 by the instrument MLS onboard the AURA satellite (Waters et al., 2006) for the stratospheric and mesospheric simulation, whereas the tropospheric profiles are provided by radiosondes measurements. Panel (d) shows a particular of the opacities calculated using the 18 July 2016 profile.

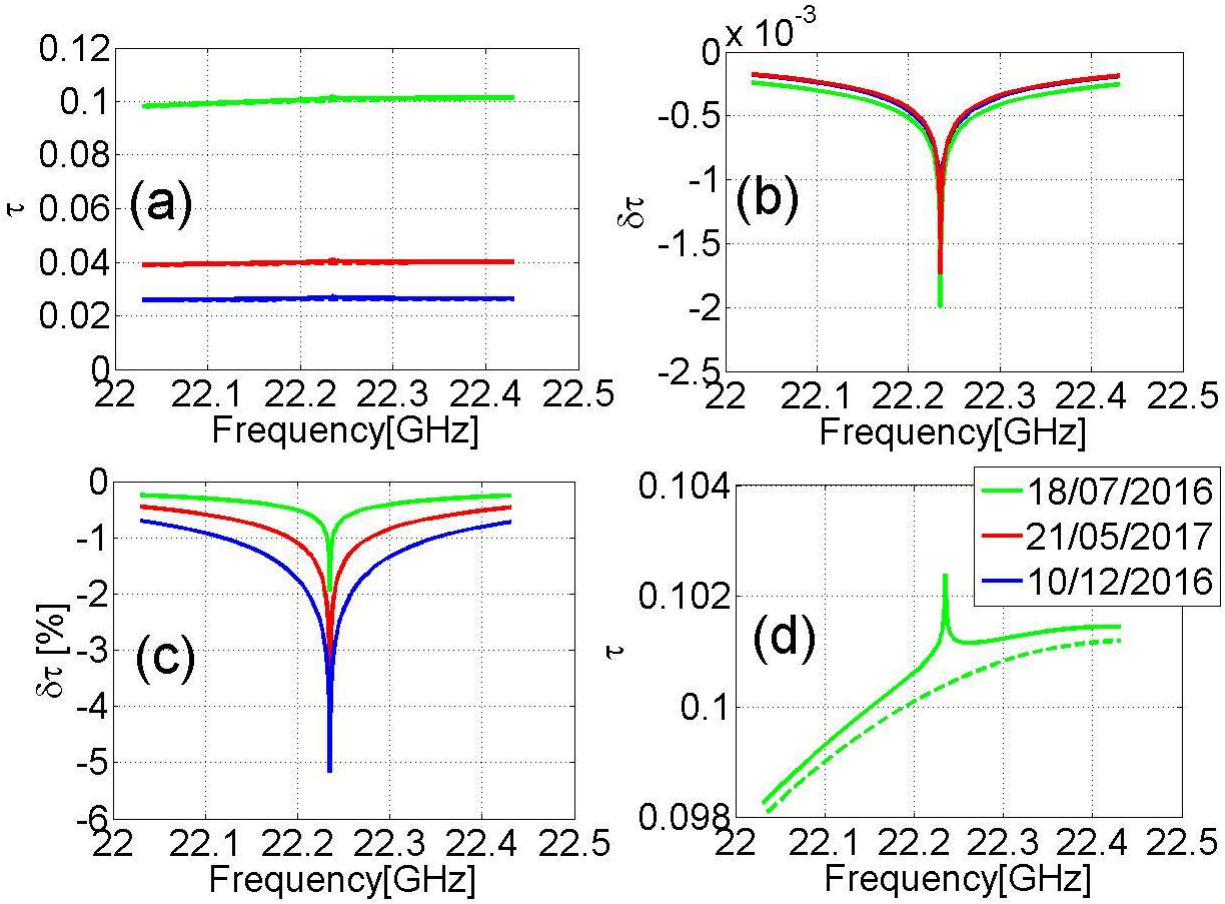

Figure 3.13: Atmospheric opacity (a) calculated by ARTS for a complete water vapor profile (solid lines) and for the same profile with no water vapor above 10 km (dashed lines); (b) absolute and (c) relative differences tropospheric opacity minus complete water vapor profile opacity for the profiles measured by radiosondes and MLS/Aura above Eureka station (80.0°N -85.9°W), Canada, on 18/07/2016 (green), 10/12/2016 (blue) and 21/05/2017 (red); (d) particular of the opacity for the 18/07/2016 profile.

- The tropospheric opacity τ_ν can be substituted by its mean value τ. The maximum difference between τ_ν and its mean value τ is between 1.6 and 3.6 % depending on the season.
- The only signal coming from outside the atmosphere, T_0, is the cosmic background radiation with a constant brightness temperature of 2.725 K.

With these approximations Eq. (3.1) can be written as

$$T_S(\theta) = T_\nu(z_{toa})e^{-\tau\mu(\theta)} + \mu(\theta)T_{trop}\int_{tropo} e^{-\tau(z)\mu(\theta)}\alpha_\nu(z)dz + \mu(\theta)\int_{strato} T(z)\alpha_\nu(z)e^{-\tau(z)\mu(\theta)}dz\ , \qquad (3.3)$$

where the integral of Eq. (3.1) was divided into two terms, the first one representing the tropospheric emission and the second representing the emission from the rest of the atmosphere. The physical temperature of the troposphere is constant as described by the approximation. Solving the first integral term Eq. (3.3) can be written as

$$T_S = T_0 e^{-\mu\tau} + T_{trop}\left(1 - e^{-\mu\tau}\right) + \mu T(\nu) e^{-\mu\tau} \ . \tag{3.4}$$

The first term on the right side is the extra-atmospheric emission, the second term of the right side is the solution of the radiative transfer equation for an isothermal domain and it represents the tropospheric emission with T_{trop} as the mean tropospheric temperature weighted with the water vapor concentration. The third term is the result of the second integral term and represents the emission coming from the stratosphere and mesosphere, with $T(\nu) = \int_{strato} T(z)\alpha_\nu(z)dz$ the stratospheric signal brightness temperature (in the integral the stratospheric auto-absorption was neglected as described in the approximation). The stratospheric signal is proportional to the air mass factor μ and attenuated by the troposphere.

In all the previous terms $e^{-\mu\tau}$ is the tropospheric signal absorption. $T(\nu)$ is the stratospheric signal that has to be inverted in order to retrieve the water vapor stratospheric profile. It's important to note that $T(\nu)$ is the only frequency dependent term of the right side of Eq. (3.4), as the tropospheric opacity was approximated as constant in frequency.

3.8 The calibration equations

The signals received by VESPA-22 are measured in terms of counts, proportional to their brightness temperature. The relation between signal brightness temperature and measured counts is linear, as expressed by Eq. (2.25) repeated here for clarity:

$$V = g\left(T + T_{rec}\right) \ , \tag{3.5}$$

where V and T are respectively the signal intensity in term of counts or brightness temperature.

In order to calculate the calibration parameters g and T_{rec}, two independent measures of two sources at different brightness temperature are required: the *hot source* and the *cold source*. From Eq. (3.5) knowing the brightness temperature of the sources, the calibration parameters can be calculated according to the Eq. (3.6) and (3.7) (de Zafra el al., 1995):

$$g = \frac{V_{hot} - V_{cold}}{T_{hot} - T_{cold}} \ , \tag{3.6}$$

$$T_{rec} = \frac{T_{hot}V_{cold} - T_{cold}V_{hot}}{V_{hot} - V_{cold}} \ . \tag{3.7}$$

V_{hot} and V_{cold} are the spectra of the hot and cold sources measured in terms of counts whereas T_{hot} and T_{cold} their respective brightness temperatures. The instrument collects some measurements adding to the incoming signal the emission of the noise diode, for example during the observation of the cold body in the liquid nitrogen calibration described in paragraph 3.8.1. The counts measured in this situation, V_{x+nd} are described by the Eq. (3.11)

$$V_{x+nd} = g\left(T_x + T_{nd} + T_{rec}\right) . \tag{3.8}$$

In this thesis work, the subscript x in Eq. (3.8) is substituted by "R", if the instrument adds the noise diode emission to the reference beam (see Section 3.9) or by "cold", if the noise diode emission is added to the cold source emission (paragraphs 3.8.1and 3.8.2). T_{nd} is the noise diode brightness temperature and T_x is the brightness temperature of the reference beam/cold source. Comparing Eq. (3.5) and (3.8), T_{nd} can be obtained using the following equation

$$T_{nd} = \frac{V_{x+nd} - V_x}{g} . \tag{3.9}$$

The T_{nd} value is used to calibrate the measured spectra, as will be shown in Section 3.9. T_{nd} can be measured in two ways: through liquid nitrogen calibration or a tipping curve calibration.

3.8.1 The calibration using liquid nitrogen

This operation is used to obtain the parameter g and T_{rec}, described in Eq. (2.25), used to associate the correct brightness temperature to a signal expressed in counts. In order to calculate the parameters, two independent measures of two emitting sources at different brightness temperature are required.

The instrument observes the emissions from two black bodies made of eccosorb CV-3 panels by Emerson and Cuming, one at ambient temperatures and the other immersed in the liquid nitrogen. In this thesis, I will refer to the black body at ambient temperature as *hot body* or *hot source*, whereas the other will be called *cold body* or *cold source*. The brightness temperature of a black body is equal to its physical temperature. The VESPA-22 temperature sensors measure the physical temperatures of the two sources. These sensors are inserted during measurements inside the eccofoam black bodies.

During the observation of the cold body, the noise diodes are alternately turn on and off. Therefore, for every couple of hot body, cold body observations four spectra are observed: the hot body spectrum, the cold body spectrum, the cold body spectrum to which is added the emission of the first noise diode and the cold body spectrum to which is added the emission of the second noise diode. The noise diodes spectra in term of counts are calculated according to Eq. (3.10)

$$V_{nd} = V_{cold+nd} - V_{cold} . \tag{3.10}$$

Each spectrum has an integration time of 3 seconds. This operation is repeated 5 times for both positions of the path length modulator, resulting in ten quartets of hot body, cold body and noise diodes spectra.

During the liquid nitrogen calibration the calibration parameters g and T_{rec} are calculated according to Eq. (3.6) and (3.7). For the liquid nitrogen calibration, V_{hot} and V_{cold} are the spectra of the hot and cold body measured in terms of counts

whereas T_{hot} and T_{cold} their respective physical temperatures. As described, the noise diodes are switched on during the observation of the cold body; the counts measured in this situation $V_{cold+nd}$ are described by the Eq. (3.11)

$$V_{cold+nd} = g\left(T_{cold} + T_{nd} + T_{rec}\right), \tag{3.11}$$

where T_{nd} is the noise diode brightness temperature. Confronting Eq. (3.5) and (3.11), T_{nd} can be obtained from Eq. (3.9) obtaining

$$T_{nd} = \frac{V_{cold+nd} - V_{cold}}{g}. \tag{3.12}$$

The Figure 3.14 (a) is a picture of VESPA-22 executing a liquid nitrogen calibration. The hot body is on the left, whereas the cold body is under the reflector. Both the black bodies present on their surface many conical structures, designed to minimize the reflection and so the standing waves formation. The cold body in inserted in a wooden box, inside a cradle made of Plastazote LD15 and totally immersed in the liquid nitrogen, Figure 3.14 (b). The use of plastazote as a container for the LN_2 strongly reduces its evaporation with respect to using a stainless steel vessel. Avoiding the excessive evaporation is important in order to reduce the amount of liquid nitrogen needed to perform the operation, an important feature for an instrument working in remote locations.

(a)  (b) 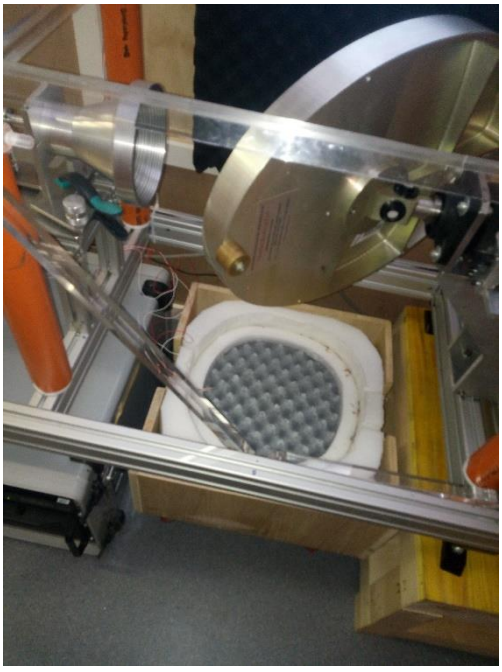

Figure 3.14: (a) A photo of the instrument performing a liquid nitrogen calibration. The hot body is situated on the left in the picture, whereas the cold body is below the reflector; (b) the cold body is positioned inside a wooden box, easily movable through four wheels. The plastazote containing LN_2 reduces the amount of evaporation.

In Figure 3.15 the spectra collected during the liquid nitrogen calibration performed on 20 February 2017 are showed. Figure 3.16 presents the calculated spectra of the noise diodes. The noise diodes produce a signal that can be considered constant in frequency within 1.5%. This value is calculated by means of the maximum difference between the values assumed by the noise diodes brightness temperature on the frequency bandwidth.

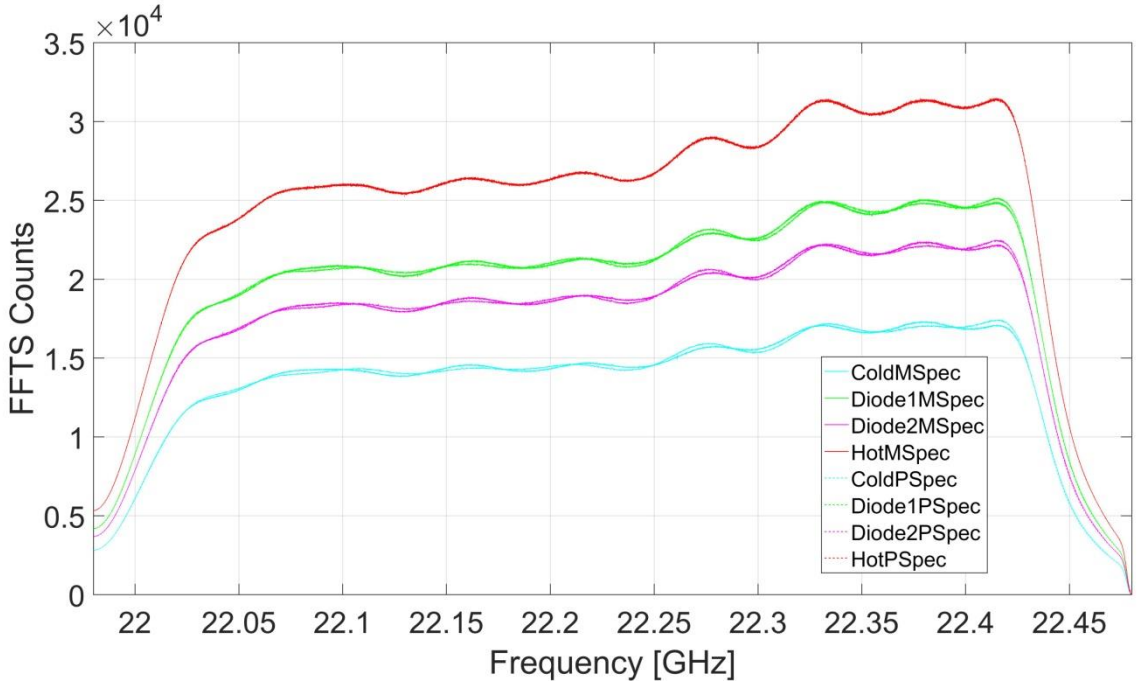

Figure 3.15: The spectra measured during a liquid nitrogen calibration. The cold body spectrum is in cyan, the hot body spectrum in red, the spectra measured observing the cold body with noise diodes switched on are in green and purple. The solid and dashed lines represent the spectra measured with the two different positions of the path length modulator.

The spectra originated from the black body immersed in LN_2 can be affected by standing waves due to interaction of the radiation with the air-LN_2 separation surface, as can be seen observing the cyan solid and dotted lines in Figure 3.15. Figure 3.17 displays the difference between hot body emission spectra measured averaging together only the data acquired with the path length modulator on respectively the $-\lambda/4$ and $+\lambda/4$ position (blue and yellow lines) and the mean hot body spectrum. Note that eventually standing waves on the hot body spectrum are characterized by a relative amplitude lower than 0.1%, the thermal noise intensity, therefore are not visible in Figure 3.17; this is due to the low eccosorb reflectance (see Section 3.5). In order to avoid transferring the cold body spectrum standing waves to the sky signal during the calibration process, T_{nd} is averaged over the central 11000 channels of the FFT spectrometer, as suggested by Gomez et al. (2012). Therefore, using Eq. (3.12) and (3.6), the mean value of T_{nd} is:

$$T_{nd} = \left(T_{hot} - T_{cold}\right) \sum_{i=3000}^{14000} \frac{V_{cold+nd,i} - V_{cold,i}}{V_{hot,i} - V_{cold,i}} \ . \tag{3.13}$$

In this equation, the sum is on the channels indicated by the subscript i.

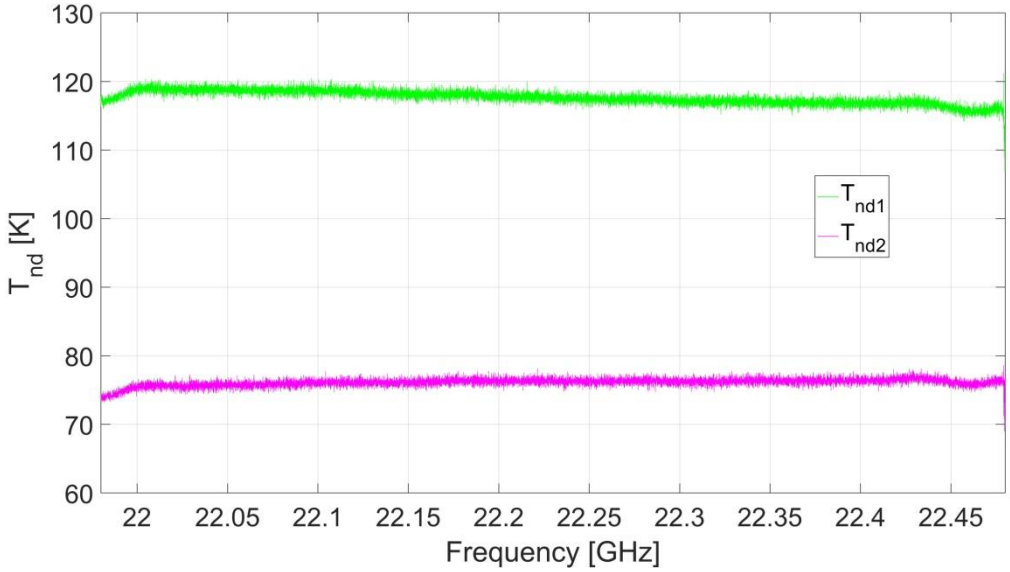

Figure 3.16: The spectra in Kelvin of the two noise diodes obtained from Eq. (3.12). In green the noise diode used for the instrument calibration, in magenta the second noise diode used as reference (mean values respectively 117.8 K and 76.2 K).

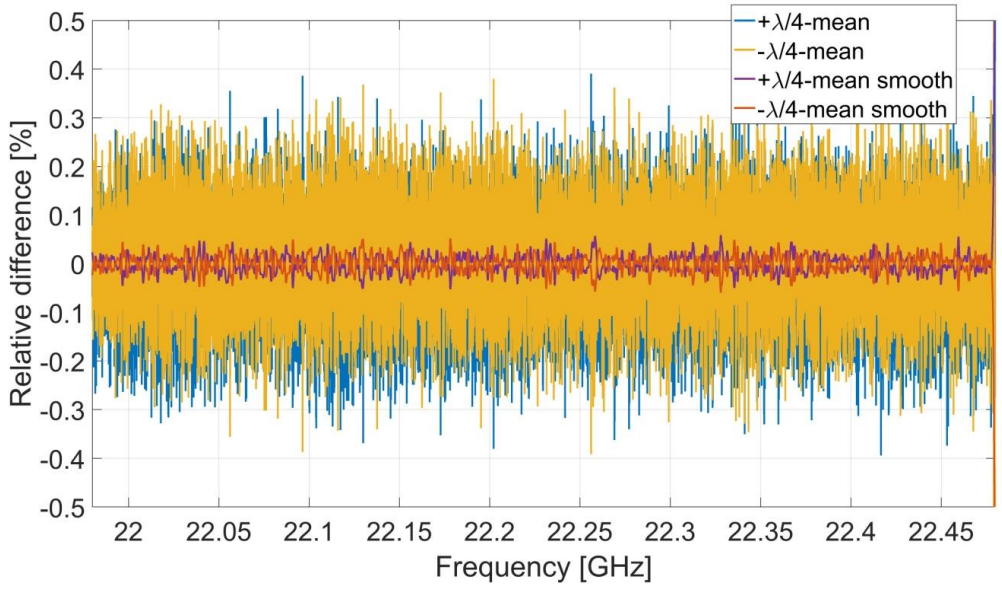

Figure 3.17: the difference between hot body emission spectra measured averaging together only the data acquired with the path length modulator on respectively the $-\lambda/4$ and $+\lambda/4$ position (blue and yellow lines) and the mean hot body spectrum. The purple and orange lines represent a 50-channel moving average of the same difference described above.

Figure 3.18 displays the receiver temperature as a function of the frequency calculated by means of the liquid nitrogen calibration. As the spectra shown in Figure 3.15, T_{rec} is afflicted by oscillations due to the standing waves of the hot and cold body spectra.

Due to the needing of liquid nitrogen, this operation cannot be executed automatically and is performed about twice a year, when expert personnel are at the THAAO.

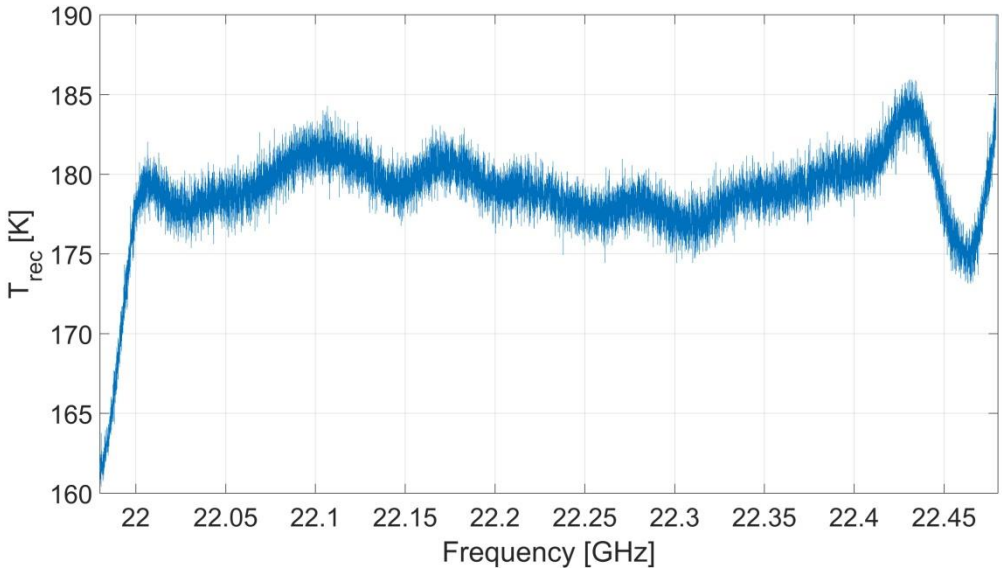

Figure 3.18: The receiver temperature as a function of the frequency obtained from the liquid nitrogen calibration (mean value 179 K).

3.8.2 The tipping curve technique

Although the liquid nitrogen calibration allows an accurate estimation of the calibration parameters g and T_{rec} and of the noise diode temperature, it requires the presence of expert personnel, so it can be executed only during VESPA-22 maintenance, for a limited number of times during the year, most likely twice a year. The noise diodes brightness temperature can vary with time, for example, due to annex temperature variations. The need for monitoring these variations requires a different calibration technique that can be executed automatically by the instrument.

The *tipping curve calibration technique*, also called *skydip* (Nedoluha et al., 1995, Deuber et al., 2004), allows both to measure the noise diodes brightness temperatures and the atmospheric opacity. During this procedure, the instrument measures T_{nd} through the observation of the black body at ambient temperature (the same used for the liquid nitrogen calibration) as hot source and of the sky at 60° of elevation as cold source. The retrieved atmospheric opacity and T_{nd} are used to calculate the stratospheric water vapor emission spectrum, as described in Section 3.9 by Eq. (3.24).

The tipping curve procedure is performed twice every hour and lasts about one minute. During a tipping curve, VESPA-22 collects the radiation coming from different elevation angles, approximately every 5° from 35° to 60° above the horizon. The measured spectra are averaged using the 11000 central channels of the spectrometer. Radiation from the stratosphere contributes less than 1% and can be neglected, so the mean signal intensity from the observed angles $\bar{T}(\theta_i)$ can be described by means of the following:

$$\overline{T}(\theta_i) \cong T_0 e^{-\mu(\theta_i)\tau} + T_{trop}\left(1 - e^{-\mu(\theta_i)\tau}\right) . \quad (3.14)$$

In absence of independent measurements of temperature and water vapor mixing ratio in troposphere, I estimated the tropospheric temperature T_{trop} from the surface temperature T_{surf} :

$$T_{trop} = T_{surf} - d \ , \quad (3.15)$$

where the value of d can be affected by seasonal variations. In order to characterize this parameter, several radiosondes were launched during July, November and December 2016, and February 2017. I computed the value of the parameter d as a function of time from a linear interpolation between the mean values of $T_{surf} - T_{trop}$ measured during these four periods, as described in Table 3.1. I obtained T_{trop} according to Eq. (3.2).

Table 3.1: Mean values and standard deviation of $T_{surf} - T_{trop}$ obtained from the radiosoundings

Month	Mean ($T_{surf} - T_{trop}$)
July	14.4±2.8 K
November	8.3±3.6 K
December	9.4 ±3.8 K
February	9.4±2.1 K

Using Eq. (3.14), it is possible to explicit the relation between the opacity and the mean brightness temperature of the received signal:

$$\mu(\theta_i)\tau = \ln\left(\frac{T_0 - T_{trop}}{\overline{T}(\theta_i) - T_{trop}}\right) . \quad (3.16)$$

A linear regression between the opacities at θ_i, $ln\left(\frac{T_0 - T_{trop}}{\overline{T}(\theta_i) - T_{trop}}\right)$, and the air mass factors $\mu(\theta_i)$ allows to calculate of the opacity at the zenith, τ, (de Zafra, 1995). Substituting for $\overline{T}(\theta_i)$ using Eq. (3.5), the Eq. (3.16) can be written as:

$$\mu(\theta_i)\tau = \ln\left(\frac{T_0 - T_{trop}}{\frac{\overline{V}(\theta_i)}{g} - T_{rec} - T_{trop}}\right) , \quad (3.17)$$

where it appears that T_{rec} and g are needed to perform the calculation. In order to obtain an estimate of these two parameters, during the tipping curve procedure VESPA-22 measures also the emission from a CV-3 eccofoam panel, considered as a black body at ambient temperature (hot source). The sky signal at an elevation angle of 60° (T_{cold}^{sky}) acts as second calibration source (cold source). The emission from these two sources is used to calculate g and T_{rec} according to Eq.

(3.6) and Eq. (3.7). However, since the sky brightness temperature T_{cold}^{sky} is not known, I used an iterative procedure to obtain both τ and T_{cold}^{sky}. An initial opacity value, τ_0, is used as first guess to obtain $T_{cold,0}^{sky}$ using Eq. (3.14) with $\theta = 60°$. $T_{cold,0}^{sky}$ is then used to obtain g_0 and T_{rec_0} from Eq. (3.6) and Eq. (3.7); $\mu(\theta_i)\tau$ is calculated for different elevation angles using Eq. (3.17), and ultimately a linear fit allows calculating a new estimate for τ, τ_1. The iterative procedure goes on until the intercept value is minimized.

The value of T_{cold}^{sky} measured with this procedure is used in Eq. (3.13) to estimate the mean value of T_{nd} used for the automatic calibration. In order to avoid the use of data measured during inhomogeneous-sky condition the T_{nd} values from measurements producing fits with a root mean square higher than 0.4 are discarded.

The threshold was chosen in order to reduce the noise diode temperature oscillations due to the sky inhomogeneities, maintaining however a reasonably large number of measurements covering the whole time period examined in this work. Figure 3.19 shows the T_{nd1} timeseries examined using different values of threshold. The use a lower of threshold (0.2 in the figure) would have strongly reduced the number of measurements during winter and summer.

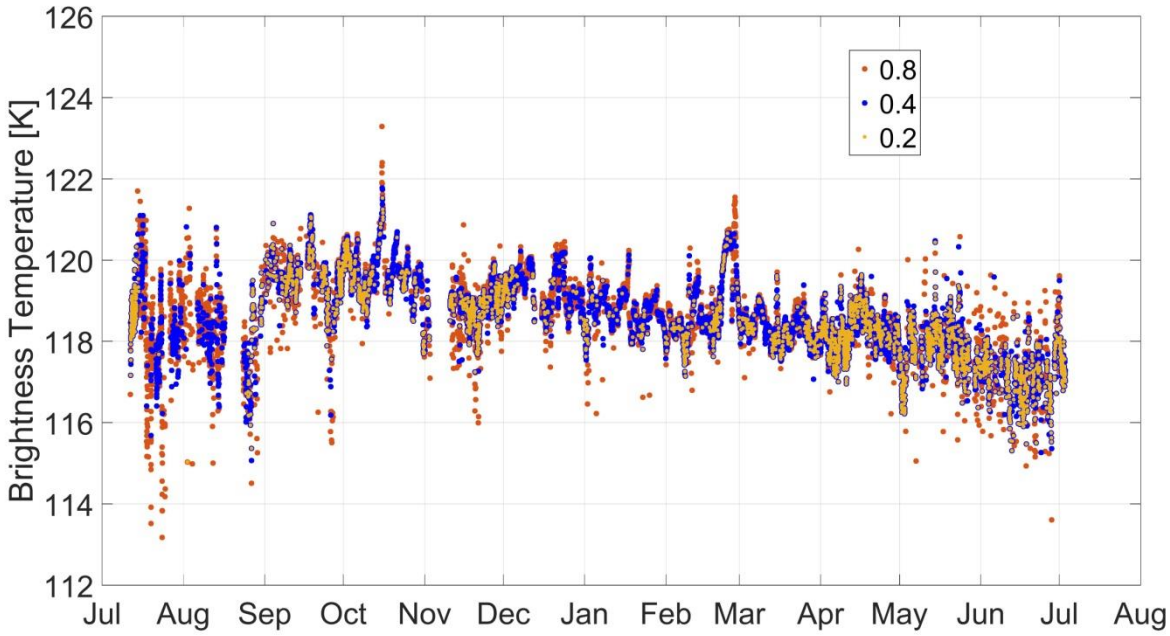

Figure 3.19: the T_{nd1} time series examined using different values of threshold, as described in the legend.

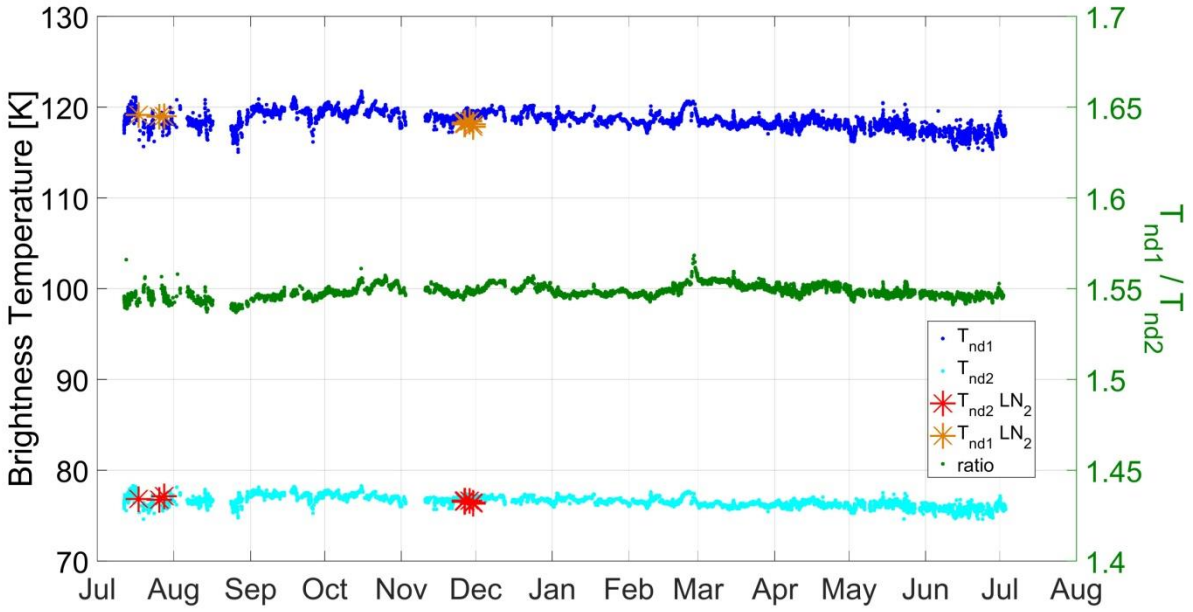

Figure 3.20: (left y-axis)Time series of the noise diodes brightness temperature calculated by means of the tipping curve procedure (blue and cyan full circles) compared with values obtained using LN2 calibrations (red and orange stars); (right y-axis) ratio between the two noise diodes (green dots).

Figure 3.20 shows the time series of both noise diodes brightness temperatures (blue and cyan) and their ratio (green dots referred to the right y-axis) from July 2016 to Jul 2017. The noise diode in blue is the one used as calibration diode and its emission temperature computed by means of the tipping curve is used to automatically calibrate the measured spectra. Both the noise diodes show fluctuations due principally to the sky inhomogeneities, equal to about 1% of the mean value of the noise diodes brightness temperatures. In the same plot, T_{nd} values obtained using an LN_2 cooled eccofoam CV-3 as the cold source are also depicted (orange and red stars). The mean relative difference between T_{nd} values calculated with the two calibration schemes (tipping curve and LN_2) is (0.4±0.4)% and (0.2±0.3)% for the calibration and the backup diodes, respectively. The ratio between the two noise diodes is useful to evaluate potential drifts of the signal emission temperature of the calibration noise diode: the ratio fluctuations displayed in Figure 3.20 are characterized by a mean value of 1.55 and a standard deviation of 0.003 (0.2%). Since the estimated uncertainty on such ratio is 0.05 (3.4%), there appear to be no drift in the time frame discussed in this work.

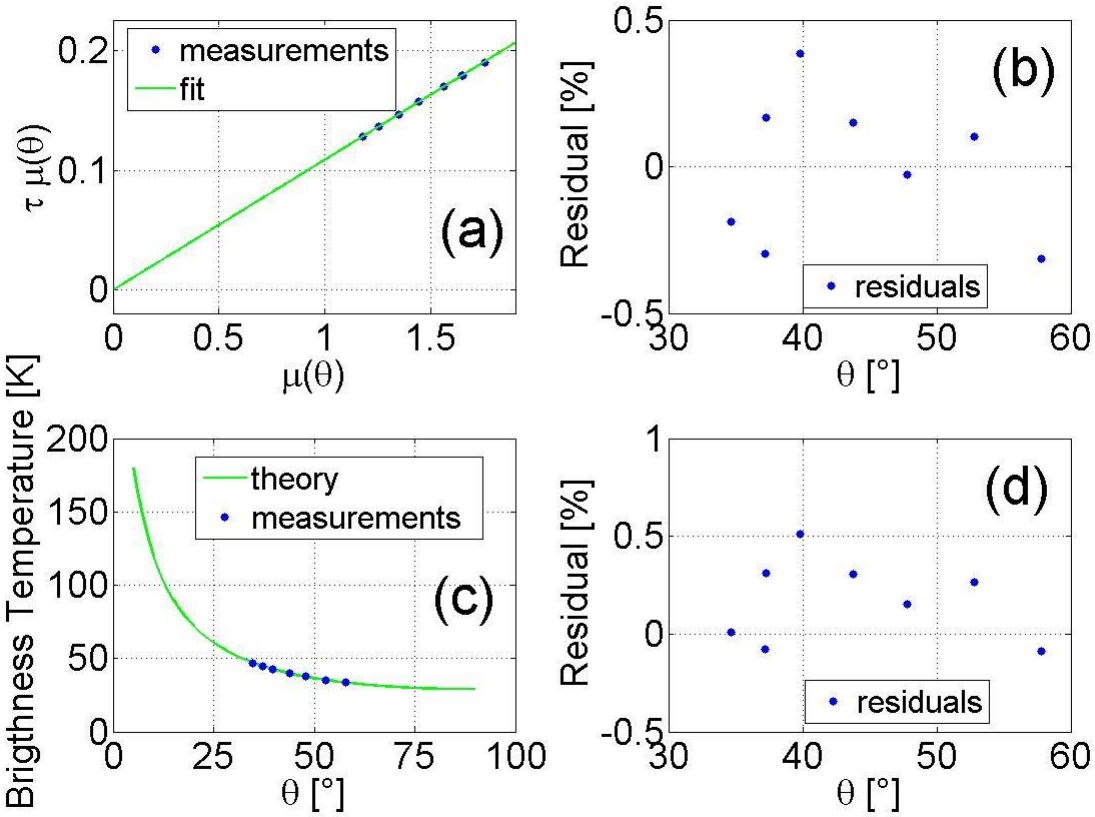

Figure 3.21: Skydip fit results. Panels (a) and (b): atmospheric opacity measured at different elevation angles (blue dots) compared with the skydip fit (green line) and fit residuals (the difference measurements minus fit); panels (c): brightness temperature measured at different elevation angles (blue dots) and emission described by Eq. (3.14) (green line) and, panel (d), their relative difference (measurements minus fit).

Figure 3.21 displays the results of a skydip. The panel (a) shows the factors $\tau\mu(\theta)$ calculated by means of Eq. (3.17) together with the resulting fit versus the air mass factor, whereas panel (b) shows the fit residuals. Panel (c) displays the mean brightness temperature received at the different angles (blue dots) compared with the emission calculated by means of Eq. (3.14) (green line) whereas panel (d) shows the relative difference between the measured brightness temperatures and the values predicted by Eq. (3.14).

In order to evaluate the T_{nd} uncertainty, I considered the 0.4% difference between the values obtained by means of the skydip and the LN_2 calibrations (Figure 3.20). On top of this, also the fluctuations of the signal produced by the calibration diode must be taken into account. These can be evaluated by using the standard deviation of the difference over time between the T_{nd} values of the two noise diodes calculated using the tipping curve calibration technique, measured to be about 1.2 K (1.1)%. Figure 3.22 shows the oscillations of the difference $T_{nd1} - T_{nd2}$ with respect to the difference mean value (42.04 K) and their relative values with respect to T_{nd1}. The tipping curve procedure allows calculating the noise

diodes brightness temperature averaged on the 11000 central channels of the spectrometer. However the noise diodes brightness temperature cannot be considered as constant in frequency (Figure 3.16) and using a mean value introduces a source of uncertainty; this contribution can be evaluated calculating the standard deviation of the T_{nd} spectra calculated by means of the liquid nitrogen calibration, equal to 0.9%. Another source of uncertainty is caused by the oscillation due to sky inhomogeneities, about 1%. All the calibration equations shown in this chapter assume a linear relation between measured FFTS counts and the sources brightness temperature (see Section 3.8). In order to verify the detector linearity, the emissions from the two sources used in the LN_2 calibration should be compared to the emission of a third source at known brightness temperature. In absence of this third source the uncertainty introduced by the detector non-linearity can be estimated observing the residuals showed Figure 3.21 panel (d). The residuals values are related mainly to the sky inhomogeneities: the residuals maximum value, during days characterized by an extreme dry atmosphere with clear sky conditions is less than 0.2%, producing fits characterized by $R^2 < 0.2$. The value 0.2% is therefore used as detector non-linearity contribute to the T_{nd1} uncertainty.

The different sources of uncertainty described are added in quadrature to obtain the T_{nd} uncertainty of 1.8%.

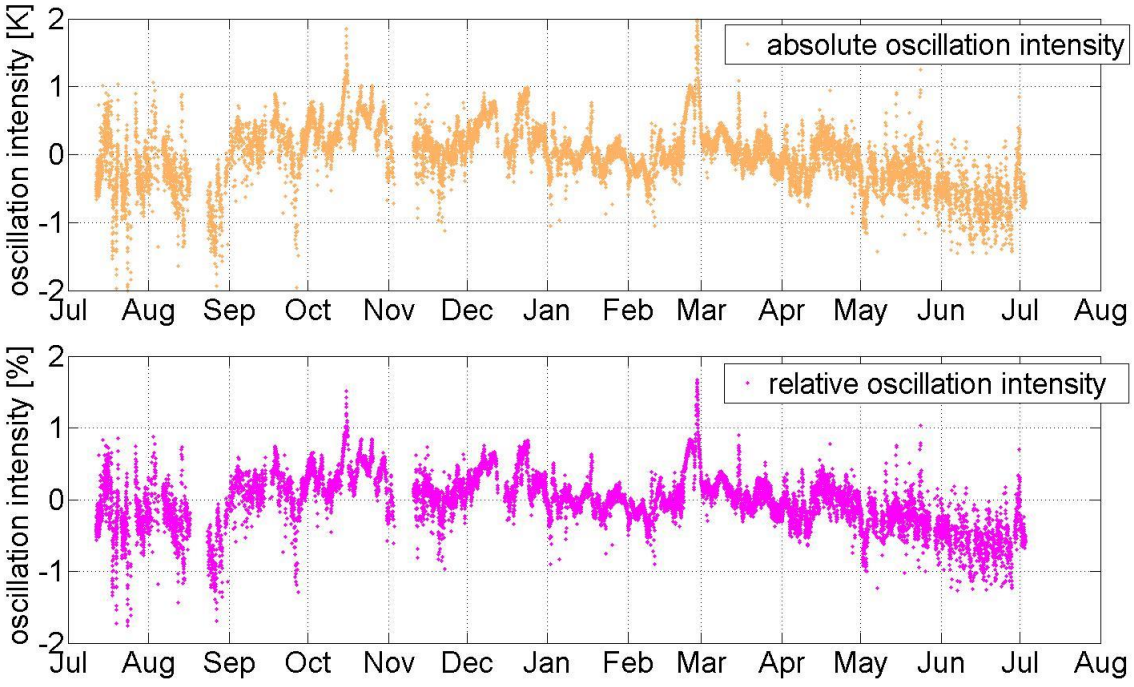

Figure 3.22: The absolute and relative intensity of the oscillation of $T_{nd1} - T_{nd2}$, measured by means of the tipping curve, around the difference mean value. The relative oscillation intensity is computed with respect to T_{nd1}.

In order to estimate the uncertainty on the measured opacity, I considered the uncertainties introduced by sky inhomogeneity and the estimation of the effective tropospheric temperature T_{trop}. The first contribute it is about 2% but can increase depending on the sky condition. It is estimated using the uncertainty of the slope parameter produced by the fit used in the

tipping curve procedure (see the Section 3.8.2). The second contribution can be evaluated observing the daily fluctuations of T_{trop} measured at the meteorological station of Eureka (Northern Canada), Aasiaat and Alert (Southern Greenland and Canada respectively). Figure 3.23 displays the difference $d = T_{surf} - T_{trop}$ measured at Eureka station. For VESPA-22 measurements this difference used to compute T_{trop} (Eq. (3.15)) is measured few times a year, when radiosonde measurements are available. Using Eq. (3.15) VESPA-22 is not able to take into account the daily fluctuations of this difference. In order to evaluate the natural day to day fluctuations intensity one year of data from Eureka station was analyzed (from July 2016 to July 2017) (Figure 3.23). In order to eliminate the seasonal fluctuations, a 100-day moving average was computed and was subtracted to the sequence. The standard deviation of the residual is about 6 K (Figure 3.23, panel (b)) and is used as uncertainty of calculated T_{trop} (the uncertainty of T_{surf} measured by the meteorological station is considered negligible with respect to the d uncertainty in T_{trop} calculation). The T_{trop} uncertainty makes the total uncertainty $\Delta\tau$ to be 5 %.

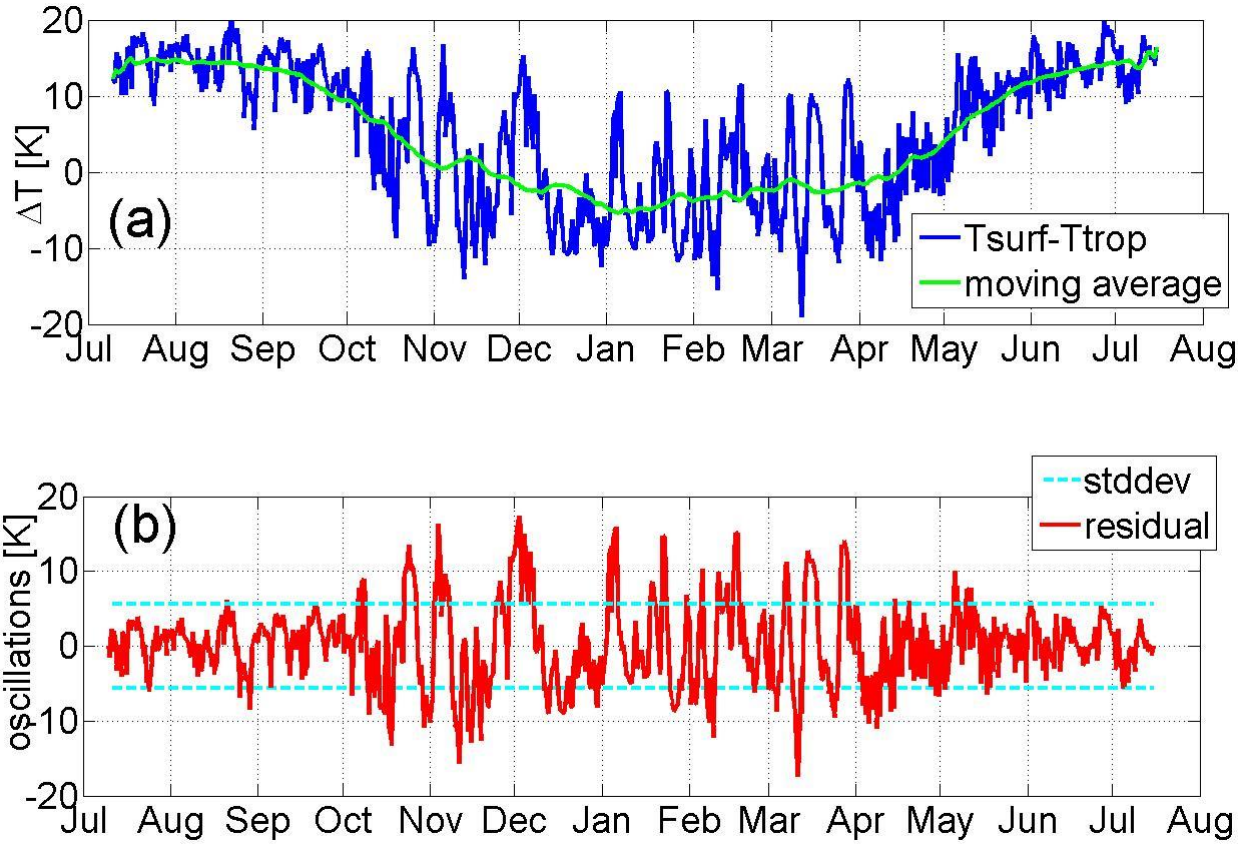

Figure 3.23: (a) Difference between surface temperature and tropospheric temperature $T_{surf} - T_{trop}$ measured by radiosondes at Eureka station (blue line) and a 100-day moving average of the previous values (green line); (b) the difference between measurements shown in panel (a) and the moving average (red line) with the computed standard deviation of about 6 K (cyan dotted lines).

3.9 The balancing beams technique

The technique that VESPA-22 employs to measure the stratospheric and mesospheric signal is called balancing-beam technique or Dicke switching technique (Parrish et al., 1988). The instrument compares the emission coming from the signal angle with a reference signal with the same mean power over the passband. The observation angle depends on the atmospheric opacity and for VESPA-22 it varies from 12° to 30° above the horizon. The reference signal used by VESPA-22 is the sky emission at the zenith. In clear sky conditions, the emission at the zenith is smaller than the emission at a much larger zenith angle. Therefore, in order to ensure that the reference beam has the same mean power with respect to the signal beam, a thin sheet of delrin is inserted in the reference beam (see Figure 3.1 and Section 3.5).

VESPA-22 collects alternatively the radiations from the two different directions. A complete measurement consists of 100 couples of signal-reference spectra. Every five couples of spectra acquired, the instrument performs an automatic calibration measuring the emission from the calibration noise diode; after that, the path length modulator shifts the antenna position of $\lambda/4$. The noise diode adds its emission to the reference beam; the noise diode spectrum can be simply calculated using the following equation:

$$\boldsymbol{V_{nd} = V_{R+nd} - V_R} \ , \tag{3.18}$$

where V_{nd} is the noise diode spectrum, V_{R+nd} is the reference beam spectrum collected with noise diode switched on and V_R is the same spectrum collected with noise diode switched off, all expressed in terms of counts.

Each spectrum collected in this mode has an integration time of 3 seconds whereas the reflector switch time from the signal angle to the zenith and vice versa is about 1.7 seconds. A complete measurement lasts about 17 minutes, resulting in 10 minutes of effectively observation of signal and reference beams.

The reference beam passes through the delrin sheet that acts as a grey body, adding the absorption factor $e^{-\tau_d}$ to the terms of Eq. (3.4) and the emission term $T_d(1 - e^{-\tau_d})$, so that:

$$T_R = T_0 e^{-\tau-\tau_d} + T_{trop}\left(1-e^{-\tau}\right)e^{-\tau_d} + T\left(\nu\right)e^{-\tau-\tau_d} + T_d\left(1-e^{-\tau_d}\right) \ , \tag{3.19}$$

where T_R is the radiation observed by VESPA-22 coming from the zenith, partially absorbed by the delrin sheet, T_d is the physical temperature of the sheet and τ_d its opacity. In this equation, the air mass factor μ is equal to 1, due to the fact the instrument is observing the zenith (see the Air Mass factor definition, Eq. (2.14)).

The signal angle is selected in order to assure that signal and reference beams have the same mean intensity. When the two beams have the same intensity, the frequency independent terms of Eq. (3.4) and Eq. (3.19) can be equated obtaining:

$$T_0 e^{-\tau-\tau_d} + T_{trop}\left(1-e^{-\tau}\right)e^{-\tau_d} + T_d\left(1-e^{-\tau_d}\right) \approx T_0 e^{-\mu\tau} + T_{trop}\left(1-e^{-\mu\tau}\right) \ , \tag{3.20}$$

where the stratospheric contribution to the mean beam intensity (about 1%) is neglected (de Zafra, 1995).

The signal from mid atmosphere $T(\nu)$ is obtained by subtracting the signal and the reference beams when the two beams are balanced. Subtracting Eq. (3.4) and (3.19), and using Eq. (3.20) it is possible to write:

$$T_S - T_R \approx T(\nu)\left(\mu e^{-\mu\tau} - e^{-\tau-\tau_d}\right), \tag{3.21}$$

$$T(\nu) = \frac{T_S - T_R}{\mu e^{-\mu\tau} - e^{-\tau-\tau_d}} . \tag{3.22}$$

Three delrin sheets with different thickness (3, 5 and 9 mm) and opacity can be employed, depending on the season, in order to maintain the observation angle between 12° and 30° above the horizon.

Spectra collected are smoothed using a 50-channel moving average. This smoothing process is not performed in a 6 MHz interval centered on the emission line to maintain the maximum frequency resolution near the peak.

During data taking operations, VESPA-22 alternates zenith and signal angle observations. However, the sky emission intensity can vary during the measurement due to tropospheric variability, therefore the instrument constantly checks if the two beams have the same mean power and changes the signal angle to minimize the difference between them.

After each measurement of a couple signal-reference, the signal angle is modified according to the Eq. (3.23)

$$\theta_{i+1} = \theta_i + g\left(S_i - R_i\right), \tag{3.23}$$

where θ_i is the signal angle used for the last couple of spectra, θ_{i+1} is the signal angle that will be used for the next couple measurement. S_i and R_i are respectively the mean counts number associated to the signal and the reference beam and the gain g is a parameter that can be modified by the user. In this way, if the signal is more intense than the reference beam the signal angle is increased, diminishing the intensity of the signal beam and vice versa. This control system allows maintaining the difference between the two beams of the order of 0.1%.

The incoming signals are measured by the instrument in term of counts; according to the Eq. (2.25) the stratospheric signal can be expressed as

$$T(\nu) = \frac{1}{g}\frac{V_S - V_R}{\mu e^{-\mu\tau} - e^{-\tau-\tau_d}} , \tag{3.24}$$

where V_S and V_R are the intensity of the signal and reference beams in term of counts. The parameter g can be measured using the noise diode emission. As explained above, during the measurements the noise diode emission is added to some reference spectra. According to Eq. (3.9) the parameter g is

$$g = \frac{V_{R+nd} + V_R}{T_{nd}} , \tag{3.25}$$

where V_{R+nd} and V_R are the counts measured respectively for the reference beam with and without the noise diode operating. The Eq. (3.24) can be modified according to Eq. (3.25) in order to obtain the VESPA-22 measurements equation:

$$T(\nu) = \frac{T_{nd}}{V_{R+nd} - V_R} \frac{V_S - V_R}{\mu e^{-\mu\tau} - e^{-\tau-\tau_d}} \ . \tag{3.26}$$

V_{R+nd} is measured by the instrument about every minute; therefore the only unknown quantity needed in order to calibrate the signal is the noise diode brightness temperature that is measured by the tipping curve calibration (described in Section 3.8.2). Figure 3.24 shows the Monitoring Mask of the Front Panel for the Data Acquisition Mode. The Mask presents several indicators showing the number of the signal, reference and noise diode spectra collected for the two different positions of the path length modulator and the mean intensities of the last measured signal, reference and noise diode spectra (in counts). The dark signal mean intensity is also shown (labeled OFF in the mask).

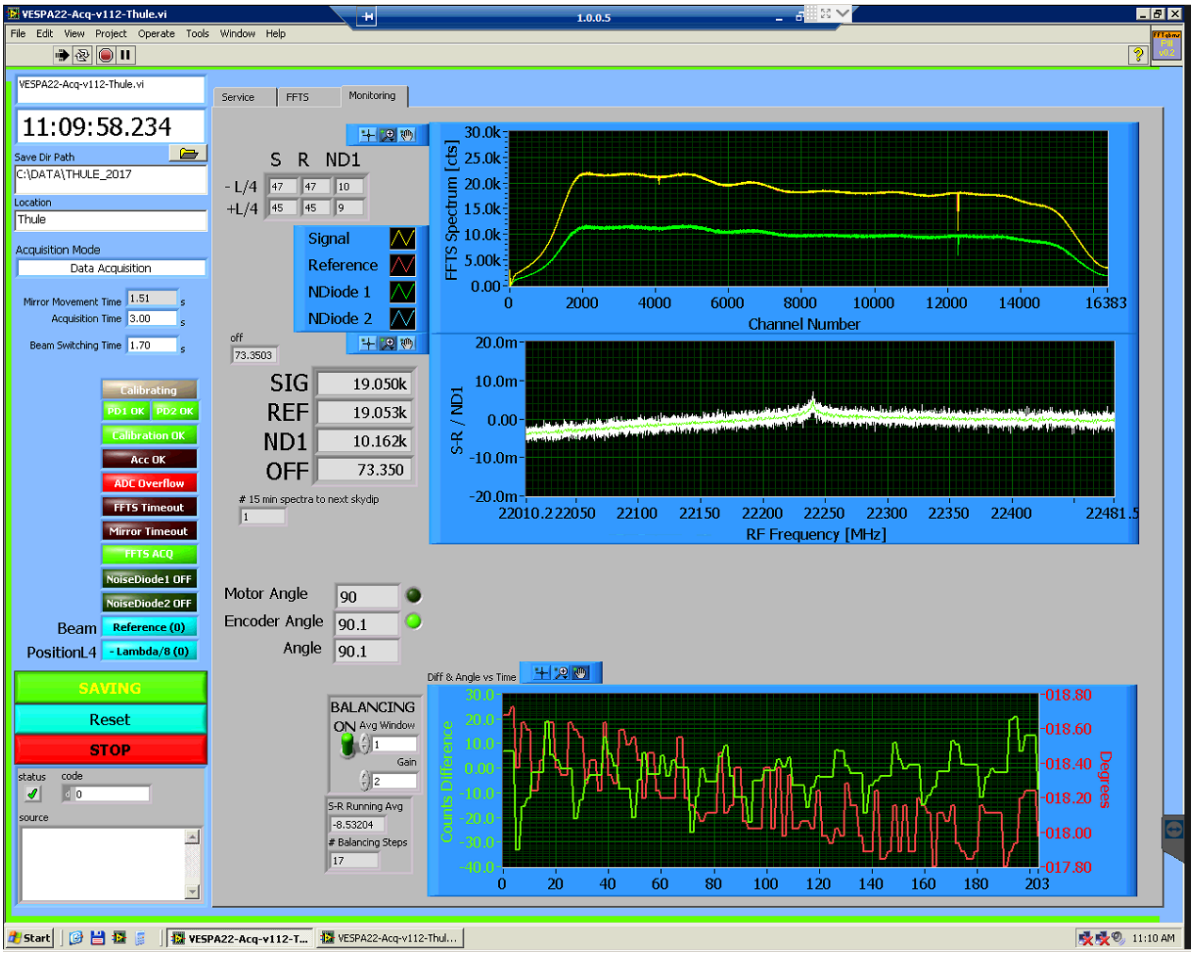

Figure 3.24: The Monitoring Mask of the Front Panel for the Data Acquisition Mode.

The first graph in the upper part of Figure 3.24 shows the signal (yellow) and reference (red) spectrum, together with the noise diode spectrum (green). The second graph in the central part of the figure shows the average difference $(V_S - V_R)/V_{nd}$ computed on the latest 50 couples of signal and reference measurements, where V_S, V_R and V_{nd} are respectively the signal

beam, the reference beam and the noise diode spectrum expressed in counts number. This difference spectrum is proportional to the stratospheric emission, as explained. The last graph shows the counts difference (green line) between each signal-reference couple averaged on the measured frequency range and the signal angle value (red line).

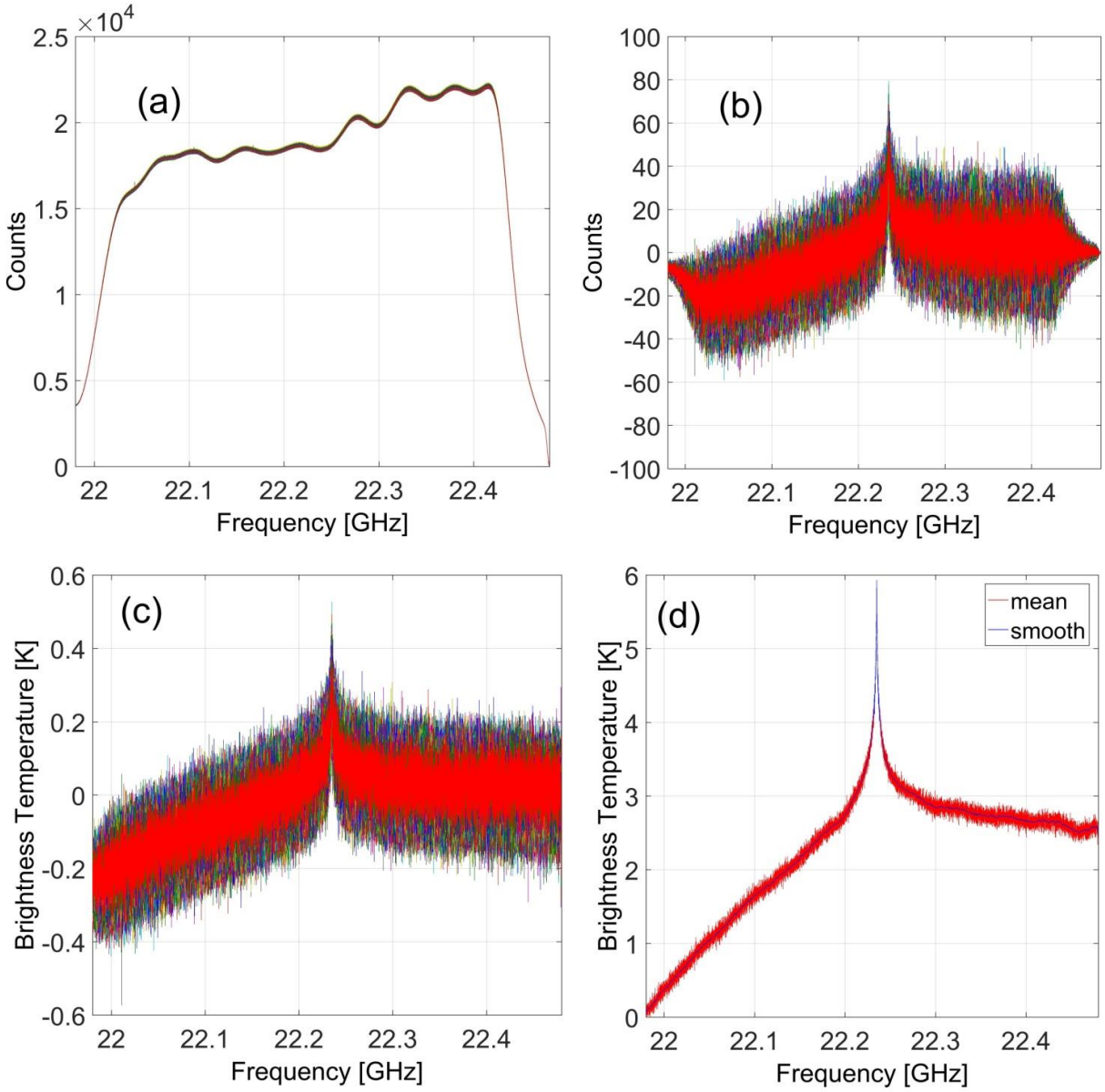

Figure 3.25: (a) The signal and reference spectra and (b) the difference spectra (signal minus reference) collected during a 24h measurement on 02/07/2017; (c): the spectra rescaled and calibrated; (d): the spectrum obtained averaging the difference spectra shown in the panel c (red) and the result of the 50-channel moving average (blue). The spectrum is normalized assigning the value of 0 K to the left end of the spectrum. Each signal and reference spectrum is the result of 5 minutes of integration.

Figure 3.25 (a) shows the signal and reference spectra collected during a 24h of integration measurement on 02/07/2017; each signal or reference spectrum results of an integration of five minutes. Figure 3.25 (b) shows the difference spectra, signal minus reference, obtained with the spectra shown in panel (a). As can be seen the difference spectra, proportional to the stratospheric signal are two orders of magnitude less intense with respect to the signal or reference spectra. The signal and reference spectra are affected by oscillations due to the frequency dependence of the instrument gain. The subtraction operation reduces the spectrum oscillations and highlights the stratospheric signal. Panel (c) displays the spectra shown in panel (b) rescaled and calibrated using the factor

$$\frac{T_{nd}}{V_{R+nd}-V_R}\frac{1}{\mu e^{-\mu\tau}-e^{-\tau-\tau_d}}\ . \tag{3.27}$$

The stratospheric signal intensity is of the order of 1 K, less than 1% of the total intensity measured by VESPA-22. In panel (d) the mean spectrum (red) and the result of 50-channel smoothing average (blue) are showed. The smoothing process is not performed in a 6 MHz centered on the emission peak, resulting in the overlap of the red and blue lines. The spectrum is normalized by a subtraction of an offset equal to its minimum value; as shown in Chapter 4 this operation does not modify the results of the retrieval algorithm.

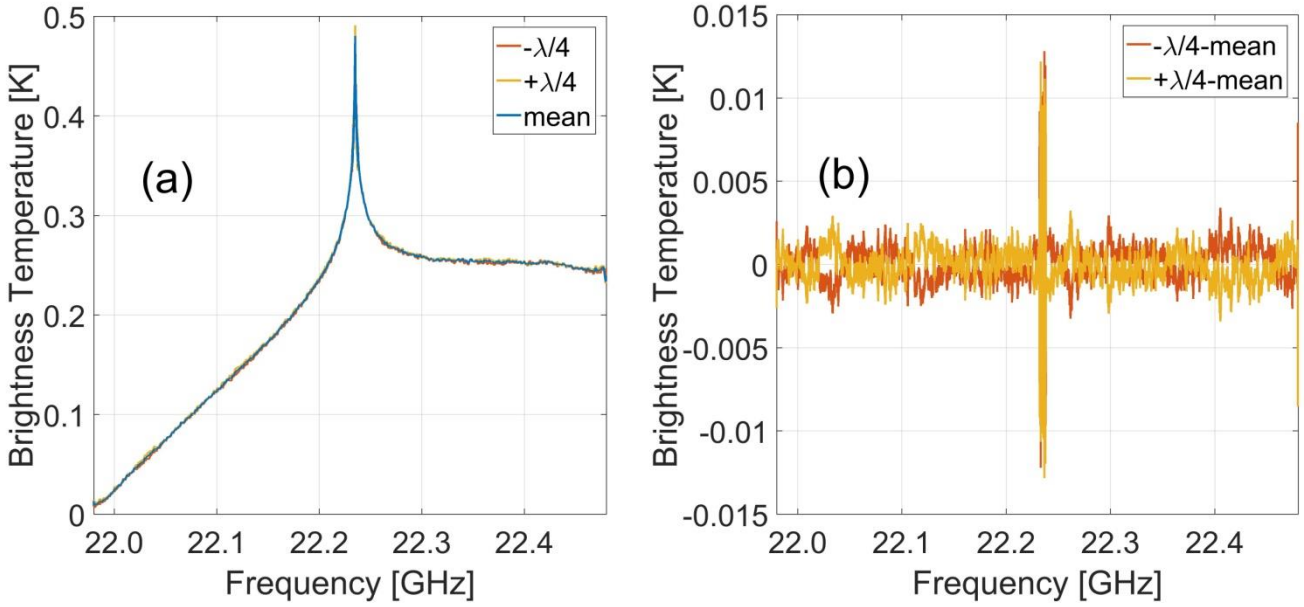

Figure 3.26: (a) the 24-hour integration calibrated and scaled spectrum showed in panel d of Figure 3.25 (blue line) together with the calibrated and scaled spectrum obtained averaging together only the 5-minute spectra acquired with the path length modulator on the $-\lambda/4$ and $+\lambda/4$ positions respectively (red and yellow lines). (b) The difference between the $-\lambda/4$ and $+\lambda/4$ spectra and the mean spectrum; the difference increases on the peak region, where no smooth is applied, due to larger measurement noise.

In order to show the effect of the path length modulator described in Section 3.3, Figure 3.26, panel a, shows the 24-hour integration calibrated and scaled spectrum showed in panel d of Figure 3.25 (blue line, here called mean spectrum) together

with the calibrated and scaled spectrum obtained averaging together only the 5-minute spectra acquired with the path length modulator on respectively the $-\lambda/4$ and $+\lambda/4$ position (red and yellow lines). The 50-channel smooth was applied to all the showed spectra tails. The difference between the $-\lambda/4$ and $+\lambda/4$ spectra and the mean spectrum is showed in panel b. The standing waves removed by the path length modulator have an intensity of about 3 mK and are clearly visible on the spectrum tails, where the 50-channel smooth reduces the measurement noise.

3.10 Grey body opacity measurements

The reference and signal spectrum are balanced by adding the emission of a grey body, a delrin sheet (see Section 3.9), to the reference beam. During regular measurement conditions, signal and reference beams are balanced with the signal angle at θ :

$$\overline{T}_S(\theta) = \overline{T}_R \ , \tag{3.28}$$

where $\overline{T}_S$ and $\overline{T}_R$ are the mean values of signal and reference beams respectively. The delrin sheet modifies the reference beam according to:

$$T_R = T_{R\_nod} e^{-\tau_d} + T_d \left(1 - e^{-\tau_d}\right) , \tag{3.29}$$

where T_d is the sheet physical temperature and T_{R_nod} is the intensity of the reference beam without the sheet (see also Eq. (3.19) description). In order to estimate τ_d, during normal data taking operations the signal angle is locked to its balanced position and the delrin sheet is removed from the reference beam. According to Eq. (3.28) and (3.29) the difference between signal and reference beam in this condition is equal to:

$$\overline{T_S}(\theta) - \overline{T}_{R\_nod} \simeq \overline{T_R} - \overline{T}_{R\_nod} = \overline{T}_{R\_nod} e^{-\tau_d} + T_d \left(1 - e^{-\tau_d}\right) - \overline{T}_{R\_nod} , \tag{3.30}$$

where $\overline{T}_{R\_nod}$ is the mean value of the reference beam without the delrin sheet. The Eq. (3.30) can be rewritten as

$$\overline{T}_S - \overline{T}_{R\_nod} = \left(\overline{T}_{R\_nod} - T_d\right)\left(e^{-\tau_d} - 1\right) . \tag{3.31}$$

Therefore the delrin opacity τ_d is equal to

$$\tau_d = -\ln\left(\frac{T_d - \overline{T}_S}{T_d - \overline{T}_{R\_nod}}\right) . \tag{3.32}$$

I always performed a delrin opacity measurement just after a liquid nitrogen calibration, in order to correctly calibrate the incoming signals (Eq. (3.5)). The collected spectra are integrated for 15 seconds; the integration time is limited in order to minimize changes in the balancing angle due to the variation of the sky emission during measurement. In order to carry out the mentioned procedure, qualified personnel must be at the observatory. It is important to underline that the described

procedure allows a measurement of the delrin opacity averaged on the entire frequency bandwidth. The delrin emission could introduce a baseline to the measured spectra; in order to take into account this possible frequency dependent emission, the measured spectra are fitted with a second order polynomial baseline, as explained in details in Section 4.3.1 and 4.6.

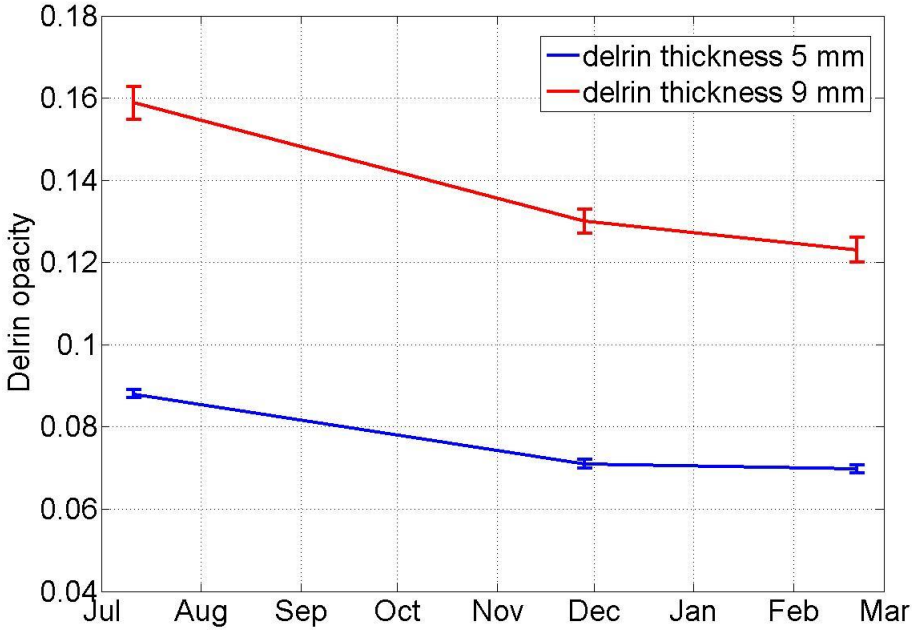

Figure 3.27: The measured Delrin opacity versus time with the respective measurement error bars for the 5 and 9 mm thickness sheets.

The τ_d value of the delrin sheets changes with time. This is caused by the degassing typical behavior of plastic sheets, the property to absorb/release water vapor molecules from/to the environment, which depends on atmospheric humidity. During wintertime, the air is drier and the compensating sheets release some water vapor and lower their own opacity. In order to consider this variation, the value τ_d used for Eq. (3.26) changes with time through a linear interpolation between the different delrin opacity measurements. Figure 3.27 and Table 3.2 shows the mean results of the Delrin opacity measurements carried out during different periods of this first year of measurement of the instrument. The uncertainty is equal to the half of the maximum difference between the different estimates measured in the same period.

Although the uncertainty of the measurements during the different periods is about 2%, the use of a linear interpolation and the possible frequency dependence of the delrin opacity suggest caution. I conservatively estimated $\Delta\tau_d$ therefore to be 10%.

Table 3.2: The mean value and uncertainty of the measured delrin opacity during different periods. The 3mm sheet was not used during this first year of measurement of the instrument.

Thickness	July 2016	November 2016	February 2017
9 mm	0.159 ± 0.004	0.128 ± 0.003	0.123 ± 0.003
5 mm	0.088 ± 0.001	0.072 ± 0.001	0.070 ± 0.001

3.11 Alignment procedure and angle offset measurement

The accurate knowledge of the elevation angle pointed by the instrument is needed to compute the air mass factor μ, used to process the acquired spectra (see Eq. (3.26)). The elevation angle is monitored through two independent systems: the encoder and the reflector motor firmware, as described in Section 3.6.

I developed a procedure to align the quasi-optical system of VESPA-22 using a He-Ne laser and aligned it during the installation on Thule Air Base.

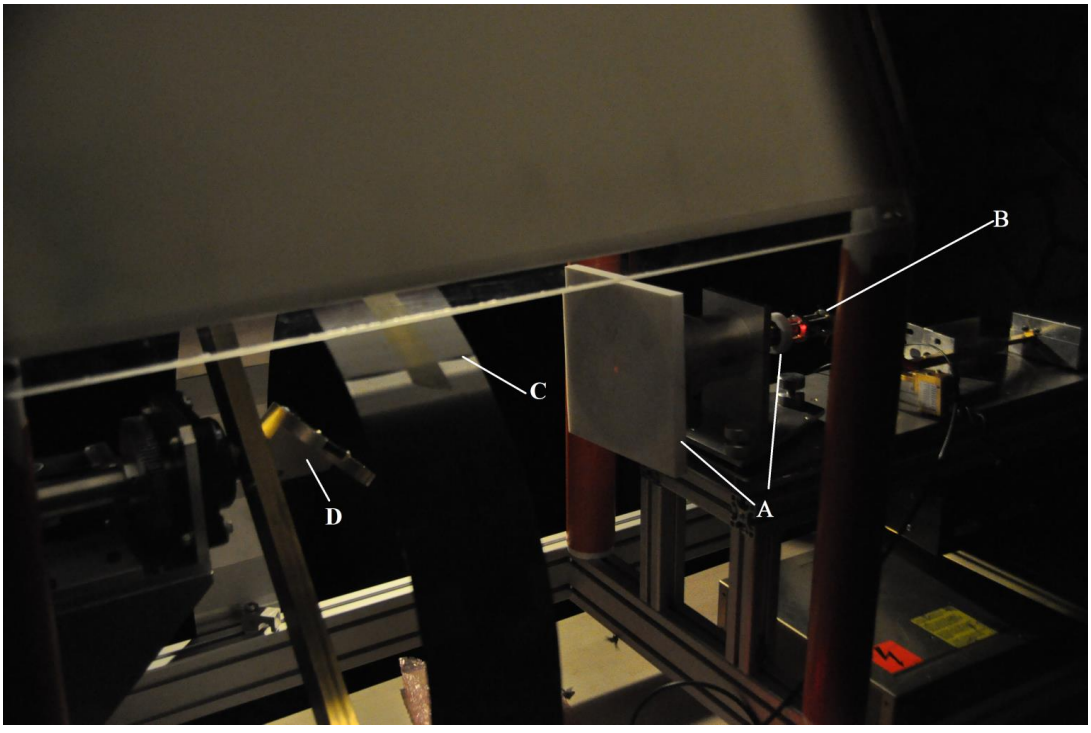

Figure 3.28: The He-Ne laser used to align the quasi-optical system; (A) Teflon elements, (B) He-Ne laser mounted on the antenna, (C) a surface on which observe the spot caused by the laser reflection on the reflector support (D). At this time, the surface (C) is replaced by an element installed directly on the reflector support (as indicated in Figure 3.29).

In this operation, the laser is applied to the back of the antenna through a specific support and the beam passes through two Teflon elements applied on the back and on the front of the antenna (Figure 3.28). These elements present a 1mm diameter hole in their center, in correspondence with the antenna optical axis. A reflecting element forming an angle of 45° with the optical axis is mounted on the reflector support. The reflecting element presents a plate intercepting the laser beam. If the antenna is aligned with the optical axis, rotating the reflecting element around the optical axis does not change the distance between the laser spot and the plate edge (see Figure 3.29).

Figure 3.29: A scheme representing the alignment procedure (see also Figure 3.28). The laser source (c, yellow box) is mounted at the back of the antenna (b); the laser beam (red line) passes through two Teflon elements applied on the antenna (green lines), it is reflected by the reflecting element (cyan line) mounted on the reflector support (a) and forming an angle of 45° with the optical axis, and is intercepted by the plate (e). If the quasi-optical system is aligned, rotating the reflector support on the optical axis does not change the distance d between the laser spot on the plate and the plate edge (dashed line).

The alignment procedure described minimizes the *offset angle* defined as the difference between the nominally observed angle and the real pointing angle. This difference can be measured through the observation of the Sun, as described by Straub et al. (2010). During spring and summer, the Sun can be directly observed by VESPA-22. The direct Sun emission produces a clearly recognizable augment of the signal received by the instrument with respect to the sky signal. During this kind of measurement, defined *Sun Pointing*, the reflector is pointed to the Sun. Knowing the exact Sun position through the ephemerides, the instrument collects the emissions from the observation angles in an interval centered on the Sun nominal position with an angular resolution of 0.04°. Each spectrum is integrated for 0.5 s. This reduced integration time is necessary in order to minimize the variation of Sun position during measurement. The difference between Sun elevation from ephemerides and the Sun observation angle resulting from this procedure is considered the angle offset. This quantity is added as a correction to all the angles indicated by the encoder and saved with the spectral data files.

Figure 3.30 displays the results of a Sun Pointing procedure collected on 07/04/2017. The green line in panel (a) represents the mean signal intensity predicted by the Eq. (3.14) whereas the red dots the mean intensity collected during a 2-minute

scan of different observation angles; the effect of the Sun is clearly visible. The values of T_{trop} and τ used in the calculation are obtained from a tipping curve procedure (section 3.8.2) executed shortly before, as the calibration parameters needed to calibrate the intensity of the signals. Panel (b) displays the difference between measurements and model; the residuals are fitted using a gaussian shape. The fit maximum corresponds to the Sun elevation angle as is detected by the instrument θ_{Sun_VESPA}

The real Sun elevation θ_{Sun_eph} angle is obtained through the ephemerides, so the offset angle θ_{off} is

$$\theta_{off} = \theta_{Sun\_VESPA} - \theta_{Sun\_eph} \ . \tag{3.33}$$

For the measurements discussed here, an offset $\Delta\theta = 0.2°$ was estimated stable with time whereas the uncertainty on the measured angle is equal to $\pm 0.1°$.

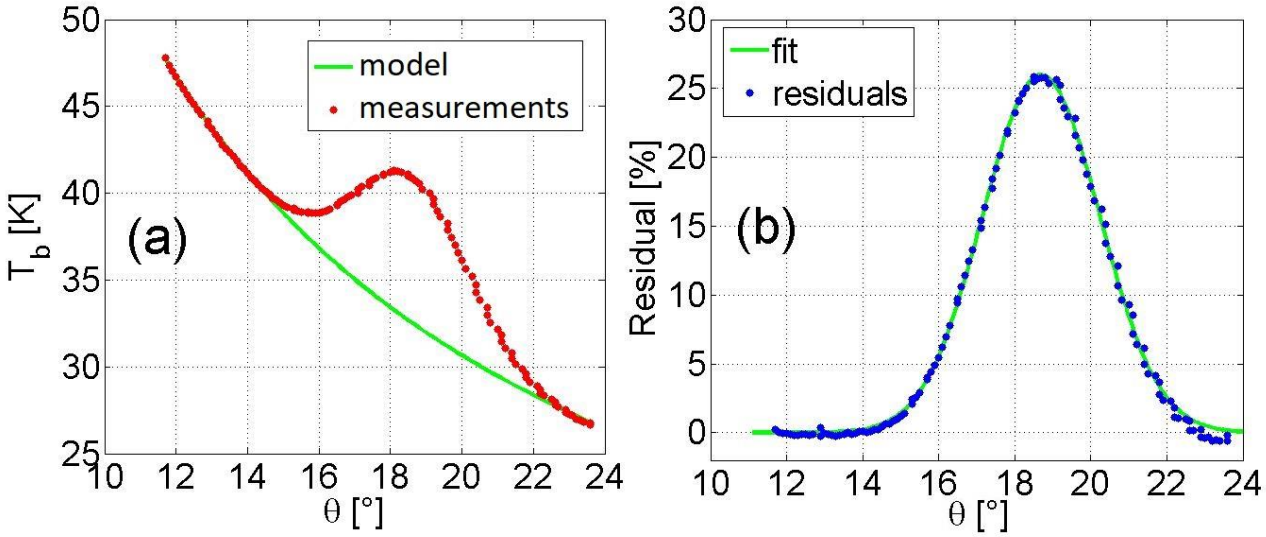

Figure 3.30: The Sun Pointing procedure results collected on 07/04/2017. (a): the mean brightness temperature measured observing the sky at different observation angles (red dots) and the mean signal intensity predicted by the Eq. (3.14) (green line). (b): the relative difference measurements minus model (blue dots) and a gaussian fit (green line).

Chapter 4

The retrieval algorithm

The development of a reliable retrieval algorithm and analysis procedure for the VESPA-22 measurements has been important tasks carried out in this Ph.D. work. The generic relation between the measured spectrum y and the real profile has been derived in section 2.6; in this Chapter, the specific features of the retrieval algorithm employed by VESPA-22 are presented.

VESPA-22 water vapor vertical profiles are obtained using the optimal estimation theory (Rodger, 2000) with the assumption of gaussian shape probability density function (paragraph 2.6.2). In order to compute the weighting functions matrix **K**, a linearization of the radiative transfer model described is performed around the apriori profile $\mathbf{x}_a$ according to the scheme described in the equation (4.1)

$$\mathbf{y} = \mathbf{y}_a + \mathbf{K}\left(\mathbf{x} - \mathbf{x}_a\right) . \tag{4.1}$$

I employed the radiative transfer simulation model ARTS (Atmospheric Radiative Transfer Simulator), described in the work of Eriksson et al. (2011) as forward model employed in the calculation of the apriori spectrum $\mathbf{y}_a$ and the matrix **K**. ARTS provides a detailed description of the radiative transfer and molecular emission for the millimeter and sub-millimeter wavelength. The software allows the user to select the spectroscopic parameters describing the emission line. A horizontally homogeneous atmosphere is employed in the software simulation, as assumed in section 3.7. The details about the calculation of the apriori spectrum and weighting functions matrix can be found in the next sections.

The retrieval algorithm analyzes the central 400 MHz of the collected spectra, cutting off the first and last 50 MHz because of spectral artifacts. The analyzed spectra are so composed of 13158 channels between 22.0293 and 22.4309 GHz with a resolution of 31 kHz. The pressure broadening and the Doppler broadening of the emission line, described in the Section 2.3, associate to the emissions generated at the different altitudes a precise spectral form, allowing the signal deconvolution.

The altitude grid used for VESPA-22 retrievals starts from 10 km and goes up to 110 km altitude, at steps of 1 km.

In the paragraph 2.6.2 the sensitivity was defined as the sum of the Averaging kernel functions, which are

$$\mathbf{A} = \mathbf{GK} , \tag{4.2}$$

with the gain matrix $\mathbf{G}$ equal to

$$\mathbf{G} = \left(\mathbf{K}^{\mathbf{T}}\mathbf{S}_{\varepsilon}^{-1}\mathbf{K} + \mathbf{S}_a^{-1}\right)^{-1}\mathbf{K}^{\mathbf{T}}\mathbf{S}_{\varepsilon}^{-1} . \tag{4.3}$$

The sensitivity is related to the amount of information extracted by the measurement at a certain altitude. A sensitivity value close to one indicates that the major part of information comes from the measurements rather than the apriori profile. In this work, following the suggestion of Tschanz et al. (2013), the retrieved profiles are considerate having a scientific relevance in the altitude range where the sensitivity is above 0.8. This altitude range is defined *sensitivity range*.

The sensitivity range is determined by many factors as the level of noise of the spectrum determining the value of $\mathbf{S}_e$ matrix (as will be explained in the following), the uncertainty covariance matrix of the apriori profile $\mathbf{S}_a$ and primarily by the weighting functions matrix **K**. As described in the paragraph 2.6.2, **K** represents the sensitivity of the spectrum to variations at different altitudes. **K** approaches zero at low pressures where the absolute amount of water vapor becomes very small and where the line width becomes smaller than the spectral resolution of the instrument. For the 22.23 GHz microwave radiometers the level where the sensitivity becomes smaller than 0.6 lies typically between 70 and 80 km (Haefele et al. 2009). Also, the weighting functions decreases at high pressures (low altitudes), where the line width becomes larger than the bandwidth of the instrument due to the pressure broadening (Haefele et al. 2009). The pressure broadening coefficient of water vapor emission at 22.23 GHz is about 2.8 MHz/mbar (Liebe, 1989) and imposes a lower limit at about 14-16 km. In practice, the lower boundary for valid water vapor retrievals lies higher than the theoretical value due to the effect of upper part of the troposphere and spectral artifacts. The emission from the upper tropospheric layer cannot be considered as constant in frequency and has a spectral form that can be approximated by a second-degree polynomial. Also, spectral artifacts due to internal signal reflections can be superimposed to the spectrum. Standing waves and upper tropospheric emission are usually accounted for in the retrieval with an empirically determined set of sine waves of one or more known periods, to be subtracted to the measured spectrum or giving to the inversion algorithm the possibility to simulate the tropospheric emission using a polynomial. These operations, however, reduce the sensitivity of the algorithm at lower altitudes, setting a higher bottom limit to the sensitivity range. The VESPA-22 retrieval algorithm employs a second-degree polynomial to simulate the upper tropospheric emission, as it is explained above whereas no sine waves simulation is added.

4.1 The EOS MLS/Aura dataset

In this thesis work, I made extensive use of the temperature and the water vapor products of the Earth Observing System Microwave Limb Sounder (EOS MLS), thereafter referred as MLS. This section is therefore dedicated giving a short overview of this instrument. MLS (Waters et al., 2006) collects measurements of atmospheric composition, temperature, humidity and cloud composition; MLS is operated on board of the Aura satellite that was launched 15 July 2004, and is part of NASA's A-train group, which is a formation of six satellites flying in close proximity. The Aura satellite is in a near-polar orbit at 705 km of altitude, covering 82° S to 82° N latitudes. The measurements are taken at fixed local solar times. As

Earth rotates underneath it, the Aura orbit stays fixed relative to the Sun, giving daily global coverage with 15 orbits per day. The MLS collects measurements globally day and night.

MLS observes thermal emission by the atmosphere in five spectral regions from 115 GHz to 2.5 THz. The Earth's limb is scanned vertically from the ground to 96 km every 25 seconds. These scans are synchronized to the Aura orbit such that vertical scans are made at essentially the same latitude each orbit. The MLS products used in this work are the water vapor mixing ratio profiles, the temperature profiles and the geopotential height profiles, used to obtain the pressure profiles as a function of the altitude. The MLS water vapor profiles are retrieved observing the 183 GHz rotational line of the H_2O molecule. Read et al. (2007) describe the characteristics of the v2.2 retrieved profile and Livesey et al. (2015) update the description to the version 4.2, used in this thesis.

Table 4.1 reports the main features of the v4.2 water vapor mixing ratio profiles retrieved by MLS as described in the work of Livesey et al. (2015).

Table 4.1: The main specifications of Aura/MLS water vapor mixing ratio profiles version 4.2 (Livesey et al., 2015)

Pressure [hPa]	Altitude [km]	Resolution V x H [km]	Single profile precision [%]	Accuracy [%]
0.002	86	10.3 x 350	152	34
0.01	76	8.8 x 725	55	11
0.046	66	7.4 x 540	35	8
0.21	55	3.6 x 670	19	7
1.0	44	2.5 x 400	6	4
4.6	35	3.4 x 350	4	7
22	26	3.2 x 265	5	7
68	18	3.1 x 190	5	6

MLS temperature is retrieved primarily from bands near the O_2 spectral lines at 118 GHz and 239 GHz. The isotopic 239-GHz line is the primary source of temperature information in the troposphere, whereas the 118 GHz line is the primary source of temperature in the stratosphere and above (Schwartz et al., 2008). MLS Geopotential height (GPH) is retrieved, along with temperature from bands near O_2 spectral lines at 118 GHz and 234 GHz (Schwartz et al., 2008).

The heights of surfaces of constant geopotential are a property of the Earth's gravitational field and do not depend upon atmospheric conditions. Geopotential differences between surfaces are equal to the integral with height of the gravitational acceleration, $g(z)$. gph is geopotential difference from the Earth's surface geopotential to a given location, scaled by the mean sea-level gravitational acceleration, g_0, to give units of height.

MLS products, including gph, are reported on pressure surfaces depending on temperature and height through hydrostatic balance and the gas law.

$$gph = \frac{1}{g_0}\int g(z)\,dz = \frac{R}{Mg_0}\int \frac{T(z)}{P(z)}\,dP \ , \tag{4.4}$$

where M is the molar mass of air and R is the gas constant. Thus, when MLS retrieves temperature and pressure using radiometric measurements gph differences between pressure surfaces are simultaneously retrieved.

The MLS geopotential height gph is converted in geometrical altitude gmh through the following equations.

The surface gravity g_s can be computed as a function of the latitude ϕ through the Somigliana's formula:

$$g_s = g_{eq}\frac{1+k_s\sin^2(\phi)}{1-\left(e_c\sin(\phi)\right)^2} \ , \tag{4.5}$$

where $k_s = 1.932\cdot 10^{-3}$ is the Somigliana's constant, $g_{eq} = 9.78\ m/s^2$ is the surface gravity at the equator and $e_c = 0.082$ is the Earth eccentricity. The Earth radius r as function of latitude can be computed according to

$$r = \frac{R_{eq}}{1+f_l+g_r-2f_l\sin^2(\phi)} \ , \tag{4.6}$$

where $R_{eq} = 6378\ km$ is the Earth equatorial radius, f_l the ellipticity defined as

$$f_l = \frac{R_{eq}-R_{pol}}{R_{eq}} = 0.003352811 \ , \tag{4.7}$$

and $g_r = 0.00345$ is the gravity ratio.

The geopotential height is converted into geometrical height through the Eq. (4.8)

$$gmh = \frac{gph\cdot r}{r\frac{g_s}{g_o}-gph} \ , \tag{4.8}$$

where $g_0 = 9.80665\ m/s^2$ is the gravity constant.

4.2 The water vapor apriori vertical profile and covariance matrices

The water vapor concentration vertical profile in the Arctic region presents strong differences between summer and winter, especially in mesosphere, due to the subsidence of the air mass caused by the Polar Vortex (see Section 1.1). The variation of the water vapor profile during the year is showed by the Figure 4.1 that displays the monthly averages of AURA/MLS (Waters et al., 2006) water vapor vertical profiles (version 4.2) from the years 2014, 2015, and 2016, collected 300 km

around VESPA-22 *observation point*. The VESPA-22 observation point coordinates are chosen to be 74.8° N and 73.5° W, and represent an estimate of the geographical coordinates of the air mass that is observed by VESPA-22 (which points South-West, at about 220°) at 60 km altitude when the instrument aims at an elevation of 15° above the horizon.

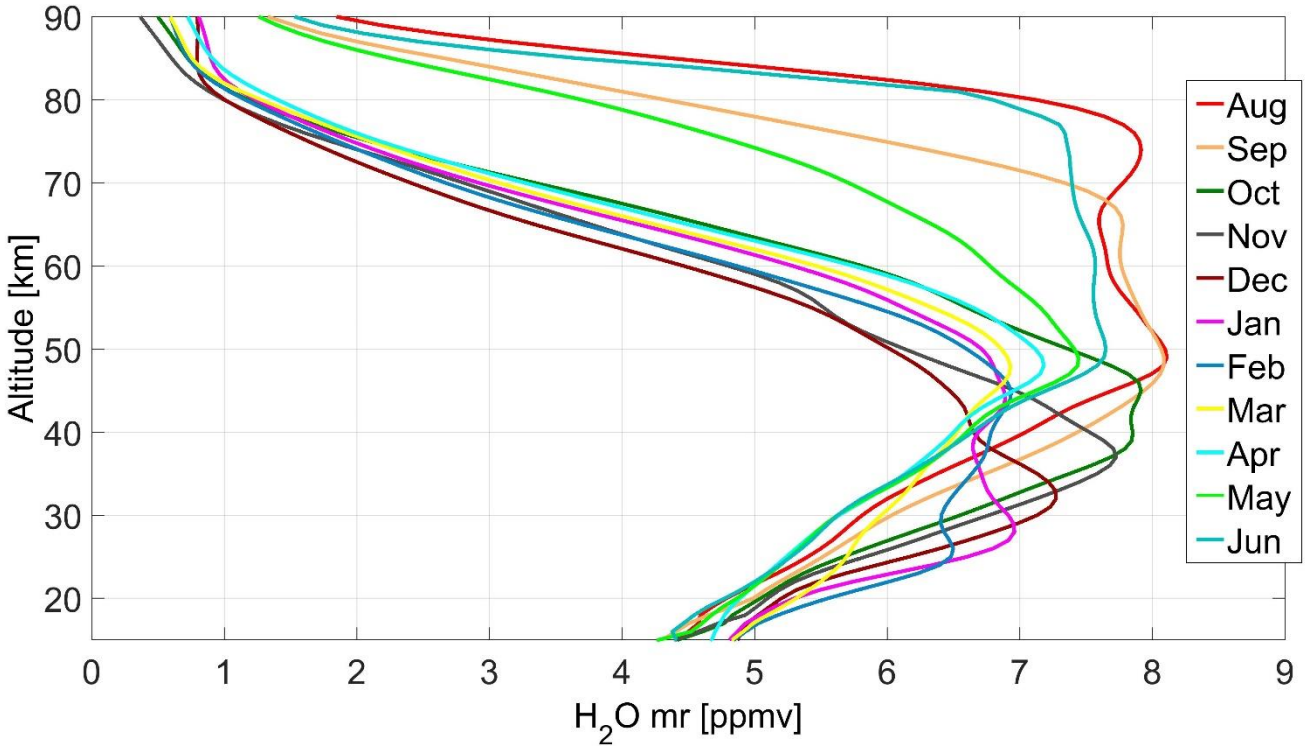

Figure 4.1: The monthly averages of the MLS/Aura profiles collected 300 km around the observation point during the year 2014, 2015 and 2016.

In order to take into account the strong summer variation of the water vapor concentration in mesosphere, the retrieval algorithm employs two different water vapor apriori profiles (Figure 4.2), the first one used during summer months (summer apriori), from the 1st of June to the 15th of September, and the second one used during autumn, winter and spring (here simply defined winter apriori), from the 15th of October to the 31th of April. During the periods from the 16th if September to the 14th of October and from the 1st to the 31th of May the apriori profile varies gradually day by day through a linear interpolation from one apriori profile to the other. The two apriori profiles are identical below 48 km of altitude. The use of a fixed apriori in stratosphere and in mesosphere for the major part of the year, with the exception of the two transition periods, assures that the measured daily variations in the water vapor vertical concentration profile are not caused by changes in the apriori profile.

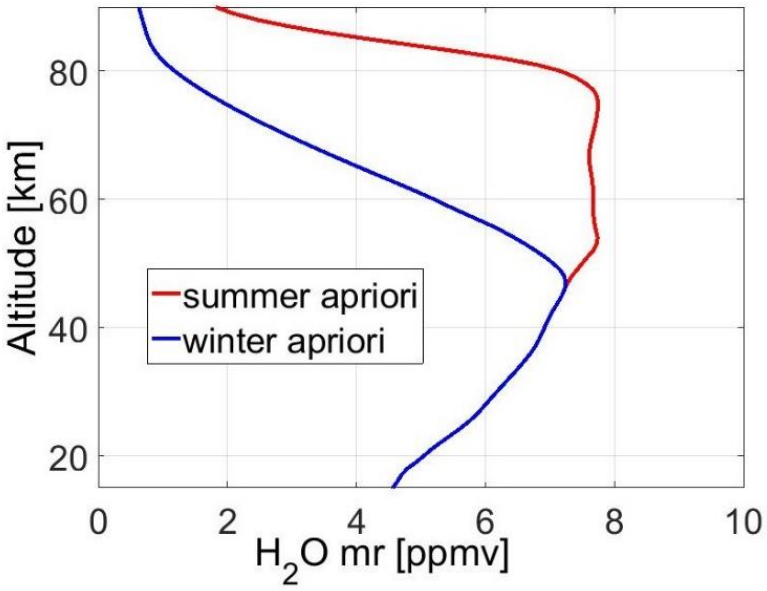

Figure 4.2: the summer and winter apriori profiles used in the retrieval algorithm.

The measurement covariance matrix $\mathbf{S}_e$ is an estimate of the spectrum uncertainty and is related to the level of noise afflicting the spectrum. In order to represent the random spectral noise, $\mathbf{S}_e$ is defined as a diagonal matrix (no correlation between the noise afflicting different channels) with its diagonal elements constant. The value of the diagonal elements is calculated using a two-step process. A first retrieval is performed using an unsmoothed spectrum $\mathbf{y}_{uns}$ (without the 50-channels smooth on the spectral tails) and a fixed value ($1\text{x}10^{-5}$) for the $\mathbf{S}_e$ diagonal elements and the obtained profile $\mathbf{x}_0$ is used to calculate a synthetic spectrum $\mathbf{y}_{0\_fit}$ by means of Eq. (2.69). In order to consider the measurement noise in the retrieval process, a second and final inversion is then performed, this time with the $\mathbf{S}_e$ diagonal elements set equal to the $\left(\mathbf{y}_{uns} - \mathbf{y}_{0\_fit}\right)^2$ mean value. It is important to underline that the $\mathbf{S}_e$ diagonal elements are constant; the computation does not take into account the noise reduction provided by the 50-channel smoothing process, resulting in an overestimation of the measurement noise of the spectrum tails (see Chapter 5 for a detailed uncertainty description). This method of $\mathbf{S}_e$ computation was chosen in order to provide a realistic estimate of the uncertainty due to spectral noise and artifacts and to minimize the computational time needed for retrievals.

The $\mathbf{S}_a$ matrix is computed according to:

$$S_{a,ij} = \sigma_i \sigma_j e^{-\frac{|z_i - z_j|}{h}}, \tag{4.9}$$

where σ_i and z_i are respectively the root square of the variance (expressed in volume mixing ratio, or vmr) and altitude of the apriori profile (Figure 4.3), whereas h is a correlation altitude set to be 5 km.

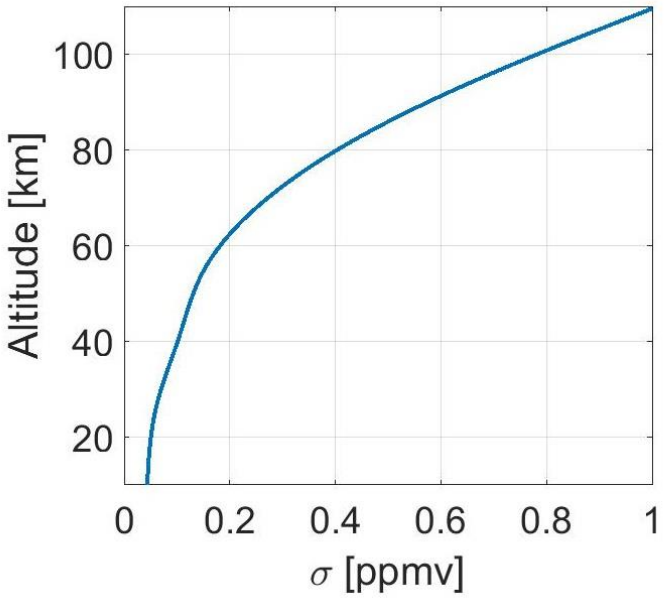

Figure 4.3: The profile σ used to compute the apriori covariance matrix in Eq. (4.9) as a function of the altitude.

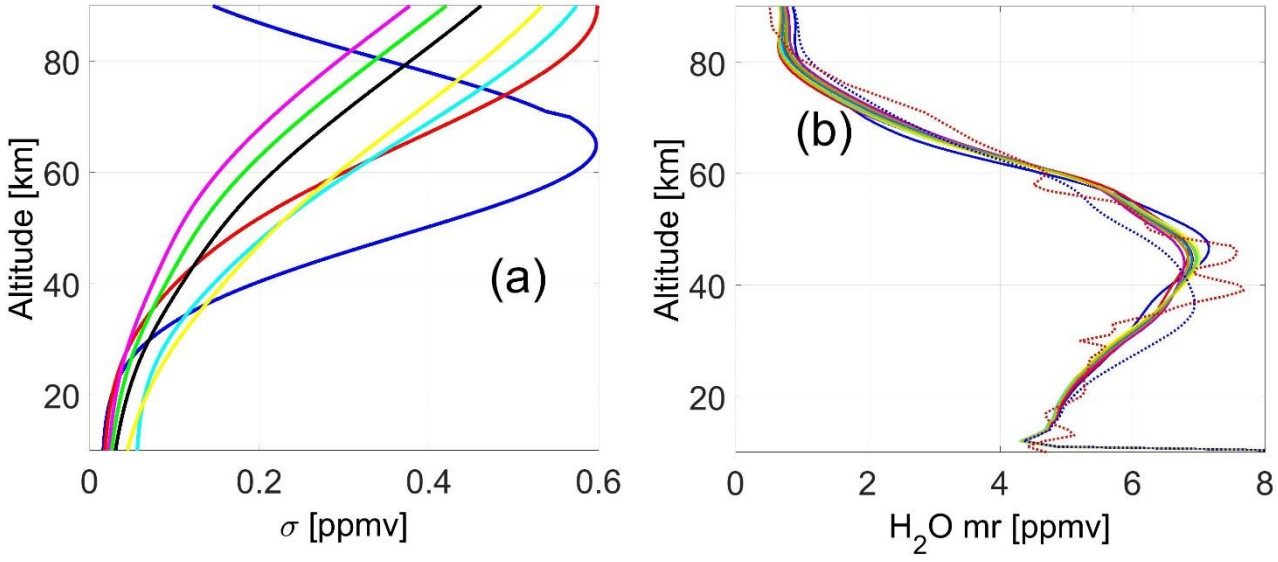

Figure 4.4: An example of the test for the apriori covariance matrix composition: (a) several σ profiles have been tested observing their associated retrieved profile (b) from a same measured spectrum (measurement of 20/10/2016). In panel (a) and (b) each σ profile and its correspondent retrieved profile are marked with the same color. The blue dotted line in panel (b) is the apriori profile used in the test, whereas the red dotted line is the water vapor profile measured by MLS that day.

The σ definition for the computation of the apriori covariance matrix is one of the most important issues to "tune" the generic retrieval algorithm theory to a specific instrument. During this Ph.D. work, I carried out many tests in this sense. Figure 4.4 displays an example of these tests: a 24-hour integration spectrum measured on 20/10/2016 is analyzed using different σ profiles (panel (a)), to find the shape producing a retrieved profiles with better characteristics (larger sensitivity range and better resolution, absence of oscillations). In the figure is reported also the correspondent profile measured by MLS (red dotted line in panel (b)) that day.

The profile shape increasing with altitude is selected to contrast the loss of sensitivity of the retrieval algorithm caused by the diminishing of the weighting functions intensity in the mesosphere.

4.3 The forward model and the meteorological profiles

I employed the radiative transfer simulation software ARTS (Eriksson et al., 2011) in order to describe the physics of the processes producing the spectra measured by VESPA-22. ARTS is used to compute the matrix **K** and the apriori spectrum $\mathbf{y}_a$. ARTS simulates the emission using a Voigt-Kuntz line shape (see section 2.3). The JPL 2012 catalog (Pickett et al., 1998, reference site https://spec.jpl.nasa.gov/) provides the line intensity used to simulate the water vapor emission. Following the work of Seele (1999) and Tschanz et al. (2013), I decided to divide the line described by the JPL 2012 catalog into three emission lines indicating the hyperfine splitting of the 22.235 GHz water vapor line. In the cited studies, the sum of the intensities of the splitted lines matches the intensity reported by the 1985 version of the JPL catalog, so the intensities presented by Tschanz et al. (2013) were rescaled to have their sum equal to the intensity provided by the JPL 2012 catalog. The employed pressure broadening and self-broadening parameters are those reported by Liebe (1989). Table 4.2 summarizes the spectroscopic parameters used for the analysis of VESPA-22 spectral measurements.

Following Tschanz et al. (2013), the emission line intensity and the pressure broadening parameter were assigned an uncertainty of 8.7 10^{-22} m^2 Hz and of 1014 Hz Pa^{-1}, respectively.

Table 4.2: Spectroscopic parameters used in VESPA-22 retrieval algorithm. Indicated parameters, from left to right, are: emission line frequency, intensity, lower state energy, pressure broadening parameter, pressure broadening temperature dependence, self-broadening, and self-broadening temperature dependence. The line intensity is given for a reference temperature of 296 K.

ν_0 [GHz]	S [m^2 Hz]	E [J]	γ_{air} [Hz Pa^{-1}]	n_{air}	γ_{self} [Hz Pa^{-1}]	n_{self}
22.235043990	5.3648 10^{-19}	8.869693 10^{-21}	28110	0.69	134928	1
22.235077056	4.5703 10^{-19}	8.869693 10^{-21}	28110	0.69	134928	1
22.235120358	3.9740 10^{-19}	8.869693 10^{-21}	28110	0.69	134928	1

The water vapor mixing ratio vertical profile $\mathbf{x}_{ARTS}$ is the profile used in the forward model calculations to compute the apriori spectrum and the weighting functions. Although the retrieval grid starts at 10 km the forward model calculation are processed using complete vertical atmospheric profiles of pressure, temperature and water vapor mixing ratio, from the ground to 110 km of altitude. I set up the ARTS calculations to compute the weighting functions matrix starting from 10 km of altitude.

The water vapor profile $\mathbf{x}_{ARTS}$ matches the apriori profile from 12 km of altitude upward and, below 9 km, it is consistent with the measurements of precipitable water vapor (PWV) collected by the HATPRO radiometer (Rose and Czekala, 2009; Pace et al., 2015) installed at the THAAO. This lower part of $\mathbf{x}_{ARTS}$ is calculated according to:

$$\mathbf{x}_{ARTS}\left(\textit{from the ground to } 9km\right) = \frac{PWV_{Hatpro}}{PWV_{Eu}}\mathbf{x}_{Eu}\ , \tag{4.10}$$

where $\mathbf{x}_{Eu}$ is a water vapor mixing ratio profile obtained by monthly averages profiles calculated from radiosondes launched at the Eureka station (80.0°N -85.9°W)), Canada, displayed in Figure 4.5.

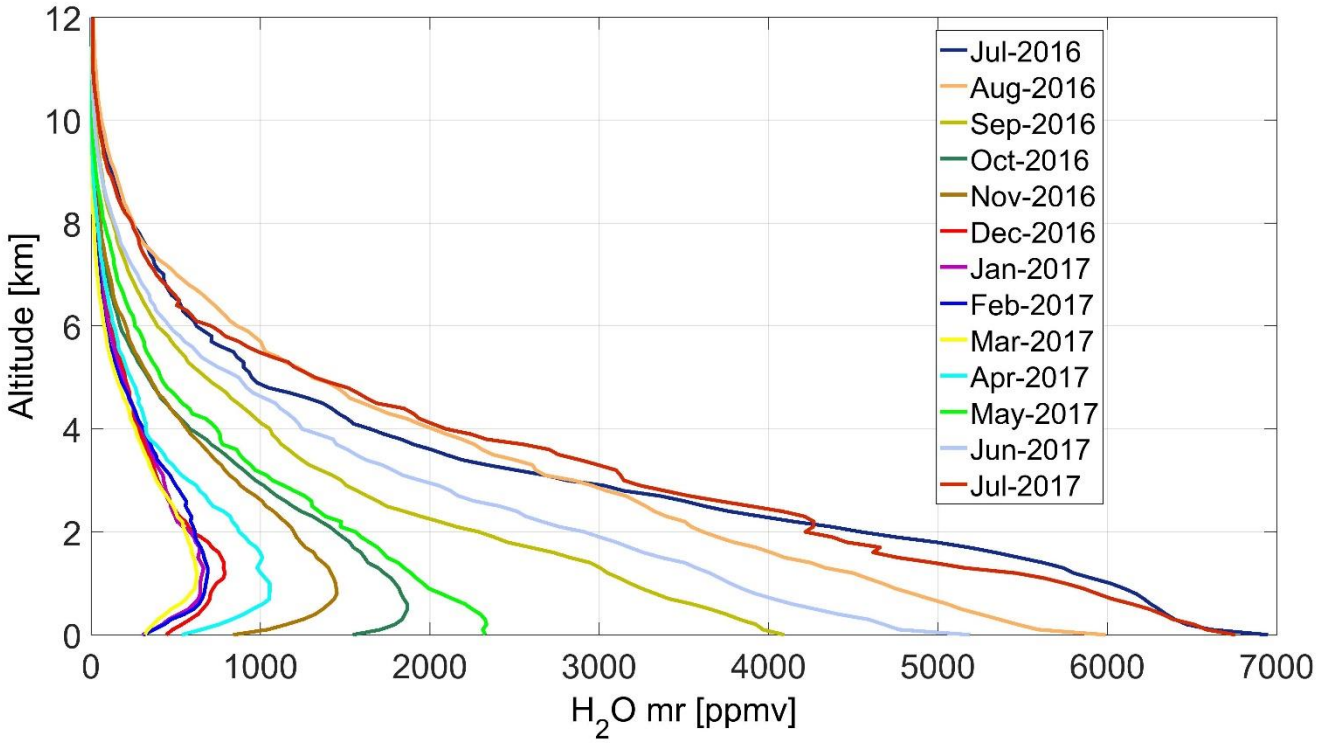

Figure 4.5: The mean monthly water vapor profiles measured from radiosondes at Eureka station, Canada, from July 2016 to July 2017.

These monthly averages are "assigned" to the 15th day of each month and then, at each altitude, are linearly interpolated to build daily apriori profiles that vary gradually, day by day, from the 15th of one month to the next. PWV_{Eu} is the associated water vapor column content, and PWV_{Hatpro} is the column content measured by the HATPRO. $\mathbf{x}_{ARTS}$, therefore, represents

the monthly average $\mathbf{x}_{Eu}$ profile simply rescaled to be consistent with the column content measurements of the HATPRO at Thule. An example of $\mathbf{x}_{ARTS}$ in the troposphere is shown in Figure 4.6. I chose the data from Eureka (instead of those from Alert, Canada, for example) because they show the closest resemblance to the tropospheric profiles measured at Thule by local radiosondes when the latter are available. In order to avoid discontinuities in $\mathbf{x}_{ARTS}$, values at altitudes between 9 and 12 km are obtained with a linear interpolation between $x_{ARTS}(9\ km)$ and $x_{ARTS}(12\ km)$.

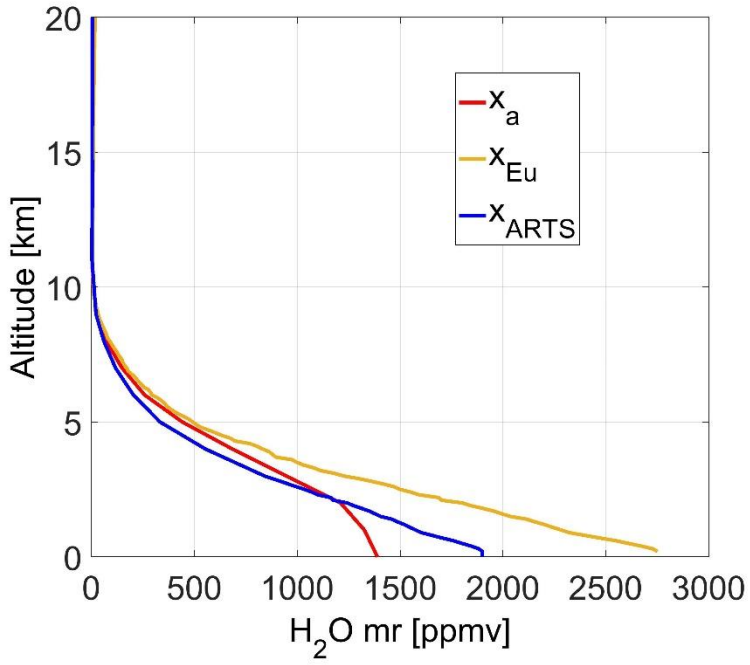

Figure 4.6: An example of the vertical water vapor mixing ratio profiles used in the forward model calculation for the inversion of a spectrum measured on the 24/05/2017: the monthly mean water vapor apriori vertical profile $\mathbf{x}_a$ interpolated at measurement time (red, the monthly means of the water vapor apriori vertical profile are shown in Figure 4.1) and the $\mathbf{x}_{ARTS}$ profile (blue) obtained rescaling the monthly mean Eureka profile interpolated at the measurement time $\mathbf{x}_{Eu}$ (yellow, see Figure 4.5)

The pressure and temperature vertical profiles from the ground to 110 km needed to run the forward calculation are built merging NASA Goddard Space Flight Center (GSFC), AURA/MLS and climatological temperature and pressure profiles (Figure 4.7). The NASA GSFC profiles by Goddard Automailer Service (Lait et al., 2005) are used to build the tropospheric meteorological state, from the ground up to 9 km of altitude. For the altitude range between 10 and 87 km, the MLS temperature and pressure profiles collected during VESPA-22 observations, in a radius of 300 km from the observation point of VESPA-22, are averaged together to produce a single set of daily meteorological vertical profiles. Daily temperature and pressure profiles from 86 to 110 km of altitude are obtained by daily smoothing of zonal monthly averages from the COSPAR International Reference Atmosphere (Rees et al., 1990) for the 75° N latitude.

A first smoothing process performed at the altitudes where the three different datasets (GSFC, MLS, and climatological profiles) are stitched together, between 9 and 12 km and between 87 and 97 km, assures the absence of vertical discontinuities in the temperature and pressure daily profiles. I then run a second smoothing process to avoid the presence of spikes or large gradients. Figure 4.8 displays the different COSPAR reference atmosphere temperature profiles used for the upper part of the temperature profiles used in the forward model calculation.

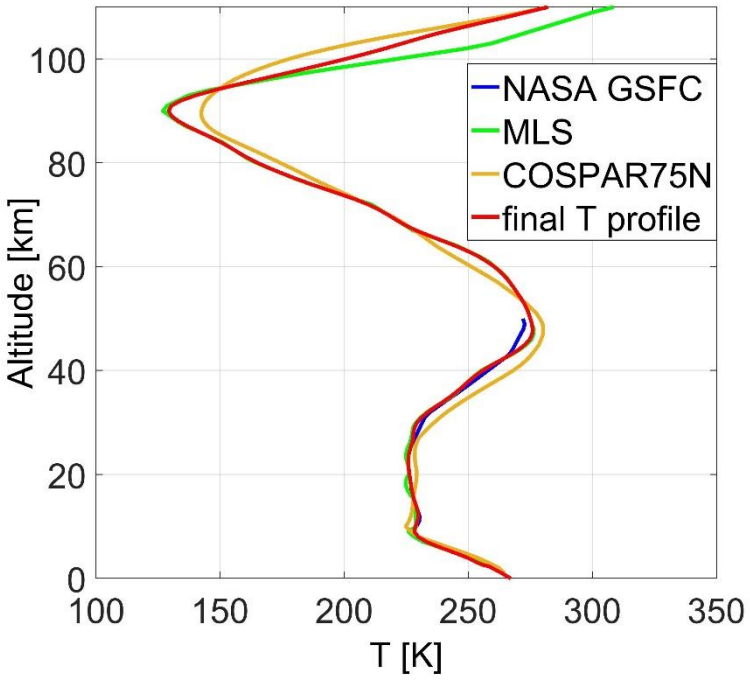

Figure 4.7: An example of the temperature profiles used in the forward model calculation for the inversion of a spectrum measured on the 24/05/2017: the temperature profile (red) computed merging the MLS (green) the NASA GSFC (blue) and the COSPAR (yellow) temperature profiles.

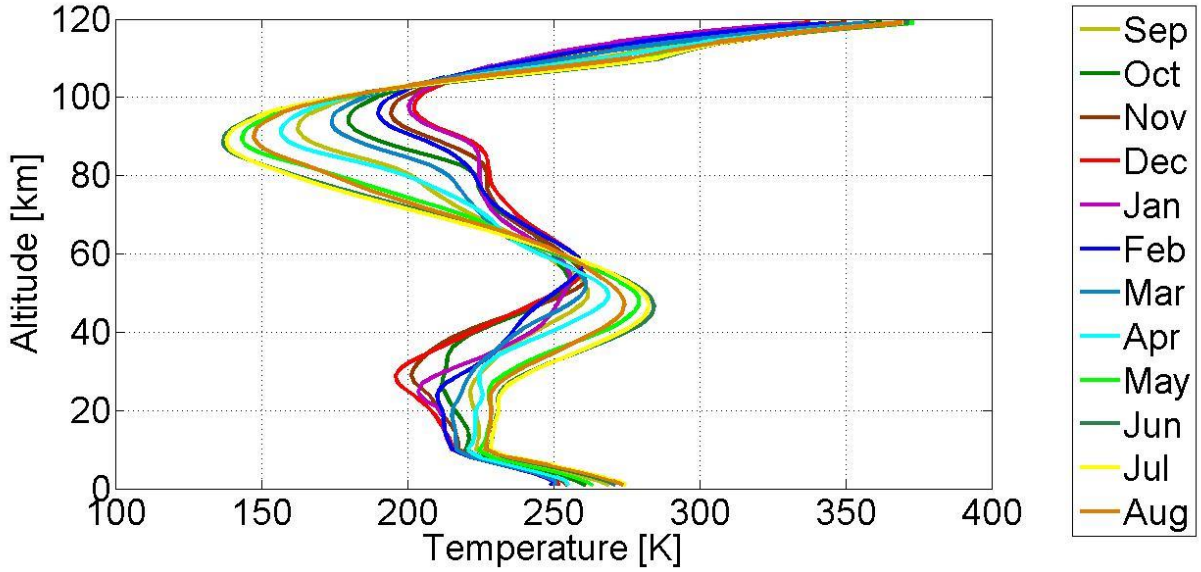

Figure 4.8: The COSPAR monthly zonal temperature profiles for 75° N of latitude

4.3.1 The forward model calculation and the polynomial baseline

In order to correctly simulate a real VESPA-22 measurement, I employed the software ARTS to calculate the emission from the zenith, $\tilde{y}_r$, and from an angle close to the horizon, y_s . I rescaled the emission $\tilde{y}_r$ using Eq. (4.11), simulating the effect of the compensating sheet.

$$y_r = \tilde{y}_r e^{-\tau_d} + T_d \left(1 - e^{-\tau_d}\right) . \tag{4.11}$$

The opacity τ_d used in Eq. (4.11) is the opacity of the compensating sheet, whereas the temperature T_d is the temperature of the sheet, measured by a sensor installed next to it. The value of the signal angle imposed in the simulation, $\tilde{\theta}$, is chosen in order to minimize the mean difference $y_s - y_r$, as it is in fact attained by VESPA-22 in its data taking process. The apriori spectrum y_a is calculated according to the same equation used for the measured signal (Eq. (3.21) and (3.22)):

$$y_s - y_r = y_a \left(\tilde{\mu} e^{-\mu\tilde{\tau}} - e^{-\tilde{\tau}-\tau_d}\right) , \tag{4.12}$$

$$y_a = \frac{y_s - y_r}{\tilde{\mu} e^{-\mu\tilde{\tau}} - e^{-\tilde{\tau}-\tau_d}} . \tag{4.13}$$

$\tilde{\mu}$ and $\tilde{\tau}$ are the air mass factor associated to the simulated signal angle and the opacity calculated from the x_{ARTS} profile. Deriving Eq. (4.13) and using Eq. (2.49) and Eq. (4.11), the retrieval weighting function matrix can be obtained as:

$$\mathbf{K} = \frac{\partial}{\partial \mathbf{x}}\left(\frac{\mathbf{y}_s - \mathbf{y}_r}{\tilde{\mu} e^{-\mu\tilde{\tau}} - e^{-\tilde{\tau}-\tau_d}} \right)_{x_a} \cong \frac{\left.\frac{\partial \mathbf{y}_s}{\partial \mathbf{x}}\right|_{x_a} - \left.\frac{\partial \mathbf{y}_r}{\partial \mathbf{x}}\right|_{x_a}}{\tilde{\mu} e^{-\mu\tilde{\tau}} - e^{-\tilde{\tau}-\tau_d}} = \frac{\mathbf{K}_s - \mathbf{K}_r e^{-\tau_d}}{\tilde{\mu} e^{-\mu\tilde{\tau}} - e^{-\tilde{\tau}-\tau_d}} \ , \tag{4.14}$$

where $\mathbf{K}_s$ and $\mathbf{K}_r$ are the weighting function matrices that ARTS calculates for the simulated signal and reference beams. As first approximation, the dependence of $\tilde{\tau}$ on the stratospheric water vapor profile in Eq. (4.14) is neglected.

VESPA-22 does not benefit of independent measurements of the water vapor concentration profile in upper troposphere. This part of the atmosphere is also outside of the sensitivity range of the retrieval algorithm. Also, the delrin emission could introduce a baseline dependent on frequency to the measured spectrum. In order to take into account these contributions, I modified the **K** matrix obtained by Eq. (4.14) adding three columns allowing the possibility to the retrieval algorithm to simulate the upper tropospheric and delrin emissions by means of a second order polynomial.

The first of these three columns represents the second order term of the polynomial, Eq. (4.15), the second the first order term, Eq. (4.16), and the last the order zero term, Eq. (4.17)

$$K_{ex1,i} = \left(\frac{i - i_{\max}}{N} \right)^2 \ , \tag{4.15}$$

$$K_{ex2,i} = \frac{i}{N} \ , \tag{4.16}$$

$$K_{ex3,i} = 1 \ . \tag{4.17}$$

In these three equations, the subscript *i* denotes the element of the column and *N* the total number of elements (13158, the same number of the spectral channels used in the retrieval). In the first of these three equations i_{max} is the number of channel corresponding to the emission line peak. The addition of these three columns to **K** allows the inversion algorithm to compute three extra parameters, together with the retrieved profiles that are the coefficients of the second order polynomial that is added to the fit. According to Eq. (2.63) and (2.69) the retrieved profile and the apriori profile need to have the same number of elements. Therefore, in order to compute the equations, I added three extra values to the apriori profile, corresponding to the apriori values of the coefficients describing the second order polynomial. These three values are set to zero.

Also the $\mathbf{S}_a$ matrix needs to be modified; the number of columns and rows of $\mathbf{S}_a$ is equal to the number of elements of the apriori profile. I modified the apriori covariance matrix $\mathbf{S}_{a\_tot}$ according to Eq. (4.18):

$$\mathbf{S}_{a\_tot} = \begin{pmatrix} \mathbf{S}_a & 0 & 0 & 0 \\ 0 & 1\cdot 10^{-5} & 0 & 0 \\ 0 & 0 & 1\cdot 10^{-5} & 0 \\ 0 & 0 & 0 & 1\cdot 10^{-5} \end{pmatrix} . \tag{4.18}$$

The value $1{\cdot}10^{-5}$ was selected after that the response of the retrieved profile to different values of this parameter was tested, as described for the σ profile.

Using the modified quantities the fit spectrum can be computed as

$$\mathbf{y}_{fit} = \mathbf{y}_a + \mathbf{K}\left(\hat{\mathbf{x}} - \mathbf{x}_a\right) + \sum_{l=1}^{3}\left(\hat{x}_{ex,l} - x_{a\_ex,l}\right)K_{ex,l} \quad . \tag{4.19}$$

The parameter l indicates the extra values added to the apriori (x_{a_ex}) and retrieved profiles ($\hat{x}_{ex}$) and the extra columns K_{ex} added to the weighting functions matrix. According to the definition of K_{ex}, the sum describes a second order polynomial.

It is important to underline that the second order polynomial coefficients are computed individually for each retrieval. The effect of the second order polynomial is taken into account in all the retrievals shown in this work. In order to show the effect of the polynomial, the Figure 4.9 displays the sensitivity of the retrieval algorithm employing the second order polynomial and the sensitivity of retrieval allowed to add just an offset to the fit spectrum as extra degree of freedom.

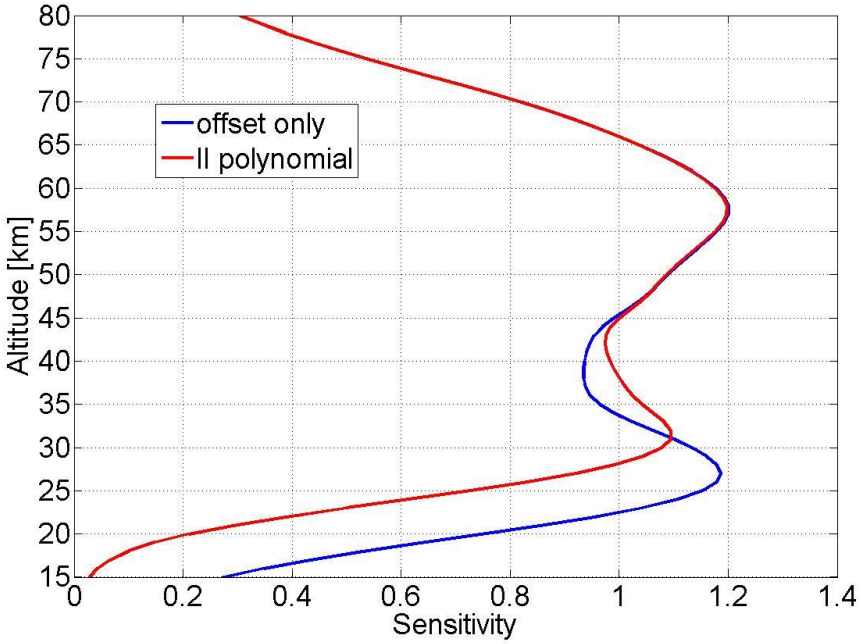

Figure 4.9: The sensitivity of the retrieval algorithm employing a second order polynomial or just an offset as extra degree of freedom respectively.

The sensitivities computation was performed using the same set of covariance and weighting functions matrices. The **K** matrix was modified in the calculation relative to "offset retrieval" adding the column described by the Eq. (4.17), whereas the apriori covariance matrix was modified according to:

$$S_{a\_off} = \begin{pmatrix} S_a & 0 \\ 0 & 1{\cdot}10^{-5} \end{pmatrix} . \tag{4.20}$$

As expected, the introduction of a second degree polynomial reduces the sensitivity in the lower part of the stratosphere.

4.4 Retrieval example

Figure 4.10 a shows a VESPA-22 spectrum integrated for 24 hours (blue) on 23 December 2016, its corresponding synthetic spectrum y_{fit} (red) and the apriori spectrum (green), whereas the residual (defined as the difference between fit and measured spectrum, $y_{fit} - y$) is plotted in Figure 4.10 (b). The cyan line is the second-degree polynomial retrieved by the inversion algorithm to simulate the upper tropospheric emission. Figure 4.11 shows the result of the inversion of the measured spectrum depicted in Figure 4.10 with the apriori profile and uncertainty. The details about uncertainty calculation are discussed in Chapter 5.

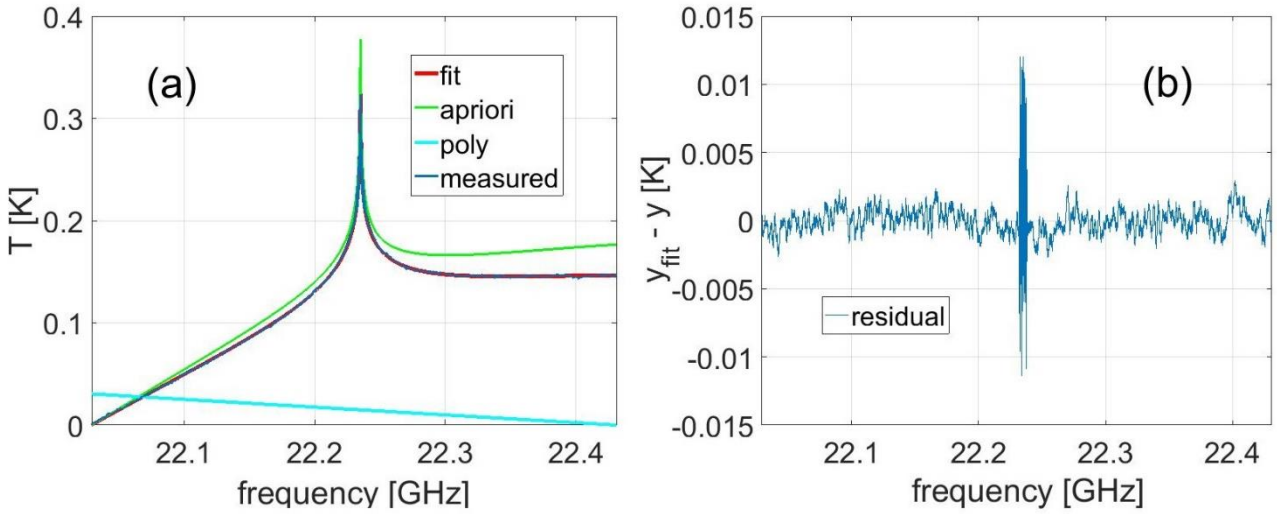

Figure 4.10: (a) an example of VESPA-22 measured spectrum (blue) collected on 23 December 2016, the apriori spectrum (green) and the fit spectrum (red); (b) the residual $y_{fit} - y$. The central part of the spectrum is unsmoothed in order to maintain the maximum spectral resolution near the peak and its residual is higher.

Figure 4.11 displays the previous retrieval averaging kernels (black and colored solid lines), multiplied by a factor of 10, and the sensitivity (red). In a typical VESPA-22 retrieval the sensitivity is above 0.8 in a range between 26 and 72 km. The sensitivity was computed taking into account the extra parameters added to the retrieval algorithm.

Figure 4.12 (a) shows nominal altitude referred to the AKs versus the altitude of their peaks (blue line) together with the ideal case (red line) and (b) the full width at half maximum (FWHM) of the AKs. The difference between peak altitudes and nominal altitudes is about 1 km at 25 km, the lower limit of the sensitivity range of this retrieval with a FWHM of 11 km (see Figure 4.12), increasing to 6 km with a FWHM of about 22 km at the upper extreme of the sensitivity range.

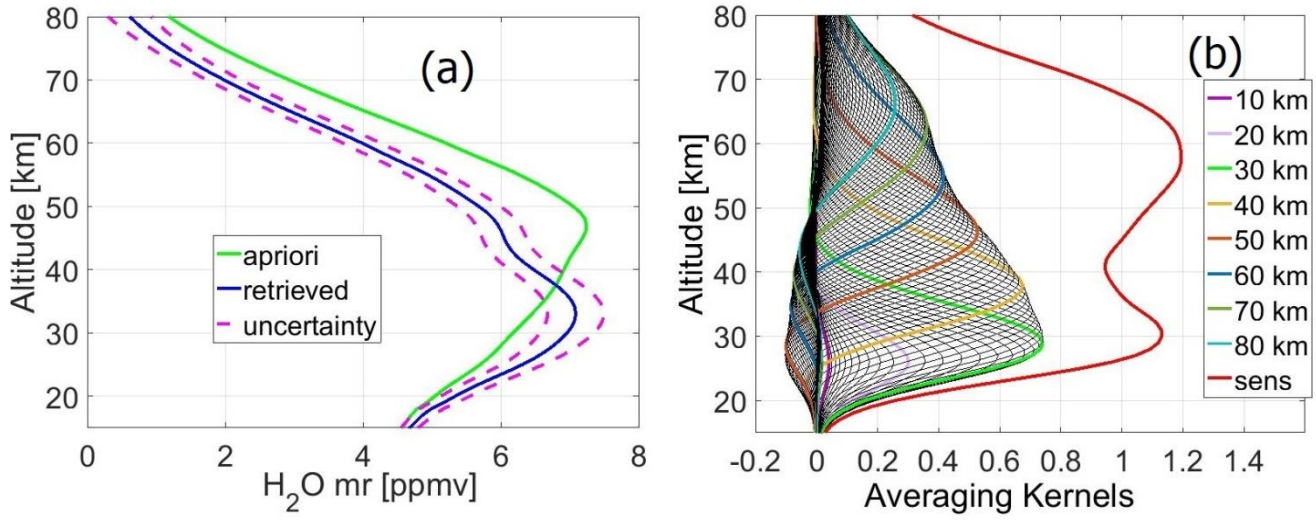

Figure 4.11: (a) The retrieved VESPA-22 profile (green solid line) correspondent to the spectrum shown in Figure 4.10 and the apriori profile (blue solid line). The two red dashed lines describe the uncertainty of this VESPA-22 retrieval (for details on the estimated uncertainty on VESPA-22 mixing ratio vertical profiles see Chapter 5). (b) Rows of the A matrix multiplied by a factor of 10 as a function of altitude (some A functions are highlighted in color). The vertical profile of the sensitivity is shown in red.

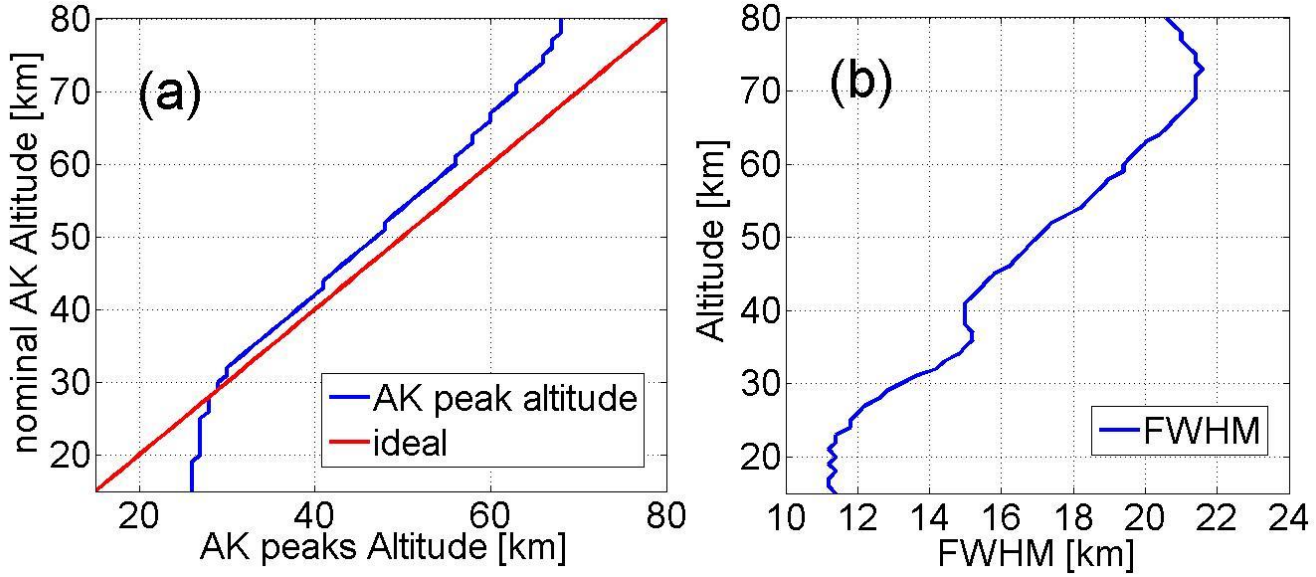

Figure 4.12: (a) Nominal altitude of the AK versus altitude of their peaks (blue line) and ideal case (red line) and (b) FWHM of the AK.

4.5 Retrieval parameters and integration time

The retrieval is sensitive to the level of noise of the spectrum by means of the $\mathbf{S}_e$ matrix. Many retrieval parameters, as the sensitivity range, the FWHM of the AK and the uncertainty depend on the noise level. The level of noise is inversely proportional to the square root of the integration, according to the Eq. (2.27). Therefore, retrieved profiles with better characteristics can be obtained at the cost of measurements resolution time. In this thesis, the retrieved profiles presented in Chapter 6 are obtained through 24-hour measurements, but in this section, the retrieval parameters variations as a function of the integration time are displayed.

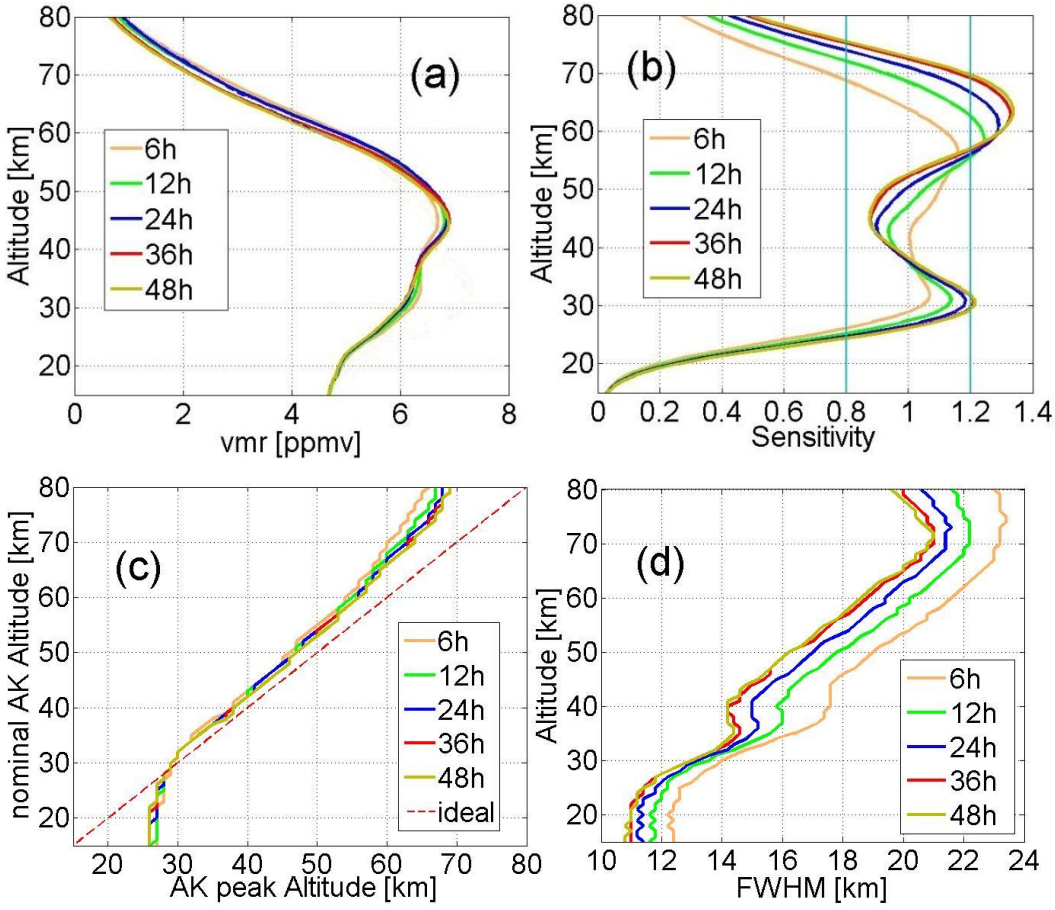

Figure 4.13: (a) Retrieval obtained with different average time spectra; (b) their sensitivities; (c) Averaging Kernels peaks altitude versus nominal altitude and (d) FWHMs.

Each spectrum examined here is centered on 10/12/2016 at 12:00 UT; for example a 24-hour measurement spectrum is the result of the integration of data collected from 10/12/2016 at 00:00 UT to 11/12/2016 at 00:00 UT, a 12 hours measurement spectrum from 10/12/2016 at 06:00 UT to 10/12/2016 at 18:00 UT and so on. As can be seen from Figure 4.13, panel a, the retrieved profiles are not very different for this particular test, however, the sensitivity range of these retrievals (panel b) shows a stronger dependence on the noise level. The lower limit of the sensitivity range does not show significant variations (it varies from 26 km for 6h measurement spectrum to 24 km for 48h measurement spectrum), whereas the upper limit varies from 69 km for the 6h measurement spectrum to 76 km for 48h measurement spectrum. The lower sensitivity of the bottom limit to the measurement integration time is partly due to the 50-channel smoothing that reduces the measurement noise; the peak, the part of the spectrum associated to the mesosphere, is not smoothed, therefore the mesospheric retrieval has an increased sensitivity to the measurement integration time. Panel (c) and (d) displays the AKs nominal altitude versus their peak altitude and the FWHM of the AKs.

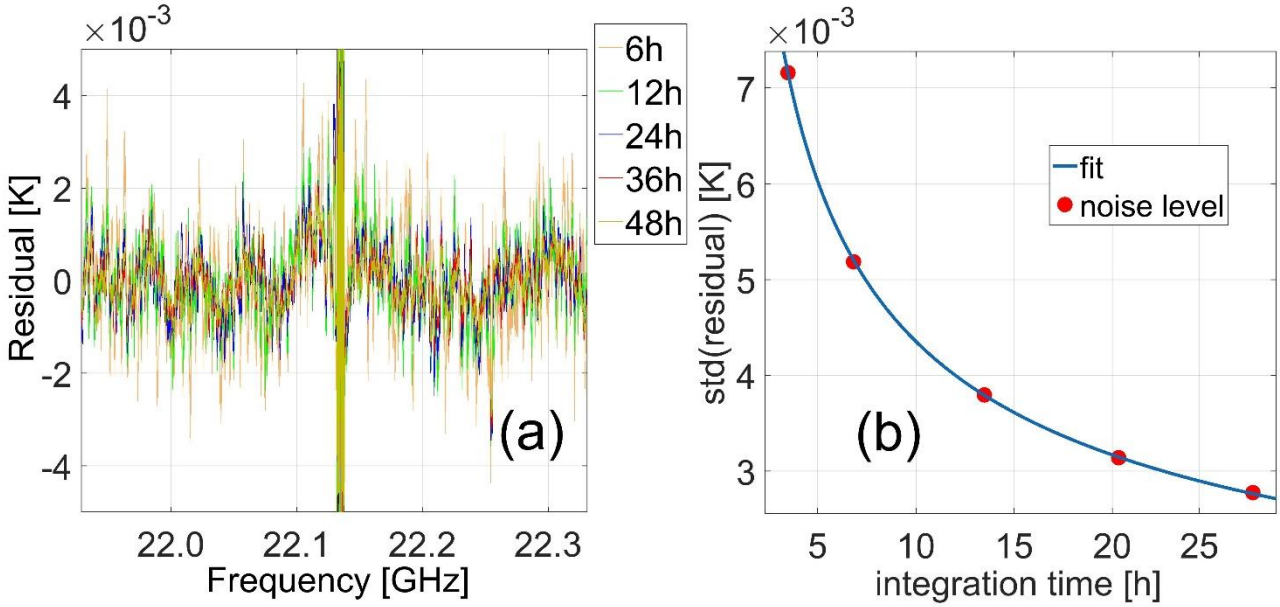

Figure 4.14: (a) Residuals ($y_{fit} - y$) of the retrievals showed in Figure 4.13. (b) The standard deviation of the residuals as an estimate of the noise level versus the integration time in hours (red dots), together with the fit function shown in Eq. (4.21).

Figure 4.14, panel (a) and Figure 4.15 display the residuals of the different spectra; note that the 50-channel smooth reduces the noise on the spectrum tails. In order to study the noise-integration time dependence I estimated the level of noise through the standard deviation of the unsmoothed residuals ($\boldsymbol{y_{fit} - y_{uns}}$**).** The level of noise is shown versus the effectively integration time (signal and reference total acquisition time, about 60% of the measurement time) in Figure 4.14 panel (b), together with a blue line representing a fit with the equation

$$fit(x) = \frac{2a}{\sqrt{\Delta\nu \cdot t}} + b \ , \tag{4.21}$$

resembling the Eq. (2.27). The quantity $\Delta\nu$ was expressed in Hz and the time in seconds. The fit results are $a = 67.1\ K$ and $b = 3.1 \cdot 10^{-4}\ K$ with a $R^2 = 1.00$. The value of the parameter a is very different from the VESPA-22 T_{sys}; however the Eq. (2.27) was referred to just thermal random noise, not taking into account the effect of standing waves on the residuals. The oscillations produced by standing waves cannot be reduced simply increasing the integration time; this justifies the presence of parameter b in the fit. The residual oscillations on the residuals shown in Figure 4.14 panel a have amplitude of about $2 \cdot 10^{-4}\ K$.

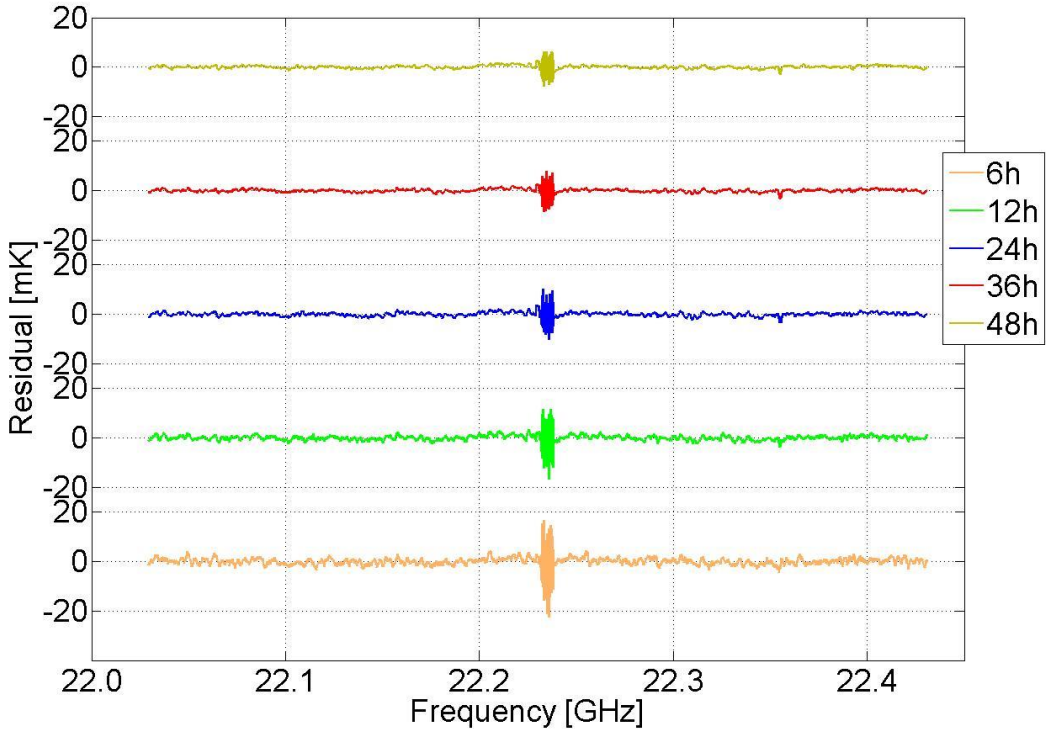

Figure 4.15: Particular of the residuals calculated using different integration times.

Figure 4.16 displays the uncertainty due to the presence of spectral noise and artifacts of the measured spectrum, hereafter defined as "spectral uncertainty", σ_{spec}. The spectral uncertainty computed according to Eq. (2.59) as the square root of the diagonal terms of the matrix **S** (see the paragraph 2.6.2 and Rodger, 2000).

$$\mathbf{S} = \left(\mathbf{K}^{\mathbf{T}}\mathbf{S}_{\boldsymbol{\varepsilon}}^{-1}\mathbf{K} + \mathbf{S}_{a}^{-1}\right)^{-1} \ . \tag{4.22}$$

The spectral uncertainty is not the total uncertainty associated with the retrieved profiles but it is the component sensitive to the measurement integration time (see Chapter 5 for the complete uncertainty description). The values of $\mathbf{S}_e$ diagonal elements are related to the level of random noise and to the spectral artifacts on the measured spectrum (see Section 4.2); therefore increasing the integration time reduces the diagonal elements values.

The spectral uncertainty does not show significant variations increasing the measurement time. This is due to the higher values of the second term in Eq. (4.22), representing the uncertainty contribute of the apriori, with respect to the first term, representing the uncertainty due to measurement noise and spectral artifacts. Only the first term in Eq. (4.22) depends on the measurement integration time. Figure 4.17 shows the values of the diagonal of the terms of Eq. (4.22) versus their associated altitude. Dashed lines represent the diagonal values of the term $\mathbf{K}^T\mathbf{S}_e^{-1}\mathbf{K}$ computed for different integration times; the cyan solid line represents the diagonal values of the term $\mathbf{S}_a^{-1}$ whereas the other solid colored lines represent the sum of the two terms.

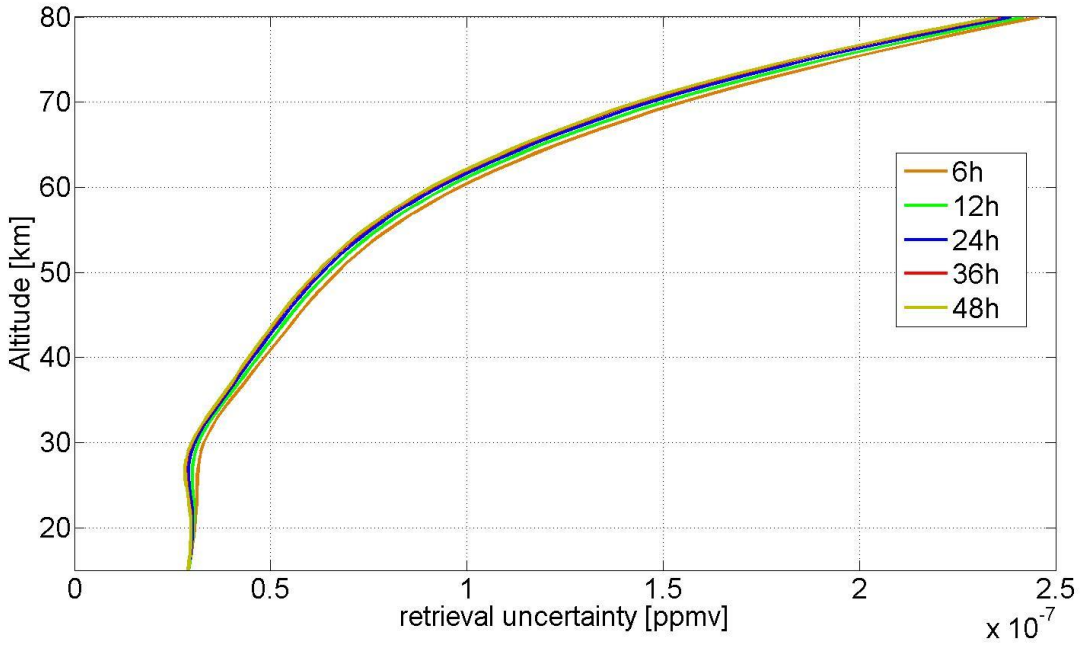

Figure 4.16: The retrieval uncertainty computed for the different measurement time spectra.

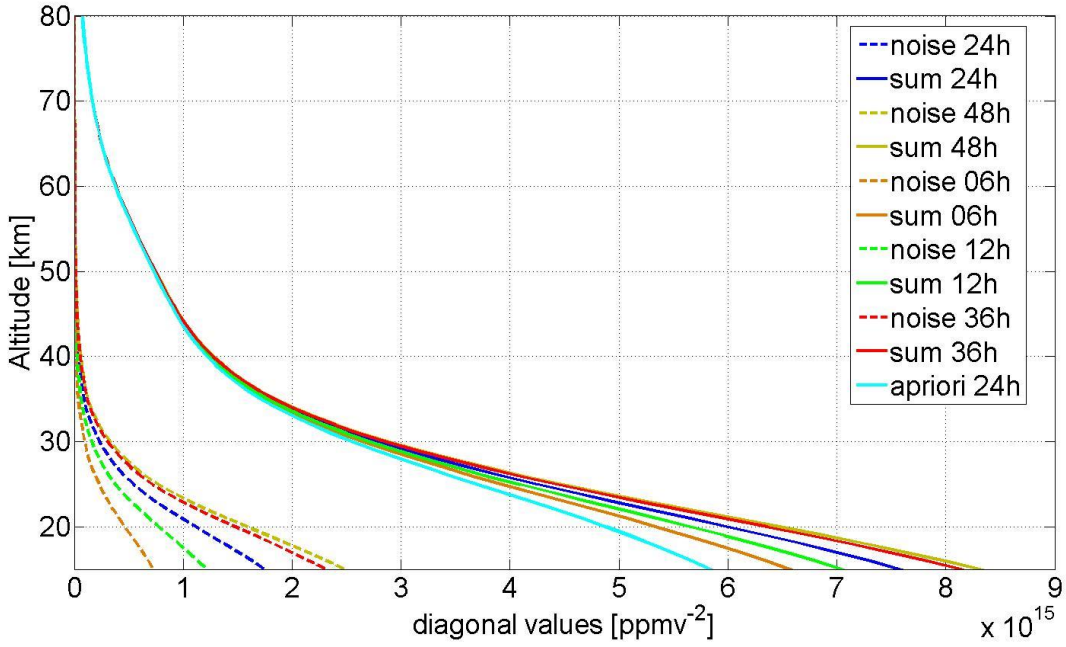

Figure 4.17: The values of the diagonal elements of the first and second term of Eq. (4.22), representing the contribution to the retrieval uncertainty of respectively the apriori profile and measurement noise and their sum, computed for different measurement integration times.

4.6 The grey body absorber and the retrieval algorithm

The second order polynomial computed by the retrieval algorithm is mainly related to the observation angle and the delrin sheet used in the measurements (as briefly explained in the Section 4.3.1). In particular the delrin sheet has a large impact: its opacity is directly related to the observation angle (see Section 3.9) and it could potentially introduce a frequency dependent baseline on the measured spectra. Figure 4.18 shows two 24-hour measurement spectra measured respectively on 29th and 30th November 2016. The panel a cyan spectrum was measured using a 9 mm thickness delrin sheet, whereas the orange spectrum using a 5 mm thickness. The panel a displays also the two baselines (blue and red curves) computed in the inversion process of the two spectra; both the first and second order terms of the polynomial baseline are higher using a 9 mm thickness delrin sheet. This test was performed during fair weather condition in order to minimize the influence of tropospheric variations on the baselines. Panel b shows the results of the tipping curves during the measurements. The 9 mm

spectrum measurement is characterized by a larger tropospheric variability during the second part of the day; however the mean value of the tropospheric opacity for both the 5 and 9 mm spectrum is about 0.05.

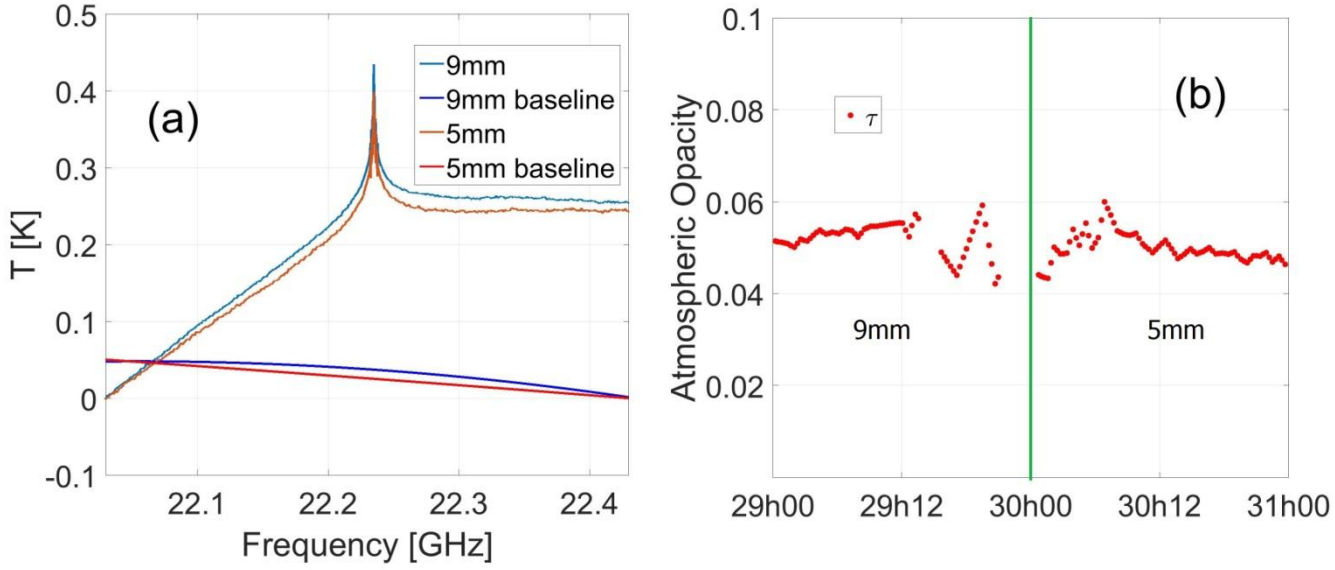

Figure 4.18: (a) The spectra measured using two different delrin sheet (9 mm thickness, cyan line and 5 mm thickness, orange line) with the baselines computed by the spectra inversion process (blue and red line). (b) The opacity measured by means of the tipping curve during the spectra acquisition. The green line shows the moment when the delrin sheet was changed.

The use of the delrin absorber to perform the balancing beam technique is a peculiar feature of VESPA-22. In literature the delrin is replaced quite commonly by a black body bar (for example see Nedoluha et al, 2011). The black body bar absorbs part of the zenithal beam radiation and adds its black body emission to the reference beam, therefore can be treated using the same measurement equations described in Sections 3.7 and 3.10. In order to compare the VESPA-22 results obtained using the delrin and the black body bar a test was performed on 19th February 2017. For 12 hours the 5 mm thickness delrin sheet used during winter was replaced by a black body bar of eccosorb CV-3 panel by Emerson and Cuming. The τ_d associated to the bar was measured using the procedure described in the Section 3.10, resulting in a value of 0.07. The retrieval results of a 12-hour integration spectrum measured immediately before the delrin substitution and the 12-hour spectrum acquired using the bar have been compared. The test was performed during fair weather conditions in order to minimize differences in the retrievals due to tropospheric inhomogeneities. Figure 4.19 displays the opacity measured by means of the tipping curves during the test (red dots). The green line in the figure indicates the passage between measurements effectuated using the 5 mm delrin and measurements effectuated using the black body bar. Both the delrin and bar measurements are characterized by the low opacity values peculiar of the Arctic winter troposphere, with the delrin measurements opacity quite larger with respect to the bar ones.

Figure 4.19: the atmospheric opacity measured by means of the tipping curves during the test.

Figure 4.20 displays the test results. Panel a shows the two measured spectra with the baselines computed by their respectively retrievals; as can be seen from this panel the "bar" spectrum shows more oscillations. Furthermore the baselines of the two retrievals are very different, although Figure 4.19 does not reveals large variation in the atmospheric opacity, pointing out the dependence of the baseline on the grey absorber used in the measurements. Panel b shows the water vapor profiles retrieved inverting the two spectra (blue and red lines) together with the apriori profile (green line). Panel c displays a particular of the two baselines and panel d shows the residuals of the two retrievals. This last panel reveals clearly that the use of the black body bar produces more standing waves with respect to the delrin sheet despite the bar measurements were characterized by lower values of atmospheric opacity. According to this test result the use of the delrin sheet proves to fit better the VESPA-22 features with respect to the black body bar.

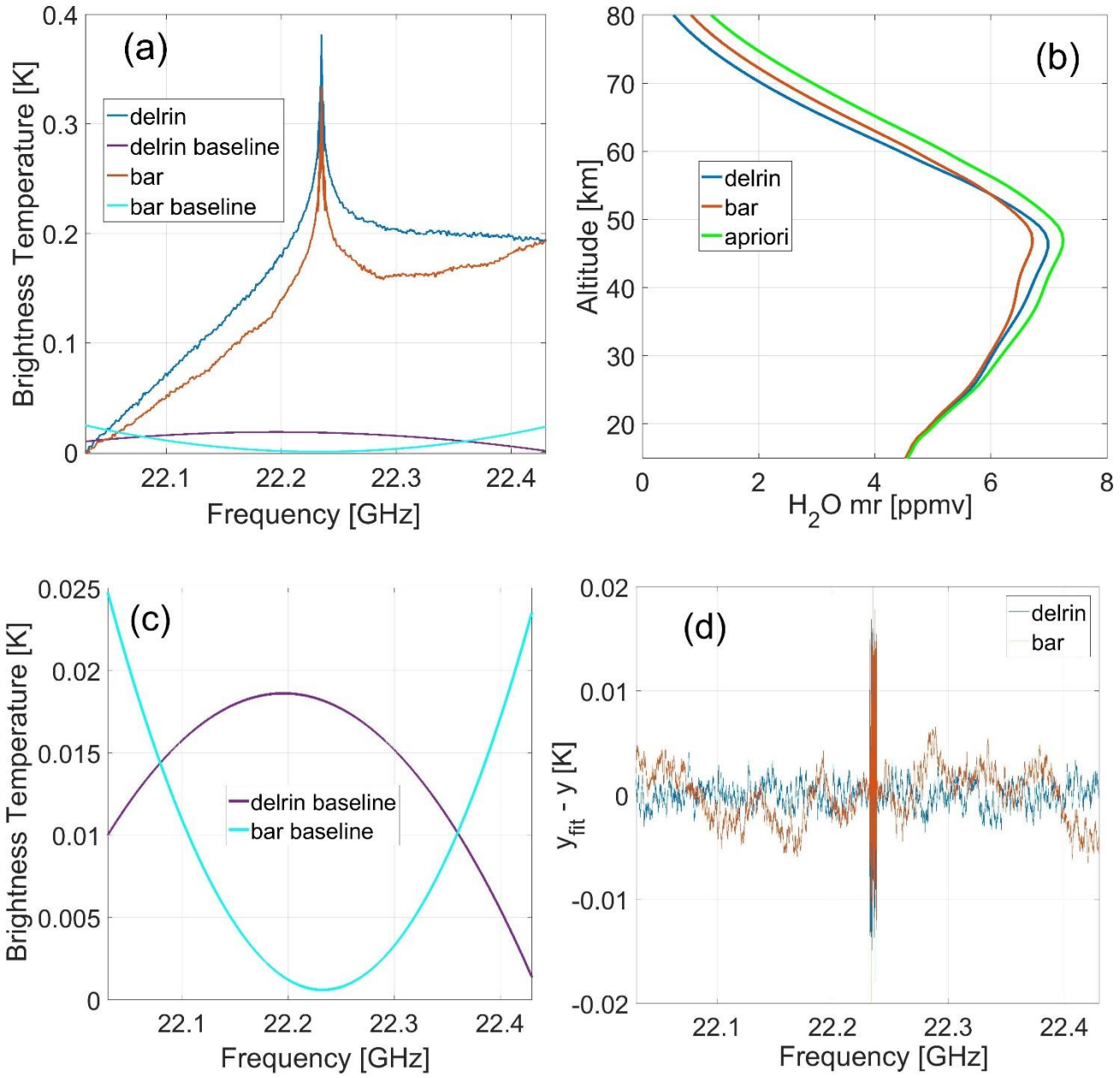

Figure 4.20: (a) the 12-hour spectra measured on 19th February using the delrin or the black body bar (blue and red lines) with the baselines used in the retrievals (purple and cyan lines). (b) The water vapor vertical profiles retrieved from spectra showed in panel a (blue and red lines) and the apriori profile (green line). (c) Particular of the baselines of the two retrievals. (d) The residuals of the two retrievals.

Chapter 5

Uncertainty description

The uncertainty characterizing VESPA-22 retrieved profiles can be divided into four major contributions:

- the uncertainty due to the linear approximation used in Eq. (2.48);
- the pre-processing uncertainty due to the uncertainties of the various parameters used in the spectra calibration and in the forward model computations;
- the spectral uncertainty due to random noise and spectral artifacts ;
- the uncertainty introduced by the use of the second order polynomial baseline in the retrieval algorithm.

One additional error source is the limited vertical resolution inherent to concentration vertical profiles obtained by means of this ground-based observing technique. This leads to solution profiles that can be considered a smoothed version of the real atmospheric concentration profiles. In discussing the Optimal Estimation method, Rodgers (2000) suggests that this error, called "smoothing error", should be estimated only if accurate knowledge of the variability of the atmospheric fine structure is available. This approach is used here and the smoothing error is not included in the error estimate.

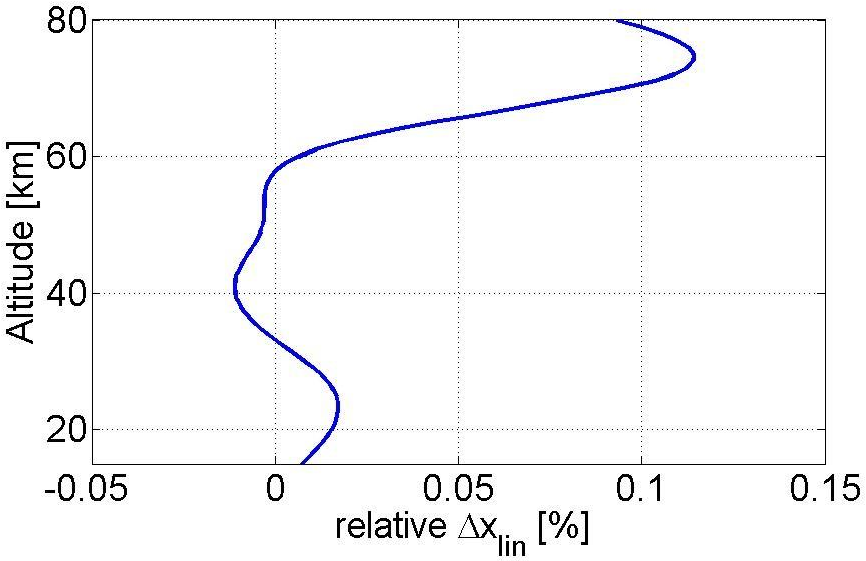

Figure 5.1: The relative uncertainty due to nonlinear approximation used in the retrieval algorithm.

All the pictures and tests shown in this chapter are referred to the inversion of the 24h of measurement spectrum collected on 10/12/2016 used to illustrate a retrieval example in Section 4.4.

The first contribution can be evaluated observing the difference $\Delta\mathbf{y}_{lin}$ between the fit spectrum without the addition of the second order polynomial, $\mathbf{y}^{*}_{fit}$, and the spectrum obtained using ARTS to calculate the emission expected from the retrieved profile $\hat{\mathbf{x}}$. ARTS does not perform a linear approximation of the general function f described in Eq. (2.47), therefore $\Delta\mathbf{y}_{lin}$ is equal to:

$$\Delta\mathbf{y}_{lin} = \mathbf{y}^{*}_{fit} - f\left(\hat{\mathbf{x}}\right) . \tag{5.1}$$

The uncertainty $\Delta\mathbf{x}_{lin}$ that $\Delta\mathbf{y}_{lin}$ causes on the retrieved profile can be calculated with

$$\Delta\mathbf{x}_{lin} = G\Delta\mathbf{y}_{lin} \tag{5.2}$$

and it has a negligible contribution to the total uncertainty, with a maximum of about 0.1 % at 73 km altitude, see Figure 5.1. In order to evaluate the second contribution listed above, the effects on the retrieved profile due to the variation of each single parameter used in the measurements calibration and pre-processing was investigated. The difference between the profile retrieved using the "correct" value of a specific parameter and the retrieval obtained by changing such value by the estimated relative uncertainty of the parameter is considered the contribution $\boldsymbol{\sigma_i}$ of this parameter to the total calibration and pre-processing uncertainty. The total uncertainty from these sources is simply called pre-processing uncertainty in what follows. Table 5.1 summarizes the uncertainties of the various parameters involved in the calibration and pre-processing of VESPA-22 spectra; when the uncertainty is a function of altitude the minimum and maximum values of the uncertainty are reported.

Table 5.1: Uncertainties of the various parameters used in the calibration process and in the forward model computations. When the uncertainty is a function of altitude the minimum and maximum values of the uncertainty are reported.

Parameter	Uncertainty (relative or absolute)
Signal angle θ	±0.1°
Noise Diode brightness temperature T_{nd}	±1.8%
Atmospheric opacity τ	±5%
Air Temperature profile	[±2.1 ± 5.0] K
Geopotential height	[±30 ± 110] m
Delrin opacity τ_d	±10%
Spectroscopic parameters	[±1% ±10%]

The total uncertainty σ_{pre} is therefore given by:

$$\sigma_{pre} = \sqrt{\sum \sigma_i^2} \ . \tag{5.3}$$

In Eq. (5.3) the several pre-processing uncertainty contributes are considered independent, with the exception of the noise diode and opacity uncertainties. These two parameters are measured together during the tipping curve procedure and cannot

be considered independent. Therefore the noise diode and opacity uncertainties are summed together to get the maximum uncertainty from these two sources. This contribute is then summed in quadrature with the other terms of Eq. (5.3).

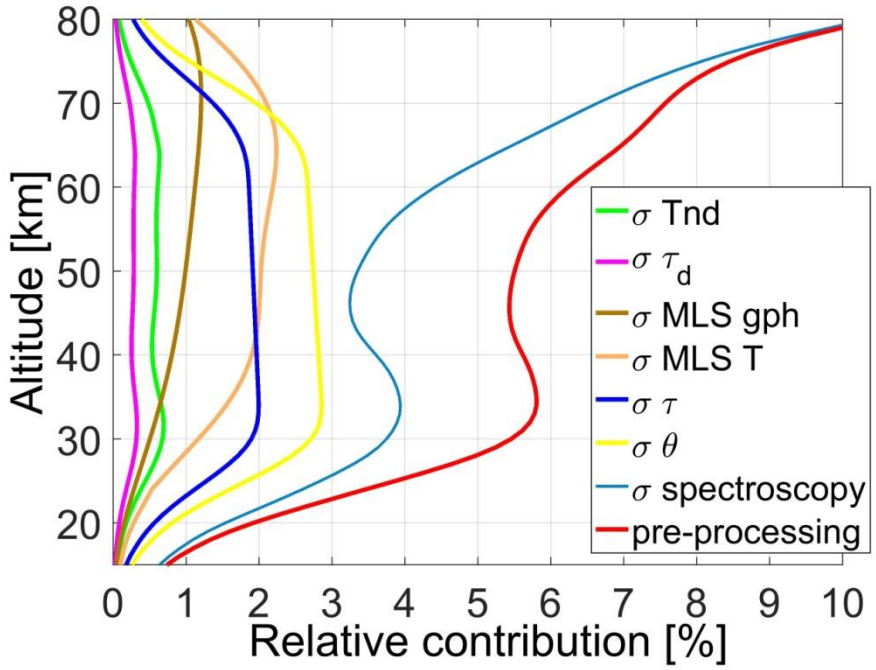

Figure 5.2: Relative contributions to pre-processing uncertainty (red curve). The contributions are: the signal beam angle (yellow), the noise diode temperature (green), the opacity (blue), the MLS meteorological profile (orange and brown), the compensating sheet opacity (magenta), the spectroscopic parameters (cyan).

In Figure 5.2, the relative contributions of the various parameters used in the calibration and pre-processing are shown.

The yellow line shows the σ_i contribution due to the uncertainty on the signal beam angle due to the uncertainty to the angle offset measurement (Section 3.11). The green solid line shows the potential relative error on the water vapor mixing ratio vertical profile due to the uncertainty on the noise diode temperature T_{nd}. The blue line in Figure 5.2 shows the contribution due to the uncertainty $\Delta\tau$ on the sky zenith opacity τ (paragraph 3.8.2).

The brown and orange lines in Figure 5.2 show the σ_i's due to the temperature and geopotential height uncertainties in the meteorological profiles used in the forward calculation. The uncertainties on these parameters are obtained from the MLS data quality and description document (Livesey et al., 2015). The magenta line shows the contribution of the uncertainty of the compensating sheet opacity, $\Delta\tau_d$ (see Section 3.10). The cyan line in Figure 5.2 shows the contribution due to uncertainties in spectroscopic parameters used in the forward model in order to compute the apriori spectrum and the weighting functions (see Section 4.3.1). This spectroscopic contribution has the largest impact on the pre-processing uncertainty.

Figure 5.3 shows the results of the retrieval of the VESPA-22 data from October 2016 to May 2017 analyzed with the spectroscopic model eventually adopted for the analysis of VESPA-22 spectra, hereafter reference model, and the same data analyzed with other spectroscopic models.

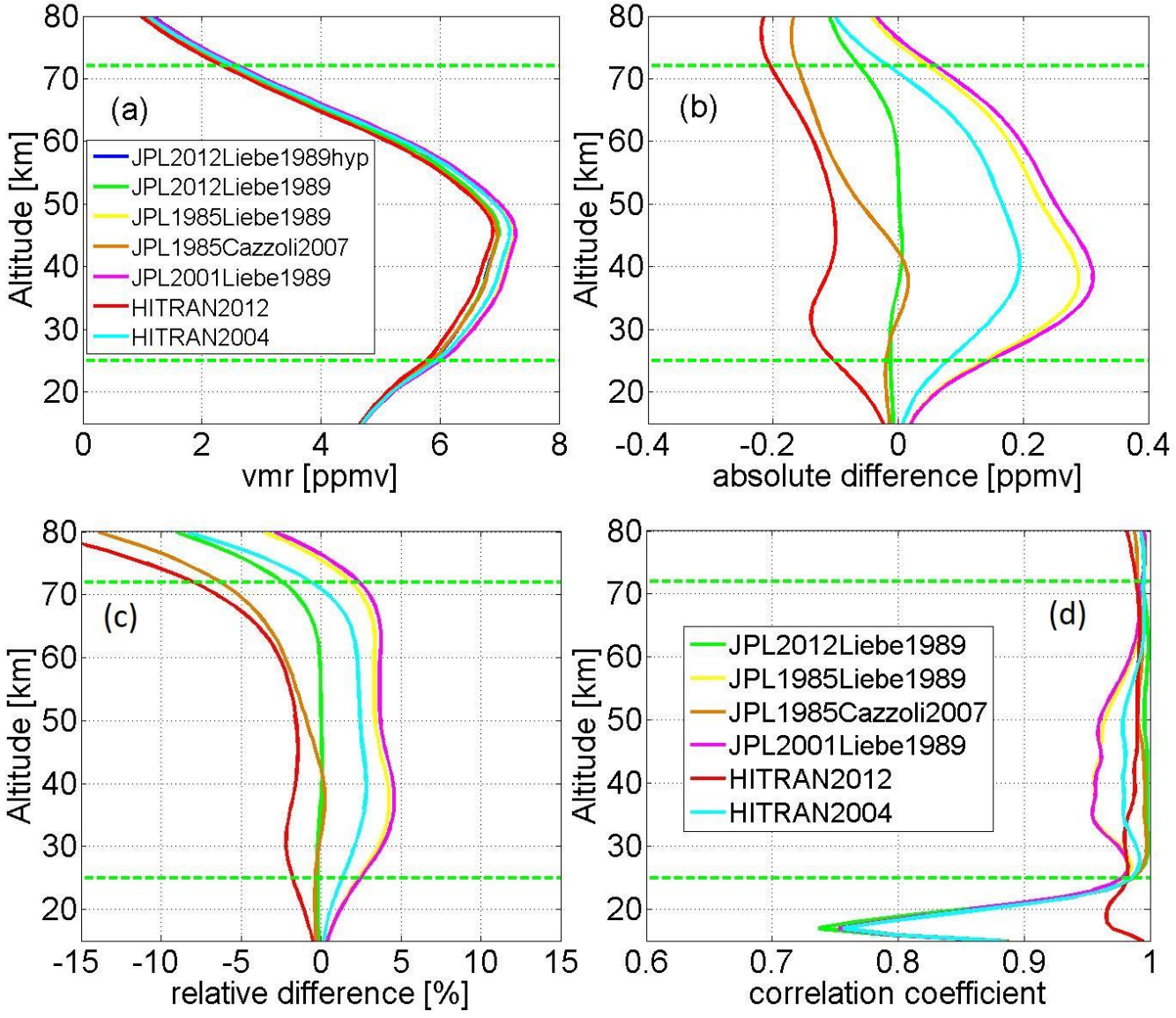

Figure 5.3: (a) averaged water vapor vertical profiles obtained using different spectroscopic models (the blue line is the model eventually adopted for the analysis of VESPA-22 spectra, called reference model) and vertical profiles of (b) and (c) the mean absolute and relative difference between VESPA-22 profiles obtained using different spectroscopic models minus the reference model and (d) their correlation coefficients. The data represented here range from 4 October 2016, to 22 May 2017. The retrieval sensitivity range is marked by the dashed horizontal green lines. The spectroscopic parameters are taken from different versions of the JPL catalog (versions of years 1985, 2001 and 2012) with the pressure broadening parameter taken from the works of Liebe (1989) or Cazzoli et al. (2007) or from the HITRAN catalog (versions 2004 and 2012).

As stated in section 5.1, the reference model line intensity is taken from the JPL 2012 catalog, modified by adding the hyperfine splitting of the H_2O line (Tschanz et al., 2013) whereas the pressure broadening parameters are taken from the work of Liebe (1989). Parameters coming from HITRAN (Rothman et al., 2012) and JPL catalogs (Pickett et al., 1998) from different years were compared with one another, as described in the work of Haefele et al. (2009). The JPL catalog does not include the pressure broadening and self-broadening parameters, so JPL models were integrated with information coming from the work of Liebe (1989) or Cazzoli et al. (2007). Figure 5.3, panel a, shows the mean profiles retrieved using the different models. The blue line represents the mean profile obtained using the reference model. Figure 5.3, panels b and c, shows the mean absolute and relative difference between the retrieved profiles obtained using other spectroscopic models and the reference model. It can be noticed that the water vapor mixing ratio retrieved profile strongly depends on the spectroscopic model of choice, with a relative difference between profiles obtained using different models reaching a maximum of 10% at the top of the sensitivity range. The correlation coefficient (Figure 5.3, panel d) of the datasets obtained with the different models with respect to the reference model dataset is above 0.9 in the sensitivity range. This strong correlation indicates that the time series variation of the water vapor profile measured by VESPA-22 is quite independent from the model used.

The spectral uncertainty σ_{spec} can be evaluated using the **S** uncertainty matrix discussed in Section 4.5 and obtained with Eq. (4.22). This uncertainty component shows a minor dependence by the level of noise afflicting the spectra, as shown in Figure 4.16; here is presented a 24h measurement uncertainty. The square root of the diagonal elements of S represents the uncertainty of the retrieved profile at different altitudes. VESPA-22 retrieval algorithm employs a second order polynomial baseline in order to handle the contribution to the measured spectrum of the higher troposphere-lower stratosphere layers below the bottom limit of the sensitivity range and all the spectral contributions to the measurement unaccounted by the forward model, such as the potential delrin frequency-dependent emission. The use of a second order polynomial baseline in the retrieval process introduces a source of uncertainty in the retrieved profile, hereafter defined "polynomial uncertainty", σ_{pol}. Albeit the use of a first order polynomial is commonly accepted in literature (Nedoluha et al., 2011) the use of the second order term can have an impact on the lower stratospheric part of the retrieved profile. In order to estimate the uncertainty due to the use of the second order polynomial I take the uncertainty associated to the second order coefficient (Δa2) in the retrieval process (say for example 20%, e.g., a2 = (-5 ± 1) x 10-3) and then perform two retrievals for the same spectrum with fixed values of the second order coefficient equal to a2 ± Δa2 (in the example they would be a2 = -4 x 10-3 and a2 = -6 x 10-3). The resulting two vertical profiles would then provide an estimate for the uncertainty of the regular retrieved profile associated with the uncertainty in the second order coefficient. I found that the average uncertainty of the second order coefficient calculated by the optimal estimation routine over the entire dataset (from July 2016 to July 2017) is 6%, with few retrievals showing more than 20%. I therefore decided to employ a fixed maximum uncertainty on the coefficient of 20% for the whole data set, rejecting from the data set those few retrievals (less than 5% of the total) that had

an uncertainty larger than 20% in the determination of a2. As expected the polynomial uncertainty computed in this way has its maximum impact in the lower stratosphere.

Figure 5.4 shows the uncertainty calculated for the retrieval shown in Figure 4.11. The overall pre-processing uncertainty is shown as a red curve, the spectral uncertainty is indicated as a blue curve, whereas the polynomial uncertainty is indicated as a green curve. Finally, the total uncertainty is obtained as

$$\sigma_{tot} = \sqrt{\sigma_{pre}{}^2 + \sigma_{spec}{}^2 + \sigma_{pol}{}^2} \tag{5.4}$$

and it is represented as a magenta line in Figure 5.4. The pre-processing uncertainty contribute dominates the altitude range between about 30 and 60 km. From 60 km the spectral and pre-processing uncertainty are comparable whereas the altitude above the upper extreme of the sensitivity range (about 72 km) are dominated by the spectral uncertainty that increases its intensity with the altitude. The mesospheric water vapor profile is characterized by the maximum of the relative uncertainty. This is due to the loss of sensitivity of the instrument due to the limited frequency resolution and to the increase of the dominance of the Doppler broadening with respect to the pressure broadening in the mesosphere that not allows to correctly resolve the emission from this layer and to the lower values of water vapor concentration characterizing the mesosphere.

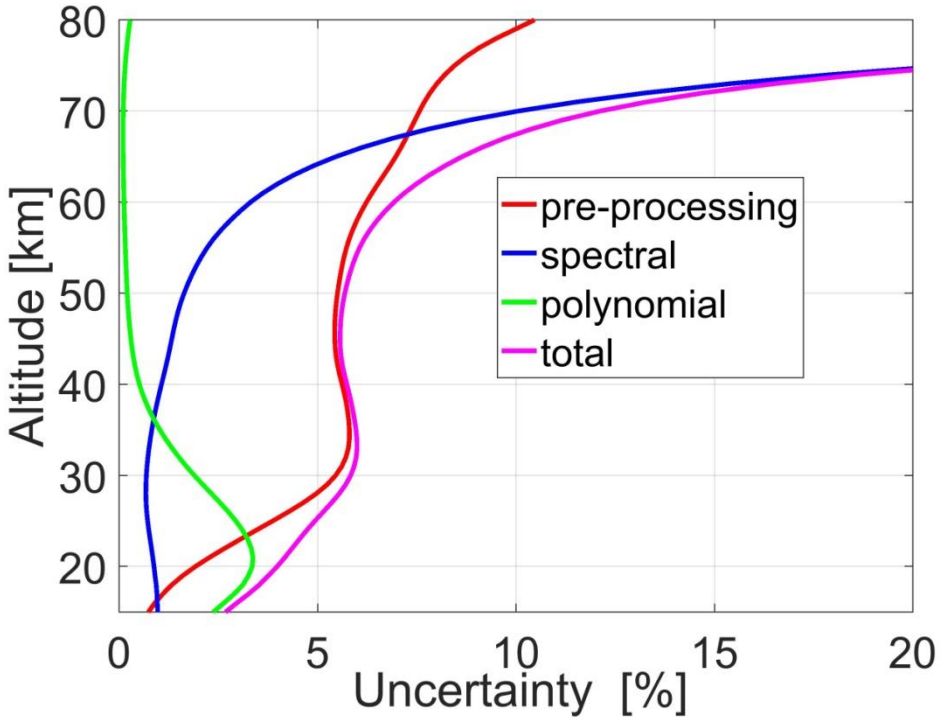

Figure 5.4: Vertical profiles of the pre-processing uncertainty (red), the spectral uncertainty (blue), the polynomial uncertainty (green), and the total uncertainty (magenta) of VESPA-22 water vapor mixing ratio vertical profiles obtained inverting a 24-hour integration spectrum collected on 23 December 2016.

The $\mathbf{S}_e$ matrix used in the spectral uncertainty computation is a diagonal matrix with constant diagonal values as described in the Section 4.2. The $\mathbf{S}_e$ diagonal value is computed before the smoothing process on the spectrum tails and is constant for all channels, so it represents an overestimation of the noise of the spectrum tails on which a 50-channel moving average is performed. Figure 5.5, panel a, displays the relative difference between the spectral uncertainty computed using the standard $\mathbf{S}_e$ matrices of our retrieval algorithm and the spectral uncertainty computed with a non-constant diagonal $\mathbf{S}_e$ matrix that takes into account the noise reduction on the spectrum tails produced by the 50-channel moving average. The relative difference has been computed for different days of the year; the standard $\mathbf{S}_e$ matrix computation leads an increment of about 15-35% on the spectral uncertainty between 25 and 50 km of altitude with respect to the other method, depending on the season. The overestimation produces small variations on the total uncertainty that, between 25 and 50 km, is dominated by the pre-processing and polynomial terms. Figure 5.5, panel b, displays the uncertainty analysis of the 2016/12/10 retrieval. The spectral and total uncertainty computed using the standard $\mathbf{S}_e$constant matrix are marked as "standard" in the legend whereas the spectral and total uncertainty computed using a non-constant $\mathbf{S}_e$ matrix are marked as "tails centre".

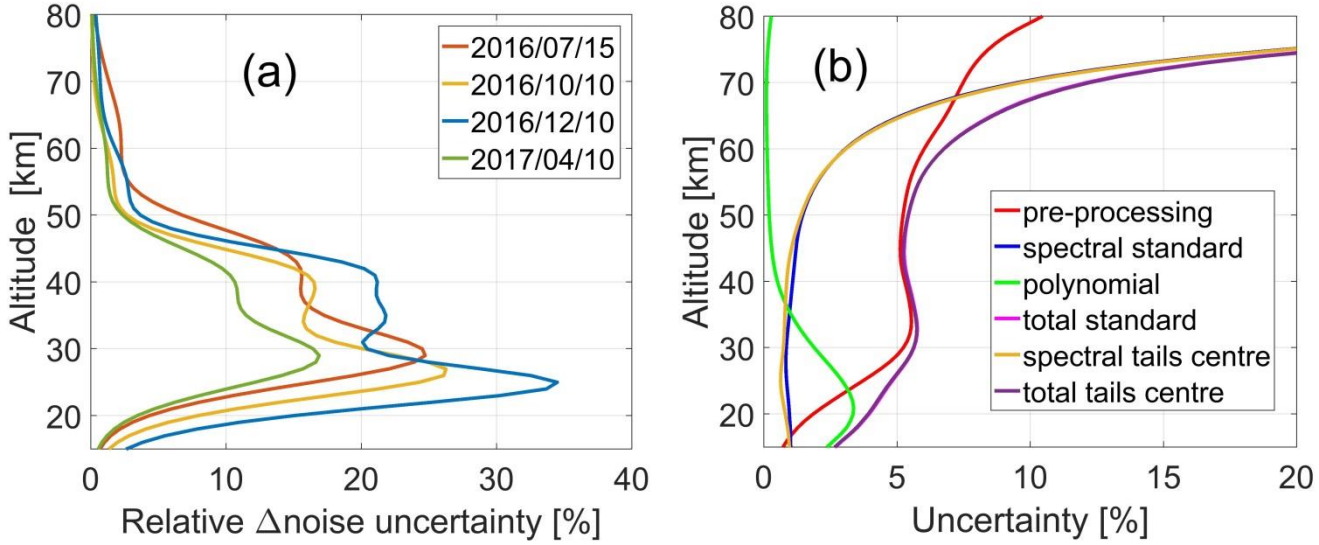

Figure 5.5: (a) The overestimation of the spectral uncertainty caused by the use of a constant S_e matrix respect to a computational method that take into account the noise reduction due to the moving average on the spectrum tails, computed for different days. (b) The effect of the overestimation on the total uncertainty computed on December 10, 2016. The spectral and total uncertainty computed using the standard $S_e$constant matrix are marked as "standard" in the legend whereas the spectral and total uncertainty computed using a non-constant S_e matrix are marked as "tails centre".

Chapter 6

VESPA-22 datasets and intercomparison with Aura/MLS

As part of my Ph.D. work, I analyzed the first year of data of VESPA-22 and compared it with the AURA/MLS dataset. In this chapter, I briefly describe the installation and preparatory campaigns I participated to at Thule, and the results of the VESPA-22 data analysis and comparison.

6.1 The VESPA-22 installation campaigns

The Ph.D. work described in this thesis included two campaigns at Thule, with the aim to install the instrument at the THAAO observatory. The two campaigns were part of the Study of the water Vapour in the polar AtmosPhere (SVAAP) project, founded by the Italian Progetto Nazionale Ricerche in Antardite (PNRA). Figure 6.1 shows two pictures of the THAAO during the two different seasons.

The first one was a preparatory campaign; it took place from the mid of February to the mid of March 2016 with the aim of preparing the THAAO to the installation of the instrument. During this period several operations of laboratory and instrumentation maintenance were effectuated and the design and construction of the laboratory annex and observing windows was completed. The instruments already operating at Thule observatory were:

- a LIDAR system for the stratospheric temperature profile (during night-time) and of the tropospheric backscattering profile (di Sarra et al., 1998; di Sarra et al., 2002; Di Biagio et al., 2010);
- Eppley PSP pyranometer and Kipp&Zonen CGR4 pyrgeometer for the downward shortwave (SW) and longwave (LW) irradiance (di Biagio et al. 2012);
- the millimetre-wave spectrometer GBMS (Muscari et al., 2007) capable of measuring the stratospheric and mesospheric concentrations of trace gases such as O_3, N_2O, CO, and HNO_3, as well as the H_2O continuum, with a spectral window of 600 MHz tunable between approximately 230 and 280 GHz.

- Cimel solar photometer (Holben et al., 1998) for solar radiation measurements at 340, 380, 440, 500, 670, 870, 940, e 1020 nm.

During the preparatory campaign, data were collected with the LIDAR system and the GBMS.

The VESPA-22 installation campaign took place in July 2016. During this period, I installed VESPA-22 and aligned the quasi-optical system using the He-Neon laser (Section 3.11). The annex was completed by placing the two fans to blow off the snow and was implemented in the laboratory a UPS system in order to minimize damages to the instrumentation due to tension losses. In addition, other instruments for the surface radiative budget and for the characterization of the atmospheric state were installed for the campaign (Figure 6.2):

- Eppley PSP pyranometer and PIR pyrgeometer for the upward SW and LW irradiance, respectively,
- two Licor 190R sensors for the upwelling and downwelling photosynthetically active radiation (PAR),
- a Metcon actinometer for the downward actinic flux in the 280-700 nm spectral range,
- a modified CG3 pyrgeometer measuring downward irradiance in the 8-14 μm infrared window,
- the HATPRO microwave radiometer for the tropospheric profiles of temperature and relative humidity, for the precipitable water vapour (PWV), and for the liquid water path (LWP) (Rose and Czekala, 2009; Pace et al., 2015),
- Heitronics infrared (9.6-11.5 μm) pyrometer for the sky brightness temperature (BT), visible and infrared sky cameras for the cloud cover. During the measurement campaign, 23 radiosondes were launched.

Figure 6.1: The THAAO observatory in winter and summer.

Figure 6.2: Top left and right: down-looking and up-looking radiometers, bottom left: the HATPRO radiometer, bottom right: a radiosonde launch.

6.2 Overall measurements and MLS comparison

In order to test the goodness of data collected by VESPA-22, I compared the retrieved profiles obtained from 24-hour integration spectra (from 00:00 to 23:59) with version 4.2 of AURA/MLS water vapor vertical profiles. The MLS profiles used for this intercomparison are daily mean profiles obtained averaging all MLS profiles collected within a radius of 300 km centered around VESPA-22 observation point (74.8° N, 73.5° W, see Section 5.1). A measurement of the horizontal resolution of VESPA-22 is the horizontal area highlighted by the full width at half maximum angle; for an observation angle of 15° at a height of 60 km it is an ellipse with axes of about 55 x 14 km. The horizontal resolution of MLS is reported in Table 4.1.

The intercomparison is carried out using data from 15 Jul 2016 to 2 July 2017. The spectra collected during July, August and September 2016 are less continuous and noisier due to testing of the equipment, poor weather conditions, and snow covering the zenith observing window (in November 2016 a more powerful fan was installed outside the windows to minimize snow deposition). Additionally, there are no measurements carried out by VESPA-22 between 4 and 22 November 2016, and between 12 and 16 February 2017, due to poor weather conditions and snow covering the reference beam window, and from 11 to 16 December 2016, due to technical issues. A few isolated days in which large sky inhomogeneities do not allow the correct balance of signal and reference beams have also been removed from the intercomparison. It is worth recalling that the signal to noise ratio of VESPA-22 spectra, and therefore the quality of the retrievals, depends on the sky opacity and, consequently, on the season, being noticeably better during winter and poorer in summer. This is particularly true for microwave instruments installed in the Polar Regions, where the seasonal fluctuations in tropospheric water vapor column content are significant.

Table 4.1 summarizes the characteristics of the Aura/MLS water vapor version 4.2 retrievals (Livesey et al., 2015).

In order to compare the two datasets, MLS vertical profiles are convolved with VESPA-22 averaging kernels in order to match the vertical resolution of VESPA-22 profiles according to:

$$x_{MLS} = x_a + A\left(\tilde{x}_{MLS} - x_a\right), \tag{6.1}$$

where $\tilde{x}_{MLS}$ is the raw (high resolution) MLS water vapor vertical profile, x_a is the apriori profile, A is Averaging Kernel Matrix and x_{MLS} is the convolved MLS profile.

Figure 6.3 shows the MLS measured profile on 23 December 2016 with its full vertical resolution (purple line) convolved using Eq. (6.1) (red line), together with the apriori profile (green line) and the VESPA-22 retrieved profile (blue line). The MLS convolved profile tends to the apriori profile below 25 km and above 72 km, where the retrieval sensitivity drops.

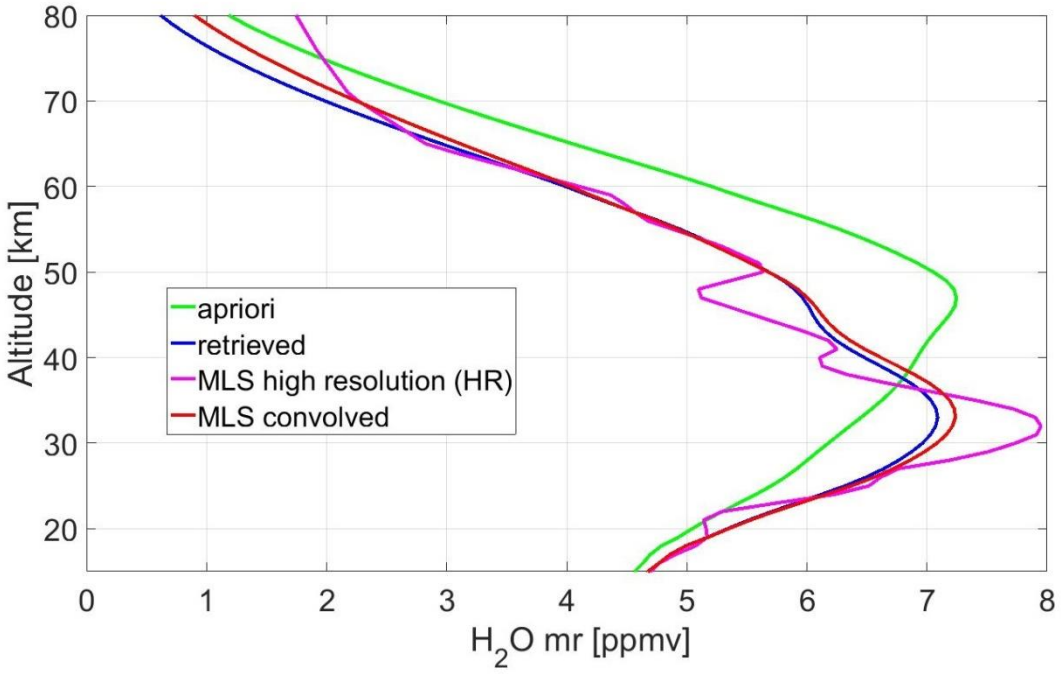

Figure 6.3: The MLS profile measured on 23 December 2016 with high vertical resolution (purple line) compared with the convolved profile obtained from Eq. (6.1) (red line) and with the VESPA-22 retrieved profile (blue line) and the apriori profile (green line).

Additionally, VESPA-22 profiles were also compared with MLS profiles smoothed in the vertical by using a 10 km moving average and defined as MLS smoothed in what follows. This second set of degraded MLS profiles was generated in order to study the correlation between VESPA-22 and MLS datasets without introducing the dependency from one another brought by the convolution process (affecting MLS convolved profiles).

Figure 6.5, panel (a), shows the mean VESPA-22 retrieved profile (in blue) and the mean MLS convolved profile (in red) during the comparison period, with their standard deviations indicated with dashed lines. Panel (b) shows the mean sensitivity of VESPA-22 retrieved profiles with its standard deviation (solid and dashed lines respectively), which is larger than 0.8 from 25 to 72 km altitude. This interval can vary from day to day depending on the noise level of the 24-hour integrated spectrum. Panels (c) and (d) display the relative and absolute differences of VESPA-22 water vapor mixing ratio mean vertical profile with respect to the MLS mean convolved profile (red line) and with respect to the MLS smoothed mean vertical profile (blue line). The largest relative and absolute differences between the two datasets occurs at 72 km, the upper limit of the VESPA-22 sensitivity range, and are about -5% and -0.2 ppmv, respectively, with Aura/MLS convolved mean profile being larger than VESPA-22 mean retrieval. The mean difference between the two datasets at the extremes of the sensitivity range could be reduced using an apriori for VESPA-22 retrievals that is closer to the real atmospheric state, as it would be for example a monthly average of MLS mean profiles collected during the same month of the measurement.

However, as already discussed in Section 4.2, a climatological apriori allows the identification and study of potential interannual water vapor variations.

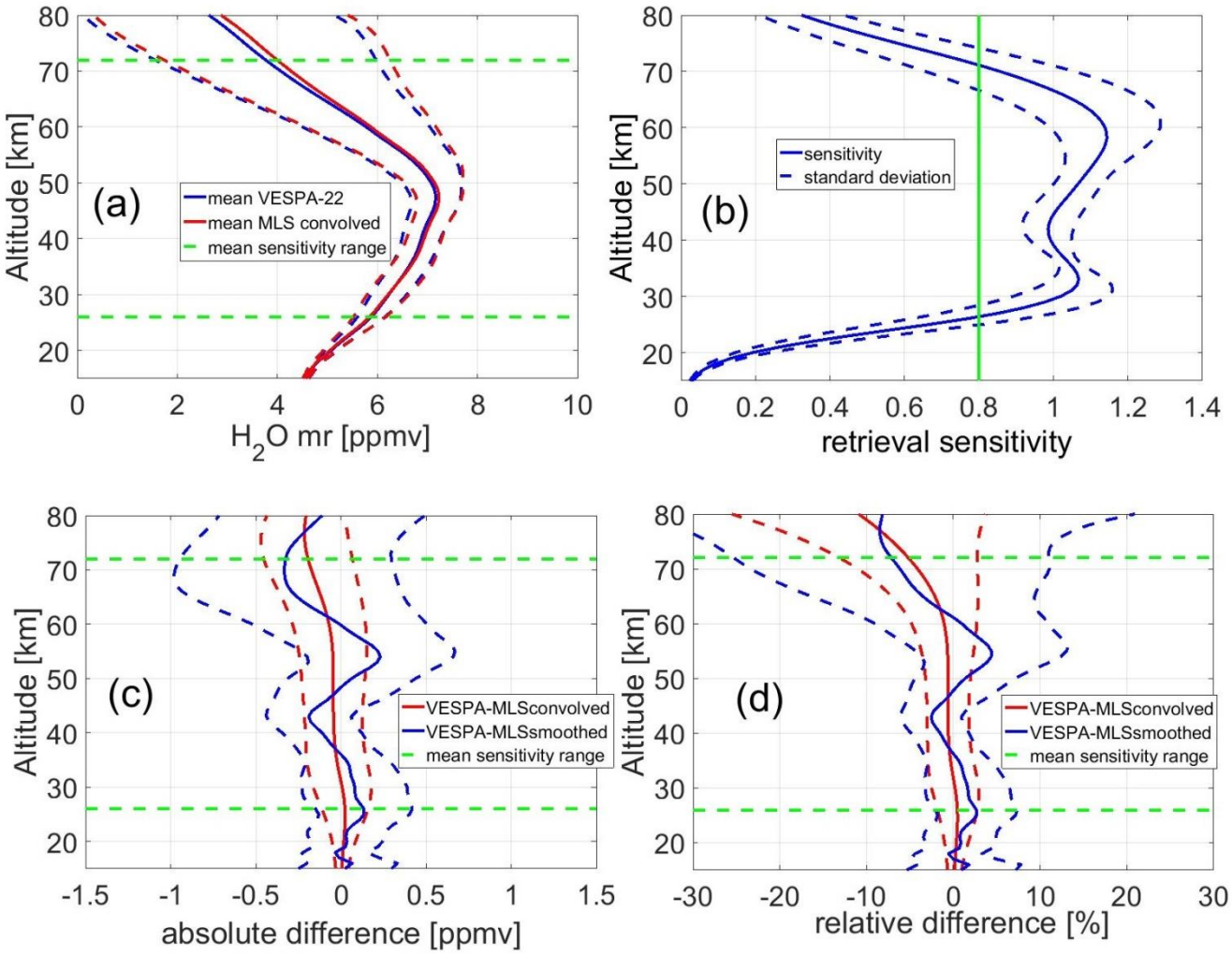

Figure 6.4: (a) VESPA-22 averaged water vapor mixing ratio vertical profile with its standard deviation (blue line and blue dotted lines) and the mean MLS convolved profile with its standard deviation (red line and red dotted lines); (b) the mean retrieval sensitivity profile with its standard deviation (dashed lines); (c) relative and (d) absolute differences vertical profiles between VESPA-22 and MLS convolved mean profiles (VESPA-22 minus MLS, red line) with their standard deviation (red dashed lines), and between VESPA-22 and MLS smoothed mean profiles (VESPA-22 minus MLS, blue line) with their standard deviation (blue dashed lines).

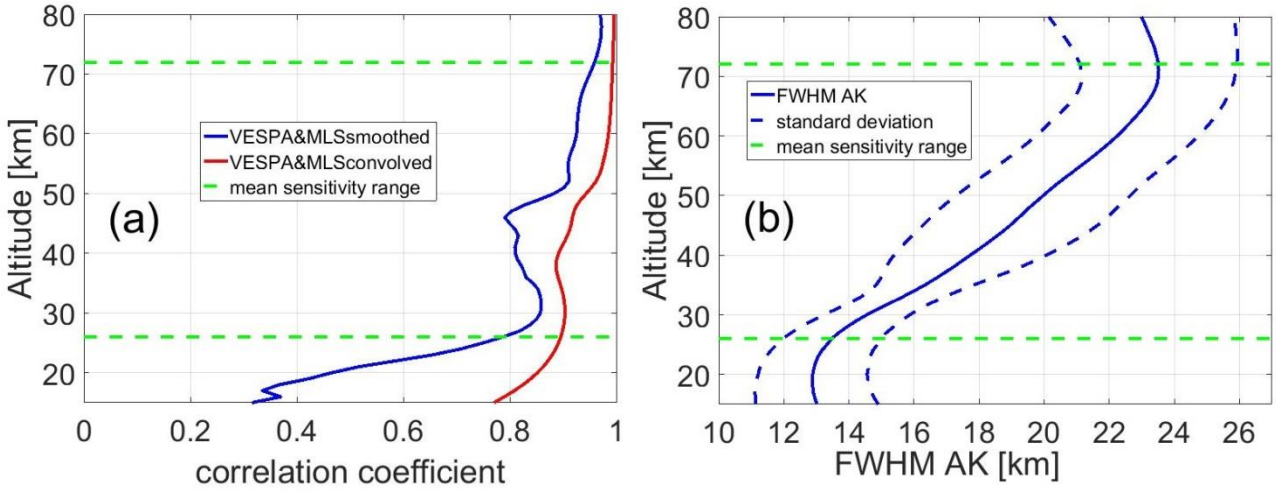

Figure 6.5: (a) vertical profiles of the correlation coefficient between VESPA-22 and MLS convolved profiles (red line), and between VESPA-22 and MLS smoothed profiles (blue line); (b) vertical profile of the mean full width at half maximum of VESPA-22 averaging kernels. The data used for the intercomparison range from 15 July 2016 to 02 July 2017.

In Figure 6.5, panel (a), the vertical profiles of the correlation coefficient between VESPA-22 and MLS convolved data (red), and between VESPA-22 and MLS not convolved data (blue) are shown. The former correlation is about 0.9 or higher over the entire sensitivity range whereas the latter is between 0.8 and 0.96. The correlation between VESPA-22 and MLS high resolution water vapor profiles is useful to illustrate how the two datasets correlate over the extended altitude range from 10 to 80 km.

Figure 6.5, panel (f), shows the vertical profile of mean values of the full width at half maximum (FWHM) of VESPA-22 averaging kernels calculated over the comparison period with its standard deviation (blue dashed lines). The FWHM of the averaging kernels is a measure of the retrieval vertical resolution (Rodgers, 2000). The single profile vertical resolution can vary depending on the level of noise affecting the measured spectrum.

The correlation between the water vapor mixing ratio profiles of VESPA-22 and Aura/MLS can be evaluated also by looking at Figure 6.6, where MLS values at different altitude levels (high resolution in blue and convolved in red) are displayed as a function of the VESPA-22 values at the same altitudes. The green lines represent the linear regression of the MLS convolved vs. VESPA-22 measurements and the yellow lines the ideal case of perfect agreement. Table 6.1 displays the parameters of the linear regressions. The good agreement between VESPA-22 and MLS showed in the previous figures demonstrate the good quality of VESPA-22 measurements in the sensitivity range.

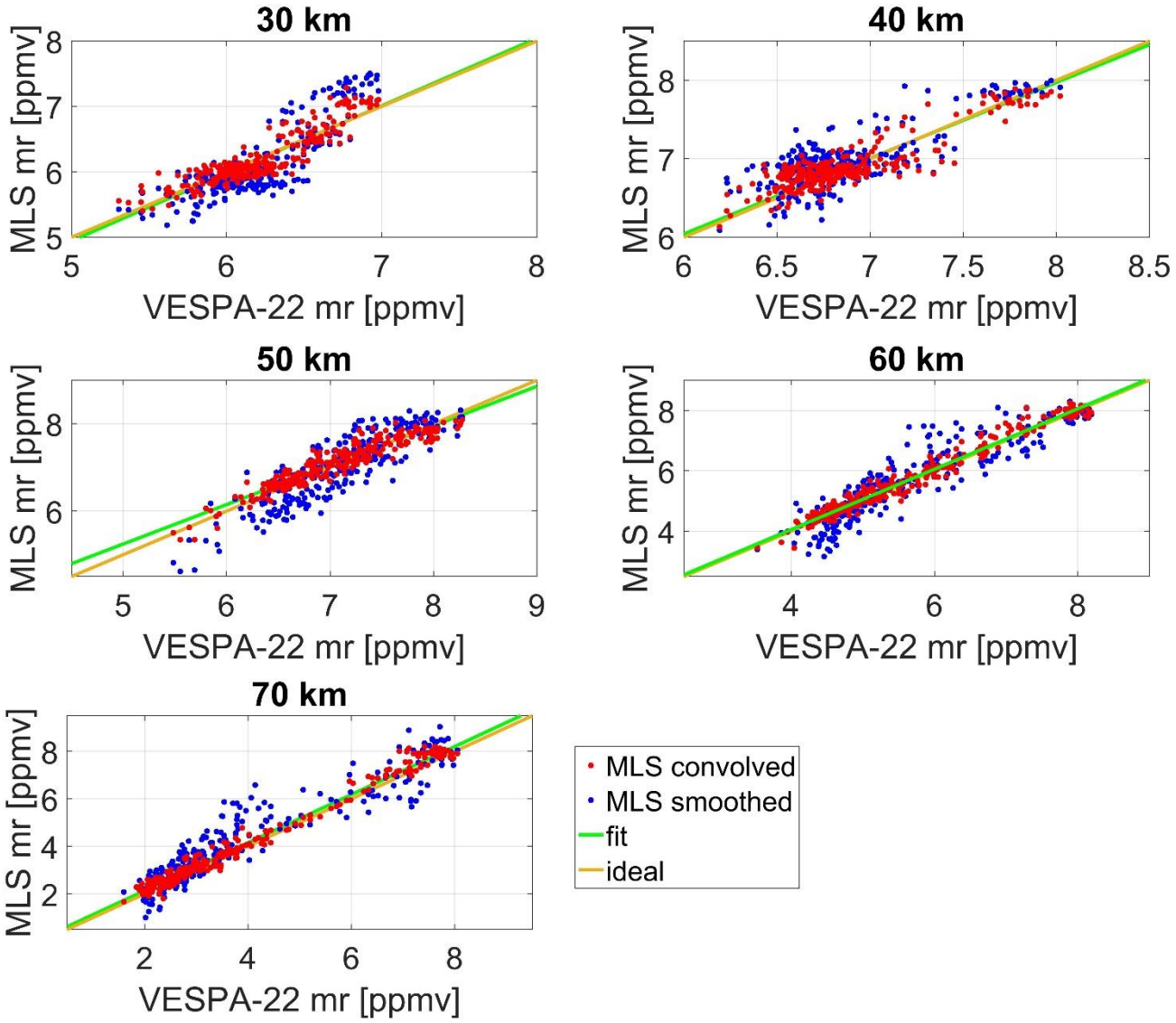

Figure 6.6: Smoothed (blue dots) and convolved (red dots) MLS water vapor mixing ratio values at five different altitudes plotted as a function of the corresponding VESPA-22 measurements obtained during the intercomparison period. The green line shows the linear regression between MLS convolved and VESPA-22 measurements whereas the orange line represents the ideal case of perfect agreement. The data used for the intercomparison range from 15 July 2016 to 02 July 2017.

Table 6.1: Values obtained from the linear regressions between MLS convolved and VESPA-22 measurements at the indicated altitudes.

$y = ax + b$	a	b [ppmv]	R^2
30 km	1.032	-0.214	0.804
35 km	0.965	0.252	0.787
40 km	0.815	1.31	0.789
50 km	0.904	0.725	0.890
60 km	1.000	0.065	0.972
65 km	1.011	0.056	0.980
70 km	1.012	0.109	0.985

In order to show that the convolution operation on the MLS data does not introduce large bias or artificial structures in the MLS convolved profiles in Figure 6.7 is shown the mean difference between MLS convolved profiles and MLS high resolution profiles (panel (a) and (b)) and their correlation coefficient (c).

The mean difference between MLS convolved high resolution datasets is within 0.3 ppmv (about 4%) with a maximum at about 58 km altitude. The correlation coefficient is about 0.9 in the sensitivity range with the exception of the kilometers from 37 to 47 and 25 to 28 where it decreases at about 0.8.

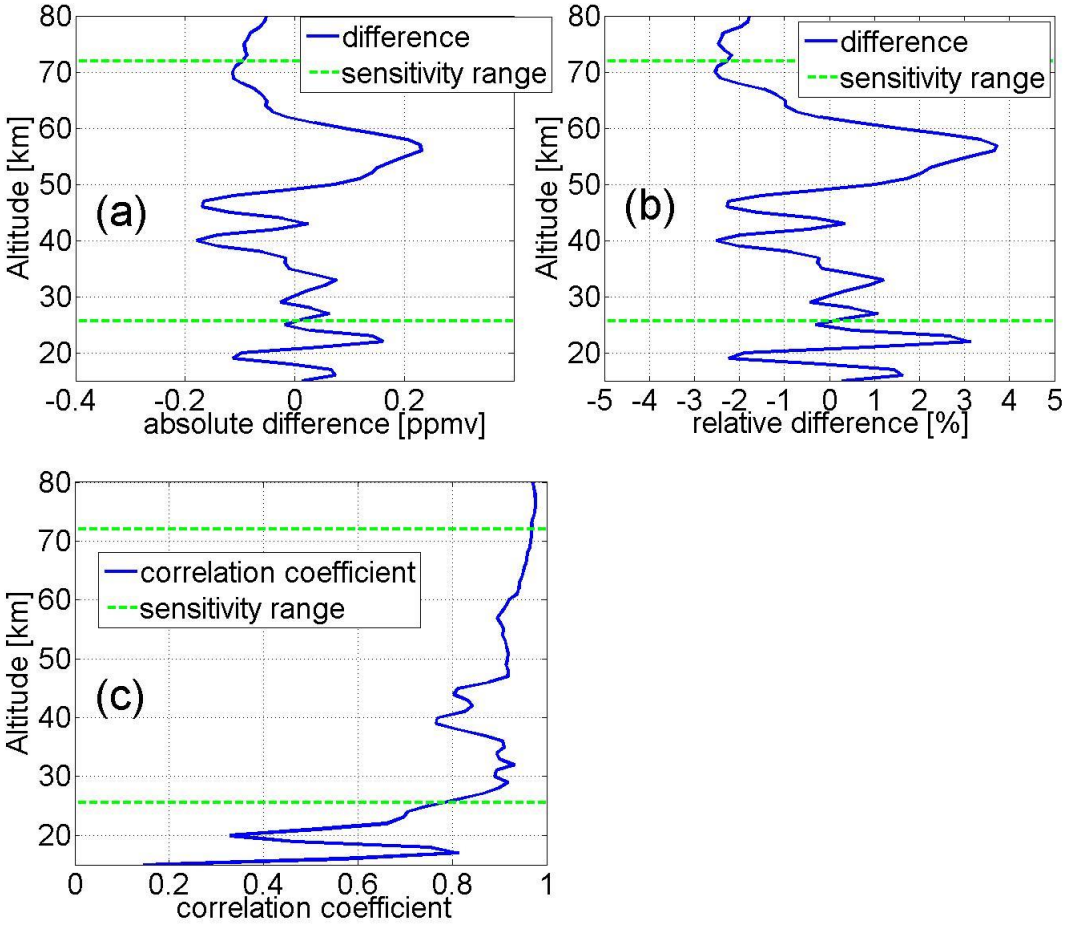

Figure 6.7: The MLS convolved profiles and MLS high-resolution profiles (a) absolute and (b) relative mean difference (MLS convolved minus MLS high resolution) and (c) correlation coefficient.

In Figure 6.8 the mean residual obtained from the collected profiles is displayed. These graphs are useful to understand the intensity and nature of the baseline of VESPA-22 because the measurement noise is largely reduced by the mean operation on a period of about one year. The panel (a) reveals a sine wave baseline of intensity of about 1 mK and a positive maximum of about 6 mK correspondent to the line emission peak. It is important to remember that the central 6 MHz are not smoothed using the 50-channels moving average resulting in a higher noise level. The peak residual, although represents just the 1% of the measurement, can suggest the need for a further improvement to the forward model algorithm in order to better represent the emission collected from the higher mesosphere.

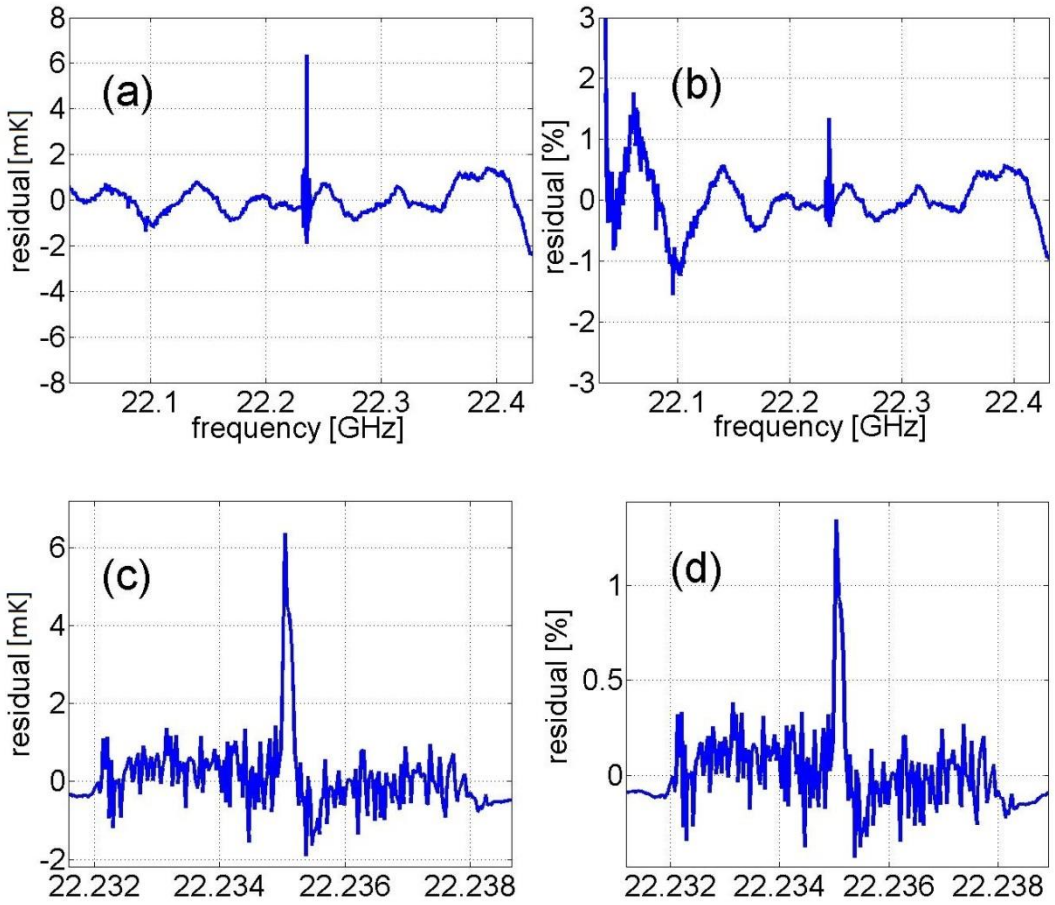

Figure 6.8: the absolute (a) and relative (b) mean residual ($y_{fit} - y$) obtained from measurements collected between July 2016 and July 2017, with a particular of the emission peak (c) and (d).

Figure 6.9 and Figure 6.10 show the time series of water vapor mixing ratio values measured at different altitudes by means of VESPA-22 (blue dots) and obtained by convolved (red dots) and smoothed (yellow dots) MLS datasets. Note that the y-axis range changes from one panel to another in order to better display the water vapor variations. In each panel the apriori profile value as function of time is showed as a green dashed line.

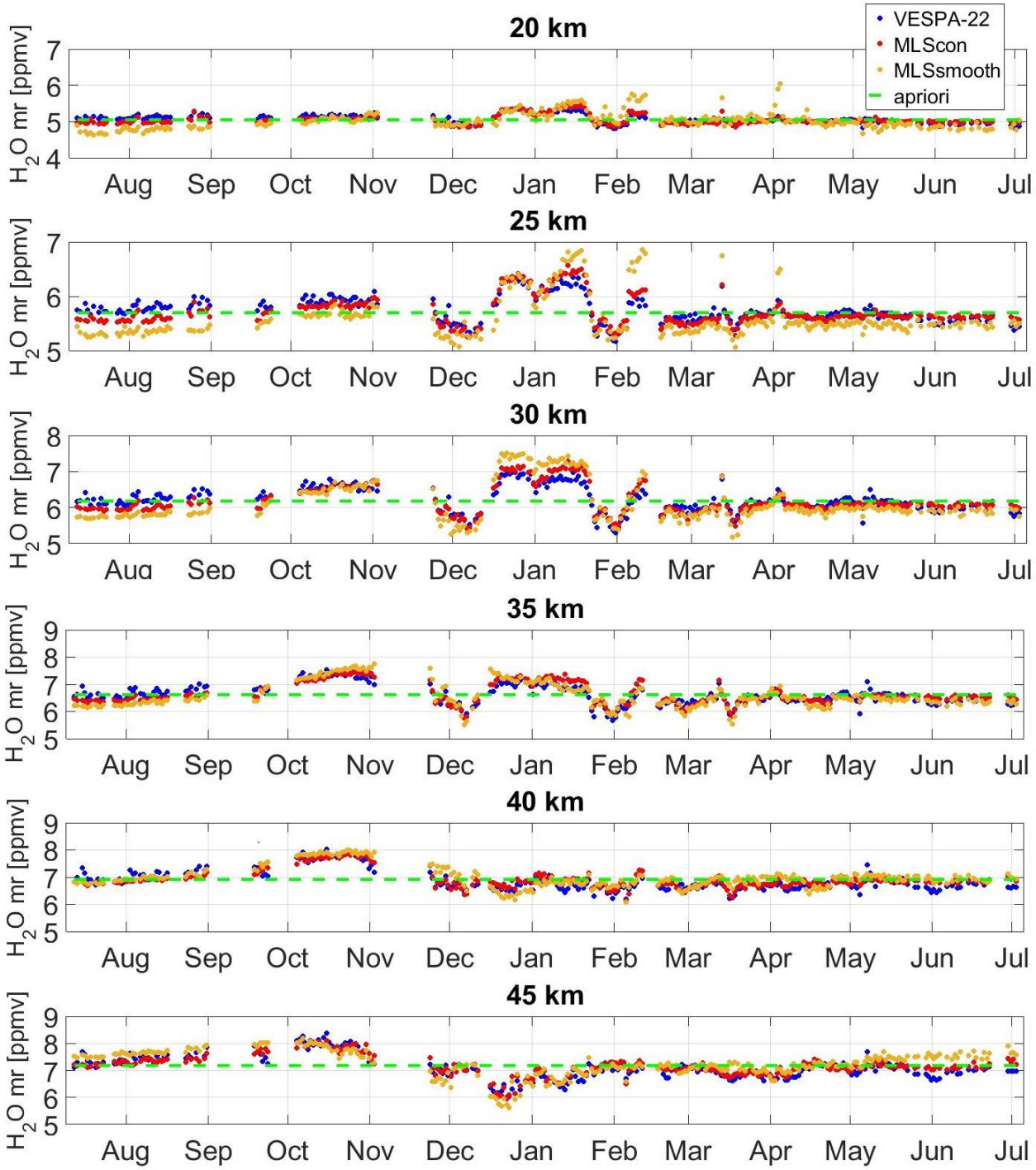

Figure 6.9: Time series at different altitudes (20-45 km) of water vapor mixing ratio values obtained by VESPA-22 measurements (blue) and by MLS convolved (red) and smoothed (yellow) datasets, showed with the apriori profile value at the correspondent altitude (green dashed line).

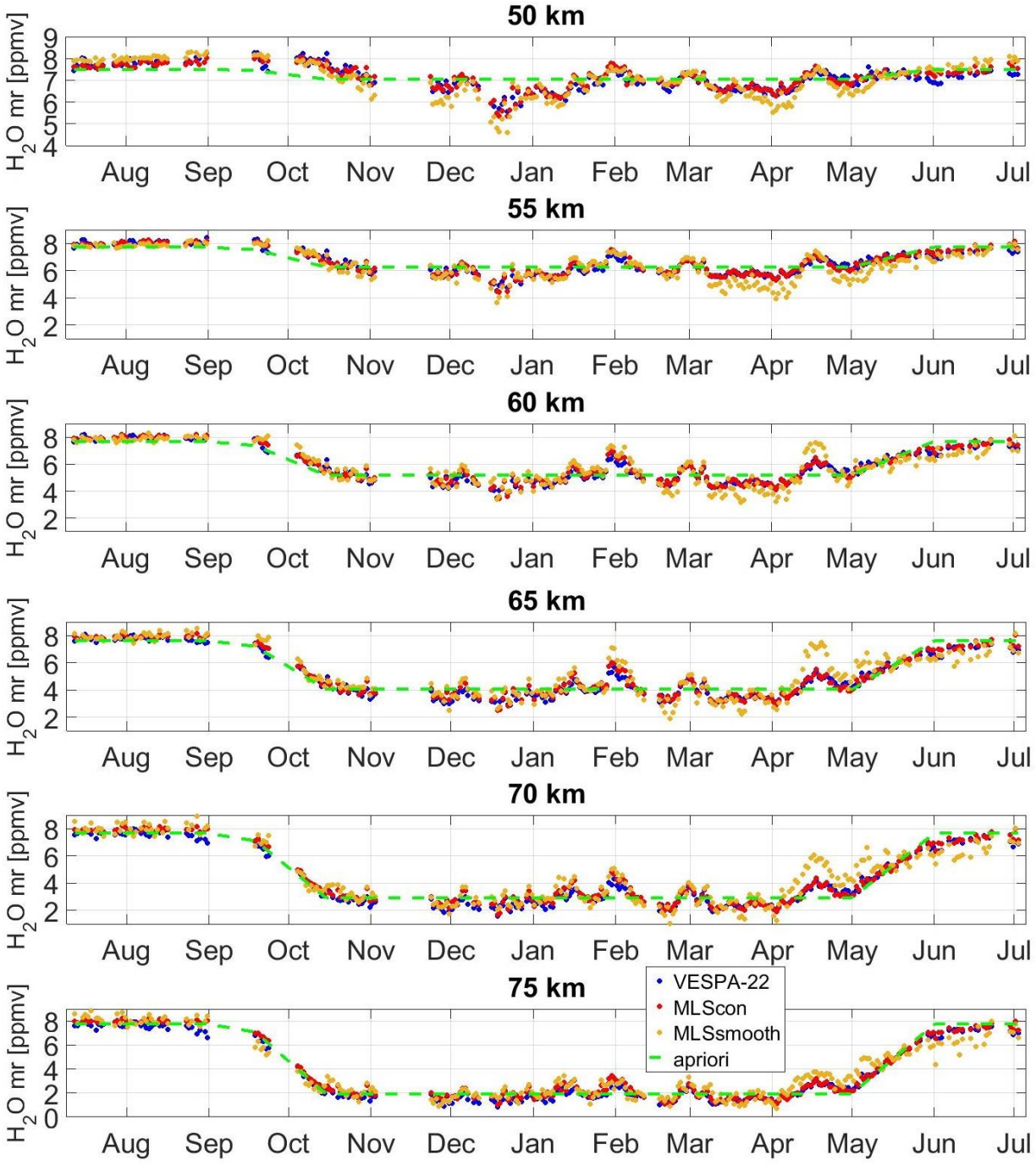

Figure 6.10: Time series at different altitudes (50-75 km) of water vapor mixing ratio values obtained by VESPA-22 measurements (blue) and by MLS convolved (red) and smoothed (yellow) datasets, showed with the apriori profile value at the correspondent altitude (green dashed line).

The time series, again, show a good agreement between VESPA-22 and MLS measurement. The 60, 65 and 70 km time series of both the instruments between April and May show a relative maximum that VESPA-22 underestimate with respect to the MLS smoothed measurements; even the 25 km time series shows a difference between VESPA-22 an MLS smoothed datasets of about 0.5 ppmv during summer 2016. These differences are caused by the reduced sensitivity of VESPA-22 retrieval at these altitudes due to the large sky opacity and poor weather conditions characterizing these periods of the year that constrains the retrieval more strictly to the apriori profile. The winter 25 km time series (when the sensitivity at this altitude is above 0.8) demonstrates the quality of VESPA-22 measurements at the bottom limit of the sensitivity range and the absence of unphysical results introduced by the use of the second order polynomial baseline in the retrieval algorithm.
Figure 6.11 displays the difference time series between VESPA-22 and MLS smoothed datasets for three different altitude levels.

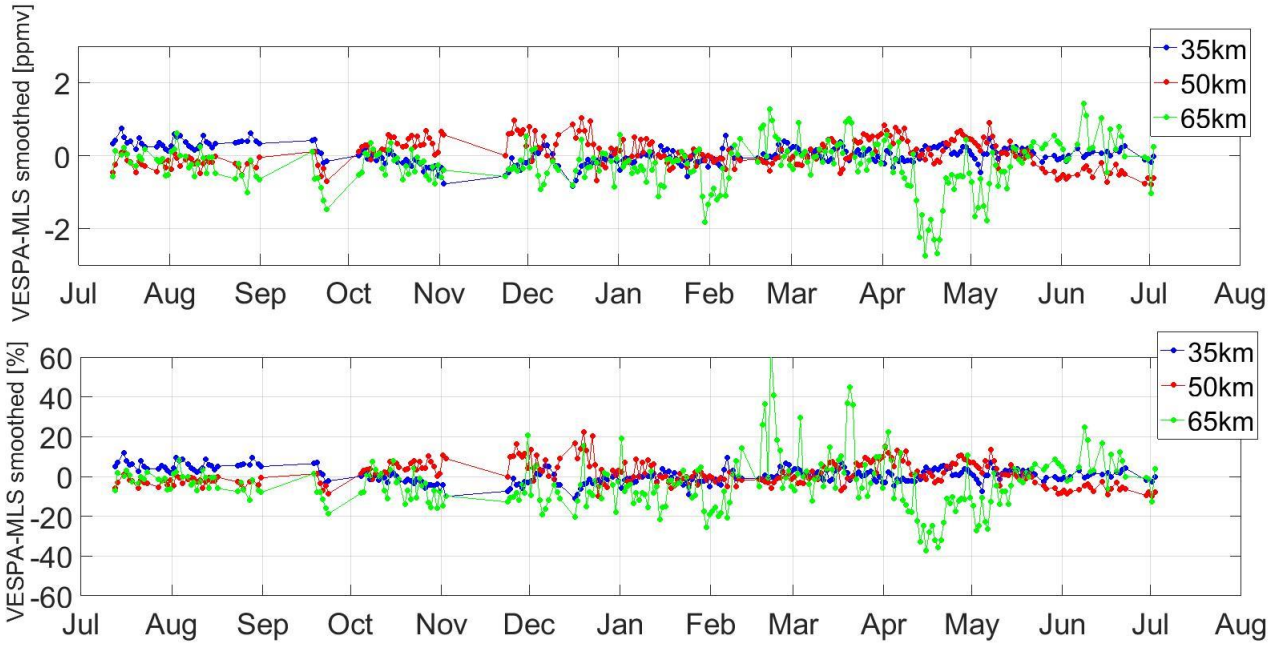

Figure 6.11: Time series of absolute and relative difference VESPA-22 minus MLS convolved dataset for three different altitudes.

In order to provide a more complete, albeit less quantitative, overview of the VESPA-22 and convolved MLS time series, Figure 6.12 shows contour maps of VESPA-22 (in color) and MLS convolved (black line) water vapor profiles. Two white lines represent the altitudes of the extreme of the sensitivity range; the extreme altitude depends both by the season and by the weather condition. In this picture, the large seasonal variability experienced by the water vapor vertical profile can be appreciated. The data collected by both instruments revealed a large scale summer upwelling with the water vapor profiles reaching an absolute maximum in August 2016 at 50 km of height of about 8.3 ppmv (see Section 1.2).

During fall and winter, the maximum of the water vapor mixing ratio profile lowers its altitude to about 30 km in January 2017, due to the air subsidence inside the polar vortex (Section 1.2). The great difference between water vapor profiles in the regions inside and outside of the polar vortex can be noted on the map in the measurement of both instruments. A steep gradient in water vapor mixing ratio is observed between 25 and 40 km altitude in December and in the second half of January, due to the polar vortex that shifts away from Thule for periods of about two weeks. A large variability characterizes the spring, from the second part of March to May. Both instruments also observe the return of the water vapor mixing ratio to pre-winter values in mid-April, possibly indicating the occurrence of the vortex final warming, with the re-establishment of a maximum in the mixing ratio profile at about 50 km altitude.

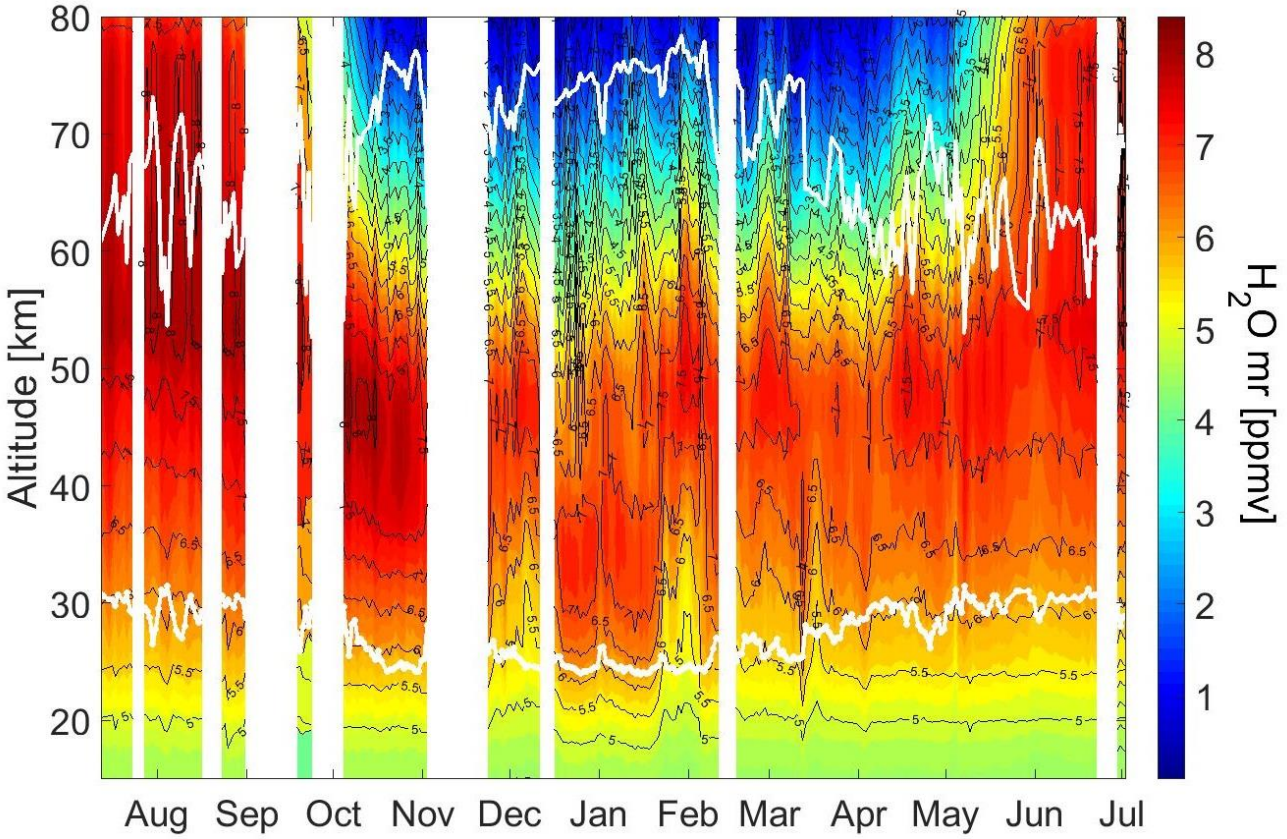

Figure 6.12: A map showing the VESPA-22 retrieved profiles (colored map) compared to MLS convolved profiles (black lines). The blank areas characterize the interruption period longer than three days. The white lines represent the extremes of the sensitivity range.

In order to show a further argument to demonstrate that the convolution operation does not introduce artificial structures on MLS dataset but is just a "smoothing" process, the Figure 6.13 offers a qualitative comparison between VESPA-22 dataset and MLS high resolution dataset. In order to take into account the higher MLS vertical resolution, 3-days moving averages is

applied on both dataset. Observing the two maps of this section it can be seen as they present the same structures, as for example the step gradient in the second part of January and the higher variability in spring.

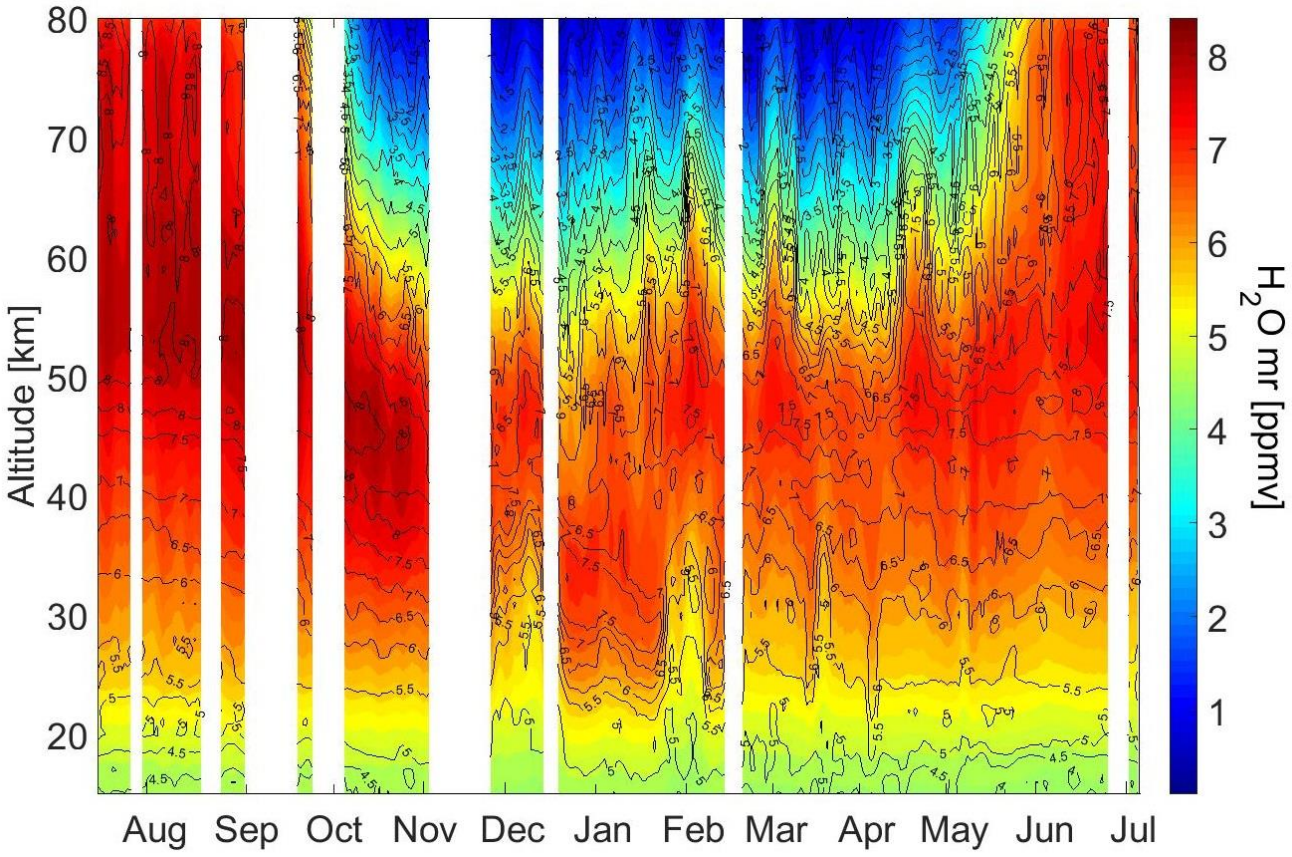

Figure 6.13: A map composed using 3 days moving average of the VESPA-22 (color) and MLS high resolution (black contour lines) measurements. The blank areas characterize the interruption period longer than three days.

6.3 The polar vortex and the VESPA-22 measurements

The polar vortex formation started at the end of September; the vortex lays above Thule region until the second part of February, when it moved to the Siberian region. The evolution of the vortex is shown by the maps of water vapor mixing ratio on the Northern hemisphere at 850 K of potential temperature measured by MLS, reported in Figure 6.15.

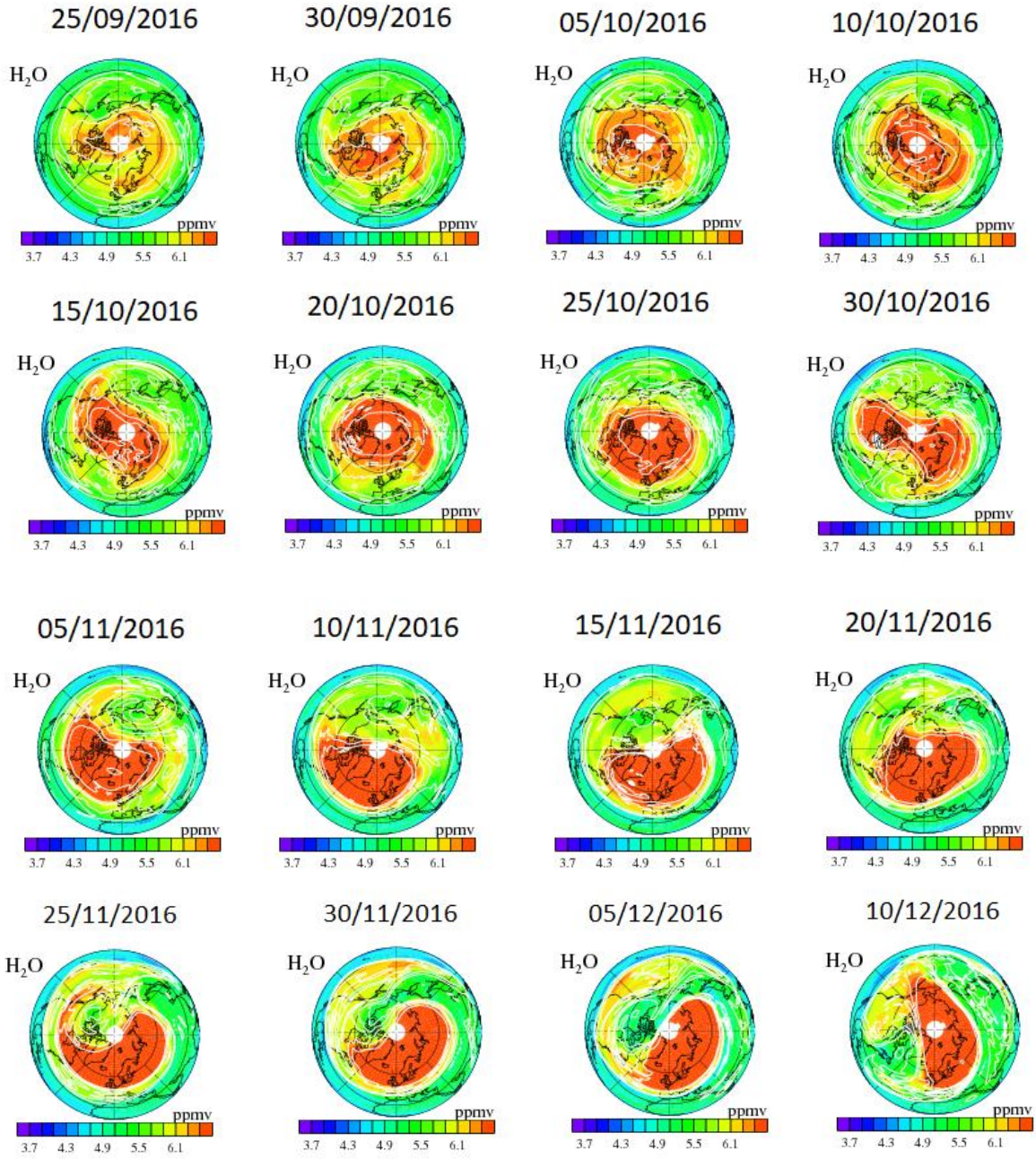

Figure 6.14: The maps of water vapor mixing ratio at 850 K of potential temperature measured by MLS measurements (https://mls.jpl.nasa.gov/data/gallery.php).

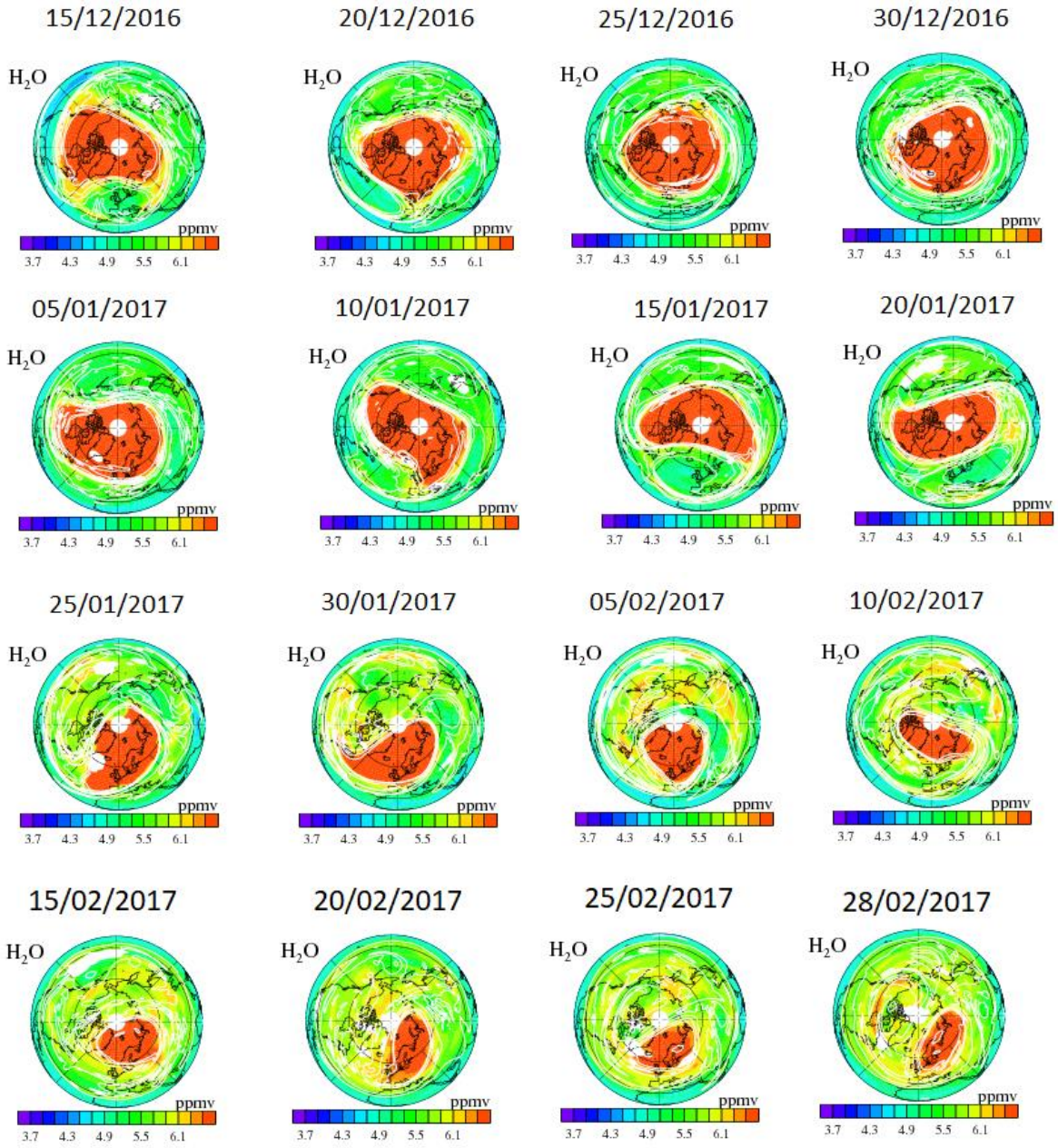

Figure 6.15: The maps of water vapor mixing ratio at 850 K of potential temperature measured by MLS measurements (https://mls.jpl.nasa.gov/data/gallery.php).

The potential temperature is the temperature that the parcel would acquire if adiabatically brought to a standard reference pressure. This quantity can be used to characterize the different altitude levels and is computed according to

$$\theta_T = T\left(\frac{P_0}{P}\right)^{\frac{R}{c_p}}, \tag{6.2}$$

where T and P are respectively the air pressure and temperature, P_0 is the reference pressure, R and c_p are the air gas constant and specific heat at constant pressure.

The air inside the polar vortex is characterized by a high amount of water vapor at the 850 K potential temperature level due to the subsidence; therefore, the steep gradient in the water vapor concentration shown in the maps can identify the vortex edge. The great difference between water vapor profiles in the regions inside and outside the polar vortex can be noted in Figure 6.12 in the measurement of both instruments. A steep gradient in water vapor mixing ratio is observed between 25 and 40 km altitude in December and in the second half of January, due to the polar vortex that shifts away from Thule for periods of about two weeks (see 5/12, 10/12 and 30/01 maps in Figure 6.14 and Figure 6.15).

The relation between the polar vortex edge position and the steep gradients in the VESPA-22 measurements can be verified also observing the evolution of the MLS temperature profiles measured during winter shown in Figure 6.16.

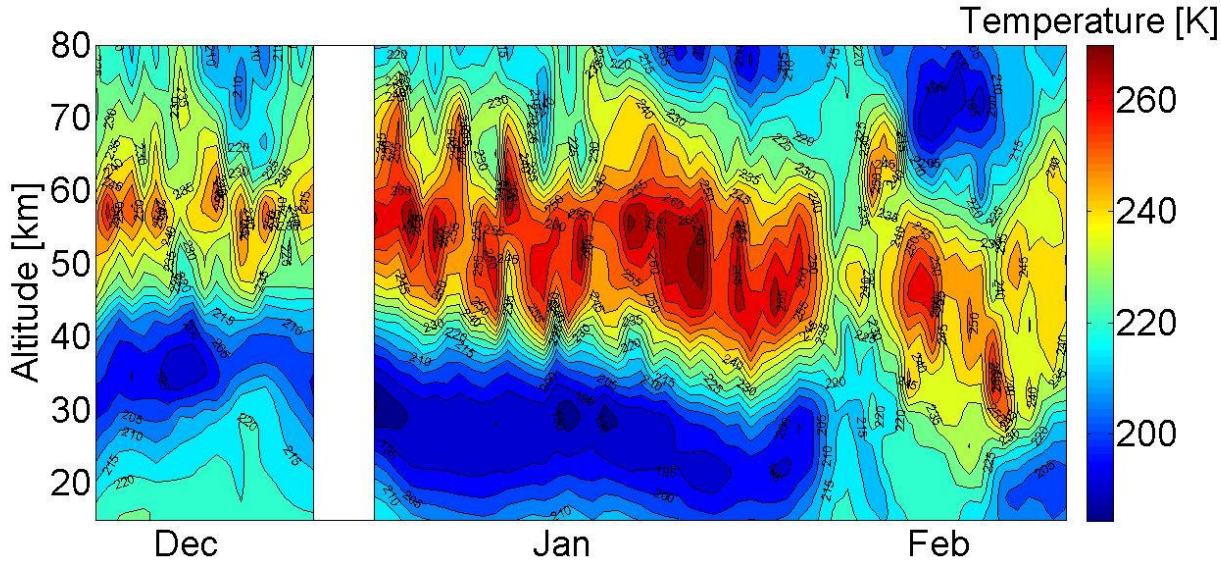

Figure 6.16: The temperature profiles measured by MLS in correspondence with VESPA-22 winter measurements.

A stable polar vortex lays above Thule from the second part of December to the last week of January, determining the minimum of 190 K in stratosphere at about 30 km. The polar vortex shifting away from Thule provokes the temperature rises measured by MLS in December and last part of January. The polar vortex returns above the observation point during the first part of February, then moved to Siberian region.

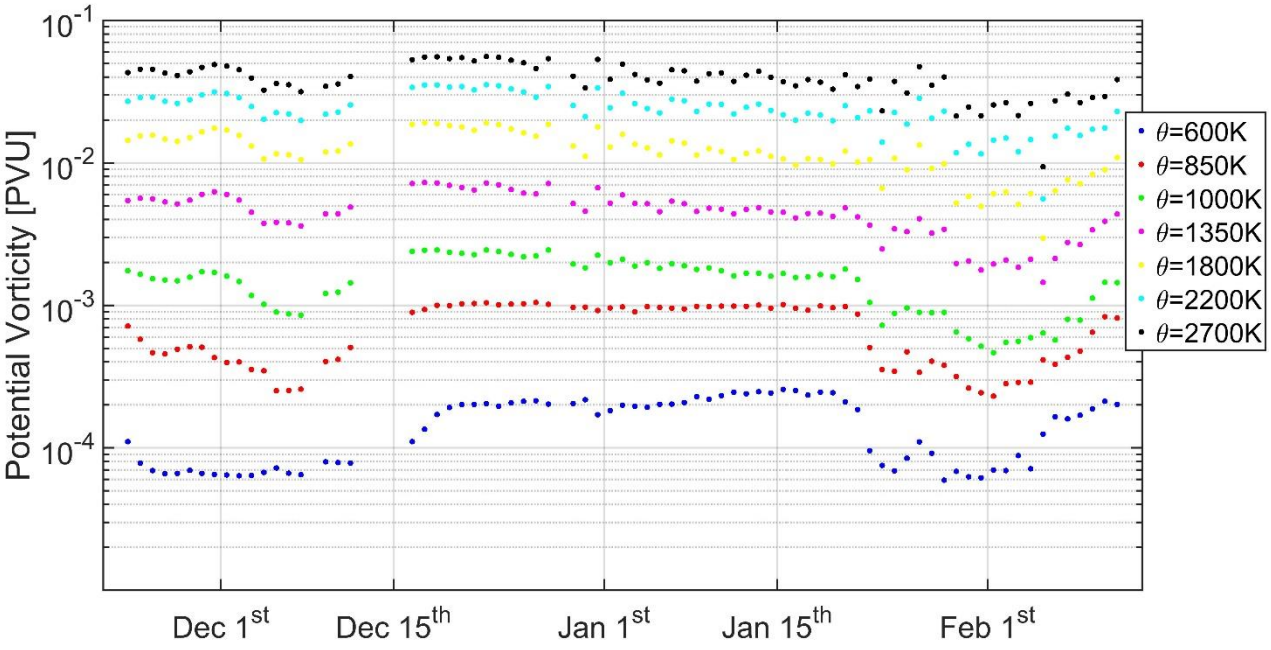

Figure 6.17: The potential vorticity over the observation point versus time at different potential temperature levels (from Goddard Space Center Automailer).

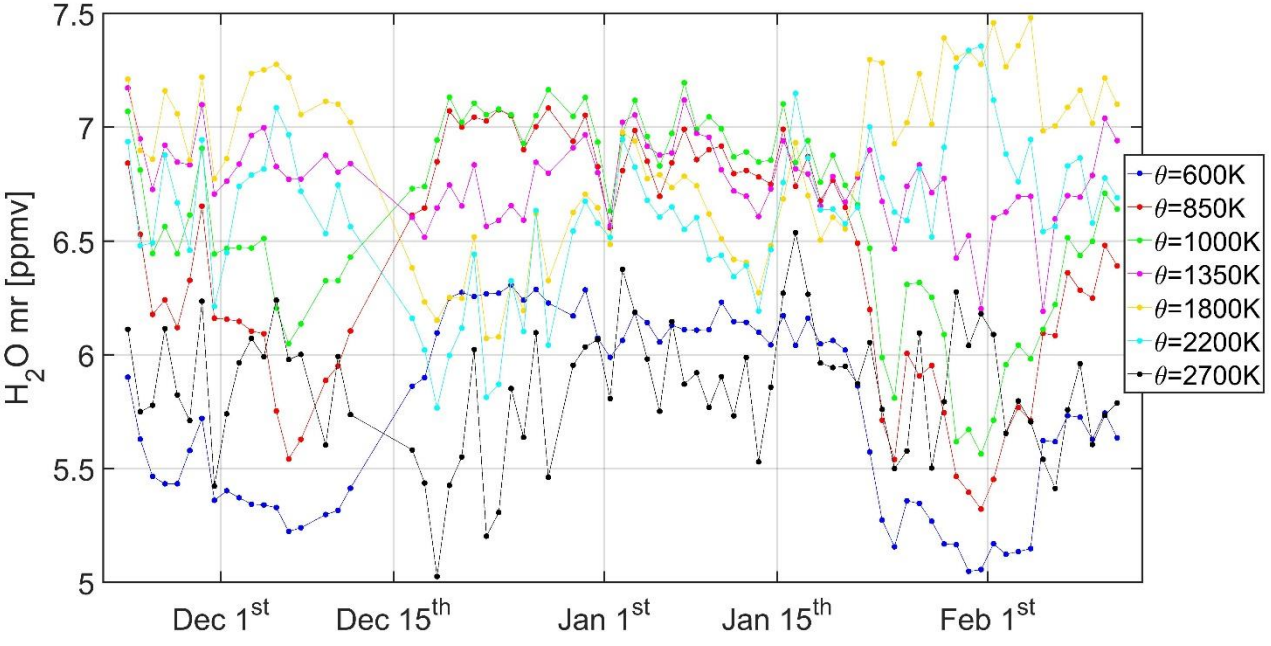

Figure 6.18: The water vapor vmr measured by VESPA-22 versus time at different potential temperature levels.

Figure 6.17 and Figure 6.18 show respectively the potential vorticity over the observation point during winter (data from Goddard Space Center Automailer, Lait et al., 2005) and the water vapor vmr measured by VESPA-22 versus time at different altitude levels, expressed in terms of potential temperature. The levels of potential temperature shown are referred to about 24, 31, 35, 40, 45, 50 and 55 km altitude.

The air inside of the polar vortex is characterized by a higher value of potential vorticity with respect to the mid-latitude so it is useful to describe the vortex development (Di Biagio et al 2010). The potential vorticity can be computed according to:

$$PV = \frac{1}{\rho_{air}} \boldsymbol{\zeta}^{\mathbf{a}} \cdot \nabla \theta_T \ , \tag{6.3}$$

where ρ_{air} is the air density ζ^a is the absolute vorticity and θ_T is the potential temperature.

According to what seen in Figure 6.15 and Figure 6.16 the period from 15 December 2016 to 22 January 2017 is characterized by high value of potential vorticity and water vapor vmr in the mid stratosphere because of the subsidence effect. The step gradient characterizing the vortex edge is present on the 600 K, 850 K and 1000 K time series (24, 31, 35 km). The high stratosphere and the lower mesosphere time series (1800, 2200 and 2700 K) show a decrease during the same period caused by the air from upper region moving to the stratosphere due to the subsidence inside the vortex. Table 6.2 shows the correlation coefficients computed between the potential vorticity and water vapor vmr time series shown in the previous figures. As described a strong positive correlation characterizes the mid-stratospheric time series and a negative correlation the high stratosphere and mesosphere. The 1350 K level (40 km) don't seem to be influenced by the polar vortex passage, maybe due to the small gradient between the air inside and outside the vortex at this altitude with respect to the natural daily water vapor fluctuations (see Figure 6.12 and Figure 6.18).

Table 6.2: The correlation coefficient between VESPA-22 water vapor vmr measurements and the potential vorticity over the observation point (from Goddard Space Center Automailer) at different potential temperature levels.

Potential temperature [K]	Approximate altitude [km]	Correlation coefficient
600	24	0.891
850	31	0.937
1000	35	0.877
1350	40	0.287
1800	45	-0.638
2200	50	-0.667
2700	55	-0.231

Figure 6.19 and Figure 6.20 show the altitude of some levels of vmr in the VESPA-22 retrieved profiles. As suggested by Di Biagio et al. (2010), during the periods in which the polar vortex prevents intrusions from mid-latitude air, these figures

allow recognizing the subsidence of air masses. The dots and stars in Figure 6.19 represent the vmr levels respectively below and above the profile maximum. For certain measurements the dot and the star are coincident; this indicates that the indicated vmr is the profile maximum for that measurement. Figure 6.20 displays the time series of the altitudes of the different vmr levels with their uncertainties. The uncertainties have been calculated by half of the differences between the altitudes associated to the profiles $\hat{x} + \sigma$ and $\hat{x} - \sigma$, where $\hat{x}$ is the VESPA-22 measured profile and σ the profile uncertainty (see Chapter 5). A downward movement characterizes the autumn and winter, interrupted by the vortex shifting away from Thule in December and January. The steep gradients identified in December and January can be recognized by the peaks in the altitude time series. Examining individually the stratosphere during the months of October and January does not reveal a recognizable tendency due to the uncertainty afflicting the altitudes time-series; these are constant within their uncertainty, although the altitudes of the vmr levels are lower in January, with respect to October. It is not possible to provide a good estimate of the downward velocity in stratosphere merging together the information of the period October-January due to the possible air mixing caused by the vortex shifting on December. A downward tendency characterizes the mesospheric air in October. The vertical velocity can be estimated by means of a linear fit.

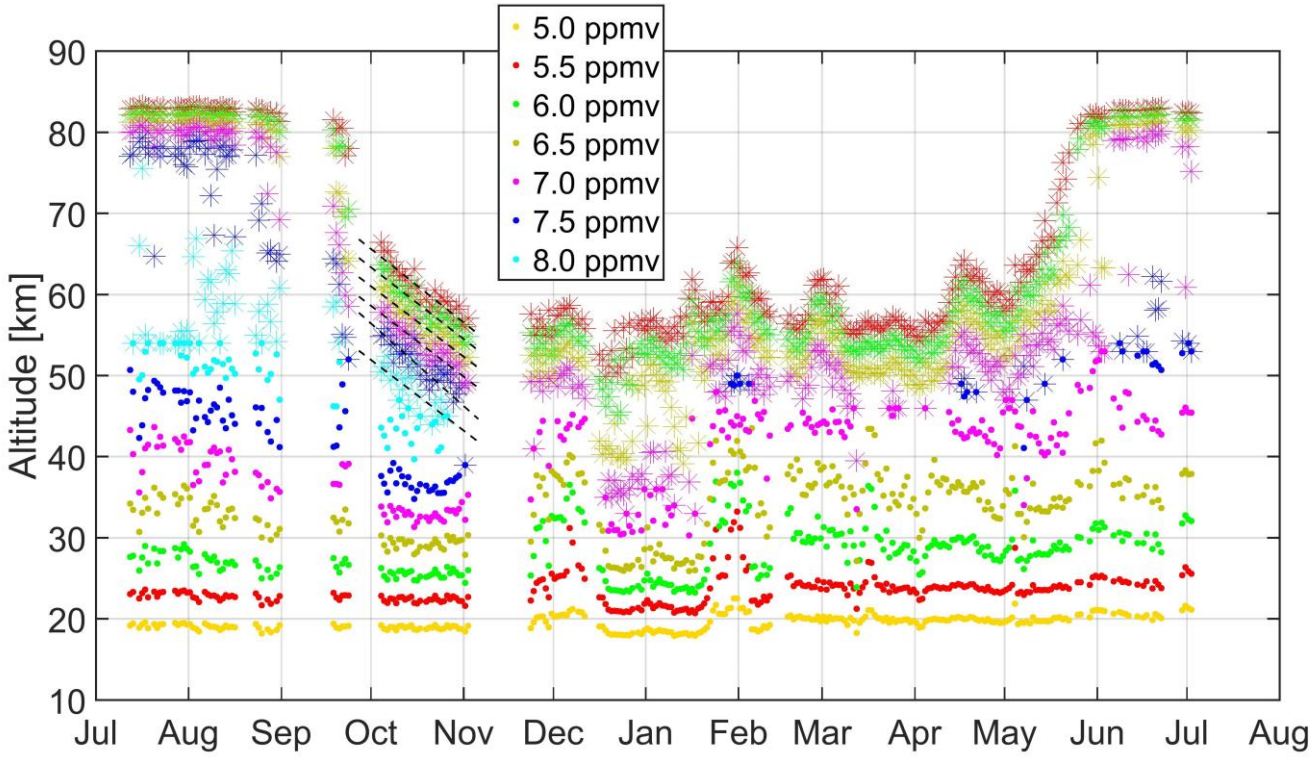

Figure 6.19: The altitude of different levels of vmr in the VESPA-22 water vapor retrieved profiles. The dots and the stars represent the altitude of vmr levels below and above the profile maximum, respectively. The black dashed lines show the fit results for the different vmr levels.

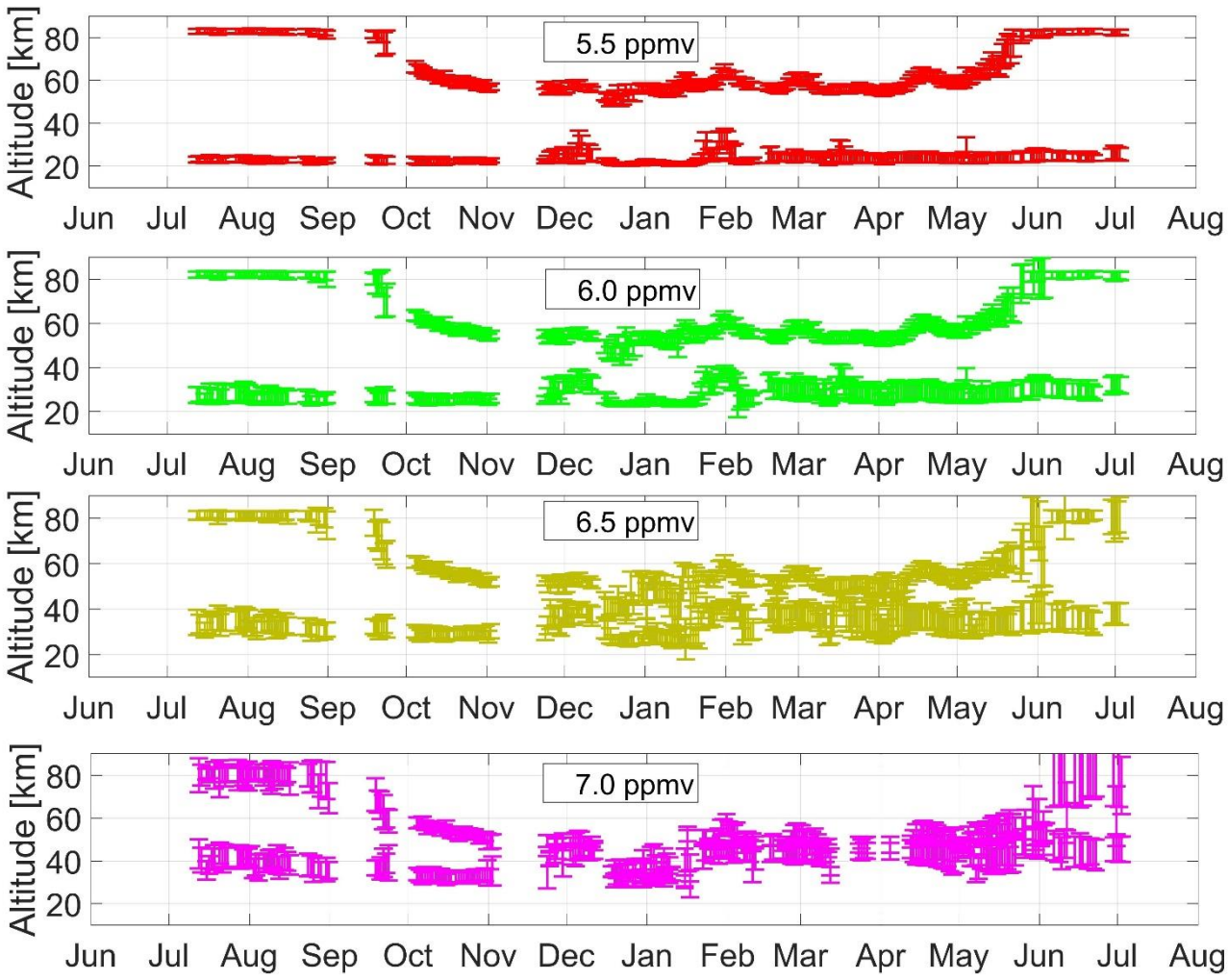

Figure 6.20: the altitude of some of the different levels of vmr in the VESPA-22 water vapor retrieved profiles and their uncertainties, represented by the error bars.

The fit results for the different vmr levels are reported in Table 6.3. The vertical velocity uncertainty is calculated as the half of the difference between the maximum and minimum values of the angular coefficient of the linear fits within the altitude uncertainty. Defined $h(t_i)$ the altitude time-series and $\delta(t_i)$ the altitude uncertainty time-series, the uncertainty is therefore computed by means of the difference between the angular coefficients of the $h(t_i) \pm p(t_i)\delta(t_i)$ fits, where $p(t_i)$ is a linear function which is equal to -1 for the first measurement of the time-series and 1 for the last one. From December to the end of March the mesospheric air does not show evident tendencies. The late spring is characterized by the disappearing of the polar vortex with the intrusions of mid-latitude air.

Table 6.3: The calculated vertical velocity of the air characterized by different vmr levels during autumn and winter with the calculated uncertainty, the R^2 values of the different fits and the altitude calculated for the vmr levels on the 04/10/2016.

vmr level	Vertical velocity [km/day]	R^2	Altitude(04/10/2016) [km]
5.5 ppmv (above maximum)	-0.29±0.13	0.85	66±2
6.0 ppmv (above maximum)	-0.29±0.13	0.86	64±3
6.5 ppmv (above maximum)	-0.28±0.13	0.86	61±3
7.0 ppmv (above maximum)	-0.28±0.17	0.85	58±3
7.5 ppmv (above maximum)	-0.33±0.21	0.68	55±3
8.0 ppmv (above maximum)	-0.28±0.19	0.60	50±3

6.4 Measurements monthly analysis

Given the large variability that stratospheric water vapor mixing ratio profiles can experience in Polar Regions, in particular during winter and spring, Figure 6.22 and Figure 6.22 are meant to illustrate the variations of VESPA-22 averaged mixing ratio profiles over the twelve months of reported measurements, and how the difference between VESPA-22 and MLS profiles and the retrieval characteristics varies from month to month. Figure 6.21, panel a, shows the monthly average profiles collected by VESPA-22. The maximum of mixing ratio in summer can be noticed in panel a, decreasing over time and lowering its altitude in winter due to the polar vortex. The inverse process occurs in spring at the disappearing of the polar vortex with the large scale upwelling characterizing the summer. Panel (b) displays the monthly mean of the sensitivity during the different months. The noise increases in summer and spring due to the increased amount of water vapor and atmospheric opacity and unstable meteorological conditions. Therefore, the sensitivity range during these seasons is reduced with a minimum reached in spring 2017, months characterized by prolonged periods of bad weather. In these months, the sensitivity range is from about 30 to 65 km. In winter the dryer atmosphere and more stable weather conditions produce cleaner spectra. The maximum sensitivity is reached in January 2017, with a sensitivity range from 24 to 75 km. Panel (c) and (d) show the absolute and relative difference with the monthly average of convolved MLS profiles. In stratosphere and lower mesosphere the differences are within 0.25 ppmv (4%). In the upper mesosphere the absolute value of the difference increases, reaching about -0.4 ppmv at 68 km in September and -0.35 ppmv at 75 km in January. The extreme low values of water vapor mixing ratio in winter mesosphere lead an increment of the absolute value of the relative difference of the winter months that reaches a maximum of -14% at 75 km, in January. These larger differences are not present in the summer, due to the higher values of water vapor concentration reached in this period. The summer months (July-September 2016) and the month of January show relative maxima in the absolute value of the difference in stratosphere that reaches +0.25 ppmv

(+4%) in August at about 30 km of altitude and -0.25 (-4%) at 32 km of altitude in January. A bias of about -10% between MLS and measurements of other instruments is documented in the literature as in the relation produced by The SPARC Data Initiative of 2017 (SPARC, 2017) and in Read et al. (2007).

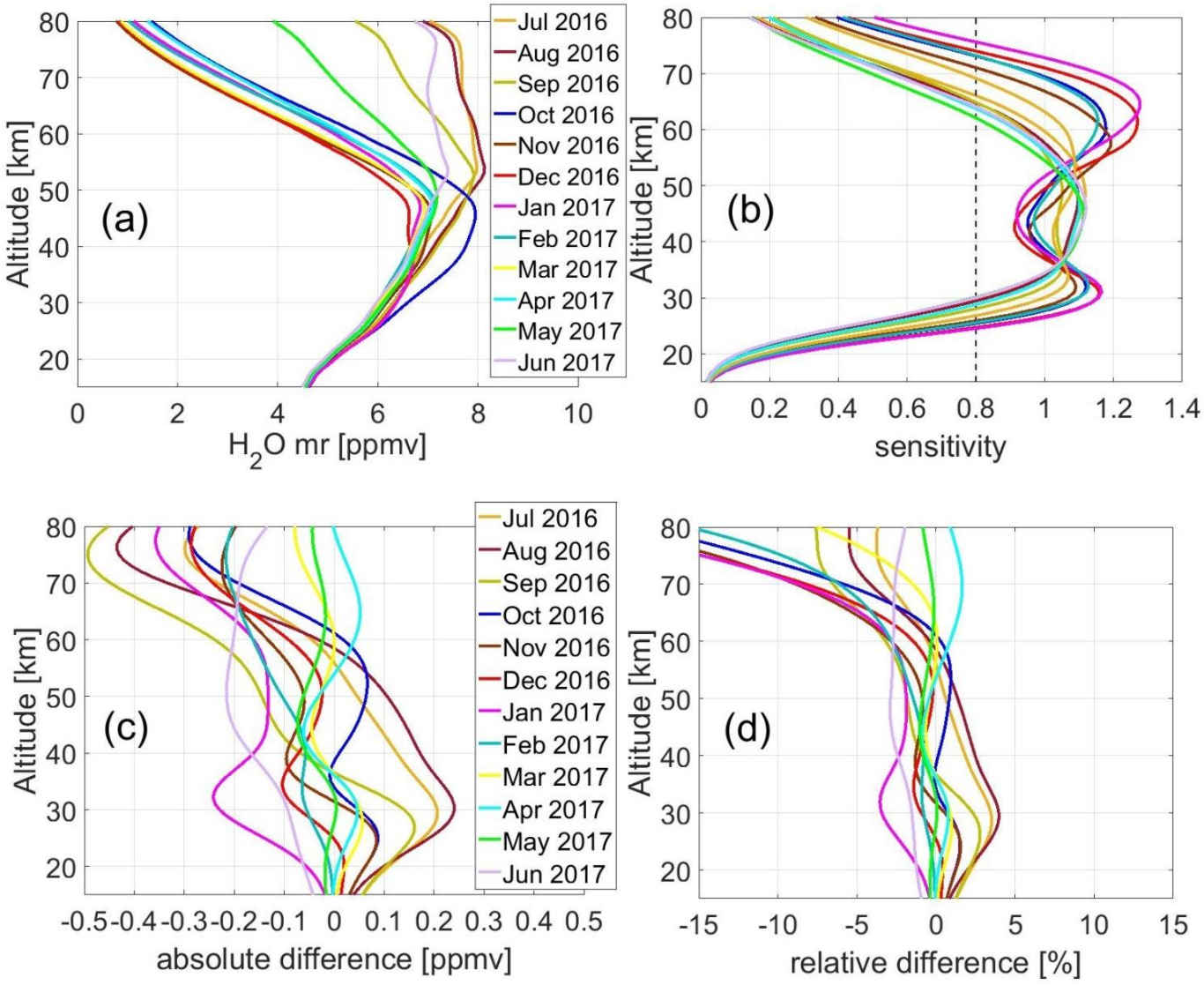

Figure 6.21: (a) Monthly averages of the VESPA-22 water vapor mixing ratio profiles, (b) monthly means of the sensitivity range of the retrieved profiles. Panels (c) and (d): absolute and relative monthly means of the difference between VESPA-22 and MLS convolved datasets (VESPA-22 minus MLS).

Figure 6.22 panels (a) and (b), displays the difference between VESPA-22 retrievals and the MLS smoothed dataset. The difference is within 0.6 ppmv, about 10% in the stratosphere and lower mesosphere, with the exceptions of peaks in March and April at 57 km where the relative difference reaches 12%. Even in the upper mesosphere the relative differences are

within 10% in the sensitivity range, with the exception of the months of April and January, where the absolute value of the differences reaches maxima of respectively -14% (-0.7 ppmv) at 65 km and -14% (-0.4 ppmv) at 75 km, the upper limits of the sensitivity range for those months. The January peak in the relative difference is due to the extreme low values of water vapor mixing ratio in winter mesosphere. Panel (c) displays the nominal altitude of the AKs versus the peak altitudes: according to what stated in Section 4.5, there is not a strong variation during the different months. Panel (d) displays the AKs' FWHM. Both these parameters depend on the noise level, with worse values during summer and spring and better ones in winter.

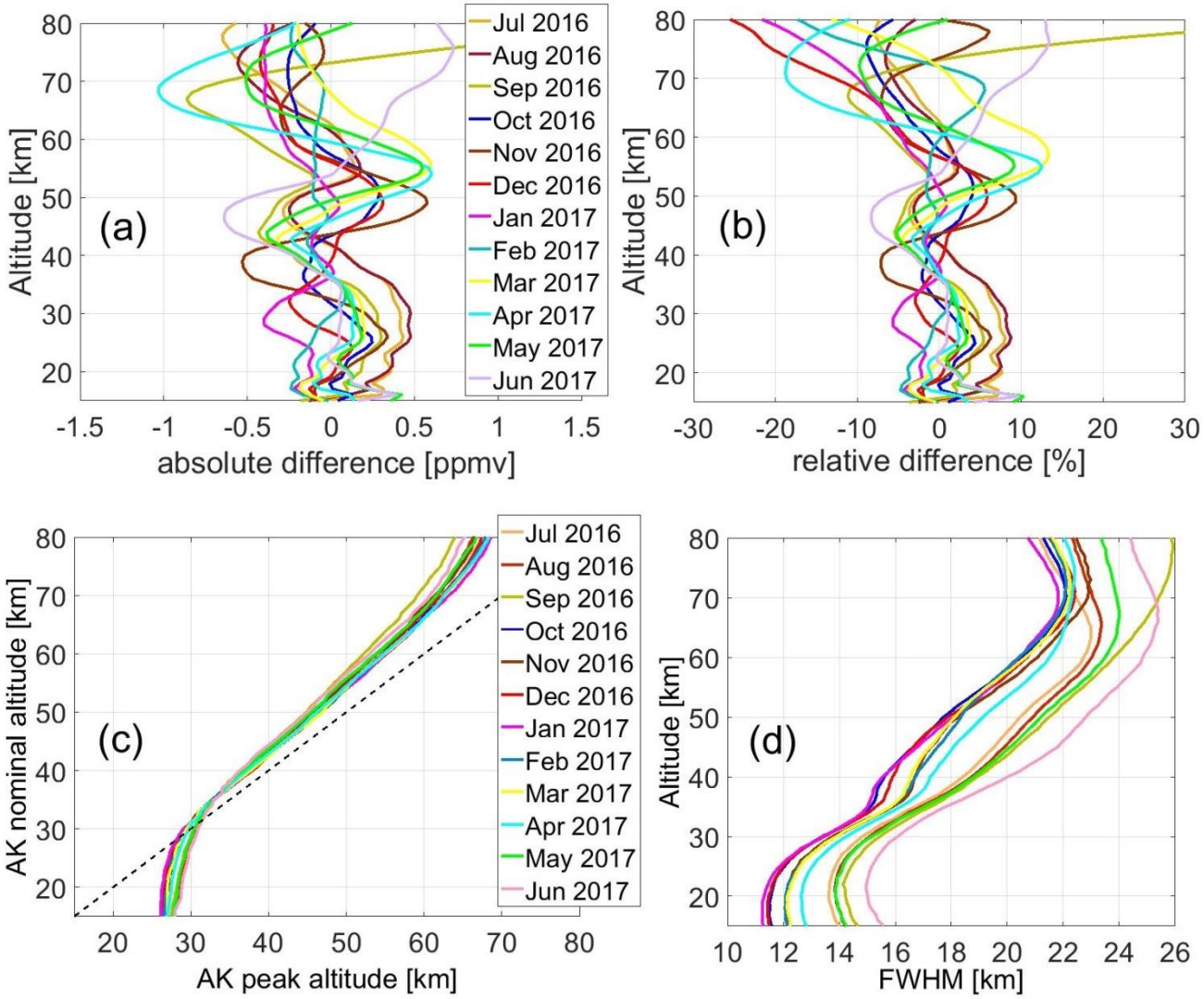

Figure 6.22: Panels (a) and (b) display absolute and relative monthly means of the difference between VESPA-22 and MLS smoothed datasets. Panels (h) and (g) display monthly means of the peak altitude versus their nominal altitude and the FWHM of the AKs.

The noise level can be argued observing Figure 6.23 in which the monthly means of the residual are displayed. In particular, stronger oscillations are present on spectra collected in August and September 2016 and June 2017. The higher residuals are caused by the unstable weather conditions characterizing these months and water molecules deposition on the observing windows, increasing their reflectivity.

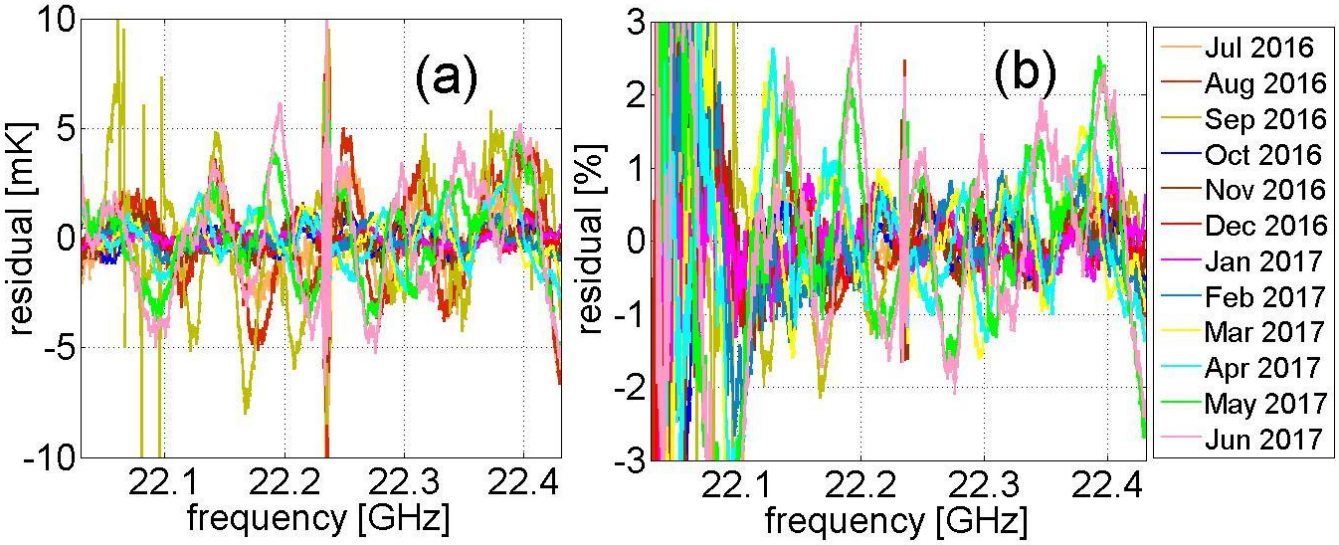

Figure 6.23: The absolute (a) and relative (b) monthly means of the VESPA-22 residual $\mathbf{y}_{fit} - \mathbf{y}$.

Figure 6.24 shows the absolute and relative difference between MLS convolved and MLS high-resolution datasets. The differences are within 0.8 ppmv (10%) in the stratosphere and lower mesosphere in all the examined months with the exceptions peaks at 38 km in November 2016 and at 58 km in spring. The difference increases above 65 km where the retrieval sensitivity decreases.

The monthly variability can be quantified through the standard deviation of the retrieved profiles, shown in Figure 6.25. The upper mesosphere is characterized by a higher variability; the standard deviation is higher than the VESPA-22 uncertainty characterizing retrieved profiles in this layer (Figure 5.4) so this cannot be ascribed uniquely to a loss of precision of the instrument, but it is related to the air mass dynamics. The panel (b) reveals that the summer months are characterized by a lower relative variability with respect to other periods of the year. The relative standard deviation maxima measured in December and January at about 30 km of altitude are caused by the gradients measured in the stratosphere in these months caused by the movements of polar vortex with respect to Thule (see Figure 6.12).

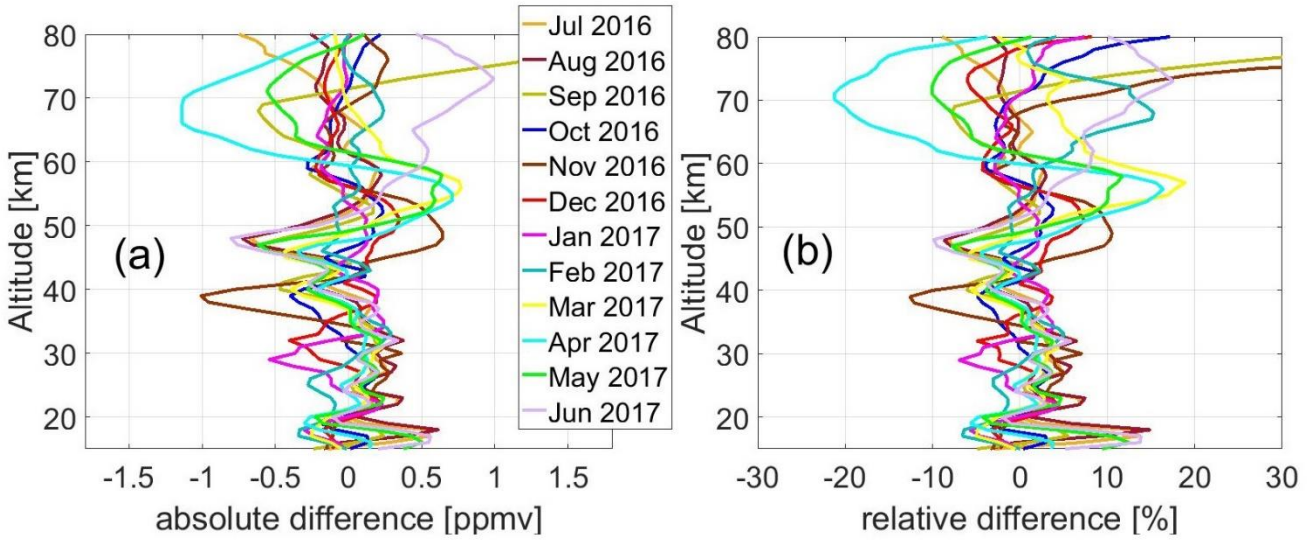

Figure 6.24: The absolute (a) and relative (b) monthly means of the difference between MLS convolved and MLS high resolution datasets (convolved minus high resolution profiles).

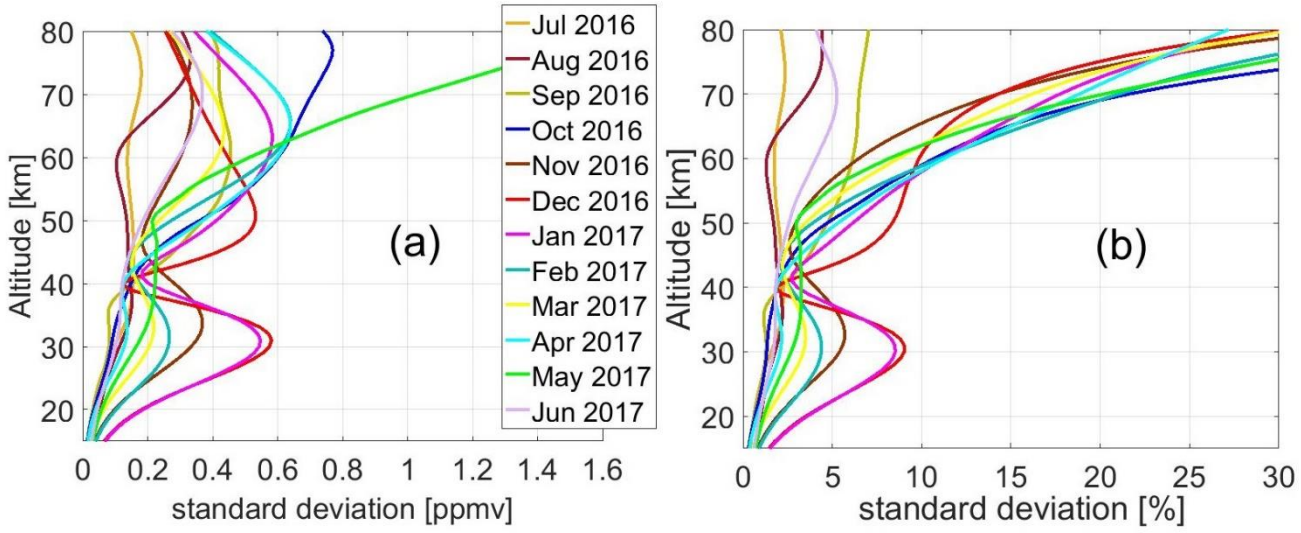

Figure 6.25: The absolute (a) and relative (b) value of the monthly standard deviation of VESPA-22 retrieved profiles.

6.5 Opacity and precipitable water vapor measurements

Deuber et al. (2005) provide an estimation of the amount of precipitable water vapor (PWV) presented in the atmosphere from opacity measurements using a simple technique. The PWV is measured in mm and is defined according to

$$PWV = \frac{\int_{z_0}^{z_{toa}} \rho(z)\,dz}{C_{H_2O}}\ , \tag{6.4}$$

where the integral is from the ground to the top of the atmosphere $\rho(z)$ is the water vapor density and C_{H_2O} is the water vapor mass for volume unit.

The atmospheric opacity in the 22.23 GHz region depends on the amount of water vapor in the atmosphere. Deuber et al. 2005 assume a direct proportionality between PWV and optical depth τ.

$$PWV = k_1\tau + k_2\ . \tag{6.5}$$

The coefficients k_1 and k_2 are site dependent and can be computed through a linear fit between VESPA-22 and HATPRO measurements (Rose and Czekala, 2009; Pace et al., 2015) installed at the THAAO. HATPRO can measure the PWV with an uncertainty of the order of 0.06 mm. The Eq. (6.5) does not take into account the contribution to the opacity due to the liquid water so it should be used only during fair weather.

In order to take into account the contribution of the air oxygen and nitrogen to the measured opacity, I simulated the opacity of a dry atmosphere during different periods of the year using ARTS. The meteorological profiles used for the calculation were the same used to compute the weighting functions for the retrievals (see Section 4.3). The calculations were performed on the altitude grid from the ground to 110 km of altitude. Figure 6.26 displays the opacity as function of frequency obtained from these simulations whereas Table 6.4 reports the mean values obtained averaging on the frequency grid of the different simulations. The dry contribution to the opacity τ_{dry} shows small variations during the year with respect to the total opacity, with a standard deviation less than 0.01. In the followings calculation the dry opacity is represented as constant with time and equal to the mean results of the simulation, equal to 0.016. This value is subtracted to all the VESPA-22 opacity measurements in order to take into account only the water vapor contribution τ_{H_2O} in the calculations:

$$\tau_{H_2O} = \tau - \tau_{dry} \tag{6.6}$$

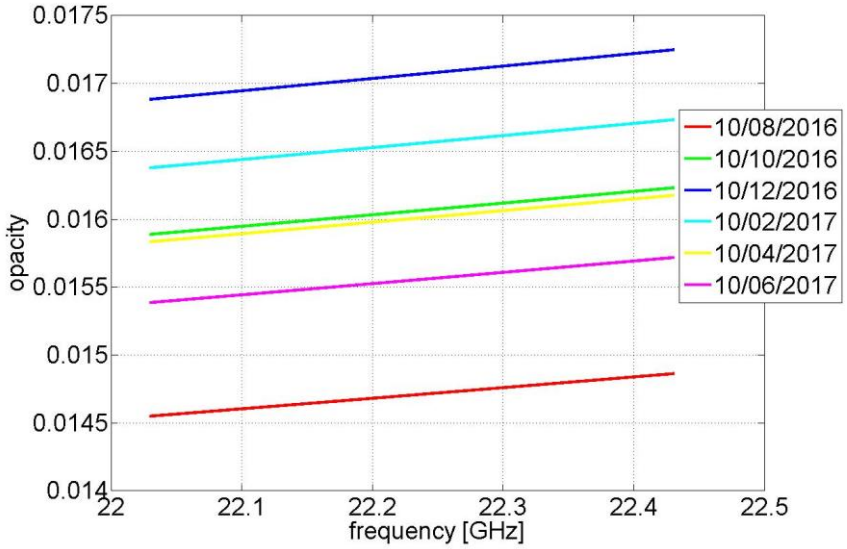

Figure 6.26: the opacity of a dry atmosphere simulated using ARTS during different periods of the year.

Table 6.4: the value of the dry atmosphere opacity averaged on the frequency range of the different simulations.

Date	opacity averaged on frequency
10/08/2016	0.0147
10/10/2016	0.0161
10/12/2016	0.0171
10/02/2017	0.0166
10/04/2017	0.0160
10/06/2017	0.0156

In Figure 6.27 the HATPRO PWV measurements from July 2016 to February 2017 are shown versus the VESPA-22 τ_{H_2O} measurements, both collected during fair weather. The green line is the result of a linear regression between the two datasets. The fit results are reported in Table 6.5.

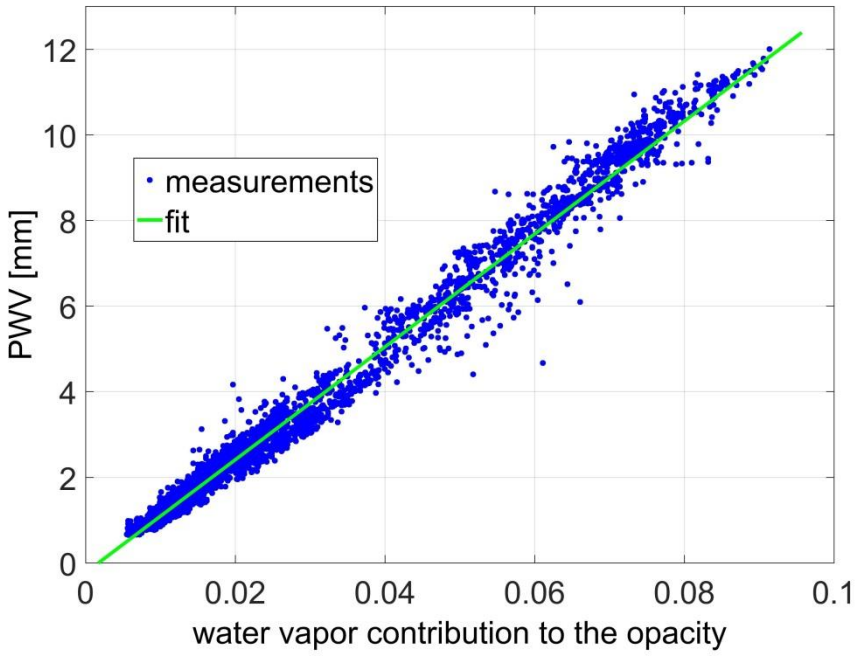

Figure 6.27: the PWV versus the τ_{H_2O} (blue dots) both measured during clear sky conditions by HATPRO and VESPA-22 respectively and the linear fit (green line).

Deuber et al. (2005) suggest a small correction to the linear relation shown in Eq. (6.5), taking into account the tropospheric temperature T_{trop}

$$PWV = a\,\tau + b\,\tau\,T_{trop} + c \ . \tag{6.7}$$

Eq. (6.7), as Eq. (6.5), does not take into account the contribution of clouds liquid water content to the measured opacity and therefore can be used only during cloud-free conditions.

The coefficients a, b and c used in the Eq. (6.7) are site dependent and can be calculated fitting the values of τ_{H_2O} measured by VESPA-22 and the T_{trop} estimated from surface temperature by means of Eq. (3.15) (see Section 3.8.1) with the PWV measurements of HATPRO during clear sky condition as in the linear fit. The results are reported in Table 6.6. For the calculations of the coefficients were used HATPRO data collected during fair weather from July 2016 to February 2017. Figure 6.28 displays the PWV as function of τ_{H_2O} for different values of T_{trop} as modeled by Eq. (6.7) using the parameters reported in Table 6.6.

Figure 6.29 displays the opacity measured by VESPA-22 during the twelve months analyzed. The peaks in the time sequence characterize the bad weather periods. The opacity is higher in summer and reaches a minimum in winter when the atmosphere is drier. In order to select the measurements collected during fair weather a threshold values as function of time was set. The threshold is equal to a three months moving average of the collected values multiplied by a factor 1.1; this operation exclude the opacity peaks and all the values collected during cloudy conditions. In Figure 6.29 the threshold is

represented by the red line, whereas the orange and blue dots are the measurements collected during cloudy and fair weather respectively.

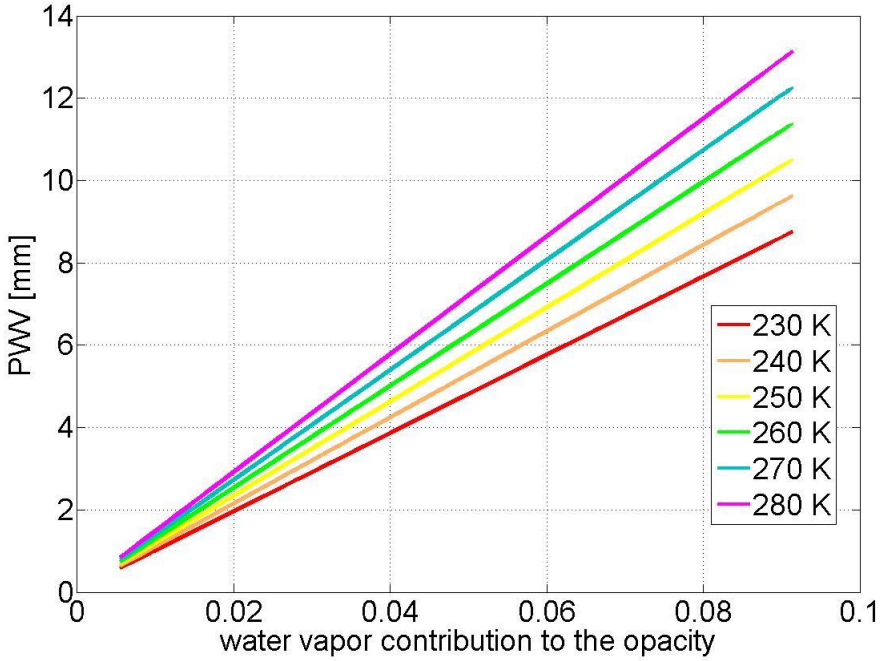

Figure 6.28: the PWV as function of $\tau_{H_{2O}}$ for different T_{trop} values as modeled by Eq. (6.7) with the parameters reported in Table 6.6.

Table 6.5: The linear fit results

k_1	131.8±0.4 [mm]
k_2	-0.22±0.02 [mm]
R^2	0.986

Table 6.6: Eq. (6.7) fit results

a	-126±11 [mm]
b	0.96±0.04 [mm K^{-1}]
c	0.06±0.02 [mm]
R^2	0.995

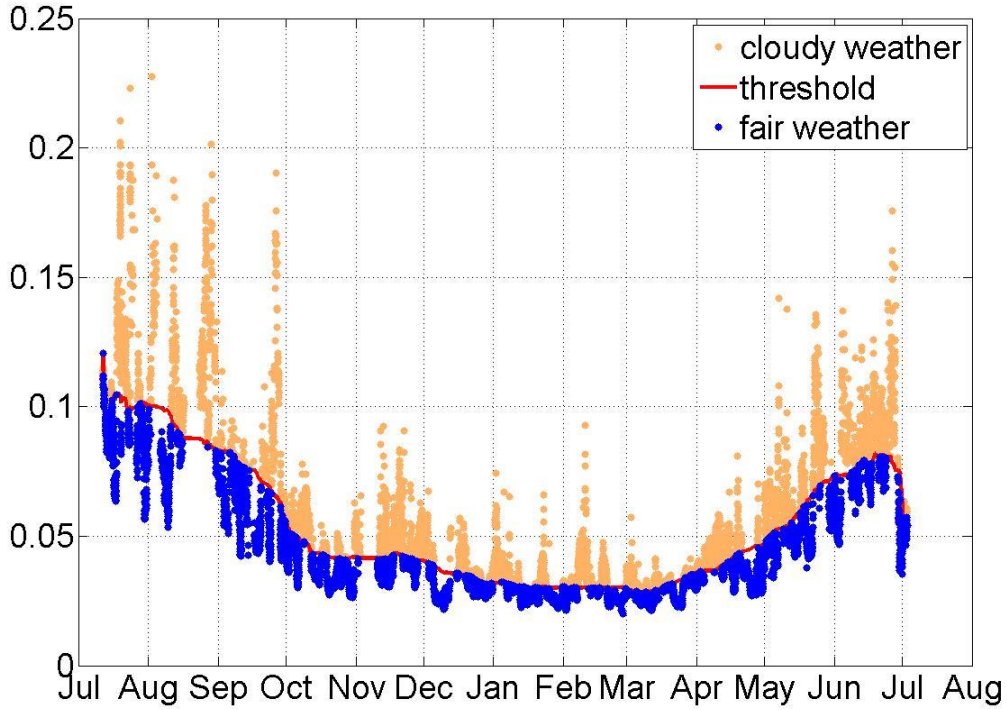

Figure 6.29: The opacity measured by VESPA-22. The orange dots are above the threshold (red line) and are identified as cloudy weather, whereas the blue dots, below the threshold, are identified as fair weather.

The values of T_{trop} versus time are displayed in Figure 6.30. Figure 6.31 shows the time series of the PWV measured by HATPRO during fair weather (red dots) used to calibrate the parameters of Eq. (6.7). The green dots display the measurement collected by HATPRO during cloudy weather and precipitation. These measurements were not used in the parameters calculation. The blue dots are the PWV values obtained from VESPA-22 measurements using Eq. (6.7) with the Table 6.6 coefficients during fair weather whereas the orange dots are the VESPA-22 measurements collected during cloudy weather. These last data are not reliable due to the not-negligible liquid water content in the atmosphere. The cyan stars are the measurement of PWV obtained by means of radiosondes. As expected, the PWV has a maximum in summer and decreases in winter. The peaks in the PWV sequence characterize the periods of precipitation or cloudy weather.

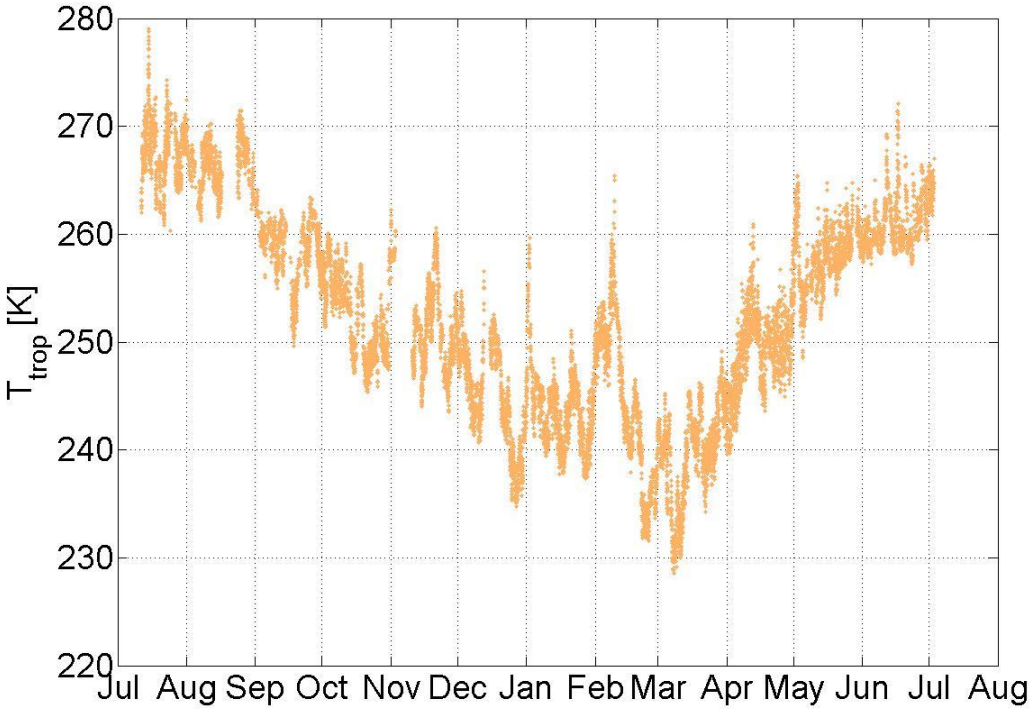

Figure 6.30: The tropospheric temperature estimated from surface temperature (see Section 3.8.1) T_{trop} used to analyze the VESPA-22 data.

In order to evaluate the uncertainty of the PWV values obtained by means of Eq. (6.7) in Figure 6.32 are shown the absolute and relative difference between VESPA-22 and HATPRO PWV measured with fair weather during the calibration period and between VESPA-22 PWV, HATPRO PWV and the PWV measured by means of radiosondes. The mean of the difference between VESPA-22 and HATPRO PWV time series is 0.024 mm (1.2%) whereas its standard deviation is 0.27 mm (8%). This last value can be used as the uncertainty of VESPA-22 PWV estimation. The mean difference between the estimate of PWV of VESPA-22 and the radiosondes measurements is about 0.1 mm (6%) while the difference standard deviation is about 0.3 mm (9%). The greater relative difference between VESPA-22 PWV and radiosondes measurements is due to the low amount of PWV (of the order of 1 mm) in the atmosphere although the absolute difference is comparable to the values measured in summer and autumn. Both VESPA-22 and HATPRO overestimate the PWV with respect to the radiosondes of about 0.2 mm during winter period.

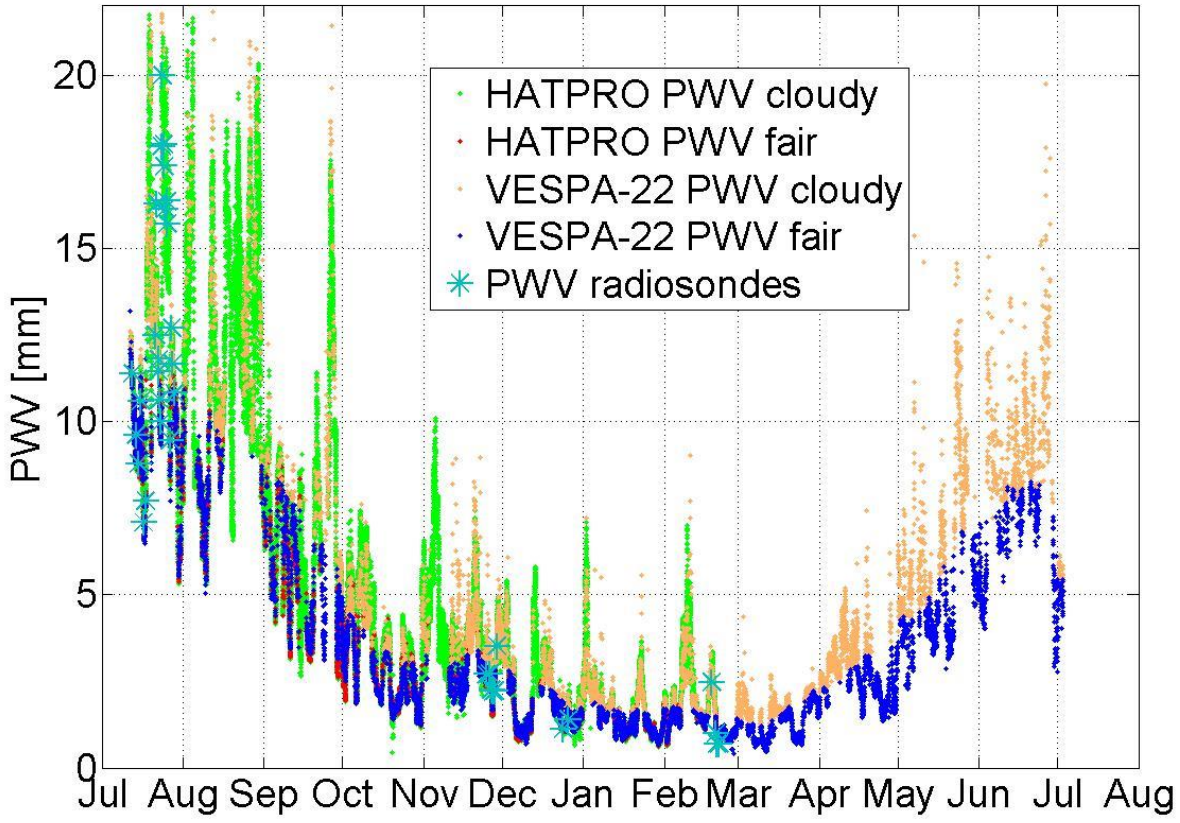

Figure 6.31: The PWV measured by HATPRO during fair weather (red dots) and cloudy weather (green dots) and the VESPA-22 measurements obtained by means of Eq. (6.7) during fair weather (blue dots) and cloudy weather. The periods of fair weather from July 2016 to February 2017 are used to calibrate the coefficients of the equation. The cyan stars are the PWV measurements obtained by means of radiosondes.

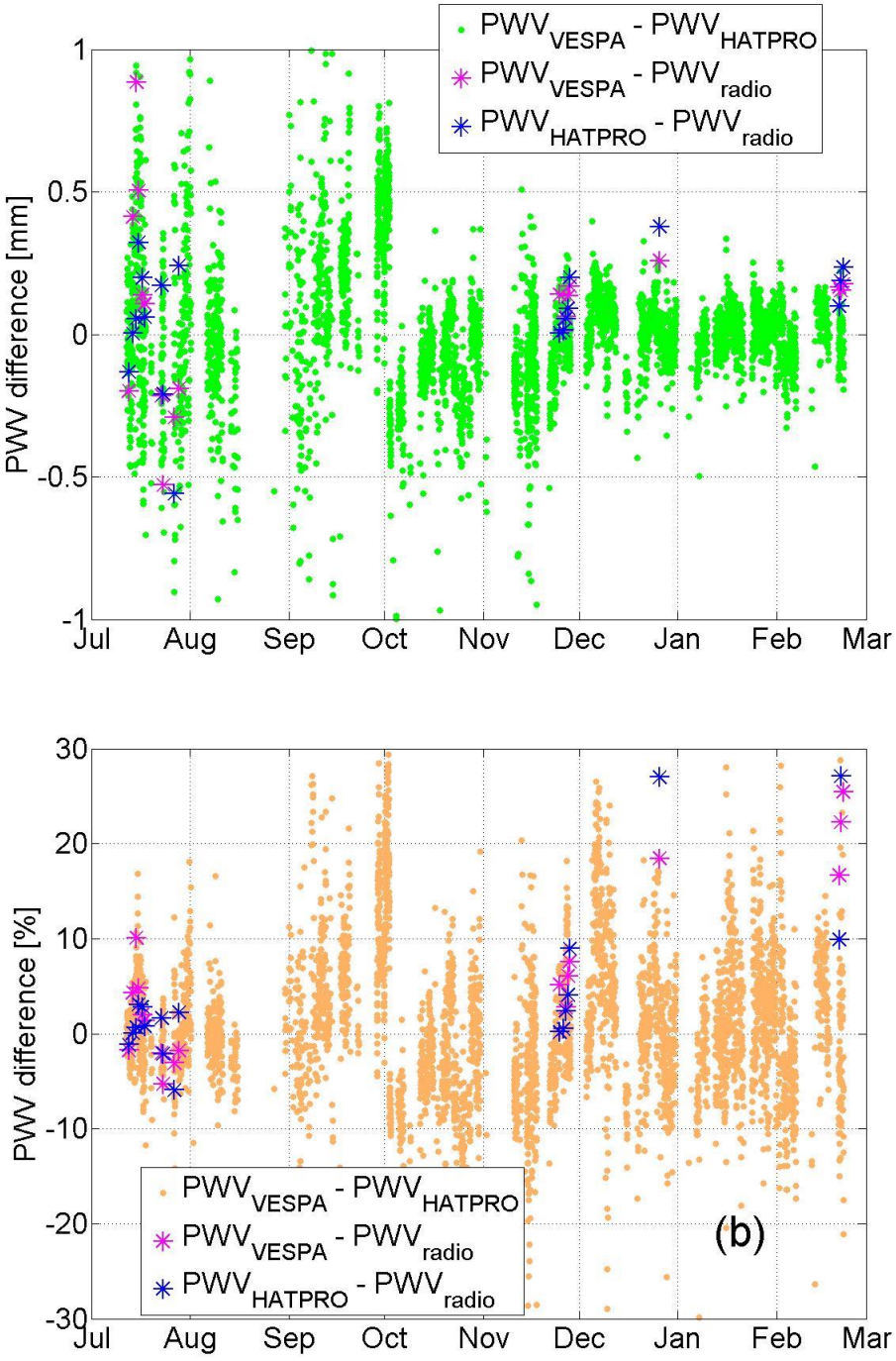

Figure 6.32: The absolute (a) and relative (b) difference between the PWV measured by HATPRO and the PWV calculated from VESPA-22 τ and T_{trop} by means of Eq. (6.7) and between VESPA / HATPRO PWV and radiosondes measurements during fair weather.

Summary and future work

This Ph.D. thesis is centered on the development and improvement of the acquisition software and the data analysis algorithms of the ground-based 22.23 GHz spectrometer VESPA-22 (water Vapor Emission Spectrometer for Polar Atmosphere at 22 GHz), on the instrument installation and on the analysis of the first year of data collected.

The instrument is characterized by a full width at half maximum encompassing 3.5°, granting the observation of the signal beam at angles as low as about 12° above the horizon. VESPA-22 observes the stratospheric emission by means of the balancing beam technique; a delrin sheet is employed as grey body absorber adding its emission to the reference beam.

There are no evident artifacts larger than 2 mK affecting the measured spectra. Instrument calibration is regularly performed using two noise diodes and occasionally liquid nitrogen. The brightness temperature of the diodes is measured during tipping curve calibrations and checked periodically against liquid nitrogen calibrations. The calibrating noise diode temperature is estimated with an uncertainty of 1.3%, evaluated confronting calibration results obtained by means of tipping curves and liquid nitrogen, and the standard deviation of the differences between the two noise diodes time series.

The main goals of my work were to improve, automate and develop the instrument acquisition software, the measurement procedures, the data analysis and retrieval algorithms, to analyze the data collected by the instrument and validate them against concurrent well validated data sets.

In order to achieve these tasks many features have been added to the VESPA-22 acquisition software, as the implementation of a second noise diode, the automatic mode that allows the instrument to execute the ordinary measurement operations automatically, the implementation of a meteorological station into the system, the development of the Sun Pointing procedure, the installation of two photodiodes, the development of the antenna repositioning procedure and the development of the alignment procedure. I also prepared the instrument for the installation at the THAAO and I participated in the preparatory and installation campaign at Thule, Greenland in February-March 2016 and July 2016.

VESPA-22 operated automatically with minimum need of maintenance for about one year, proving the robustness of the hardware and the acquiring system. As part of the Ph.D. work, an evaluation technique of the mean tropospheric temperature T_{trop} needed in the VESPA-22 calculations has been developed from the measured surface temperature, taking into account the seasonal variations through the measurements obtained by radiosondes launched during the year.

The retrieval algorithm of VESPA-22 spectral data is based on the optimal estimation technique; the retrieval altitude range is from 10 to 110 km of altitude, but the retrieved profiles from 24-hour integration spectra have a mean sensitivity larger than 0.8 from about 25 to 72 km of altitude and a mean vertical resolution from about 12 to about 23 km. The instrument is able to retrieve profiles from spectra integrated for less time reducing its sensitivity range and its vertical resolution. A

second-degree polynomial is added to the spectrum fit in order to simulate the effect of the upper tropospheric emissions and a possible delrin baseline.

I elaborated a procedure to estimate the measurement noise affecting the measured spectra through a two-step retrieval in which the noise is computed through the difference between a first step retrieval fit spectrum and the measured spectrum. In order to provide a forward model for the retrieval algorithm, as part of this thesis work, the ARTS software (Eriksson et al., 2013) was programmed to simulate the VESPA-22 measurement technique; ARTS produces a virtual measurement resulting in the difference of two simulated spectra, one at the zenith and another to an angle close to the horizon, just as a real VESPA-22 measurement. In order to improve the forward model tropospheric simulation in the calculations, the PWV measured by the HATPRO (Rose and Czekala, 2009) radiometer operating side by side with VESPA-22 at the THAAO is also taken into account.

As part of this thesis work, I analyzed the first year of data collected by the instrument at the THAAO. The uncertainties of the various parameters used in the data processing and calibration have been evaluated; the total uncertainty is the square sum of the contributions of calibration, pre-processing and spectroscopic parameters, measurement noise, and the uncertainty due to the use of the second order polynomial baseline. In the sensitivity range of VESPA-22 retrievals, the total uncertainty is about 5-6 % from 26 to 60 km increasing to about 12% at 72 km. The VESPA-22 and AURA/MLS (Waters et al., 2007) retrieved profiles during a period from July 2016 to July 2017 have been analyzed and compared. The VESPA-22 data used in the comparison are the results of retrievals from 24-hour integration spectra while MLS data are the daily mean profiles collected by MLS in a radius of 300 km around VESPA-22 observation point. VESPA-22 and MLS convolved datasets show a good correlation with a correlation coefficient of about 0.9 or higher. No significant bias between the two datasets was observed in the altitude range from 25 to 60 km, whereas in the altitude range from 60 to 72 km the value of the mean difference (VESPA – MLS) reaches -5% (-0.2 ppmv) at 72 km.

The results described in this work proved that VESPA-22 is capable of carrying out reliable water vapor stratospheric measurements during different seasons and weather conditions, even during spring and summer, although the data collected in these periods are affected by larger noise with respect to other seasons, due to larger amounts of tropospheric water vapor.

VESPA-22 is capable of observing the seasonal variations of the water vapor concentration vertical profile in the stratosphere, as for example the water vapor subsidence occurring inside and at the edge of the polar vortex. The monthly averages of VESPA-22 retrieved profiles and MLS convolved dataset in stratosphere and lower mesosphere are within 0.25 ppmv (4%); in the upper mesosphere the absolute value of the difference increases, reaching about -0.4 ppmv at 68 km in September and -0.35 ppmv at 75 km in January. The extreme low values of water vapor mixing ratio in winter mesosphere lead an increment of the absolute value of the relative difference of the winter months that reaches a maximum of -14% at 75 km, in January. Furthermore, VESPA-22 retrievals correctly represent the rapid variations that can occur in the stratosphere, as demonstrated by the large water vapor gradients measured in December and late January/early February and then during April and May (see Figure 6.12) by both VESPA-22 and Aura/MLS. The monthly analysis of the VESPA-22 dataset reveals a larger variability characterizing the mesosphere in particular during autumn, spring and summer.

The autumn-winter air mass descending rate has been evaluated by means of VESPA-22 measurements, resulting in a mean value of 0.28±0.15 km/day for mesospheric air. In stratosphere the measurements collected during October and January does not reveal a recognizable tendency due to the uncertainty afflicting the altitudes time-series; these are constant within their uncertainty. Although the altitudes of the vmr levels are lower in January, with respect to October, it is not possible to provide a good estimate of the downward velocity in stratosphere merging together the information of the period October-January due to the possible air mixing caused by the vortex shifting on December.

VESPA-22 measurements proved a useful tool to study the polar vortex development; in order to show this, the measurements of the period from the second half of November to the first half of February have been correlated with the potential vorticity over Thule (data from Goddard Space Center Automailer Service). In this period the vortex shifted away from Thule two times, in December and at the end of January. The correlation coefficient is about 0.8 for the 24, 31 and 35 km time series, while the upper altitudes reveal a negative correlation, according to the subsidence effect following the polar vortex.

I applied the technique described by Deuber et al. (2005) for the estimation of PWV from the measured opacity and tropospheric temperature to the VESPA-22 dataset. The coefficients needed to compute the PWV were obtained fitting VESPA-22 and HATPRO measurements collected during the calibration period from July to February with fair weather condition. This technique allows VESPA-22 to estimate the PWV during clear sky conditions, with an uncertainty of about 8% obtained from the difference between HATPRO measured PWV and VESPA estimations during the calibration period.

The peak in the mean residual in correspondence to the emission line peak, shown in Figure 6.8, could suggest the needing of a further improvement in the forward model simulation of the mesosphere. A comparison between VESPA-22 and other ground-based spectrometers data analysis and retrieval algorithms could be interesting to investigate the dependence of the measurement results from the algorithms employed for the analysis. The retrieval algorithm could be improved in order to obtain some information on the water vapor concentration profile on the lower part of the stratosphere, above 25 km.

The Cimel photometer installed at the THAAO provides measurements of PWV (Holben et al., 1998, Bertagnolio, 2013). It should be interesting to compare CIMEL and VESPA-22 PWV measurements and the PWV obtained from the AIRS/Aqua dataset (Fetzer at al., 2003). The data collected could be used to investigate the evolution of both water vapor concentration in the atmosphere and dynamic processes such as the polar vortex development in order to monitor the climate changes affecting the Arctic region on pluriannual scale, due to the long lifetime characterizing the ground-based spectrometers. The data collected could be analyzed together with the results of the other instruments installed at the THAAO to improve the knowledge of the Arctic atmosphere. The instruments installed at the THAAO provide measurements of water vapor concentration in both troposphere and mid atmosphere, temperature profiles, clouds composition, trace gases concentration and upwelling and downwelling radiation at the surface in both visible and infrared range. All this information composes a quite complete picture of the atmosphere and could be used to study the interconnection between the various atmospheric properties and the goodness and reliability of radiative transfer and climatic models.

Aknowledgements

The One who calls you is faithful, and He will fulfil His promises. 1 Thessalonians 5:25

During the time of this thesis I received counsels and helps from many people. I would like to thank:

Giovanni Muscari for his precious advices and teachings, his patience and friendship and for the possibility to live this adventure together.

Prof. Wolfango Plastino that supported and believed in this project from the first time we met.

Alcide di Sarra, Giandomenico Pace, Daniela Meloni, Tatiana Di Iorio Marco Cacciani and the little Gaia and Niko (the youngest Arctic explorer).

Pietro Paolo Bertagnolio, Irene Fiorucci and Massimo Mari: they did a lot of work on VESPA-22 before me and they helped me many times.

I received a lot of help also from the INGV personnel, in particular Michael Pezzopane, Enrico Zuccheretti and my friends Alessio Pignalberi, Maria Carmela Mingolla and Dario Sabbagh.

I would like to thank also all the known and unknown reviewers whose comments improved the quality of this work.

A special thank to my girlfriend Federica, my brothers, my friends and all my family who are with me on this journey.

References

Alley, R. B., Nordhaus, W. D., Overpeck, J. T., Peteet, D. M., Pielke Jr., R. A., PierreHumbert, R. T., Rhines, P. B., Stocker, T. F., Talley, L. D., and Wallace, J. M.: Abrupt climate change, Science 299, 2005–2010, 2003.

Bertagnolio, P. P., Muscari, G. and Baskaradas, J.: Development of a 22 GHz ground-based spectrometer for middle atmospheric water vapor monitoring, European Journal of Remote Sensing 45.1, 51-61, doi: 10.5721/EuJRS20124506, 2012.

Bertagnolio, P. P.: Osservazione del vapore acqueo nell'atmosfera artica Studio dell'impatto radiativo con misure da terra e sviluppo di un nuovo spettrometro a microonde, Scuola di Dottorato in Scienze Polari XXV Ciclo, 2013.

Bevilacqua, R. M., Wilson, W. J., Ricketts, W. B., Schwartz, P. R., and Howard, R. J.: Possible seasonal variability of mesospheric water vapor, Geophysical Research Letters, 12(6), 397-400, 1985.

Brewer, A. W.: Evidence for a world circulation provided by measurements of helium and water vapour distribution in the stratosphere, Quarterly Journal of the Royal Meteorological Society, *75*(326), 351-363, 1949.

Cazzoli, G., Puzzarini, C., Buffa, G., and Tarrin, O.; Experimental and theoretical investigation on pressure-broadening and pressure-shifting of the 22.2 GHz line of water, Journal of Quantitative Spectroscopy and Radiative Transfer, 105, 438–449, doi: 10.1016/j.jqsrt.2006.11.003, 2007.

de Zafra, R. L.: The Ground-Based Measurement of Stratospheric Trace Gases Using Quantitative Millimeter Wave Emission Spectroscopy, in Diagnostic Tools in Atmospheric Physics: Varenna on Lake Como, Villa Monastero, 22 June-2 July 1993, edited by G. Fiocco and G. Visconti, Società Italiana di Fisica, pp. 23–54, 1995.

Deuber, B., Kampfer, N., and Feist, D. G.: A new 22-GHz radiometer for middle atmospheric water vapor profile measurements, IEEE Transactions on Geoscience and Remote Sensing, 42(5), 974-984, doi: 10.1109/TGRS.2004.825581, 2004.

Deuber, B., Morland, J., Martin, L., and Kämpfer, N.: Deriving the tropospheric integrated water vapor from tipping curve–derived opacity near 22 GHz, Radio science, 40(5), doi: 10.1029/2004RS003233, 2005.

Di Biagio, C., di Sarra, A., and Meloni, D.: Large atmospheric shortwave radiative forcing by Mediterranean aerosols derived from simultaneous ground based and spaceborne observations and dependence on the aerosol type and single scattering albedo, Journal of Geophysical Research: Atmospheres, 115(D10), doi: 10.1029/2009JD012697, 2010.

Di Biagio, C., di Sarra, A., Eriksen, P., Ascanius, S. E., Muscari, G., and Holben, B.: Effect of surface albedo, water vapour, and atmospheric aerosols on the cloud-free shortwave radiative budget in the Arctic, Climate dynamics, *39*(3-4), 953-969, 2012.

di Sarra, A., Bernardini, L., Cacciani, M., Fiocco, G., and Fuà, D.: Stratospheric aerosols observed by lidar over northern Greenland in the aftermath of the Pinatubo eruption, Journal of Geophysical Research: Atmospheres, 103(D12), 13873-13891, doi: 10.1029/98JD00901, 1998.

di Sarra, A., Cacciani, M., Chamard, P., Cornwall, C., DeLuisi, J. J., Di Iorio, T., Disterhoft, T., Fiocco, G., Fuà, D., and Monteleone, F.: Effects of desert dust and ozone on the ultraviolet irradiance at the Mediterranean island of Lampedusa during PAUR II, Journal of Geophysical Research: Atmospheres, 107(D18), doi: 10.1029/2000JD000139, 2002.

Eriksson, P., Buehler, S. A., Davis, C. P., Emde, C., and Lemke, O.: ARTS, the atmospheric radiative transfer simulator, version 2, Journal of Quantitative Spectroscopy and Radiative Transfer, 112(10), 1551-1558, doi: 10.1016/j.jqsrt.2011.03.001, 2011.

Fetzer, E., McMillin, L.M., Tobin, D., Aumann, H. H., Gunson, M.R., McMillan, W.W., Hagan, D. E., Hofstadter, M. D., Yoe, J., Whiteman, D. N., Barnes, J. E., Bennartz, R., Vomel, H., Walden, V., Newchurch, M., Minnett, P. J., Atlas, R., Schmidlin, F., Olsen, E. T., Goldberg, M. D., Zhou, S., Ding, H. J., Smith, W. L., and Revercomb, H.: AIRS/AMSU/HSB validation, Geoscience and Remote Sensing, IEEE Transactions on 41, 2, 418-431, 2003.

Fiedler, J., G. Baumgarten, and F. J. Lübken: NLC observations during one solar cycle above ALOMAR, Journal of Atmospheric and Solar-Terrestrial Physics, 71, 424-433, 2009.

Forster, P. M. d. F. and K. P. Shine: Assessing the climate impact of trends in stratospheric water vapor. Geophysical Research Letters, 29(6), doi: 10.1029/2001GL013909, 2002.

Forster, P., Ramaswamy, V., Artaxo, P., Berntsen, T., Betts, R., Fahey, D., Haywood, J., Lean, J., Lowe, D., Myhre, G., Nganga, J., Prinn, G. R. R., Schulz, M., and Dorland, R. V.: Climate Change 2007: The Physical Science Basis. Contribution of Working Group I to the Fourth Assessment Report of the Intergovernmental Panel on Climate Change, chapter 2, Cambridge University Press, Cambridge, United Kingdom and New York, NY, USA, 2007.

Gomez, R. M., Nedoluha, G. E., Neal, H. L., & McDermid, I. S.: The fourth-generation Water Vapor millimeter-Wave Spectrometer. Radio Science, 47(1), doi: 10.1029/2011RS004778, 2012.

Gori, F: Elementi di Ottica, Accademica, 1997.

Haefele, A., De Wachter, E., Hocke, K., Ka¨mpfer, N., Nedoluha, G. E., Gomez, R. M., Eriksson, P., Forkman, P., Lambert, A., and Schwartz, M. J.: Validation of ground-based microwave radiometers at 22 GHz for stratospheric and mesospheric water vapor, J. Geophys. Res., 114, D23305, doi: 10.1029/2009JD011997, 2009.

Haefele, A.: Measurements of Tropospheric, Stratospheric and Mesospheric Water Vapor by Ground Based Microwave Spectro Radiometry. Inauguraldissertation der Philosophisch-naturwissenschaftlichen Fakultät der Universität Bern, 2009.

Held, I. M., and Soden, B.: Water vapor feedback and global warming. Annu. Rev. Energy Environ., 25, 441-475, 2000.

Holben, B. N., Eck, T. F., Slutsker, I., Tanre, D., Buis, J. P., Setzer, A., Vermote, E., Reagan, J. A., Kaufman, Y. J., Nakajima, T., Lavenu, F., Jankowiak, I. and Smirnov, A.: AERONET—A Federated Instrument Network and Data Archive for Aerosol Characterization, Remote Sensing of Environment, 66(1), 1–16, doi:10.1016/S0034-4257(98)00031-5, 1998.

Holton, R., J, Haynes, H. P., Mckintyre, M. E., Douglass, A., R., Rood, R., B. and Poster, L.: Stratosphere-Troposphere Exchange, Review of Geophysics, 1995.

Hurst, D. F., Oltmans, S. J., Vomel, H., Rososenlof, K. H., Davis, S. M., Ray, E. A., Hall, E. G., Jordan, A. F.: Stratospheric water vapor trends over Boulder, Colorado: Analysis of the 30 year Boulder record, Journal of Geophysical Research: Atmospheres, 2011.

Jannsen, M. A.: Atmospheric remote sensing by microwave radiometry, John Wiley and Sons, Inc. 1993.

Jones, P. D., New, M., Parker, D. E., Martin, S., and Rigor, I. G.: Surface air temperature and its variations over the last 150 years, Reviews Geophysics 37, 173–199, 1999.

Kämpfer, N., Nedoluha, G., Haefele, A. and DeWachter, E.: Microwave Radiometry. In Monitoring Atmospheric Water Vapour (pp. 71-93), ISSI Scientific Report Series 10, Springer New York, doi 10.1007/978-1-4614-3909-7_5, 2013.

Lahoz, W. A., Carr, E. S., Froidevaux, L., Harwood, R. S., Kumer, J. B., Mergenthaler, J. L., Peckham, G. E., Read, W. G., Ricaud, P. D., Roche, A. E., and Waters, J. W.: Hemisphere Mid-Stratosphere Vortex Processes Diagnosed from H2O, N2O and Potential Vorticity. Geophysical Research Letters, 20(23), 2671-2674, 1993.

Lait, L., Newman, P., and Schoeberl, R.: Using the Goddard Automailer, NASA Goddard Space Flight Cent., Greenbelt, Md. Available at http://code916.gsfc.nasa.gov/Dataservices/, 2005.

Liebe, H. J.: MPM – An atmospheric millimeter-wave propagation model, International Journal of Infrared and millimeter waves, 10, 631–650, doi: 10.1007/BF01009565, 1989.

Livesey, N. J., Read, W. G., Wagner, P. A., Froidevaux, L., Lambert, A., Manney, G. L., Millan Valle, L. F., Pumphrey, H. C., Santee, M. L., Schwartz, M. L., Wang, S., Fuller, R. A., Jarnot, R. F., Knosp, R. F., and Martinez, E.: Earth Observing System (EOS) Aura Microwave Limb Sounder (MLS) Version 4.2x Level 2 data quality and description document. Jet Propulsion Laboratory California Institute of Technology, Pasadena, California, 2015.

Manney, G. L., Santee, M. L., Rex, M., Livesey, N. J., Pitts, M. C., Veefkind, P, Nash, E., R., Wohltmann, I., Lehmann, R. Froidevaux, L., Poole, L., Schoeberl, M., R., Haffner, D., P., Davies, J., Dorokhov, V., Gernandt, H., Johnson, B., Kivi, R., Kyro, E., Larsen, N., Pieternel, L., F., Makshtas, A., McElroy, T., C., Nakajima, H., Parrondo, M., C., Tarasick, D., W., von der Gathen, P., Walker K., A. and Zinoview, N., S.: Unprecedented Arctic ozone loss in 2011, Nature, 478(7370), 469, doi: 10.1038/nature10556, 2011.

Muscari, G., di Sarra, A. G., de Zafra, R. L., Lucci, F., Baordo, F., Angelini, F., and Fiocco, G.: Middle atmospheric O3, CO, N2O, HNO3, and temperature profiles during the warm Arctic winter 2001–2002. Journal of Geophysical Research: Atmospheres, 112(D14), doi: 10.1029/2006JD007849, 2007.

Nedoluha, G. E., Bevilacqua, R. M., Gomez, R. M., Thacker, D. L., Waltman, W. B., and Pauls, T. A.: Ground-based measurements of water vapor in the middle atmosphere, Journal of Geophysical Research 100.D2, 2927-2939, doi: 10.1029/94JD02952, 1995.

Nedoluha, G. E., Bevilacqua, R. M., Gomez, R. M., Hicks, B. C., and Russell, J. M.: Measurements of middle atmospheric water vapor from low latitudes and midlatitudes in the Northern Hemisphere, 1995–1998, Journal of Geophysical Research: Atmospheres, 104(D16), 19257-19266, doi: 10.1029/1999JD900419, 1999.

Nedoluha, G. E., Gomez, R. M., Hicks, B. C., Helmboldt, J., Bevilacqua, R. M., and Lambert, A.: Ground−based microwave measurements of water vapor from the midstratosphere to the mesosphere, Journal of Geophysical Research, 116, D02309, doi: 10.1029/2010JD014728, 2011.

Pace, G., Junkermann, W., Vitali, L., Di Sarra, A., Meloni, D., Cacciani, M., Cremona G., Iannarelli A. M., and Zanini G.: On the complexity of the boundary layer structure and aerosol vertical distribution in the coastal Mediterranean regions: a case study. Tellus B, 67, doi: 10.3402/tellusb.v67.27721, 2015.

Parrish, A., de Zafra, R. L., Solomon, P. M., and Barrett, J. W.: A ground- based technique for millimeter wave spectroscopic observations of stratospheric trace constituents, Radio Science, *23*(2), 106-118, doi: 10.1029/RS023i002p00106, 1988.

Pickett, H. M., Poynter, R. L., Cohen, E. A., Delitsky, M. L., Pearson, J. C., and Müller, H. S. P.: Submillimeter, millimeter, and microwave spectral line catalog, Journal of Quantitative Spectroscopy and Radiative Transfer, 60(5), 883-890., doi: 10.1016/S0022-4073(98)00091-0, 1998.

Oltmans, S. J., Vömel, H., Hofmann, D. J., Rosenlof, K. H., and Kley, D.: The increase in stratospheric water vapor from baloonborne frostpoint hygrometer measurements at Washington, D. C., and Boulder, Colorado, Geophysical Research Letters, vol. 27, no. 21, 3453–3456, doi: 10.1029/2000GL012133, 2000.

Randel, W. J., Wu, F., and Gaoen, D. J.: Interannual variability of the tropical tropopause derived from radiosonde data and NCEP reanalyses. Journal of Geophysical Research, 105(D12):15, 509-15,523, 2000.

Randel, W. J., Wu, F., Vömel, H., Nedoluha, G. E., and Forster, P.: Decreases in stratospheric water vapor after 2001: Links to changes in the tropical tropopause and the Brewer- Dobson circulation. Journal of Geophysical Research, 111(D12312), doi: 10.1029/2005JD006744, 2006.

Rees, D., Barnett, J. J., and Labitzke, K.: COSPAR International Reference Atmosphere: 1986. Pt. 2: Middle atmosphere models, Advances in space research, 10, 1990.

Remsberg, E., Russell III, J. M., Gordley, L. L., Gille, J. C., and Bailey, P. L.: Implications of the Stratospheric Water Vapor Distribution as Determined from the Nimbus 7 LIMS Experiment, Journal of the atmospheric sciences, 41, 2934-2945, doi: 10.1175/1520-0469(1984)041<2934:IOTSWV>2.0.CO; 2, 1984.

Rodgers, C. D.: Inverse method for atmospheric sounding, Series on atmospheric, oceanic and Planetary Physics – Vol. 2, edited by: Taylor, F. W., World Scientific Publishing Co. Pte LTd, Singapore, 2000.

Rose, T. and Czekala, J., RPG-HATPRO Radiometer Operating Manual, Radiometer Physics GmbH, Version, 2009

Rosenkranz, P. W.: Water vapor microwave continuum absorption: A comparison of measurements and models, Radio Science, 33(4), 919–928, doi: 10.1029/98RS01182, 1998.

Rosenlof, K. H., Oltmans, S. J., Kley, D., Russell, J. M., Chiou, E. W., Chu, W. P., D. G. Johnson, Kelly K. K., Michelsen H. A., Nedoluha G. E., Remsberg, E. E., Toon G. C., and McCormick M. P.: Stratospheric water vapor increases over the past half-century, Geophysical Research Letters, 28(7), 1195-1198, doi: 10.1029/2000GL012502, 2001.

Rosenlof, K. H., and G. C. Reid. Trends in the temperature and water vapor content of the tropical lower stratosphere: Sea surface connection, Journal of Geophysical Research, 113(D06107), doi: 10.1029/2007JD009109, 2008.

Rothman, L. S., Gordon, I. E., Babikov, Y., Barbe, A., Benner, D. C., Bernath, P. F., Birk M., Bizzocchi L., Boudon V., Brown L. R., Campargue A. Chance K., Cohen E. A., and Coudert L. H.: The HITRAN2012 molecular spectroscopic database, Journal of Quantitative Spectroscopy and Radiative Transfer, 130, 4-50, doi: 10.1016/j.jqsrt.2013.07.002, 2013.

Schwartz, M. J., Lambert, A., Manney, G. L., Read, W. G., Livesey, N. J., Froidevaux, L., Ao, C., O., Berhat P. F., Boone, C. D., Cofield, R. E., Daffer, W. H. Drouin, B. J., Fetzer E. J., Fuller, R. A., Jarnot, R. F., Jiang, J. H., Jiang, Y. B., Knosp B. W., Kruger, K., Li, J. L. F., Mlinczak, M. G., Pawson, S., Russel, J. M., Santee, M. L., Snyder, W. V., Stek, P. C., Thurstan, R. P., Tompkins, A. M., Wagner P. A., Walker, K. A., Waters, J. W., and Wu, F. L.: Validation of the Aura Microwave Limb Sounder temperature and geopotential height measurements, Journal of Geophysical Research: Atmospheres, 113(D15), doi: 10.1029/2007JD008783, 2008.

Seele, C.: Bodengebundene Mikrowellenspektroskopie vonWasserdampf in der mittleren polaren Atmosph¨are, Ph.D. thesis, University of Bonn, 1999.

Serreze, M. C., and Francis, J. A.: The Arctic amplification debate, Climatic change, *76*(3-4), 241-264, doi: 10.1007/s10584-005-9017-y, 2006.

Simmons, A. J., A. Untch, C. Jakob, P. Kåallberg, and P. Undén: Stratospheric water vapor and tropical tropopause temperatures in ECMWF analyses and multi-year simulations. Quarterly Journal of the Royal Meteorological Society, 125, 353-386, 1999.

Soden, B. J., D. L. Jackson, V. Ramaswamy, M. D. Schwarzkopf, and X. Huang. The Radiative Signature of Upper Tropospheric Moistening, Science, 310: 841-844, 2005.

Solomon, S.: Stratospheric ozone depletion: A review of concepts and history, Reviews of Geophysics, 37(3), 275-316, doi: 10.1029/1999RG900008, 1999.

Straub, C., Murk, A., and Kampfer, N.: MIAWARA-C, a new ground based water vapor radiometer for measurement campaigns, Atmospheric Measurement Technique 3(5), 1271, doi: 10.5194/amt-3-1271-2010, 2010.

Solomon, S., Rosenlof, K. H., Portmann, R. W., Daniel, J. S., Davis, S. M., Sanford, T. J., and Plattner, G. K.: Contributions of stratospheric water vapor to decadal changes in the rate of global warming, Science, 327(5970), 1219-1223, doi: 10.1126/science.1182488, 2010.

Summers, M. E. and R. R. Conway. Insights into Middle Atmospheric Hydrogen Chemistry from Analysis of MAHRSI OH Observations, AGU, 2000.

Summers, M. E. and Siskind, D. E.: Surface recombination of O and H2 on meteoric dust as a source of mesospheric water vapor, Geophysical Research Letters, 26(13): 1837-1840, 1999.

Teniente, J., Goñi, D., Gonzalo, R., and del Río, C.: Choked Gaussian antenna: Extremely low sidelobe compact antenna design, IEEE Antennas and Wireless Propagation Letters, 1(1), 200-202, doi: 10.1109/LAWP.2002.807959, 2002.

Tschanz, B., Straub, C., Scheiben, D., Walker, K. A., Stiller, G. P., and Kämpfer, N.: Validation of middle-atmospheric campaign-based water vapour measured by the ground-based microwave radiometer MIAWARA-C, Atmospheric Measurement Techniques, 6(7), 1725-1745, doi: 10.5194/amt-6-1725-2013, 2013.

Waters, J. W., Froidevaux, L., Harwood, R. S., Jarnot, R. F., Pickett, H. M., Read, W. G., Siegel, P., Cofield, R. E., Filipiak, M., Flower, D., Holden, J., Lau, G. K., Livesey, N. J., Manney, G. L., Pumphrey, H., Santee, M. L.,Wu, D. L., Cuddy, D. T., Lay, R. R., Loo, M., Perun, V. S., Schwartz, M. J., Stek, P. C., Thurstans, R. P., Boyles, M., Chandra, S., Chavez, M., Chen, G.-S., Chudasama, B., Dodge, R., Fuller, R. A., Girard, M., Jiang, J. H., Jiang, Y. B., Knosp, B. W., LaBelle, R. C., Lam, J., Lee, K. A., Miller, D., Oswald, J. E., Patel, N., Pukala, D., Quintero, O., Scaff, D., Snyder,W. V., Tope, M.,Wagner, P. A., and Walch, M.: The Earth Observing System Microwave Limb Sounder (EOS MLS) on the Aura satellite, IEEE Transactions on Geoscience and Remote Sensing, 44, 1075– 1092, doi:10.1109/TGRS.2006.873771, 2006.

WMO/UNEP International Scientific Assessments of Ozone Depletion: 2010, avaible at https://www.esrl.noaa.gov/csd/assessments/ozone/2010/, 2010.